UNIVERSITÉ DE LORRAINE
FACULTÉ DES SCIENCES ET TECHNOLOGIES
École Doctorale SESAMES

THESIS

Submitted for the degree of

Doctor of Philosophy of the University of Lorraine

In Chemistry, Speciality Crystallography

By

Mariya BREZGUNOVA

Charge Density Analysis and Topological Properties of Weak Intermolecular Interactions – Halogen and Chalcogen Bonding – and their Comparison with Hydrogen Bonding

Public defense **6 March 2013**

Members of the Jury:

Referees:

    Prof. Tayur N. GURU ROW   Professor, Indian Institute of Science, Bangalore, India

    Dr. Piero MACCHI   *Privat Dozent*, University of Bern, Bern, Switzerland

Examinators:

    Dr. Marc FORMIGUÉ   *Directeur de Recherche* CNRS, MaCSE, "UMR CNRS 6226" University of Rennes 1

    Prof. Xavier ASSFELD   Professor, SRSMC "UMR CNRS 7565", University of Lorraine, Nancy

    Prof. Claude LECOMTE   Professor, CRM² "UMR CNRS 7036", University of Lorraine, Nancy

Supervisor:

    Prof. Enrique ESPINOSA   Professor, CRM² "UMR CNRS 7036", University of Lorraine, Nancy

Guests:

    Dr. Slimane DAHAOUI   *Maître de conférences*, CRM² "UMR CNRS 7036", University of Lorraine, Nancy
    (Co-Supervisor)

    Dr. Emmanuel AUBERT   *Maître de conférences*, CRM² "UMR CNRS 7036", University of Lorraine, Nancy

Laboratoire de Cristallographie, Résonance Magnétique et Modélisations UMR CNRS 7036

Acknowledgements

The realization of this Ph.D. thesis would not be possible without a kind support and help of a large number of people. And here I would like to thank each of them.

First of all, I would like to express my sincere gratitude to my supervisors – Prof. Enrique ESPINOSA and Dr. Slimane DAHAOUI. Without their continuous support, understanding, tactful guidance and endless patience this thesis would not have been possible. Passing on some of their impressive knowledge to me, they helped me to develop independent thinking and research skills. They gave me a possibility to interact with people around the world during the scientific schools and a conference that I attended. It has been a great experience that I will always remember with deep appreciation.

I sincerely express my thanks and regards to the *directors' team* of the CRM² laboratory – Prof. Claude LECOMTE and Prof. Dominik SCHANIEL – for giving me the opportunity to undertake this research project.

I am thankful to Dr. Emmanuel AUBERT for introducing me to the subtleties of theoretical and computational chemistry and for our discussions, his valuable ideas and useful tips and tricks for this field.

I would like to show my appreciation to Dr. Christian JELSCH for opening the doors of charge density world for me. The continued improvements in MoPro really 'made my Ph.D. life better'. I would like to acknowledge the help of Dr. Benoît GUILLOT. His straightforward approach to problems and his art of imparting knowledge and skills have been instructive and inspirational to me.

It is my great pleasure to thank Dr. Marc FORMIGUÉ and his group for the successful collaboration on the H*alogen Bonding* project and for his never-ending enthusiasm and encouragement. I am grateful to Dr. János ÁNGYÁN for his active participation in the development of the *Halogen Bonding* project. I wish to express my warm regards to Dr**.** Pierre FERTEY for taking care of me during my visit to the synchrotron SOLEIL. I am also thankful to Prof. Gautam R. DESIRAJU and Prof. Philip COPPENS for showing their interest on my research work and for fruitful discussions during their visit to our laboratory.

I wish to thank *École Doctorale* SESAMES and its director Prof. Xavier ASSFELD for being always ready to help and answer all the possible questions. The *European Doctoriales* and the annual scientific meetings of the Ph.D. students gave me the opportunity of experience exchange with the other students.

I wish to express my sincere thanks to Abdelatif DOUDOUH, for his accurate crystal growth experiments. I am grateful for Bruno ROCK and Cristian IORDACHE for their computer troubleshooting skills. Special thanks to the secretaries of the CRM² laboratory – Valérie RICHALET, Anne CLAUSSE and Christine MAY for their help, tenderness and kindness.

It has been a very pleasant experience to work in the warm and friendly atmosphere of the laboratory CRM² with the support and encouragement from all my senior lab-mates, Ph.D.

students, and post-docs. I sincerely thank my senior lab-mates Pierrick DURAND, El-Eulmi BENDEIF, Nicolas CLAISER, Emmanuel WENGER, Sébastien LEBEGUE, Massimo NESPOLO, Paul ALLÉ, Pascal PAROIS. I want especially to thank my comrades Maxime, Kuan-Ying, Bertrand, Agnieszka, Bastien, Katya, Isabella, Dorothee, Dorothea, Amine and Thomas for our interesting discussions and for the good times we spent together. I think we have learnt many things from each other.

I would like to thank all my friends for helping and supporting me unconditionally on this long and sometimes difficult journey and for being with me whenever I needed. The memories and stories from time we spent together would fill a book thicker than this one.

Last, but most importantly, I wish to thank my beloved parents and family for their never-ending support, care and love. I would like to express my heartful thanks to my husband, Anton MARKOVETS, for his patience and love. He encouraged and inspired me every time, teaching to never give up no matter how tough it goes.

Mariya Brezgunova

Nancy, France
6 March 2013

Content

General introduction

One of the principal objects of theoretical research in any department of knowledge is to find the point of view from which the subject appears in its greatest simplicity
J. W. Gibbs

Everything must be made as simple as possible
But not simpler.
A. Einstein

1. Motivation

Crystal structure analysis is a very important component in the subject of crystal engineering. It is understood as a combination of molecular conformations, intermolecular interactions of different strength, angular preferences, and distance dependence characteristics. Thereby, to simplify the analysis of the picture, it is convenient to dissect a crystal packing and highlight only one or a few interactions at a time, collecting different views of the packing. Using this approach, in the present work we concentrate on three most important types of weak intermolecular interactions – weak hydrogen bonding, halogen, and chalcogen bonding – that stand out in crystal engineering of organic solids. In this context, while conventional hydrogen bonding has been widely acknowledged, the two latter intermolecular interactions still raise many questions.

Halogen bonding, first identified in $H_3N\cdots I_2$ (1863) and $Br_2\cdots Br_2$ (1936), is nowadays a subject of intense research efforts. Strength and directionality of this interaction allows its extensive use in crystal engineering. The origin of halogen bonding was associated with the presence of an electropositive region of the electrostatic potential in the prolongation of the C–Hal bond (Hal = Cl, Br, I) – called σ-hole – that under certain geometrical conditions interacts with an electron-rich moiety of another Hal-atom or a Lewis base (LB) through an essentially electrostatic C–Hal$\cdots$X, (X = Hal, LB) interaction. Recent experimental and theoretical charge density studies involving halogen atoms has demonstrated that the origin of the σ-hole concept is found in the anisotropic distribution of the electron density $\rho(\mathbf{r})$ around the Hal-atom – feature called *polar flattening* – which gives rise to electrophilic (σ-hole) and nucleophilic regions. This feature explains why the nature and the strength of the interactions involving the Hal-atom strongly rely on the electronic structure of the interacting atoms and their relative positions. As shown on the crystal structure of C_6Cl_6, electrophilic and nucleophilic regions can be simultaneously involved in highly directional Hal$\cdots$Hal interactions, forming a cyclic trimer called Hal_3-synthon. As a result, the anisotropic bonding picture of this particular geometrical arrangement is mainly achieved by electrostatics. Noting that trimers based on Hal_3-interactions behave as structure-determining synthons in many investigated systems, it is of special importance to perform a detailed characterization and analysis of this structural unit.

The *σ-hole* concept has been extended from halogens to divalently-bonded chalcogens (Chal) to rationalize the frequent occurrence of S···O and S···S intra- and intermolecular interactions. In the interaction of chalcogens with Lewis bases, statistical analyses of crystal structures and theoretical calculations revealed that preferred conformations are observed with the Lewis base pointing toward the chalcogen atom approximately along the extension of one of its two covalent bonds. In theoretical studies, the prevalence of either electrostatic or dispersion contributions to the energetic stabilization of the chalcogen bond is underlined, noting that polarization and charge-transfer are also non negligible depending on the system. On the other hand, experimental investigations of chalcogen bonding interactions are very sparse and involve only light chalcogen atoms (O and S). In these cases, the interaction has been mostly considered in terms of the Lewis acid-base concept; however, a deeper understanding of the force driving the specific orientations between the bonded molecules has never been attempted experimentally. Similarly to halogen bonding, the study of the distribution of $\rho(\mathbf{r})$ around Chal-nuclei could permit to reveal the nature of the interaction, and to characterize and to analyze directional preferences.

Within the framework of the *Quantum Theory of Atoms in Molecules* (QTAIM), developed by R. F. Bader and collaborators, any bonding interaction can be characterized in terms of the topology of the electron density distribution. This theory permits to analyze main properties of bonding interactions and nowadays it is often used for their study. In the history of science, many luminaries expressed for the simplicity of any approach used to understand this or that phenomenon. Based on the $\rho(\mathbf{r})$ function and its topological properties only, QTAIM satisfies the requirements of simplicity, though, explaining its wide application for the characterization of interactions.

2. Aim and Purposes

In this work, we aim to perform experimental and theoretical charge density studies based on QTAIM methodology for analyzing halogen and chalcogen bonding, and for comparing them with weak hydrogen bonding, as derived from the X-ray multipole-refined electron density and from density functional theory (DFT) calculations. Among the properties of these weak interactions, we will particularly focus on strength and directionality, as well as on the correlation of the $\rho(\mathbf{r})$ properties with the interaction distance. Hence, using this methodology, we state the three main objectives as following:

1. To investigate interactions involving Hal-atoms (Hal = Cl, Br, I) in different geometries, defining their nature and strength, paying special attention to the Hal···Hal interactions in Hal$_3$-synthons (Chapter IV).

2. To investigate interactions involving Chal-atoms (Chal = O, S, Se, Te) from the viewpoint of their nature and main properties – directionality and strength (Chapter V).

3. To analyze the coexistence of hydrogen, halogen, and chalcogen bonding in crystal structures and to investigate eventual correlations between topological parameters of $\rho(\mathbf{r})$ for these intermolecular interactions (Chapter VI).

3.   The choice of compounds

To study Hal···Hal interactions, we have chosen the following crystal structures: hexabromobenzene (C_6Br_6), pentachlorophenol (C_6Cl_5OH), and pentabromophenol (C_6Br_5OH) in addition to the previously studied hexachlorobenzene (C_6Cl_6). The choice of these Cl- and Br-containing compounds was governed by the presence of similar structural units – Hal_3-synthons – that permits a straightforward comparison of Cl_3- and Br_3-synthons. A Hal···LB type halogen bonding is characterized in the crystal structure of iododithiolone (C_3HIOS_2).

Chalcogen bonding is also investigated in iododithiolone (C_3HIOS_2), as well as in selenophtalic anhydride ($C_8H_4O_2Se$), where the neighboring electron-withdrawing groups are expected to enhance the σ-*hole* structure of the chalcogen atom (S or Se). Due to this fact, Chal-atoms, which present sp^3 hybridization, are simultaneously involved in Chal···Chal and Chal···LB interactions. These similarities permit to compare S and Se atoms to each other and put them in front of the corresponding Hal-atoms (Cl and Br).

Four out of six mentioned compounds present a large variety of hydrogen bonding interactions, involving O-, Se-, and Br-atoms as electron donors. This variety permits to analyze the H···X (X = O, Se, Br) interactions between each other, and to compare them with the other intermolecular interactions in each structure.

The chosen compounds exhibit other geometrical types of intermolecular interactions involving Hal- and Chal-atoms, that are also characterized in this work.

4.   General framework of this thesis

Chapter I

Electron density – an information source about chemical bonding

Chapter I gives an overview on chemical bond analysis based on the electron density $\rho(\mathbf{r})$ function and performs the steps for $\rho(\mathbf{r})$ determination from experimental and theoretical viewpoints, followed by its multipolar modeling and treatment in the framework of QTAIM (*Quantum Theory of Atoms in Molecules*). The description of topological properties of the electron density $\rho(\mathbf{r})$, Laplacian $\nabla^2\rho(\mathbf{r})$, and electrostatic potential $V(\mathbf{r})$ functions are performed. A brief delineation of the different contributions to the total interaction energy of an intermolecular interaction is given.

The main question is now: is there a link between chemical concepts and quantum mechanics? There must be a link because we live in only one world.

P. Popelier

QTAIM offers explanations for real problems because it deals with reality and physics.

R. F. Bader

Introduction

The electronic structure investigations leading to the current descriptions of chemical bonding started almost 100 years ago when Lewis published a seminal paper entitled *The Atom and the Molecule*.[1] From that time, the chemical bonding concept developed a lot. The increasing number of the reports about new modes of chemical bonding guides the new ways of thinking about standard bonding concepts. And while the contemporary chemical community accepts the *verdict* that the chemical bond can only be correctly understood in the framework of quantum mechanics, there is a great challenge to find the link between quantum mechanical approach and chemistry.

This problem was solved by the *Quantum Theory of Atoms in Molecule* (QTAIM) of R. F. Bader.[2] This theory provides a simple and strict definition of the two cornerstones in chemistry: the atom and the bond. QTAIM is based on the notion of electron density $\rho(\mathbf{r})$ (or electron distribution), using it as an information source. Indeed, this function conserves all the ground-state properties as it is linked with the wavefunction of the system.[3] The main point of QTAIM is that it starts from the electron density and does not care about how the density was obtained.[4] QTAIM is considered to be one of the most important new bonding theories in recent decades. The theory is increasingly being applied to study an array of chemical systems, including solid-state materials and biomolecules.[5]

1. Electron density determination

Despite the fact that this work is mostly oriented on the experimental electron density analysis, the theoretical calculations play an important role, acting as a support on each step of the research process. That is why it seems important to show both ways of $\rho(\mathbf{r})$ determination. **Figure I.1** performs the bird's eye view on the whole procedure.

Electron density can be determined either from X-ray diffraction (XRD) experiment or from *ab initio* theoretical calculations, starting with a wave function. The later can be performed for the isolated molecule in the gas phase as well as for a crystal phase. After multipolar modeling against experimental and theoretical structure factors, analysis of $\rho(\mathbf{r})$ using QTAIM can be performed, giving a lot of information about a system.
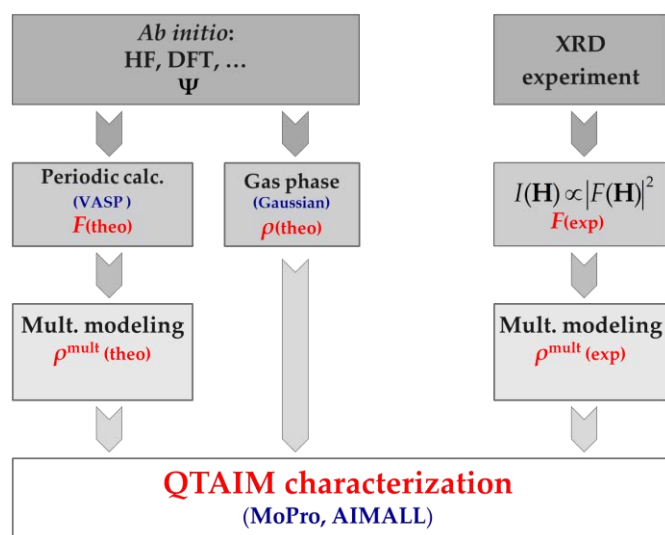
Figure I.1 **Scheme illustrating chemical bond characterization, based on electron density function, determined theoretically or experimentally and analyzed with QTAIM approach.**

1.1. Electron density from experiment

Charge density studies from multipolar modeling and QTAIM analysis put great demands on the quality of an experimentally determined electron density.

1.1.1. X-ray diffraction and Fourier transform

In X-ray diffraction experiments, the geometrical conditions under which a diffracted X-ray beam can be observed are given by Bragg's Law, which is expressed as:

$$2d\sin\theta = n\lambda$$

where θ is known as the Bragg angle, λ is the wavelength of the X-rays and d is the plane spacing. The value of n in Bragg's law can always be taken as unity, since any multiples of the wavelengths can be accounted for in the diffraction indices (h, k, l) of any particular reflection. **Figure I.2** shows rays diffracted from lattice planes and, to get constructive interference, the path difference between these rays should be a whole number of wavelengths.[6]

Figure I.2 Diffraction of X-rays from crystal lattice planes illustrating Bragg's law.

The positions of the diffracted X-ray beams enable one to determine the size and shape of the crystallographic unit cell, and to obtain the indication of the crystal class (or system). However, it tells us nothing about the distribution of the atoms inside the cell. This information can be obtained from the X-ray beams intensity $I(\mathbf{H})$, which gives access to the structure factor $F(\mathbf{H})$:

$$I(\mathbf{H}) \propto |F(\mathbf{H})|^2$$

It should be noted that the modulus sign means the phaseless quantity of F. The structure factor corresponds to the resultant wave scattered by all the atoms of the unit cell. It describes how the atom arrangement affects the scattered beam. It is obtained by simply adding together all the waves scattered by the individual atoms:

$$F(\mathbf{H}) = \sum_{j=1}^{N_{at}} f_j(\mathbf{H}) \cdot \exp(2i\pi\mathbf{H} \cdot r_j)$$

where $\mathbf{H}$ is a reciprocal lattice vector $\mathbf{H} = h\mathbf{a}^* + k\mathbf{b}^* + l\mathbf{c}^*$, $f_j(\mathbf{H})$ is the atomic scattering factor, which is given by the Fourier transform of the atomic electron density.

$$f_j(\mathbf{H}) = \int_V \rho_j(\mathbf{r}) \cdot \exp(2i\pi\mathbf{H} \cdot \mathbf{r}) dV$$

$$F(\mathbf{H}) = \int_V \rho(\mathbf{r}) \cdot \exp(2i\pi\mathbf{H} \cdot \mathbf{r}) dV$$

$\rho(\mathbf{r})$ in these expressions is an electron density at the point (x, y, z). Thus, the inverse Fourier transformation enables us to compute the electron density at any point:

$$\rho(\mathbf{r}) = \frac{1}{V} \sum_{\mathbf{H}} F(\mathbf{H}) \exp(-2i\pi\mathbf{H} \cdot \mathbf{r})$$

1.1.2. Difficulties in experimental electron density determination

The most important difficulties in the experimental analysis of the electron density distribution $\rho(\mathbf{r})$ are related to the data fineness and the loss of phase information. Several problems have to be solved in order to obtain high quality $\rho(\mathbf{r})$, especially in the case of the compounds containing heavy atoms.[7]

❖ *Scattering problem in the case of heavy atoms*

The X-ray scattering factor depends on the number of electrons in the particular atom – it decreases with increasing the scattering angle and is higher for heavier atoms. So data at low angles must be measured with higher accuracy and precision because the scattering due to the valence electrons not only becomes a smaller part of the total scattering but also is limited to lower angles with increasing atomic number.

❖ *Phase problem*

The measured X-ray intensities yield only the structure-factor amplitude and not their phases. The calculation of the electron density can not therefore be performed directly from experimental measurements and the phases must be obtained by other means. Hence, the so-called phase problem arises, being more important in the case of the noncentrosymmetric structures. Methods for overcoming the phase problem in small-molecule crystallography are the *Direct Methods* and the *Patterson search* along with the interpretation techniques.

❖ *Absorption effect*

A sample can absorb rather than diffract some of the X-ray beam. The level of absorbance, at a given X-ray wavelength, will depend on the absorption coefficient μ of a sample, which depends in turn on its elemental make-up (heavier elements generally absorb more), and the path length t of X-rays through a crystal, according to the equation:

$$I_t = I_0 \exp(-\mu t)$$

Absorption is also dependent upon the wavelength of the X-ray source: the longer the wavelength, the greater generally the absorption coefficient for a given sample ($\mu \propto \lambda^3$). That is why an appropriate absorption correction method should be used. In addition, the attention should be paid to the absorption threshold for each atom-type in the compound.

❖ *Extinction effect*

An X-ray beam can be diffracted by one lattice plane in a crystal, and then subsequently scatter off by another in a different part of the crystal. This effect is known as extinction and it causes a loss of intensity for a given reflection. Extinction occurs within a crystal domain and depends on their relative orientation and their size. Usually extinction affects strong, low-angle reflections. These are normally approximately corrected by including a single correction factor as a variable in the structure refinement. On the other hand, extinction is wavelength dependent and becoming worse with copper than with molybdenum radiation.

In order to avoid the mentioned problems, the attention should be paid to the size of a crystal and its stability, as well as to the appropriate choice of X-ray source (Mo Kα or high intensity source – synchrotron radiation) and the measurements temperature (~ 100 K using liquid nitrogen or ~ 15 K using helium). The latter is necessary in order to increase the resolution.

1.2. The electron density from theoretical calculations

According to the previously mentioned problems in the experimentally determined electron density $\rho(\mathbf{r})$, theoretical calculations can be very useful as a support for experimental studies (**Figure I.3**[8]).[9]

As the experimentally derived results are averaged over time as a consequence of thermal smearing, the two possible approaches are: the convolution of the theoretical density with the experimental thermal motion or the deconvolution of the experimental density from thermal effects.[10] The latter involves the comparison between the static densities derived from theory and from experiment, being nowadays widely used in charge density studies. In order to eliminate the discrepancies resulting from the crystal symmetry and periodicity, theoretical calculations can be performed not only for the isolated molecules but also for crystal phases.

Figure I.3 An early comparison of theory and experiment: Galilei dropped two balls with different weight from the Leaning Tower of Pisa (1590).[8]

The modern form of the *Density Functional Theory* (DFT) is one of the most commonly used and is based on the idea that the energy of an electronic system can be expressed in terms of its electron density, i.e. without reference to orbitals and based on the *Hohenberg–Kohn* (HK) theorem. There are several programs that generate structure factors. They are obtained from the electron density function calculated by the DFT method on the isolated molecule or on periodic crystal models.

The programs dealing with periodic calculations[11] work with the all-electron wave function and give access, at any time, to the complete wave function. The majority of solid state electronic structure studies are done in a plane wave basis, where the use of either norm-conserving or ultrasoft pseudopotentials or a mixed-basis augmented plane wave methodology is mandatory. *Ab initio* total energy calculations using the DFT in the *projector augmented wave* (PAW)[12] implementation are widely used for different materials. The Vienna Ab Initio Simulation Package (VASP)[13] is one of the most popular computer codes used by many research teams.

It was recently shown on the example of the hexachlorobenzene crystal structure C_6Cl_6[14] that periodic DFT calculations done with the VASP code recover the main features of the crystalline electron density distribution. A good agreement between the theoretical and experimental multipolar models shown from deformation density maps was further supported by the observed matching of their topological features at bond critical points in intermolecular regions.

2. Electron density modeling

The least-squares approach is used to fit an electron density model against the structure factors dataset. The concept is as following: by means of Fourier transformation, a set of structure factors F is calculated from the atomic model. The calculated and measured intensities are then compared to each other, in order to define the best model which minimizes M. The least-squares refinement can be performed against F^2 or against F.

$$I(\mathbf{H}) \propto |F(\mathbf{H})|^2$$

$$M = \sum_{\mathbf{H}} \omega_{\mathbf{H}} \left(\frac{1}{k} F_{obs}^2 - F_{calc}^2 \right)^2 \quad \text{or} \quad M = \sum_{\mathbf{H}} \omega_{\mathbf{H}} \left(\frac{1}{k} |F_{obs}| - |F_{calc}| \right)^2$$

F_{obs} and F_{calc} are the observed (obtained either experimentally or theoretically) and the calculated (from the model) structure factors, k is a scale factor. Each addend in the summations is multiplied by an individual weighting factor ω, which reflects our confidence in this particular datum and is derived from the standard uncertainty σ of that measurement:

$$\omega_{\mathbf{H}} = \frac{1}{\sigma^2(F_{obs})}.$$

2.1. Independent atom model

The usual least-squares treatment of X-ray diffraction data – so-called *Independent Atom Model* (IAM) – is based on the assumption that atoms are neutral and isolated with a radial dependence equal to that of free atoms in the gas phase, so as the electron density distribution around each nucleus is supposed to be non-perturbed and represents a spherically symmetric distribution. This is the basis of X-ray structure analysis since its inception.

The continuous electron density is subdivided into N independent pseudo atomic charge densities, centered in $\mathbf{r}_j$:

$$\rho_{IAM}(\mathbf{r}) = \sum_{j=1}^{N} \rho_j^{sph} \left(|\mathbf{r} - \mathbf{r}_j| \right)$$

The electron density of each atom is divided into its core and valence electron densities:

$$\rho_j^{sph}(\mathbf{r}) = \rho_j^{core}(\mathbf{r}) + \rho_j^{val}(\mathbf{r})$$

IAM provides a good approximation for the heavy atoms, for which the valence shell is a minor part of the total density, but is much less successful for the light atoms. In the case of the hydrogen atom, which has no core electrons, the IAM model causes the systematic shortening of X–H bond length. High-order refinement, taking into account mostly core electrons, can be a solution to overcome the errors. The IAM model further assumes the atoms in a crystal to be neutral. This assumption is contradicted by the fact that molecules have dipole moment and higher electrostatic moments, which are related to the charge transfer between atoms and to the

nonspherical density distribution.[15] Moreover, spherically symmetric electron density distributions do not reflect the atom–atom interactions such as chemical bonding, hydrogen bonding and van der Waals effects, as the real atomic electron density is obviously not spherical.

2.2. Multipolar model

Several nonspherical atom models have been proposed, being more elaborate than the IAM approximation.[15,16] Most of them are based on nonspherical scattering centers modeled by a superposition of real spherical harmonic functions.[17] The Hansen and Coppens atom model[18] used to analyze the crystalline electron density distribution $\rho(\mathbf{r})$, is based on a multipolar development centered at atomic positions and is one of the most widely used in the field of small-molecule charge-density studies. In the Hansen–Coppens formalism the total electron density distribution $\rho(\mathbf{r})$ is calculated as the addition of N atom centered atomic contributions:

$$\rho(\mathbf{r}) = \sum_{i=1}^{N} \rho_i(\mathbf{r})$$

where each of them is described by three terms:

$$\rho_i(\mathbf{r}) = \underbrace{\rho_{core}(\mathbf{r})}_{core} + \underbrace{P_{val}\kappa^3\rho_{val}(\kappa\mathbf{r})}_{spherical\,valence} + \underbrace{\sum_{l=0}^{l_{max}}\kappa'^3 R_l(\kappa'\mathbf{r})\underbrace{\sum_{m=0}^{l}P_{l\pm m}y_{l\pm m}(\theta,\phi)}_{non-spherical\,valence}}_{deformation\,density}$$

The first term corresponds to the core electrons, which are supposed to be unperturbed and are therefore not involved in interatomic interactions, keeping a spherical symmetry (this term is omitted in the case of the theoretical data refinement, since structure factors generated with VASP correspond to the valence electron density only).

The next two terms translate the influence of the environment (intra- and intermolecular interactions) on the valence electron distribution.

The second term takes into account a partial charge transfer (P_{val}) and a spherical expansion/contraction (κ) of the valence-shell. Both P_{val} and κ are the atomic variable parameters that can be refined in the least-squares procedure. The valence population gives the access to atomic charges (i.e. the deviation from neutrality) and the parameter κ allows the spherical valence electron density to become more contracted or more expanded around the atomic position during refinement.

The third term permits to describe the asphericity of the valence distribution. It is written as a superimposition of real spherical harmonic functions $y_{lm\pm}(\theta, \varphi)$, oriented with respect to a local axis system. This local coordinate system (xyz) is centered on the atom under consideration and is oriented with respect to the atomic neighbors. Each of these spherical harmonic functions is parameterized by multipolar populations P_{lm}, which can be refined in order to fit the deformation electron density. The sum over l indices indicates the level of the multipolar expansion, which determines the number of refined multipolar parameters P_{lm} needed to adequately model the deformation electron density of any chemical species. $R_l(\kappa'\mathbf{r})$

is a Slater-type radial function modulated by an expansion/contraction parameter (κ'), so that the shape of this radial function modulates the expansion/contraction of the multipoles which model the nonspherical part of the valence electron density.

$$R_l(\kappa' \mathbf{r}) = \frac{\zeta_l^{n_l+3}}{(n_l + 2)!} \kappa'^{nl} \mathbf{r}^{nl} \exp(-\zeta_l \kappa' \mathbf{r}) \ , \quad nl \geq l$$

While the n_l and ζ values are kept fixed, the κ' parameter modulates the radial dependence of the Slater function, allowing adjustment in the least-squares refinement of the contraction/expansion of the multipolar electron density.

The multipolar refinement of electron density based on Hansen–Coppens formalism is implemented in MoPro package.[19] The atomic parameters P_{val}, P_{lm}, κ, and κ' of the Hansen-Coppens model along with the structural parameters (xyz and U_{ij}/U_{iso}) and scale factor (SCA) are refined in the least-squares procedure against the X-ray or VASP theoretical structure factors in order to fit the deformation of the atomic electron densities.

2.2.1. Constraints and restraints on charge-density parameters

Due to limitations in the quality of the diffraction data (resolution, Fourier series truncation effects, signal to noise ratio, etc.), it is generally not realistic to refine all charge-density parameters together, since there is not necessarily a single minimum in the least-squares refinement and multipolar parameters can be very strongly correlated (e.g. P_{val} and κ or U_{ij} and quadrupoles). Multipolar refinements of $\rho(\mathbf{r})$ may lead to ambiguous or even meaningless results for non-centrosymmetric crystal structures, where most phases are unknown. The application of constraints on the electron-density models improves this situation.[20] Constraints of atomic chemical equivalence and of local symmetries are useful to guide the refinement in its first steps and may be released later on. For instance, the parameters κ and κ' are often the most difficult to estimate in electron density analyses, even for small molecules, so they were suggested be kept constrained in the beginning of the refinement.[19a,21]

Atomic chemical equivalence uses the knowledge that identical chemical moieties should share, to a first approximation, the same charge-density distribution. Appling these constraints, the advantage could be taken of the repetition of identical chemical motifs.

Local symmetry constraints are easily defined with an appropriate system of atomic local axes. With these symmetry constraints, the number of parameters is decreased and the parameters that are expected to be small are not refined initially.

Unlike a constrained refinement, where some values are fixed, the refinement with restraints allows parameters to adjust with respect to the specific chemical environment of the considered atom. In order to define the optimal restraints for the charge density model, free R factor calculations were performed.[22] This method allows for a cross validation using entirely diffraction data based factors. Five percent (1/20) of the reflections were used as a test set and the remaining 95% in the least-squares refinement. The strategy for R-free factor calculation consisted of 20 similar refinements, with the same input molecular file and the same refinement procedure. In each refinement, a different set of 5% free reflections was applied. As a result, 20 different free R factors (and conventional R factors based on 95% of the reflections) are averaged.

The optimal σ-value for restraints is found by the minimum of agreement factor $w\mathrm{R}_2\mathrm{F}_{free}$ among the totally constrained and deconstrained models. The corresponding model (R_{free} model) is normally the best charge density model, which is not far from that of the totally deconstrained refinement.[22]

2.2.2.   The choice of radial functions

The best radial function parameters can be found from the multipolar modeling of the valence electron-density distribution. The first model function analysis was performed for P-atom from theoretical and experimental data analysis.[23]

The zeta-parameters ζ are initially chosen to be consistent with atom or molecule optimized orbital exponents α ($\zeta = 2\alpha$ since $\rho(\mathbf{r}) \sim \Psi^2$). The values of n_l may be inferred from the origin of the multipole functions as a product of atomic orbitals.[18] For example, the optimization of n_l parameters for S-atoms[24,25,26] from theoretical structure factors of six organic molecules shows that, the variation of the n_l values for different l is more important than their absolute values, as parallel changes in all n_l for a given atom are compensated by a change in the refined value of the κ' parameters.

In the multipolar refinement using MoPro program,[19] initial (n_l, ζ) parameters are taken from the existing databank and in some cases are needed to be optimized in respect to the atomic environment by inspecting the residual maps.

2.2.3.   Anharmonic motion

Neglecting anharmonic motion in charge density studies has its effect on the residual density distribution and on the properties derived from charge density. In the case of dynamic disorder, vibrations of atoms increase with the temperature and with the number of core electrons.[27]

(a)   (b)
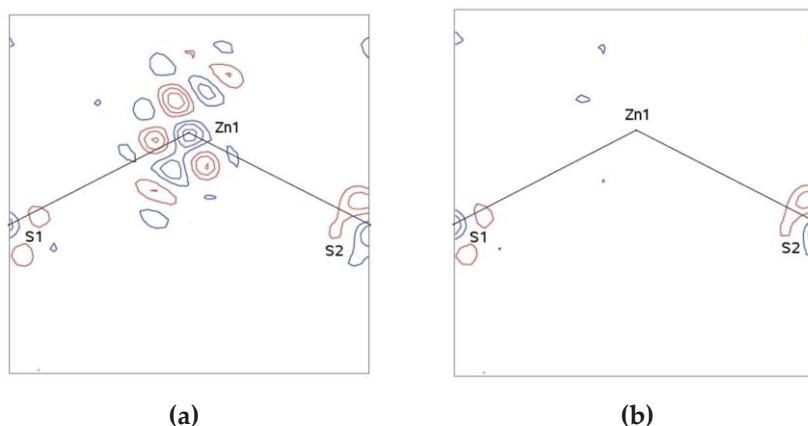
Figure I.4 Residual density maps of the complex with zinc(II): (a) harmonic refinement, (b) anharmonic refinement. $0.8 < \sin\theta/\lambda < 1.1$ Å^{-1}. Contours are at ±0.1 eÅ^{-3} level: blue – positive, red – negative.[27b]

During the last fifteen years several works were dedicated to this problem.[28] Some of them claimed that anharmonic nuclear motion cannot be distinguished from effects such as disorder in a single crystal X-ray diffraction experiment,[28a] the others proved that the deconvolution of the anharmonic motion components from charge density parameters for very heavy atoms (such as

Th), using very high resolution data (1.7 Å⁻¹) and very low temperatures (9 and 27 K) is possible.[28b] While recently, anharmonic thermal motion was introducing to the refinement of lighter atoms (such as P) under higher experimental temperature (100 K) and with significantly lower resolution (1.15 Å⁻¹).[28c] Attempts were also made to separate the anharmonic motion from asphericity of the electron density at room temperature and at 145 K.[28d]

It was also shown that anharmonic coefficients and multipole parameters are usually strongly correlated.[27a] For today, anharmonic motion can be included in the refinement by the Gram-Charlier expansion coefficients (as it is introduced in MoPro) and permit to obtain an adequate model of aspherical density (**Figure I.4**).

2.3. Validation / visualization tools of the electron density model

Refinement is a general term that refers to almost all the step-wise operations that are introduced in order to develop a trial model into one that best represents the observed data. There are some well-trodden trails to guide the analysis on every stage of the refinement, together with a growing number of validation tools.[29]

2.3.1. The agreement factors

During a least-square procedure, the refinement tends to reduce the difference between the observed and calculated structure factors. The agreement factors are widely used to evaluate the refinement quality. The two factors calculated by MoPro,[19a] are the following:

$$R = \frac{\sum_{\mathbf{H}} \left| \frac{1}{k}|F_{\mathrm{obs}}| - |F_{\mathrm{cal}}| \right|}{\sum_{\mathbf{H}} \frac{1}{k}|F_{\mathrm{obs}}|} \qquad \text{and} \qquad wR_2F = \sqrt{\frac{\sum_{\mathbf{H}} \frac{1}{\sigma^2(F_{\mathrm{obs}})}\left(\frac{1}{k}|F_{\mathrm{obs}}| - |F_{\mathrm{calc}}|\right)^2}{\sum_{\mathbf{H}} \frac{1}{\sigma^2(F_{\mathrm{obs}})}\left(\frac{1}{k}|F_{\mathrm{obs}}|\right)^2}}$$

where k is the scale factor, and $\sigma(F_{\mathrm{obs}})$ is the standard deviation. The quality of the experimental refinement is also judged from the goodness-of-fit (GOF) value:

$$GOF = \sqrt{\frac{\sum_{\mathbf{H}} \frac{1}{\sigma^2(F_{\mathrm{obs}})}\left(\frac{1}{k}|F_{\mathrm{obs}}| - |F_{\mathrm{calc}}|\right)^2}{n_{\mathrm{obs}} - n_{\mathrm{par}}}}$$

where n_{obs} and n_{par} are the number of structure factors and parameters used for the multipolar refinement, respectively. According to statistics, the refinement performed with an appropriate weighting scheme should lead to $GOF \approx 1$. For the theoretical model (VASP), standard deviations of theoretical structure factors are set to 1. In that case, the goodness-of-fit should go to 0 rather than to 1 at the convergence.

2.3.2. The electron-density maps

A useful tool in the process of structural or multipolar refinement is to visualize the obtained model and its adequacy in respect to the experimental data. The VMoPro program[19b] allows easy computation and graphical representation of different types of electron-density maps.

❖ *Residual electron-density map*

After each valuable step of the refinement, the difference density map using the Fourier structure-factor difference ($F_{obs} - F_{calc}$) can be computed:

$$\Delta\rho_{res}(\mathbf{r}) = \frac{1}{V}\sum_{\mathbf{H}}\left\lfloor\frac{1}{k}|F_{obs}| - |F_{calc}|\right\rfloor \cdot \exp i(\,\varphi_{calc} - 2i\pi\mathbf{Hr})$$

Depending on the model (spherical or multipolar), F_{calc} corresponds to F_{sph} or F_{mult}. After a refinement at high resolution using the spherical model (IAM), the residual map reveals the non-modeled bonding electron density, while after multipolar refinement it shows a model quality and should represent just random contours, which correspond to noise.

❖ *Experimental deformation-density map*

Molecular electron density is dominated by huge values near the nuclei. In order to eliminate these nuclear peaks, the deformation density has been introduced. It allows seeing the chemistry hidden in $\rho(\mathbf{r})$, e.g. chemical features such as bonding regions and long pairs.

The experimental electron deformation map $\Delta\rho_{exp}(\mathbf{r})$ corresponds to the Fourier synthesis between the absolute value of a structure factor, associated to the phases obtained by multipolar modeling φ_{mult} and F_{sph}, φ_{sph} calculated from spherical atomic scattering factors:

$$\Delta\rho_{exp}(\mathbf{r}) = \frac{1}{V}\sum_{\mathbf{H}}\left\lfloor\frac{1}{k}|F_{obs}| \cdot \exp(i\,\varphi_{mult}) - |F_{sph}| \cdot \exp(i\,\varphi_{sph})\right\rfloor \cdot \exp(-2i\pi\mathbf{Hr})$$

$\Delta\rho_{exp}(\mathbf{r})$ is generally calculated for the data with the resolution of ~ 0.9 Å^{-1} in order to represent only deformation of the valence shell electrons.

❖ *Static deformation-density map*

Static electron-density maps representing the total or the deformation electron density are computed from the multipolar charge density parameters and do not make implicit use of the diffraction intensities. Static deformation density is defined as the difference between multipolar and the spherical atoms models, take therefore the form:

$$\Delta\rho_{stat}(\mathbf{r}) = \sum_{i=1}^{N_{at}}\Delta\rho_i(\mathbf{r})$$

$$\Delta\rho_i(\mathbf{r}) = \kappa^3 P_{val}\rho_{val}^{sph}(\kappa r) - N_{val}\rho_{val}^{sph}(r) + \sum_{l=0}^{l_{max}}\kappa'^3 R_{nl}(\kappa' r)\sum_{m=-1}^{+l}P_{lm}Y_l^m(\theta,\varphi)$$

N_{at} represents the number of atoms in the crystal unit cell. $\Delta\rho_{stat}$ is the direct representation of the electron density model. It indicates the regions where the multipolar charge density is in

deficiency (δ^+) or in excess (δ^-) with respect to non-interacting spherical atoms, due to intra- and inter-molecular interactions. However, one should remember that this representation doesn't inform us about a noise level neither about the residuals that are associated to the structure factors.

VMoPro also computes the total static electron density, its gradient norm, Laplacian, and electrostatic potential functions. The topological analyses of these functions allow the observation of typical features such as critical points and atomic basins (see the following part).

2.3.3. Thermal motion analysis

Thermal motion analysis permits to estimate the motion of the atoms in the crystal around their equilibrium positions. It is a useful tool to verify the deconvolution between the refined parameters and the refined set of vibration parameters.

The Hirshfeld rigid-bond test[30] is a simple method for validation of the model rigidity for molecular vibrations in crystals. It has proved to be very effective in revealing problems in a structure. It is assumed in this test that two bonded atoms vibrate along the bond with approximately equal amplitude. Significant differences, i.e. those which deviate by more than a few standard uncertainties, need close examination.

It follows that if $Z^2_{A,B}$ denotes the radius of the vibration ellipsoid of atom A along the vector from A to B, we expect that for every covalently bonded pair of atoms A and B:

$$\Delta Z_{A,B} = Z^2_{A,B} - Z^2_{B,A} = 0$$

i.e. the two atoms have equal mean square vibration amplitudes along their mutual bond. For atoms at least as heavy as carbon, it can be estimated that this equality of two parameters should normally hold to within well under 0.001 Å^2.

3. QTAIM-based electron density treatment

In the framework of the QTAIM concept,[2] three most important scalar functions – namely, electron density $\rho(\mathbf{r})$, its negative Laplacian $L(\mathbf{r})$, and electrostatic potential $V(\mathbf{r})$ – describe an intermolecular interaction through the characterization of their topological properties.

3.1. An overview on the topology of electron density

As far as we have obtained an electron density model and, by the criteria mentioned before, have defined it as the high quality one, the topology of the electron density can be analyzed. From QTAIM, the topology of $\rho(\mathbf{r})$ is fully understood. It leads to a partitioning scheme, which defines atoms inside a molecule via the gradient vector field. The atomic and bond properties construct robust quantitative structure–property relationships models.

3.1.1. The main definitions

The **gradient vector field of electron density** is a collection of vectors (**gradient paths**), which are curves in space that follows the direction of steepest ascent in $\rho(\mathbf{r})$. The gradient path always originates and terminates at points where the gradient of the total electron density vanishes:

$$\nabla\rho(\mathbf{r}) = \mathbf{i}\frac{\partial\rho}{\partial x} + \mathbf{j}\frac{\partial\rho}{\partial y} + \mathbf{k}\frac{\partial\rho}{\partial z} = 0$$

These points are called the **critical points** (CPs) of the electron density. The magnitude of a second derivative of the function permits to study the electron density at the CP by means of the analysis of its maximum, minimum or saddle point. For this purpose one needs to use the **Hessian matrix** that contains all possible second derivatives of $\rho(\mathbf{r})$ with respect to the Cartesian position coordinates (xyz). Being real and symmetrical, the Hessian matrix of $\rho(\mathbf{r})$ can be diagonalized. The principal axes and their corresponding curvatures at a CP of $\rho(\mathbf{r})$ are obtained as the eigenvectors and corresponding eigenvalues (λ_i) of the Hessian matrix.

$$\mathbf{H} = \begin{pmatrix} \lambda_1 & 0 & 0 \\ 0 & \lambda_2 & 0 \\ 0 & 0 & \lambda_3 \end{pmatrix}, \quad \lambda_1 = \left(\frac{\partial^2\rho}{\partial x^2}\right), \quad \lambda_2 = \left(\frac{\partial^2\rho}{\partial y^2}\right), \quad \lambda_3 = \left(\frac{\partial^2\rho}{\partial z^2}\right)$$

The trace of the Hessian matrix, i.e. the sum of its diagonal elements, is invariant to rotation of the coordinate system and defines the **Laplacian of electron density** $\nabla^2\rho$:

$$\nabla^2\rho(\mathbf{r}) = \frac{\partial^2\rho}{\partial x^2} + \frac{\partial^2\rho}{\partial y^2} + \frac{\partial^2\rho}{\partial z^2} = \lambda_1 + \lambda_2 + \lambda_3$$

With this knowledge, the different types of CPs can be classified with their *rank* and *signature* (ω, σ). The rank (ω) is the number of non-zero curvatures of $\rho(\mathbf{r})$ at the CP, while its signature (σ) is the algebraic sum of the signs of the curvatures at that point. With few exceptions, the CPs of charge distributions for stable molecules are of rank three ($\omega = 3$), though there are four possible

signature values depending on the sign of the curvatures, which are listed in **Table I.1** and illustrated in **Figure I.5**.

Table I.1 **Classification of critical points.**

Name	(ω, σ)	λ_1	λ_2	λ_3
Nuclear attractor (NCP) – local maximum	(3, –3)	–	–	–
Bond critical point (BCP) – saddle point	(3, –1)	–	–	+
Ring critical point (RCP) – saddle point	(3, +1)	–	+	+
Cage critical point (CCP) – local minimum	(3, +3)	+	+	+

Figure I.5 Representation of the four possible critical points with rank three on an example of cubane molecule (C atom as black spheres, hydrogen as grey spheres): CCP – green, RCP – yellow, BCP – red, NCP – black at the nuclei position.[31]

According to the law of *Poincaré-Hopf*,[2] the number of CPs in the crystal follows a strict topological relationship which states that:

$$n_{\text{NCP}} - n_{\text{BCP}} + n_{\text{RCP}} - n_{\text{CCP}} = 1$$

In accordance with QTAIM, atoms of any kind of molecular or crystalline systems can be defined as the regions of the real space – **atomic basins** Ω – separated by the surfaces through which there is no flux in the gradient vector field of $\rho(\mathbf{r})$ (**Figure I.6a,b**). These quantum mechanical boundaries of the atoms are called **zero-flux surfaces S** of the electron density and they satisfy the following boundary condition:

$$\nabla\rho(\mathbf{r})\cdot\mathbf{n}(\mathbf{r}) = 0, \quad \forall \mathbf{r} \in S$$

where **n** is a unit vector perpendicular to **S** at any point **r** belonging to the surface.

(a)	**(b)**	**(c)**
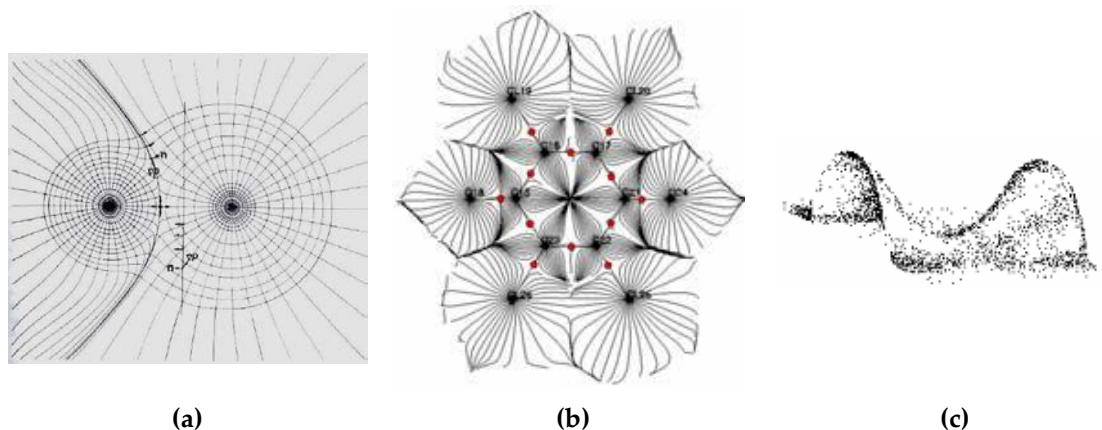
Figure I.6 (a) $\rho(\mathbf{r})$ contour map of NaCl overlaid with trajectories of $\nabla\rho(\mathbf{r})$. (b) $\nabla\rho(\mathbf{r})$ for the chloranil molecule. The BCP's are marked in red. (c) $\rho(\mathbf{r})$ exhibits a saddle distribution around the BCP and a local maximum at each nucleus.[2]

In the framework of the topological formalism, a bonding interaction between two atoms is defined by the existence of a **bond path** – a line of maximum of electron density linking their nuclei (**Figure I.6c**). In the position where the bond path crosses the zero-flux surfaces the bond critical point (3, −1) is placed.

3.1.2. Bond properties

Analysis of the $\rho(\mathbf{r})$ distribution at BCP permits to characterize any interaction according to its local topological and energetic properties: the electron density ρ^{BCP}, the curvatures of the electron density ($\lambda_1, \lambda_2 < 0, \lambda_3 > 0$) along the bonding direction (λ_3) and in the perpendicular plane, the Laplacian of electron density $\nabla^2\rho^{BCP} = \lambda_1 + \lambda_2 + \lambda_3$, and the local electron kinetic G^{BCP}, potential V^{BCP}, and total H^{BCP} ($H^{BCP} = G^{BCP} + V^{BCP}$) energy densities. These properties offer significant information about the nature and strength of an interaction (hereafter, the superscript BCP is omitted for clarity).

❖ *The electron density ρ*

For the topological construction, the value of $\rho(\mathbf{r})$ at BCP would be the smallest along the bond path. It gives us a simple starting point to evaluate and to compare these properties. A linear relation was established between the interaction energies and the electron densities at BCP of intermolecular halogen bonding (Hal···LB),[32] indicating that this topological parameter can be considered as a good descriptor of the interaction strength.

❖ *The Laplacian of electron density $\nabla^2\rho$*

As mentioned before, the Laplacian $\nabla^2\rho$ is defined as the sum of the three eigenvalues of the density Hessian matrix ($\nabla^2\rho=\lambda_1+\lambda_2+\lambda_3$). The values of λ_1 and λ_2 measure the degree of the $\rho(\mathbf{r})$ contraction towards the bond path, while λ_3 gives the $\rho(\mathbf{r})$ depletion towards each of the bonded nuclei. Though, the sign of $\nabla^2\rho$ at BCP indicates whether the electron distribution is locally concentrated or depleted:

$\nabla^2\rho(\mathbf{r}) < 0$ corresponds to a *shared-shell* interaction (SS) between the two atoms, meaning the concentration of the charge in the interatomic region. In this case the negative curvatures dominate ($|\lambda_1+\lambda_2|/\lambda_3 > 1$) and the interaction is covalent in nature.

$\nabla^2\rho(\mathbf{r}) > 0$ corresponds to a *closed-shell* interaction (CS), characterized by weakly bonded electron density between the two atoms, representing the depletion of charge. For these interactions, the positive curvature dominates ($|\lambda_1+\lambda_2|/\lambda_3 < 1$). These features are typical for ionic, halogen, hydrogen, and chalcogen bonding interactions.

❖ *The local energetic properties*

Local concentrations/depletions of $\rho(\mathbf{r})$ in the internuclear space are also connected to features of the electron energy distribution.[33] For closed-shell interactions, the direct relationships connecting topological and energetic properties of the electron density at BCP's have been shown. Thus, according to Espinosa et al.,[34] G, V and H ($H = G + V$) have been estimated from ρ and $\nabla^2\rho$ values at BCP by applying the functional proposed by Abramov[35] and the local form of the virial theorem (in a.u.):[2]

Figure I.7 $|V|/G$ as a function of an intermolecular distance.[34c]

$$G = \frac{3}{10}(3\pi^2)^{2/3}\rho^{5/3} + \frac{1}{6}\nabla^2\rho$$

$$V = \frac{1}{4}\nabla^2\rho - 2G$$

For closed-shell interactions, the estimation of G and of V at BCP is respectively within 4 % and 9 % of high-quality MP2 calculations.[34b]

Because of the mixed effects of the different valence shells involved in the interaction formation, it is not straightforward to compare interactions directly from their ρ, $\nabla^2\rho$, V, and G values only. However, one can approach the problem by using normalized quantities per charge density unit, such as the ratio $(|V|/\rho)/(G/\rho) = |V|/G$. This descriptor permits to advance quantitative classification on *pure* closed-shell ($|V|/G < 1$) and *pure* shared-shell ($|V|/G > 2$) interactions introducing an intermediate region between these electronic states ($1 < |V|/G < 2$) (as it was shown in the theoretical study involving X–H···F–Y complexes[34c], **Figure I.7**).

Another normalized value – *bond degree* parameter (BD: $H/\rho = |V|/\rho + G/\rho$) – evaluates the strength of any pairwise interaction. This parameter can be interpreted as the total pressure per electron density unit (or the total energy per electron) at BCP, where normalization permits to scale (and therefore to compare) H values associated to different quantities of charge at BCP. When $|V| > G$ and $H < 0$, the BD parameter measures the *covalence degree* of the pairwise interaction; the stronger the interaction the greater is the *covalence degree* magnitude. When $|V| < G$ and $H > 0$, the BD parameter is an index of non-covalent interaction and is indicated as a *softness degree* per electron density unit at the BCP; the weaker the interaction, the greater the

softness degree magnitude, because the total (and positive) pressure H indicates an excess of kinetic energy (and therefore of the electron mobility) at BCP.

Figure I.8 shows the calculated values of $\nabla^2\rho(\mathbf{r})$ for the pairwise H···F interaction against the corresponding internuclear distances.[34c] These data clearly show how the full range of internuclear geometries can be divided in three characteristic regions.
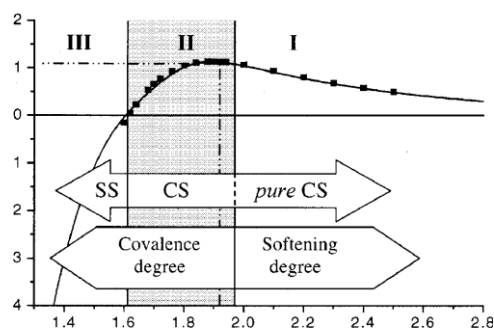
Figure I.8 $\nabla^2\rho(\mathbf{r})$ vs d(H···F). [34c]

Table I.2 summarizes the contribution of all the above mentioned parameters to the intermolecular bond classification into tree types. The border between the *pure* and *transit* CS regions is defined by $H = 0$ (dividing them into SD and CD areas) and between *transit* CS and *pure* SS by $\nabla^2\rho = 0$. As it can be seen from **Figures I.7** and **I.8**, for large distances, $\nabla^2\rho > 0$ and $H > 0$ as the contribution of the local kinetic energy is in excess in the interaction region ($|V|/G < 1$), indicating a *pure* closed-shell interaction (Region I). For short distances, $\nabla^2\rho < 0$ and $H < 0$, i.e. the potential energy is now in large excess ($|V|/G > 2$) and the interaction is shared-shell (covalent bond) – Region III. The intermediate region, corresponding to the transition between these kinds of interaction, is characterized by $\nabla^2\rho > 0$ and $H < 0$ ($1 < |V|/G < 2$) – Region II. In this intermediate region, the population of the bonding orbital grows very fast as the distance decreases due to the actual formation of the incipient covalent bond. [34c] Here, although the interaction remains mainly closed shell (the electron-density distribution is still locally depleted, as $\nabla^2\rho > 0$), it presents a shared-shell character owing to the excess of V compared to G ($H < 0$).

Table I.2 **Three regions of intermolecular interactions divided by the topological properties at BCP of $\rho(\mathbf{r})$.**

Region I	Region II	Region III
Pure closed-shell (CS)	Transit closed-shell (CS)	Pure shared-shell (SS)
ρ small	ρ medium	ρ large
$|V|/G < 1$	$1 < |V|/G < 2$	$|V|/G > 2$
$\nabla^2\rho > 0$		$\nabla^2\rho < 0$
$|\lambda_1 + \lambda_2|/\lambda_3 < 1$ (polarisation)		$|\lambda_1 + \lambda_2|/\lambda_3 > 1$
$H > 0$	$H < 0$	
$H/\rho > 0$	$H/\rho < 0$	
Softness degree	Covalence degree	

23

3.2. An overview on the topology of Laplacian of electron density

Concentration is the secret of strength.
Ralph Waldo Emerson

With the aim to interpret the solution of the Schrödinger equation in terms of chemical concept, the QTAIM theory proposes one more scalar function – the Laplacian of the electron density $\nabla^2\rho(\mathbf{r})$ – that contains complementary chemical information to that given by $\rho(\mathbf{r})$.[2] Indeed, $\nabla^2\rho(\mathbf{r})$ is characterized by a rich topology which enables one to determine the average number of electron pairs that are localized in a given atom, as well as the number of pairs that are shared between atoms. It also provides the physical underpinnings of the Lewis electron pair principal and of the empirical *Valence Shell Electron Repulsion* (VSEPR) model of molecular geometry.[36]

3.2.1. The main definitions

The Laplacian is derived from the second partial derivatives of the scalar function. In the case of $\rho(\mathbf{r})$, it reads:

$$\nabla^2\rho(\mathbf{r}) = \frac{\partial^2\rho}{\partial x^2} + \frac{\partial^2\rho}{\partial y^2} + \frac{\partial^2\rho}{\partial z^2}$$

It measures to what extent the scalar function is locally concentrated or depleted. To illustrate its practical use for the electron density analysis, we look at a one-dimensional profile of $\rho(\mathbf{r})$ for a second period of the Elements Table (**Figure I.9**). The local concentration of the function in the region between points a and b shows more features when passing to its first derivative and becomes much more evident from the second derivative function. It is more convenient to use $L(\mathbf{r}) = -\nabla^2\rho(\mathbf{r})$ function as it permits to associate the regions of charge concentration with its positive ($L(\mathbf{r}) > 0$) and the regions of charge depletion with its negative ($L(r) < 0$) values.[2] The Laplacian of electron density for an atom (free or in a molecule) oscillates between negative and positive values and reveals the internal fine shell structure of the atom. Each of the shells is characterized by a couple of alternating local maxima (CC) and minima (CD) along radial directions. In the case of Ar-atom (**Figure I.10**), three couples (CC/CD) correspond to the K, L, and M shells (or n = 1, 2, and 3 in accordance with its electron configuration

$f(x) = 8exp(-7x) + exp[-10(x-0.5)^2]$

(a) $f(x)$

(b) $\frac{df(x)}{dx}$

(c) $\frac{d^2 f(x)}{dx^2}$

(d) $-\frac{d^2 f(x)}{dx^2}$
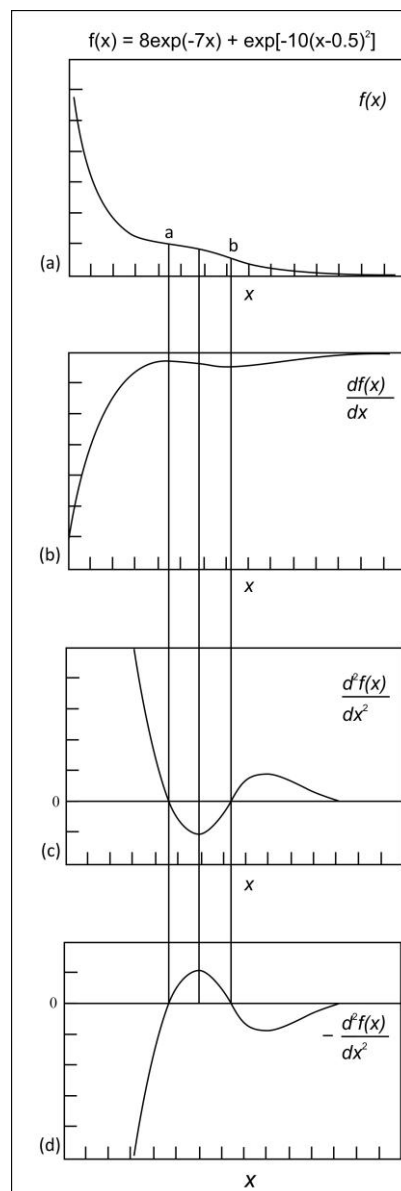
Figure I.19 Plots of monotonically function $f(\mathbf{x})$ and its first and second derivatives. The negative of the second derivative is shown to emphasize that a function is concentrated in a region where its second derivative is negative.[2]

$1s^22s^22p^63s^23p^6$). The charge concentration of the outer (valence) shell, M in this case, is of particular interest and would further be called *valence shell charge concentration* (VSCC). It should be noted, that the function $L(\mathbf{r})$ has its own topology, which is much more complicated than the one of $\rho(\mathbf{r})$, although, the same topological concept applied for their description.

(a)   **(b)**
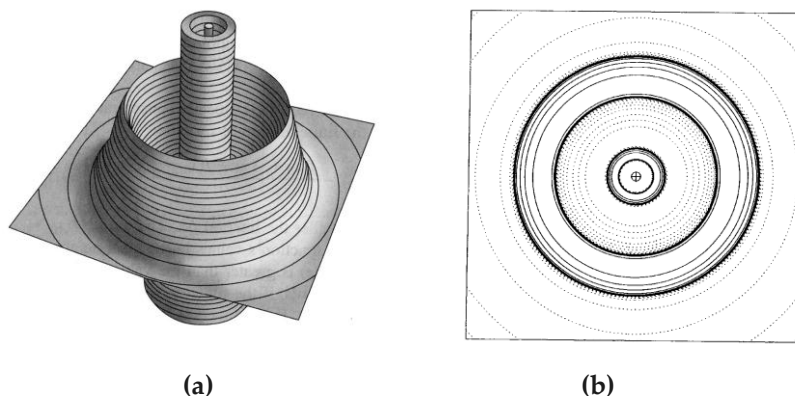
Figure I.10 (a) Truncated version of the relief map of $L(\mathbf{r}) = -\nabla^2\rho(\mathbf{r})$ function and (b) the corresponding contour map for a spherically symmetric electron density of an isolated Ar-atom.[2] Contours (eÅ^{-5}) are in logarithmic scale.

Similarly to $\rho(\mathbf{r})$, critical points in $L(\mathbf{r})$ are classified by their rank and signature (r, s). The VSCC of an atom consists of three types of CPs: local maximum $(3,-3)$ and saddle points $(3,-1)$ and $(3,+1)$, which are the minima on the surface of maximum charge concentration. The VSCC never contains $(3,+3)$ CP as it represents a minimum even in the radial direction.

Passing from an isolated atom to an atom in a molecule, the sphericity of its electron density distribution remains only for the inner shells. Indeed, the valence shell is always distorted from a spherical shape, sometimes just a little, but sometimes so extensively that it breaks up into separate charge concentrations and in some cases, in very polar molecules, it disappears completely. All the CPs in VSCC around the nucleus are linked in a polyhedron that is usually called the atomic graph, where the local density maxima in VSCC of the atom define the vertices, V ($(3,-3)$ CPs). The unique pair of trajectories of the gradient of $\nabla^2\rho(\mathbf{r})$ that originate at a saddle point and terminate at neighboring vertices define the edges, E ($(3,-1)$ CP), of the polyhedron. The set of trajectories that arise as ring critical points define the faces, F ($(3,+1)$ CP). The numbers of each type of critical point obeys the Euler's formula: $V - E + F = 2$.

3.2.2. Laplacian function applications

The key idea of the first application is to identify the critical points in $L(\mathbf{r})$ with the electron pairs in the VSEPR model.[36] This model assumes that the geometrical arrangement of the ligands about a central atom is that which maximizes the separation between the electron pairs or *domains*. The VSEPR model operates under three postulates: the nonbonding pair domains are larger than the bonding pair domains, the change in size of the bonding pair domains is a function of the electronegativity of the ligands and of the central atom, the domains of double and triple bonds are larger compared to those of single bonds. The bonding and nonbonding domains of the VSEPR model are associated with the regions of charge concentration that

QTAIM defines from the $L(\mathbf{r})$ topology. The second application of $L(\mathbf{r})$ is connected to the Lewis acid-base theory, where an acid is defined as an electrophile and a base as a nucleophile. In the frame of the $L(\mathbf{r})$ topology, nucleophilic and electrophilic sites are associated with the CC (3,–3) and CD (3,+1) sites in the VSCC region, respectively, and obey the so-called Laplacian complementarity principle, which states that local maxima and local minima of $L(\mathbf{r})$ in the valence shell of atoms belonging to different molecules combine to each other.[2]

In summary, the Laplacian of electron density acts as a 'magnifying glass' to reveal chemical features that are not evident from $\rho(\mathbf{r})$; here just its usefulness in improving the understanding of molecular geometry was illustrated.[37]

3.3. An overview on the electrostatic potential

In usual cases, the main contribution to the intermolecular interaction energy is electrostatic (see **Chapter II**), so the analysis of the molecular electrostatic potential $V(\mathbf{r})$[38] can be a useful complement to the rich information on molecular reactivity provided by the electron distribution and Laplacian functions.

3.3.1. Calculation method

For an atom, a molecule, or a group of molecules in a crystal, the electrostatic potential can be derived from the electron density function $\rho(\mathbf{r})$ of the system. The use of a precise electron-density model is essential for accurate electrostatic potential computation:

$$V(\mathbf{r}) = \int \frac{\rho(\mathbf{r})}{\mathbf{r}-\mathbf{r}'} d^3\mathbf{r}'$$

The multipolar model of Hansen-Coppens[18] permits to calculate analytically the electrostatic potential that is created by the nuclei and electrons of a molecule at any point $\mathbf{r}$ of the surrounding space.[39] It is described as an addition of atomic contributions:

$$V_{at}(\mathbf{r}) = V_{core}(\mathbf{r}) + V_{val}(\mathbf{r}) + \Delta V(\mathbf{r})$$

where each of them can be decomposed into three terms: [40]

$$V_{core}(\mathbf{r}) = \frac{Z}{|\mathbf{r}-\mathbf{R}|} - \int_0^\infty \frac{\rho_{core}(\mathbf{r}')}{|\mathbf{r}-\mathbf{R}-\mathbf{r}'|} d^3\mathbf{r}' \quad \text{- potential of core electrons with the nuclei contribution,}$$

$$V_{val}(\mathbf{r}) = -\int_0^\infty \frac{P_{val}\kappa^3\rho_{val}(\kappa\mathbf{r}')}{|\mathbf{r}-\mathbf{R}-\mathbf{r}'|} d^3\mathbf{r}' \quad \text{– potential of valence electrons describing spherical symmetry,}$$

$$\Delta V(\mathbf{r}) = -4\pi\sum_{lm}\frac{\kappa'P_{lm}}{2l+1}\cdot\left[\frac{1}{\kappa^{l+1}|\mathbf{r}-\mathbf{R}|^{l+1}}\cdot\int_0^{\kappa'|r-\mathbf{R}|}t^{l+2}\mathbf{R}_l(t)dt + \kappa'^l|\mathbf{r}-\mathbf{R}|^l\cdot\int_{\kappa'|r-R|}^\infty\frac{\mathbf{R}_l(t)}{t^{l-1}}dt\right]d_{lm}(\Omega) -$$

potential of valence electrons describing non-spherical symmetry. Z is the charge of the nucleus located at R, ρ_{core} and ρ_{val} are the core and valence electron densities.

3.3.2. Topological properties

The molecular electrostatic potential allows to identify the acidic (nucleophilic) and basic (electrophilic) sites of the molecule. These sites could be clearly defined from the lines of the electric field, which is the gradient function of $V(\mathbf{r})$ ($\mathbf{E}(\mathbf{r}) = -\nabla V(\mathbf{r})$).

In some aspects, the topology of electrostatic potential $V(\mathbf{r})$ shows equivalent features to the one of electron density $\rho(\mathbf{r})$ developed in the framework of QTAIM.[2] Indeed, both exhibit local maxima at the nuclear positions and (3, −1) bond critical points between bonded atoms, that leads to a saddle conformation with a minimum along the bond path and a maximum in the plane perpendicular to this direction. Similarly to $\rho(\mathbf{r})$, position of BCP's and the corresponding values in the topology of $V(\mathbf{r})$ values are related to properties of the bonded atoms. For instance, atomic radius or electronegativity can be derived from the topological analysis of the electrostatic potential. Moreover, the critical points are related to the existence of **zero-flux surfaces** of $V(\mathbf{r})$ which define a partition of the space in electrostatic basins (V-basins). All the features of $V(\mathbf{r})$ are shown in **Figure I.11a** on the example of the LiCN···HNC complex.

(a)	**(b)**
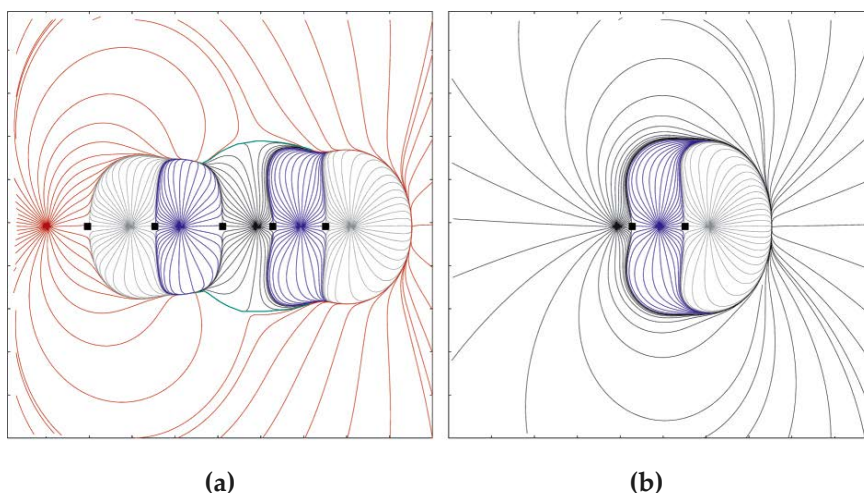
Figure I.11 Electric field lines ($\mathbf{E} = -\nabla V(\mathbf{r})$) for (a) the LiCN···HNC complex and (b) the HNC monomer. (3,−1) BCP's are denoted by black squares, zero-flux surface is in green.[41]

On the other hand, there are also important differences between the topologies of $V(\mathbf{r})$ and $\rho(\mathbf{r})$. While $\rho(\mathbf{r})$ can present local maxima outside the nuclear positions, this is not possible for $V(\mathbf{r})$. Another important difference is that, while $\rho(\mathbf{r})$ is found positive everywhere, $V(\mathbf{r})$ values can be negative in the outer regions of molecules due to the local accumulations of electrons (as, for example, in lone pair regions), showing negative local minima of $V(\mathbf{r})$ that have no counterpart in $\rho(\mathbf{r})$. Accordingly, the topology of $V(\mathbf{r})$ is more complex. It exhibits a large diversity of critical points outside the bonding region and has been less elaborated in comparison with $\rho(\mathbf{r})$. The partition of the space, defined by the zero-flux surfaces of $V(\mathbf{r})$, is different from that of electron density, as experimentally observed in crystals.[42] It is remarkable that enclosed (finite) V-basins (**Figure I.11**) exhibit zero-net charge as a consequence of the Gauss theorem and can be regarded as regions mostly electrostatically isolated.

Comparing the electrostatic potential $V(\mathbf{r})$ to the previously described Laplacian function $L(\mathbf{r})$, it could be understood that both of them can be used to reveal the location of nucleophilic and electrophilic sites around an atom. However, this is only partially true. While $L(\mathbf{r})$ distinguishes between the maxima at the nuclear position and at the nucleophilic region of the atomic valence shell (lone pairs) in any molecular environment, $V(\mathbf{r})$ defines the location of the lone pair by a local minimum value of $V(\mathbf{r})$ only in the monomer molecule. Indeed, upon complex formation, this local minimum disappears, giving rise to a $V(\mathbf{r})$ BCP in the intermolecular region. In addition, the electrophilic site is not detectable in a neutral molecule from the topology of $V(\mathbf{r})$, because the V-basin is open (see **Figure I.11b**) and it is the nucleus that acts as the electrophile site.

The mentioned reasons explain our choice of $\rho(\mathbf{r})$ and $L(\mathbf{r})$ functions for the intermolecular interactions characterization. The topological properties of these functions were found to be more reliable for the estimations of the interaction's main properties – strength and directionality.

4. The total energy of intermolecular interaction

An intermolecular interaction can be also described in terms of energy. In the framework of the following discussions, different contributions to the energy will be mentioned in order to define the nature of the interaction. The present section is devoted to the general explanation of different terms of the total interaction energy of a system.

Within the Born–Oppenheimer approximation, the energy of a diatomic AB-system can be completely described with one internal coordinate – the internuclear distance $\mathbf{r}$ (**Figure I.12**). The energy is the lowest at the equilibrium distance (r_0). It is negative for all distances $\mathbf{r} > r_0$ and also for some distances that are shorter than r_0. It is positive only for very short range. The zero-energy line separates the so-called stabilizing ($E < 0$) and destabilizing ($E > 0$) regions. Any deviation from the equilibrium distance (r_0) costs an enthalpic penalty, but this penalty is large only for large deviations of $\mathbf{r}$.

Figure I.12 A typical potential energy curve (in arbitrary units) versus internuclear separation $\mathbf{r}$ $E(\mathbf{r})$ for a diatomic system superposed with force function $F(\mathbf{r})$. At the equilibrium distance, the attractive and repulsive components of force are equal.

One must distinguish between the interaction energy and force between atoms. At the equilibrium distance r_0, the force is zero – its attractive and repulsive components are equal. This corresponds to the energetically most favorable geometry with the lowest energy. For $\mathbf{r} \neq r_0$, a force arises trying to restore the optimal geometry for the system – for $\mathbf{r} > r_0$ it is attractive and for $\mathbf{r} < r_0$ it is repulsive.

From the theoretical viewpoint, the overall energy of an intermolecular interaction can be decomposed into various physically meaningful contributions: electrostatics, induction, polarization, charge transfer, dispersion, exchange repulsion, orbital interaction, etc.; some of these terms are interchangeable depending on the decomposition procedure. Different procedures have been introduced for partitioning the interaction energy into the subsets of this collection. However, only the total interaction energy is physically observable, while its various proposed components can be hardly determined experimentally.[43]

In the frame of the perturbation theory,[44] the total interaction energy (E_{int}) consists of electrostatic, induction, dispersion, and exchange–repulsion energies.[44c,45]

$$E_{int} = E_{es} + E_{ind} + E_{disp} + E_{exrep}$$

The four contributions can be classified into two categories: these of classical origin – electrostatic contributions (E_{es}, E_{ind}), and these of quantum-mechanical origin – van der Waals contributions (E_{disp}, E_{exrep}).

❖ *Electrostatic interaction energy*

Within the perturbation approach, the electrostatic term is a leading component for polar molecules.[46] It is a cause of the attraction between groups with opposite electronic charge. The **pure electrostatic energy term** represents a classic Coulombic interaction between two unperturbed monomer charge distribution ρ_A and ρ_B:[47,48]

$$E_{es} = -\iint \frac{\rho_A(\mathbf{r}_A)\rho_B(\mathbf{r}_B)}{|\mathbf{r}_A - \mathbf{r}_B|} d\mathbf{r}_A d\mathbf{r}_B$$

However, this term always involves some degree of mutual polarization (**induction effect E_{ind}** – always attractive) between the two interacting molecules. The total electrostatic component may include the charge transfer effect, which is considered as an 'extreme manifestation of polarization'.[48a] The charge-transfer treatment of a R–A···B interaction is often presented through natural bond orbital (NBO) analysis.[49] It is based on the mathematical interpretation of the electrons transfer from an occupied orbital of B to the unoccupied σ* orbital of A, and therefore the A···B interaction becomes conceptually similar to covalency. Electrostatic energy component is characterized by inverse distance dependence (~$\mathbf{r}^{-1}$).

❖ *Van der Waals interaction energy*

The van der Waals interaction energy is combined of repulsion and dispersion components (**Figure I.13**). It can be described in terms of the Lennard-Jones (LJ) potential energy:

$$V_{LJ}(\mathbf{r}) = \frac{C_{12}}{\mathbf{r}^{12}} - \frac{C_6}{\mathbf{r}^6} = 4\varepsilon\left[\left(\frac{\sigma}{\mathbf{r}}\right)^{12} - \left(\frac{\sigma}{\mathbf{r}}\right)^6\right],$$
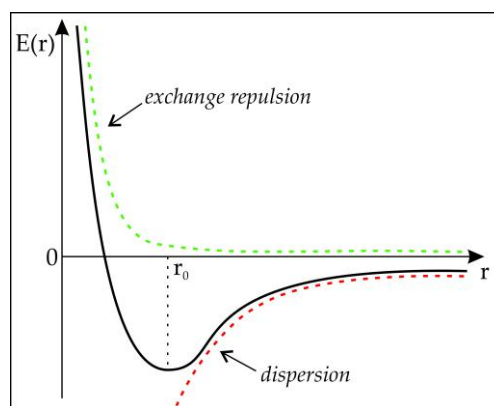
Figure I.13 A typical van der Waals interaction energy curve (in arbitrary units) versus **r**. Its repulsion and dispersion components are marked in green and red.

$$\sigma = \left(\frac{C_{12}}{C_6} \right)^{1/6} \quad \text{and} \quad \varepsilon = \frac{C_6{}^2}{4C_{12}}$$

The repulsion energy term E_{exrep} (the first one) arises from the Pauli principle[50] at short ranges of distances due to the overlapping between electron orbitals. It follows an $\mathbf{r}^{-12}$ law meaning that its important contribution at short distances rapidly diminishes with the distance increase. This is the contribution that keeps molecules apart from one another. Spackman approximated this quantity by a sum of atom-atom repulsive terms of single exponential form:[47,51]

$$E_{\text{exrep}} = \sum b_j b_j \exp\left[-(c_i + c_j) \cdot \mathbf{r} \right]$$

The dispersion energy term E_{disp} (the second one) describes attraction at long range caused by the instantaneous correlation in the fluctuations of the charge density distribution of each molecule (stabilized by van der Waals or dispersion forces). It is also approximated by a sum of atom-atom terms, each one proportional to $\mathbf{r}^{-6}$ (being in accordance with the LJ potential):

$$E_{\text{disp}} = -\sum_{i,j} a_i a_j \mathbf{r}^{-6}$$

The coefficients are related to the square root of average atomic C_6 dispersion coefficients, which appear in the LJ potential. The attractive dispersion interaction can be considered as 'the universal glue that leads to the formation of condensed phases'.[52]

Each of the mentioned energetic contributions is characterized by its own distance dependence, which is relevant to the events that precede nucleation and crystallization. Electrostatic interactions, for example, have a more gradual fall-off with distance ($\sim \mathbf{r}^{-1}$) than interactions with dispersive character ($\sim \mathbf{r}^{-6}$). Therefore, they are viable at distances that are much longer than the van der Waals limit. For this reason, the definition of the nature of an interaction, based on the character of the strongest contribution in total energy, is very important for explaining the interaction behavior.

Chapter II

Hydrogen, halogen & chalcogen bonding as weak intermolecular interactions

In this chapter we concentrate on the weak intermolecular interactions that are among the most important ones from crystal engineering viewpoint – namely hydrogen, halogen, and chalcogen bonding – which nature and strength are discussed in numerous experimental and theoretical studies. Along with the brief historical reference, the accepted definitions for these interactions are given. The attention is paid to the experimental and theoretical charge density studies, performed for different systems representing hydrogen, halogen, and chalcogen bonding interactions.

Introduction

How does the weak interaction become important in determining crystal packing? This is referred to as the Gulliver effect.

G.R. Desiraju

A molecular crystal is a periodic assembly of molecules that are held together by intermolecular (non-covalent) interactions. As the main purpose of crystal engineering is to design molecular structures with certain pre-desired properties, collecting the full knowledge about intermolecular interactions perfectly suits the scope of this research field.[53] Strength, directionality, and distance fall-off are three main characteristic properties of any intermolecular interaction.

The chemist's rough distinction between *strong* covalent and *feeble* non-covalent interactions is based on the corresponding average energetic ranges: $75 - 125$ and $1 - 15$ kcal mol^{-1}, respectively. However, the interactions, lying in the lower range of energies ($0.5 - 5$ kcal mol^{-1}) – weak intermolecular interactions – are also important in the context of crystal engineering due to their flexibility in the packing, and exactly they will be the subject matter of this work.

Based on the second property – namely, directionality – intermolecular interactions are termed as being isotropic (lacking directionality) or anisotropic (having directionality). Isotropic interactions are responsible for close packing and are mainly of the dispersion–repulsion energetic type. Anisotropic interactions, being predictable, allow one to suggest design strategies for crystals of related molecules.

The distance dependence of the interaction energy is also important to know as it defines the dominating energy contribution to the interaction (as it was described in Chapter I). Electrostatic interactions like the hydrogen bond have a more gradual fall-off with distance ($\sim r^{-1}$) than interactions with dispersive character ($\sim r^{-6}$). Therefore, they are viable at distances that are much longer than the van der Waals limit.

These energetic and spatial properties define the role of each interaction in the crystal packing: strong and directional interactions are responsible for molecular topology and connectivity, while non-directional interactions of a large distance range provide density and packing efficiency.

Hereafter, the attention will be paid to the weak intermolecular interactions such as hydrogen, halogen, and chalcogen bonding.

1. Weak hydrogen bonding

To begin this brief survey we will consider the most reliable intermolecular interaction in the toolkit of a crystal engineer – hydrogen bonding. In the majority of the cases, it is both quite strong and directional and it lies in an energy range intermediate between van der Waals interactions and covalent bonds. This energy range permits hydrogen bonds to associate and dissociate quickly at ambient temperatures.

1.1. General overview

1.1.1. Historical background

Scientists have been studying hydrogen bonds for just about 100 years. The earliest references to concepts that would be termed today hydrogen bonds occur in the German literature. Werner (1902)[54a] and Hantzsch (1910)[54b] described the binding situation in ammonia salts by the term *secondary valence*. In his paper, Pfeiffer (1913)[54c] termed an intermolecular interaction between adjacent C=O and OH groups the *inner complex salt formation*. Moore and Winmill (1912)[54d] used the term *weak union* to describe the weaker basic properties of trimethylammonium hydroxide relative to tetramethylammonium hydroxide. The description of hydrogen bonding in its most well-known setting, water, came some years later, in 1920, from Latimer and Rodebush.[54e] However, the definition of this bonding phenomenon by the term *hydrogen bond* is associated with the name of Linus Pauling (1935).[54f] The chapter on hydrogen bonding in his book *The Nature of the Chemical Bond* (Pauling 1939)[54g] drew this subject into the chemical mainstream. Pauling was clear and unambiguous in the use of the word *bond* in respect to X–H···Y–Z contact: "**Under certain conditions an atom of hydrogen is attracted by rather strong forces to two atoms, instead of only one, so that it may be considered to be acting as a bond between them**". Instead of being attracted only by X, the hydrogen atom is attracted to both X and Y.

1.1.2. Bond definition and classification

The current definition of hydrogen bond X–H···Y–Z, which has been recently accepted by IUPAC,[55] states:

"**A hydrogen bond is an attractive interaction between a hydrogen atom from a molecule or a molecular fragment X–H in which X is more electronegative than H, and an atom or a group of atoms in the same or a different molecule, in which there is evidence of bond formation.**" The three most important features of this definition are: (i) the hydrogen bond is electrostatically attractive; (ii) H is more electropositive than X, the atom to which it is covalently bonded; (iii) evidence of bond formation is needed.

A hydrogen bond is considered to be an electrostatic interaction;[56] however, depending on the nature of donors (Y) and acceptors (X), partially covalent (high electronegativity of X and Y) or dispersive–repulsive (low electronegativity of X and Y) character appears.

The case of the X–H⋯Y–Z interaction, where the electronegativities of the donor and acceptor atoms are reduced is referred to as *weak hydrogen bonding*. These kind of contacts are found in large length and angular ranges as they can be distorted by other forces in the crystal (the typical X–Y and H⋯Y distances are 3.0–4.0 and 2.0–3.0 Å, X–H⋯Y angle is 110–180 °) and correspond to the energies < 4 kcal mol^{-1}.[57] Very often X is carbon, Y may be a multiple bond like C=C or C≡C or an aromatic ring, even if other X- and Y-atoms can also appear (e.g. C–H⋯O, C–H⋯N, C–H⋯π, O–H⋯π, N–H⋯π, O–H⋯Tr (Tr – transition metal), M–H⋯O (M = any metal) etc.). In contrast to strong, weak hydrogen bonds are compressed or expanded, and bent or straightened, by other crystal packing forces; for the same reason they are often less directional. A rough classification of the weak hydrogen bonding, proposed by Desiraju, is based on the electronegative power of donors and acceptors (**Table II.1**).[57]

Table II.1 Classification of weak hydrogen bonds based on the donor and acceptor power.[57]

Category	Examples
1. Weak donor – strong acceptor	C–H⋯O/N, C–H⋯Cl$^-$
	Mo–H⋯O≡C, Ir–H⋯Cl–Ir
2. Strong donor – weak acceptor	O–H⋯Se, N–H⋯Co
	Cl–H⋯C≡C, O–H⋯C=C
3. Weak donor – weak acceptor	C≡C–H⋯π, C–H⋯M
	S–H⋯ π, C–H⋯F–C
4. Other varieties (agostic interactions)	N–H⋯H–B Formyl hydrogen bond

In weak hydrogen bonds, the relative contribution of electrostatics can be smaller than in their strong counterparts, giving way to the dispersion term; the predominance of one term over another depends on the certain preferred orientations of molecules. C–H⋯O bonds are commonly encountered in organic crystal structures owing to the frequent occurrence of the oxygen atom in simple organic molecules. These interactions can play a significant role in crystal packing. Having electrostatic character with a long range distance fall-off ($\sim r^{-1}$), these interactions are viable at distances that are equal to or longer than the van der Waals limit. So even long C⋯O separations (~4.00 Å) may need to be considered. While the part of the electrostatic contribution reduces, the dispersion term remains unchanged, so the total interaction becomes less and less directional and the hydrogen bonds fade into the van der Waals continuum.[58]

However, in many cases, weak hydrogen bonds retain many significant properties of the strong hydrogen bonds and can be as effective as their stronger counterparts. Accordingly, the study of weak hydrogen bonds is important in crystal engineering.

1.2. Topological analysis of electron density

The analysis of hydrogen bonding in the framework of QTAIM permits to characterize this interaction in terms of its electron density topology.[53] The more detailed studies of its topological parameters improved the earlier proposed hydrogen bond classification based only on its strength and directionality. The electron density, its derivatives and energy densities evaluated at the bond critical points of hydrogen bonds are known to vary with respect to interaction geometry and environment.

From the theoretical point of view, hydrogen bonding serves as a good model system for revealing the relative dependence of topological parameters that were described in **Chapter I**. In the series of studies, Espinosa et al.[34a,b 59] showed that relationships exist between the topology of $\rho(\mathbf{r})$ in the hydrogen bond region and some energetic properties, such as the local potential (V^{BCP}) and kinetic (G^{BCP}) energy densities.

In the first paper,[34a] the exponential behavior of G and V as a function of $d(\mathrm{H}\cdots\mathrm{O})$ was shown on a large set of experimentally determined X–H⋯O (X = O, N, C) hydrogen bonds; this permitted to correlate the hydrogen bond energy to the pressure exerted on the electron density around the bond critical points (V^{BCP}). The validity of this correlation was tested latter on against a set of 32 theoretically calculated X–H⋯F–Y interactions.[34d] In the second paper,[59a] the relationships between the principal curvatures λ_1, λ_2, λ_3 and energetic properties was discussed, leading to a new representation of the topological characteristics of $\rho(\mathbf{r})$ in terms of energy and *vice versa*. It was found that the positive curvature at the bond critical point λ_3 is the most meaningful parameter for the characterization and classification of hydrogen bonds. It shows a very well defined behavior versus all pertinent geometrical and energetic hydrogen bond parameters and is a good representation when closed-shell interactions are involved.

According to a theoretical study involving X–H⋯F–Y systems,[34c] both $\nabla^2\rho(\mathbf{r})$ and the total electron energy density H at BCP (or, equivalently, the ratio $|V|/G$) are indicators of the closed- or shared-shell character of the atomic pairwise interaction. From this theoretical analysis, all the topological and energetic properties show a continuous dependence with the hydrogen-acceptor distance. Associated with the values of these indicators, the complete range of distances can be divided into three regions, corresponding to three different types of interactions (see **Chapter I** for details). In the recent theoretical studies, H⋯X hydrogen bonding were classified in families according to the acceptor entity X (X = H, C, N, O, F, S, Cl, π).[60] The universal features between the electron properties at BCP were found, and were shown to be reliable applying to the experimental high-resolution X-ray diffraction data.

2. Halogen bonding

Intermolecular interactions involving halogen atoms are widely observed in crystal engineering.[61] Numerous properties characterizing this interaction have analogies with those of the hydrogen bond previously discussed. For example, the strong preference for linearity of X–Hal⋯Y parallels that known for X–H⋯Y hydrogen bonds. This analogy allows transferring the hydrogen bonding notation to the interactions involving halogens, calling them halogen bondings. However, the name is reserved just for certain types of interactions, so the attention should be paid to their nature.

The present section outlines the major findings in the field of the halogen bonding interaction, along with its definition and classification. The interaction nature is evidenced from the experimental charge density studies, supported by theoretical calculations.

2.1. General overview

2.1.1. Historical background

The first report describing systems involving halogen atoms as electrophilic '*sticky*' sites in self-organization processes can be traced back to 1814 when M. Colin[62] illustrated the behavior of iodine reacting with ammonia and reported the formation of a diiodine / ammonia system which was published and formulated as $H_3N⋯I_2$ by F. Guthrie in 1863.[63] Later in 1896 the pyridine·alkyl iodide adducts were isolated in the work of A. B. Prescott.[64] Just 40 years later the scientists came back to the investigation of the halogenated compounds. First, in 1936 B. Vonneguten described the structure of crystalline bromine,[65] while in 1952 R. L. Collin revealed the structure of crystalline chlorine,[66] which was found to be isostructural (space group *Ccma*), and formed by short intermolecular Hal⋯Hal interactions. The spontaneous complexation between I_2 and different aromatic solvents was identified in the UV/visible region by Benesi and Hildebrand in 1949.[67]

In the 1950s R. Mulliken developed a detailed theory of electron donor–acceptor complexes, classifying them into outer (which are very weak with little charge transfer) or inner (which have extensive charge redistribution) complexes.[68] Mulliken's theory has been used to describe the mechanism by which halogen bonding formation occurs. By the studies of R. M. Keefer that included Br_2, Cl_2, as well as heterohalogens ($Hal_1⋯Hal_2$), the experimental basis for the development of Mulliken's theory of charge-transfer complexes were provided.[69]

In 1954, O. Hassel *et al*. showed by means of a crystallographic study that the 1:1 molecular complex of bromine and dioxane was assembled with polarization induced $Br(\delta^+)⋯O(\delta^-)$ directional interactions (the intermolecular distance being only 2.71 Å, i.e. 80.9 % from the sum of the van der Waals radii of O- and Br-atoms, with the angle Br–Br⋯O close to 180 °) (**Figure II.1**).[70] This became a
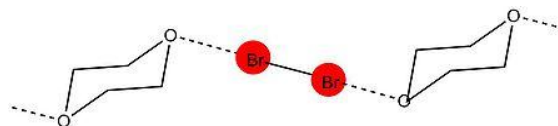
Figure II.1 Chains in the 1:1 adduct of 1,4-dioxane and bromine. In 1954, Hassel provided evidence for the first X-ray crystallography study done with halogen bonding.[70a]

turning point in the comprehension of halogen bonding formation and its characteristics. In his Nobel lecture in 1970,[71] Hassel concluded that halogen atoms are directly linked to an electron pair donor with a bond direction that coincides with the axes of the orbitals of the lone pairs in the electron pair donor molecule and unequivocally stressed the importance of intermolecular interactions involving halogen atoms as electrophilic species for directing molecular self-assembly phenomena. It should be noticed that contacts involving heavier halogens (Br, I) were studied first. Polarization effects are expected to be more pronounced in these cases; there is no doubt that halogen bonds have a considerable component from polarization.

In 1968, H. A. Bent published a review on the structural chemistry of donor–acceptor adducts where he showed that similar qualitative interactions could be formed either between halogen and Lewis base (Hal···LB, LB = O, N, S), or between homohalogens (Hal$_i$···Hal$_i$), or heterohalogens (Hal$_i$···Hal$_j$).[72]

In 1976, J.-M. Dumas had found the existence of weak interactions between the solvents of type MX$_4$ (M = C, Si; X = Cl, Br) and polar solutes (oxides, pyridine, benzene, trimethyl-1, 3,5 benzene).[73] In his work he had indicated the role of halogen atoms in the formation of these interactions, in close analogy with the hydrogen bonding interaction. In particular, he reported a charge transfer in the interaction C–Hal···LB; he classified the strength of this interaction in respect to the atomic number of the halogen (I > Br > Cl). The effect is further enhanced when an electron-withdrawing group is attached to a more electronegative central atom (C > Si): CCl$_4$ < CBr$_4$, SiCl$_4$ < CCl$_4$, SiCl$_4$ < SiBr$_4$. After a few years, in 1978, the term *halogen bond* was introduced by Dumas to call this kind of interaction.[74]

Murray-Rust, Desiraju, and Parthasarathy afforded further information on halogen bonded (X-bonded) systems in the solid state by analyzing statistically the crystal structures in the Cambridge Structure Database (CSD).[75] More recently, Legon[76] reviewed the features of the complexes between Hal-atoms and different LBs in the gas phase. A valuable tool for the theoretical understanding of the halogen bond was proposed in 1994 by P. Politzer and J. S. Murray, who identified the anisotropic distribution of the electron density around covalently bound halogens and proposed the approach of the *σ-hole*.[77] All the previously mentioned findings were put together in a unified concept where the electrophilic behavior of halogen atoms was announced as a general phenomenon of aggregation processes.[78] The first book specifically devoted to this interaction and its application was published in 2008.[61]

2.1.2. Bond definition and classification

Although halogen bond has been known for many years in crystal engineering, it is still the subject of intense research efforts. In the last two years, an IUPAC Task Group was intensively working on the definition and classification of R$_i$−Hal···Y−R$_j$ (Y = Hal, LB) halogen bonds; many international conferences and workshops were held with the aim to promote a unified conceptual frame in this subject.

Considering that the halogen atom (Hal) is supposed to be partially negatively charged, the very existence of the halogen bond was, at first sight, puzzling. This effect was explained by the anisotropic nature of the electron density $\rho(\mathbf{r})$ around the halogen nucleus, leading to a larger atomic radius in the equatorial region and a smaller atomic radius in the polar region. As a consequence, these regions exhibit concomitant negative and positive electrostatic potential

magnitudes,[77] and then the halogen atom behaves as a nucleophile at the equator and as an electrophile along the pole direction (**Figure II.2a**).[79] The anisotropic distribution of $\rho(\mathbf{r})$, called '*polar flattening*', explains why the nature and the strength of these interactions strongly rely on the involved atoms and their relative position.

(a)   **(b)**

(c)

Figure II.2 (a) Anisotropic distribution of $\rho(\mathbf{r})$ around halogen atom (X), showing different atomic radii (r_{min}/r_{max}) along polar and equatorial directions (b) Type-I interaction ($\theta_1 \approx \theta_2$); (c) Type-II interaction ($\theta_1 \approx 90°$, $\theta_2 \approx 180°$). [61]

Depending on the atoms involved in the interaction, halogen bonds can be either symmetrical ($Hal_i \cdots Hal_i$) or unsymmetrical ($Hal_i \cdots Y$, $Y = Hal_j$, LB).

Typically, it is accepted to distinguish two geometrical preferences for symmetrical contacts (e.g. $F \cdots F$, $Cl \cdots Cl$, $Br \cdots Br$, and $I \cdots I$).[75bc,80] The first arrangement (Type-I) occurs when $\theta_1 \approx \theta_2$, where θ_1 and θ_2 are the $C-X_1 \cdots X_2$ and $X_1 \cdots X_2-C$ angles, respectively (**Figure II.2b** represents one kind of Type-I geometry, however, as it will be shown later, the other variants of their respective orientation are also possible). The second geometry (Type-II) arises when $\theta_1 \approx 90°$ and $\theta_2 \approx 180°$, causing the closest linear approach (as $C-X_1 \cdots X_2 \approx 180°$) between the interacting electropositive and electronegative regions (**Scheme II.1c**).

Unsymmetrical halogen bonds ($Hal_i \cdots Y$, $Y = Hal_j$, LB) can be assigned to Type-II interaction as they also represent linear geometry between the interacting electronegative and electropositive sites. Contacts like $I \cdots Br$, $I \cdots Cl$, $I \cdots N$, $I \cdots O$, $Br \cdots O$, and $Cl \cdots N$ belong to this category.

Among Type-I and Type-II $Hal \cdots Hal$ geometries, the former is created between electrostatically identical regions of the adjacent halogens as a consequence of close packing and cannot strictly be called halogen bonds, whereas the latter is described as a polarization induced contact stabilized by the electrostatic forces and considered to be a genuine halogen bond.[81]

These considerations are strictly in accordance with a just accepted by IUPAC definition of the halogen bond,[82] which reflects the one for the previously discussed hydrogen bond:

"A halogen bond $R_i-Hal \cdots Y-R_j$ occurs when there is evidence of a net attractive interaction between an electrophilic region on a halogen atom Hal belonging to a molecule or a molecular fragment R_i-Hal (where R_i can be another atom, including Hal, or a group of atoms) and a nucleophilic region of a molecule, or molecular fragment, $Y-R_j$." The halogen bonding interaction should satisfy the following criteria: (i) distances should be of the range of the sum of the van der Waals radii of the interacting atom, (ii) the interaction should represent a linear geometry ($R_i-Hal \cdots Y$ angle $\approx 180°$).

As the contacts representing Type-I $Hal_i \cdots Hal_i$ geometry and other interactions involving Hal-atoms are quite numerous, and their nature and origin are more diverse and insinuating, hereafter we will distinguish between the genuine halogen bond (that corresponds to the definition given above) and other non-covalent interactions involving Hal-atoms that allow the bonding formation by stabilizing energy.
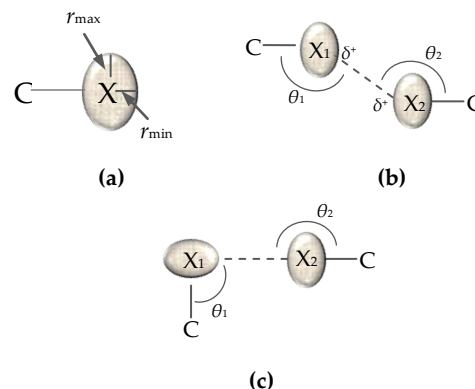
2.2. Experimental and theoretical charge density studies

The evidence for halogen bond occurrence is provided by different experimental and theoretical methods, most of them being derived from the electron density $\rho(\mathbf{r})$. Several approaches based on the electrostatic potential, the deformation density $\Delta\rho(\mathbf{r})$, and the negative Laplacian $L(\mathbf{r}) = -\nabla^2\rho(\mathbf{r})$ reveal the same features of Hal-atoms and complement each other in deriving the halogen bond nature.

Generally, halogen bonding is understood as a polarization induced contact, stabilized by the electrostatic forces. However, in many cases other contributions also play a significant role. Their relative significance may vary from one case to the other and will be illustrated later on.

❖ *Deformation density analysis*

As described in **Chapter I**, the deformation density $\Delta\rho(\mathbf{r})$ allows for the identification of the regions where the resulting charge density is in deficiency (δ^+) or in excess (δ^-) with respect to non-interacting spherical atoms. For the Cl-atom, the deformation density map (**Figure II.3a**[83]) shows a δ^+ region along the C–Cl direction and a δ^- region in the perpendicular direction. The deformation density shape is in accordance with the *polar flattening* effect, firstly described by Desiraju[79] and lately shown in C_6Cl_6 from the $\rho(\mathbf{r})$ map (**Figure II.3b**). [83]

(a)	**(b)**
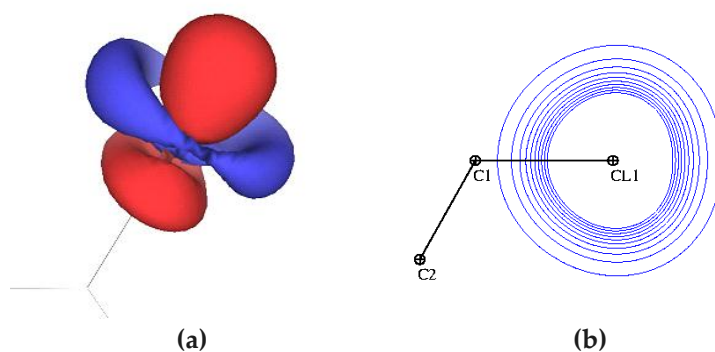
Figure II.3 Cl-atom in the crystal structure of C_6Cl_6 (a) 3D static deformation density map $\Delta\rho(\mathbf{r})$. The iso-surfaces are drawn at ±0.05 eÅ^{-3}. Blue and red indicate positive (electron excess, δ^-) and negative (electron deficiency, δ^+) regions. (b) $\rho(\mathbf{r})$ map, contours are drawn at 0.1 eÅ^{-3} Different r_{min} and r_{max} distances are observed to the iso-contours along the bonding axes and the equatorial directions. [83]

❖ *Electrostatic potential analysis*

The *σ-hole* concept proposed by Politzer and co-workers[77] revealed that the three lone pairs of a Hal-atom form a belt of negative electrostatic potential around its central region leaving a positive *σ-hole* on the outermost portion of its surface around the R–Hal axis (**Figure II.4**). This *σ-hole* can interact favorably with negative electrostatic potential sites of other molecules, giving rise to halogen bonding.

From all the halogen atoms, the most challenging one in the question of intermolecular interactions is certainly fluorine.[84] Having relatively small size, the highest electronegativity and low polarizability, it doesn't show a positive electrostatic potential in its outermost region and, accordingly, it is not capable to interact with a negative site of another molecule. However, this

type of interaction has been also observed for F-atom.[85] In the case of the Cl-atom, depending on its activation, the *σ-hole* can be present or not. For example, in the CH₃Cl molecule, the Cl-atom doesn't have a positive *σ-hole*,[77b] and consequently shouldn't be able to form a halogen bond, while the evidence of Cl···O contact between CH₃Cl and OCH₂ is available.[86] Thereby, it seems that the *σ-hole* concept is useful when electrostatic forces play the major role in stabilizing the halogen-bonded complexes, and this concept fails when other interaction energy components are significant.
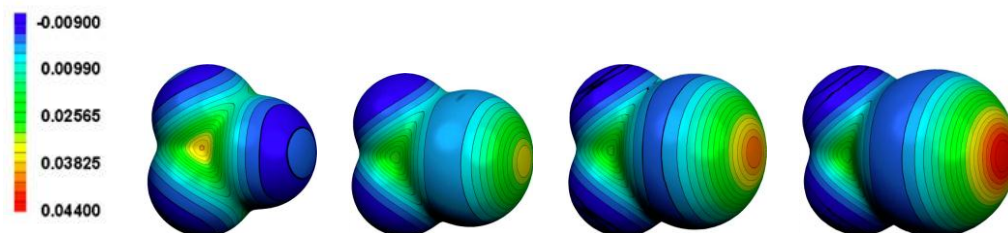
Figure II.4 Electrostatic potential for the series of model molecules CF₃Hal illustrating the presence of *σ-hole* for Cl- (activated by three fluorines), Br-, and I-atoms, and its absence for F-atom.[77c]

❖ *Laplacian analysis*

The controversial situations concerning Hal-atoms can be resolved from the viewpoint of the Laplacian of electron density (see Chapter I).[32,83,87] Eskandari[87] associated the Lewis acid-base interaction with the combination between a 'lump' in the VSCC of the base (CD region) with the *hole* in the VSCC of the acid (CC region). Within this concept, the model systems CH₃Hal were studied. For the CH₃Br and CH₃F molecules, the 'hole' existence (in the first case) and its absence (in the second case) was pointed out predicting their ability (and inability) for halogen-bond formation, being in agreement with the *σ-hole* concept of Politzer.[77b] On the other hand, the Laplacian of electron density, unlike the *σ-hole* concept, shows the capability of the Cl-atom in CH₃Cl to combine with a *lump* of another molecule, forming a halogen bond.

For Hal-atoms, the Laplacian of the electron density reflects the features observed from the deformation map – the charge concentration (CC) and charge depletion (CD) sites of $L(\mathbf{r})$ are respectively located in δ^- and δ^+ regions of $\Delta\rho(\mathbf{r})$ and correspond to nucleophilic and electrophilic sites around the Hal nuclei. So both methods indicate the anisotropic nature of charge distribution around Hal-nuclei, as it was shown experimentally in solid chlorine,[88a] chlorinefluoride,[88b] and hexachlorobenzene.[83]

The application of the three discussed approaches to the evaluation of halogen bonding interactions allow qualitative distinguishing between the genuine halogen bonding and other Hal-involved bonding contacts, while their topological analysis permits a qualitative evaluation of its character, based on the classification discussed in **Chapter I**, as will be discussed in the following section.

2.2.1. Conclusions about the halogen bond nature and character

This section concerns the discussion of halogen bonding interactions Hal_i···Y with different electron donating atoms (Y = Hal_i, Hal_j, and LB). Experimental charge density studies on this interaction are very sparse, so in several cases they are supported by theoretical calculations.

(a)   **(b)**
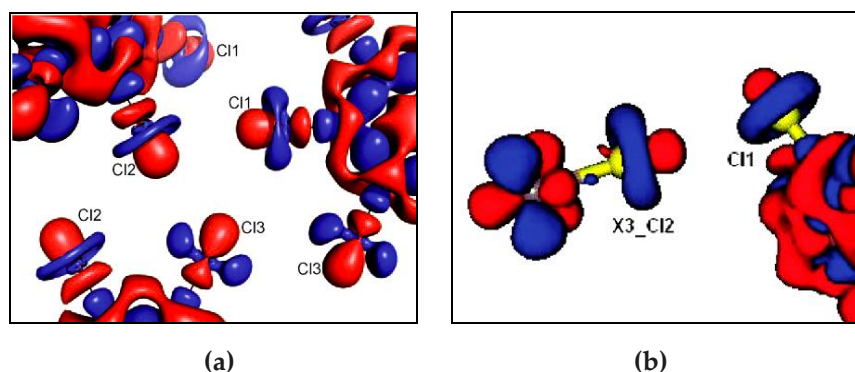
Figure II.5 3D static deformational density maps $\Delta\rho(\mathbf{r})$ representing (a) three Type-II Cl···Cl interactions forming a synthon and three Type-I Cl···Cl interactions in C_6Cl_6, iso-surfaces are drawn at ±0.05 eÅ^{-3} level [83] (b) Type-II interaction in 2-chloro-3-chloromethyl-8-methylquinoline.[89] Iso-surfaces are drawn at ±0.01 eÅ^{-3} level. Blue – positive, red – negative.

According to the analysis of geometrical preferences observed for symmetrical Hal_i···Hal_i interactions from the Cambridge Structure Database (CSD),[81] the number of Type-II contacts becomes more significant than these of Type-I as the polarizability of the Hal-atom increases. Thereby, Type-II Br···Br interactions would be more probably expected to arise from specific attractive forces between atoms than Cl···Cl interactions. Experimental charge density studies of Type-II Cl···Cl interactions have been performed for several cases of Type-II geometry (**Figure II.4**),[83,89] while experimental Br···Br cases were not yet published in the literature as X-ray diffraction data of the compounds containing heavy atoms is often of low quality for charge-density studies.

Static deformation maps (**Figure II.5**) clearly show the orientations of the electron excess (δ-) and electron deficient (δ+) regions of Cl-atoms facing each other along the interaction direction, suggesting directional and electrostatic δ+···δ- interactions. From the corresponding $L(\mathbf{r})$ maps, the interactions are understood as electrophilic–nucleophilic (CC···CD) in nature. To this extent, $\Delta\rho(\mathbf{r})$ and $L(\mathbf{r})$ distributions lead to a unique result: Type-II Cl···Cl interaction should be unambiguously considered as electrostatically attractive,[83] corresponding to Williams model.[90]

(a)   **(b)**
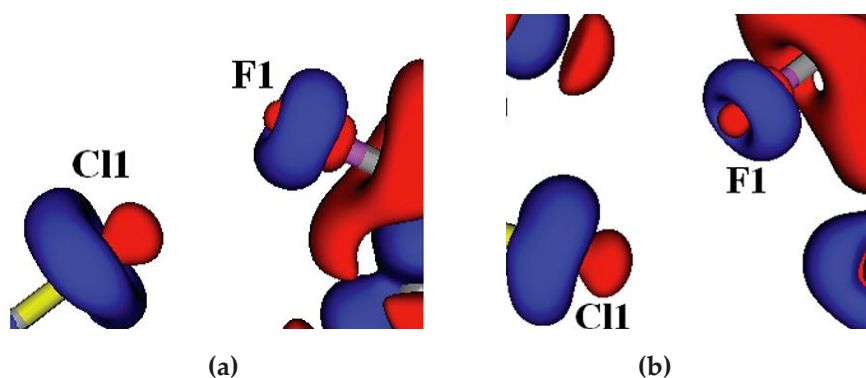
Figure II.6 3D static deformational density maps $\Delta\rho(\mathbf{r})$ representing hetero-halogen Cl···F interactions where F-atom acts (a) as a halogen bond acceptor – Cl(δ+)···F(δ-) and (b) as a halogen bond donor – Cl(δ-)···F(δ+). Iso-surfaces are drawn at ±0.1 eÅ^{-3} level. Blue – positive, red – negative.[85]

From the same viewpoint, unsymmetrical halogen bonds between two different halogens were investigated.[85,91] In the usual cases, the role of the halogen bond acceptor plays a heavier more polarized halogen, while the lighter one is electron donating (as experimentally shown in reference 91, see **Figure II.6a**). However, an inverse situation is also possible.[85] Indeed, on the example of a Cl···F hetero-halogen interaction, it has been shown that, under a suitable atomic environment (i.e. in the presence of electron withdrawing groups), the polarized F-atom can act as a halogen bond donor (**Figure II.6b**).

Topological and local energetic properties of $\rho(\mathbf{r})$ characterize the mentioned Hal···Hal interactions as *pure* close-shell type falling within the energetic range of very weak hydrogen bonds.[59c]

Experimental charge density studies, supported by theoretical calculations, have been reported to elucidate the nature and propensity of the interaction between a Hal-atom and a Lewis base (LB). The nature of the Hal···LB interactions was experimentally established for I···N,[92a] I···O,[92b] Br···N,[92c] and Cl···O[93,94] as electrostatically attractive (δ^+···δ^-) (**Figure II.7**), similarly to the previously described Type-II Cl···Cl halogen bond. This observation was supported by the net atomic charge calculations (e.g. for Cl···O being +0.14e for chlorine and –0.27e for oxygen).

(a)   **(b)**
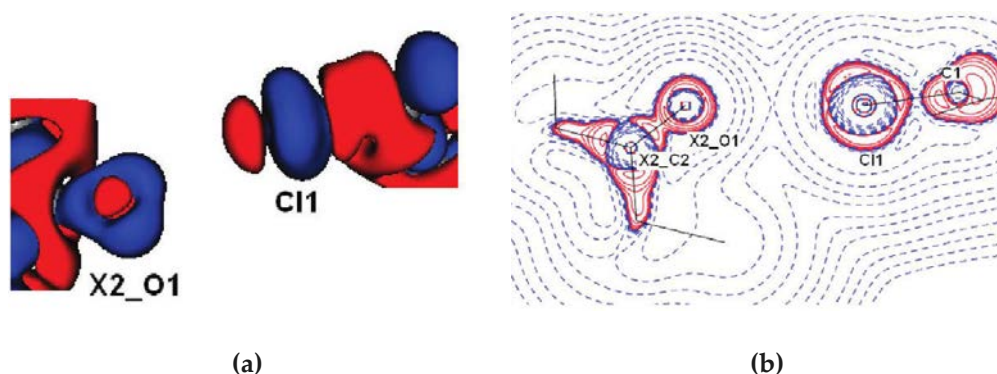
Figure II.7 (a) 3D static deformational density and (b) $L(\mathbf{r})$ maps representing an electrostatically attractive Cl(δ^+/CD)···O(δ^-/CC) interaction. Iso-surface of $\Delta\rho(\mathbf{r})$ at ±0.05 eÅ^{-3}, blue – positive, red – negative ; $L(r)$ contours (eÅ^{-5}) are in logarithmic scale, red – positive, blue – negative [94]

According to the topological properties at bond critical points, I···N and I···O interactions[92b] show close features. They are both of closed-shell character and can be put in analogy with hydrogen bonding of medium strength.[59c] It should be noted that in the case of the I···N intermolecular bond, the parameter $|V|/G$ is greater than 1, pointing to the slight covalent character of the halogen bond. As a consequence, the interaction belongs to the *transit* CS region in this case. A comparison between the topological descriptors of the Br···N and I···N halogen bonds[92c] reveals an interaction at the boundary between *pure* and *transit* closed-shell character for the former and a partial shared-shell character for the latter.

All the previous discussions indicate Hal_i···Y (Y = Hal_i, Hal_j, and LB) halogen bonding as a highly directional interaction comparable in strength to weak/medium hydrogen bonding. Both halogen and hydrogen interactions match the main criteria of non-covalent bonding in crystal engineering and they are apparently responsible for topology and connectivity in crystal packing.

A particular case of a rather short halogen bond with a halide anion (I⁻···I–I) was established to be formed in a similar way to those with neutral species.[95] In contrast to the *σ-hole* concept, which states that among two interacting halogen atoms, one is a nucleophile and another is an electrophile, in the formation of the present interaction both I_1^- and I_2 atoms simultaneously donate and accept the electron density to give only one halogen bond (**Figure II.8**). This model was confirmed by the topological analysis of the electron density, showing that this halogen bond presents CC···CD interaction (electron density transfers from I_1^- anion to I_2 atom and vice versa) instead of one expected from the *σ-hole* model. The authors concluded that the shortest Hal···Hal interactions do not oblige to be repulsive, as shown in recent charge density studies, the reason for this attractive interaction being the influence of the nature of donor species. However, more studies are needed to confirm this conclusion, as experimental charge density analysis involving iodine atoms is very difficult due to severe absorption effects when using X-ray Mo sources, which was the case of the present study.
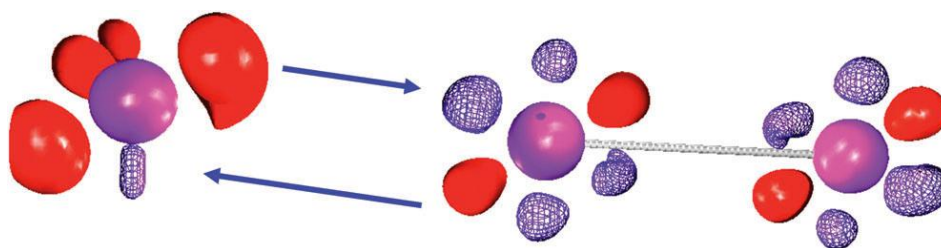
Figure II.8 3D static deformational density map $\Delta\rho(\mathbf{r})$ in the I_1^-···I_2–I_{2A} area. Iso-surface equal to 0.35 eÅ⁻³ is shown by red, iso-surface equal to –0.3 eÅ⁻³ by blue wireframe.[95]

2.2.2. Studies on other closed-shell interactions involving Hal-atoms

Intermolecular interactions that involve Hal-atoms and can not be characterized as CC···CD contacts also play an important role in crystal engineering, as in most of the cases they are responsible for packing efficiency. The contacts Hal···Hal (type-I geometry), and Hal···C_π are considered here.

As marked before, the Hal···Hal Type-I geometry is more often observed for less polarizable halogens. Indeed, the experimental evidences for Cl···Cl and F···F Type-I geometry are numerous.[83,89,91,92,93] Depending on the atoms arrangement, the range of distances for these interactions varies from significantly short (i.e. shorter than for Type-II arrangement) to very long ones (**Figure II.9**). The shortest Cl···Cl distance, found in triphenilechlorometane (**Figure II.9a**), corresponds to an almost linear geometry. According to the Laplacian topology this geometrical case can be classified as CD···CD (*head-on*) arrangement. The longest distances correspond to CC···CC (*side-side*) geometry. The distance lengthening is reflected in the topological properties of $\rho(\mathbf{r})$, which show the interaction weakening. The energetic criterion $|V|/G < 1$ for all experimentally studied cases characterize Type-I Hal···Hal interactions as closed-shell ones.

The electrostatic potential $V(\mathbf{r})$ analysis reveals a saddle topology ((3,–1) CP) in a negative region for stronger interactions of CD···CD type, and in a positive region for weaker interactions.[93] Accordingly, these contacts can be characterized as electrostatically, where the

interaction formation involves similar anisotropic regions of the electron density around the Hal-atom. This explanation corresponds to the one given earlier by Nyburg.[96] Longer and weaker interactions, which do not present a saddle topology of $V(\mathbf{r})$ in the intermolecular region, were referred to be a consequence of packing.

In general, Type-I Hal···Hal interactions can be referred to as non-directional contacts; however, their nature and features still need to be clarified by additional experiments and theoretical calculations on a large number of structures. The packing efficiency of these interactions can be illustrated on the example of C_6Cl_6 structure (**Figure II.5**), where the Cl_3-synthon is a main structural unit and satellite Type-I interactions are formed due to the current packing situation.

(a)   3.214 Å

(b)   3.613 Å

(c)   3.646 Å

(d)   3.890 Å
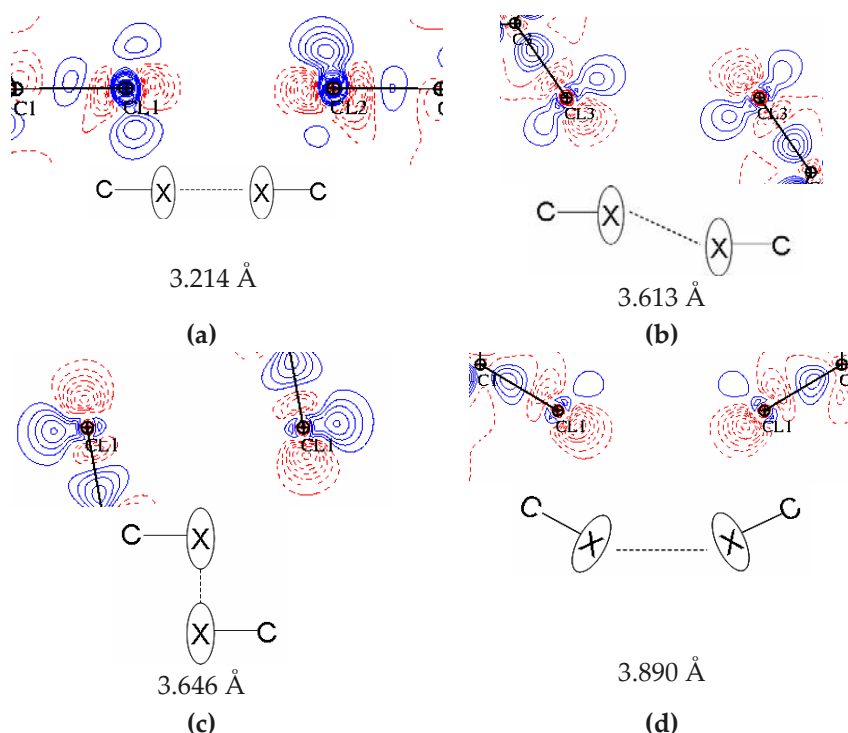
Figure II.9 Static deformational density maps $\Delta\rho(\mathbf{r})$ for different geometries Cl···Cl Type-I interaction: (a) CD···CD type, (b), (c), (d) interactions involving similar anisotropic regions of $\rho(\mathbf{r})$. $\Delta\rho(\mathbf{r})$ contours are at ±0.05 eÅ^{-3}, blue – positive, red – negative.[93]

Bonding interactions involving fluorine, such as C–H···F, O–H···F, N–H···F and C–F···π are often observed in organic compounds.[97] The relatively small size of F-atom along with its high electronegativity and low polarizability precludes its interaction with an electronegative site of another atom. The charge density analysis of highly polar C–F bonds has been a subject of interest for many years.[98] In the case of electrostatically repulsive F···F interactions, its energetic disadvantage was considered to be smaller than the energetic advantage of the sum of all crystal field effects including the stacking of the phenyl groups and the formation of hydrogen bonds.

2.2.3. Halogen bonding from theoretical investigations

Numerous theoretical studies have been performed to understand the nature and to provide a classification of halogen bonding with continuum strength.[32,99,100] The nature of halogen bonding has been discussed in the context of its electrostatic character, where the second-order contributions, such as polarization, dispersion, and charge transfer, have been demonstrated to be nonnegligible.

Amezaga and co-workers[32] performed *ab initio* calculations in order to characterize the nature of halogen interactions in 18 complexes with Lewis bases (LB) and compared them with the hydrogen bond interactions formed with the same LB. In accordance with the classification given for hydrogen bonding,[34c] the topology of $\rho(\mathbf{r})$ at BCP's of Hal···LB bondings exhibit features of an interaction of intermediate strength and must be considered as partially covalent and partially electrostatic.

Interesting results are represented in the new work of P. P. Zhou et al.,[100] where the authors performed a theoretical study for a class of systems, $H_3N \cdot X(Y) \cdot HF$ (X = Cl, Br and Y = F, Cl, Br) where X simultaneously acts as halogen bond donor and hydrogen bond acceptor. In most of the cases, closed-shell interactions of primarily covalent character are shown to take place.

Halogen bonding was also considered originating from charge transfer phenomenon, when the electron density transfers from the lone pair of the LB to the C-X σ^* antibonding orbital.

It has been shown that the intermolecular distances, as well as the origin of the halogen bonding, are significantly affected by the chemical environment of the halogen atoms.[99a] In this respect, charge-transfer and electrostatic contributions to the binding energy of halogen bonding where compared. The calculations clearly indicate that for the strongest halogen-bonded complexes with ammonia, formed by dihalogen molecules, the charge-transfer type contribution is predominant, whereas for complexes involving molecules C-Hal bonds the interaction energy mainly stems from the electrostatic contribution. For carbon-bound halogen systems, the influence of the hybridization state of the carbon atom bonded to the halogen and of the substitution upon the electron-accepting ability of the halogen atom has been explored, revealing that the strength of halogen bonding of type Hal···LB decrease in the order $sp > sp^2 > sp^3$, while in the case of Hal···Hal interactions in the order $sp^2 > sp > sp^3$.[101]

It has been observed that charged complexes have significantly greater interaction energies than the corresponding neutral complexes,[99a] indicating the electrostatic nature of the halogen bond in carbon-bound halogen systems. Halogen bond interaction energies span over a remarkably wide range, from 1 to 50 kcal mol^{-1}. A linear relationship between the interaction energies and the electron densities at the halogen bond critical points was established.

By the smaller range of the interaction energy for the electrophile interaction with the different substitutions (from 1.96 to 6.58 kcal mol^{-1}) in comparison with the nucleophile interaction (from 1.54 to 17.20 kcal mol^{-1}), it was shown that the effect of the chemical environment on the electrophile *side-side* interaction of halogens is less pronounced than that on the corresponding nucleophile *head-on* interaction.[99]

3. Chalcogen bonding

The third type of intermolecular interaction analyzed in this work – chalcogen bonding – is of special importance in crystal engineering, as in most cases it combines two essential properties: strength and directionality. Chalcogen bonding has been attracted scientific interest. In the literature, discussions concerning the strength, the directional preferences and the nature of this non-covalent interaction in the framework of Quantum Chemistry are found, along with its wide application in crystal engineering.

3.1. General overview

3.1.1. Bond definition

For a halogen atom, the existence of a negative electrostatic potential belt was explained by the presence of three long pairs around its nucleus, leaving the *σ-hole* to interact as an electron acceptor.[77] The *σ-hole* concept has been extended to covalently bonded atoms from Group VI. Similarly to halogens, chalcogen atoms (Chal = O, S, Se, Te) also have an electropositive region at its outermost end, although it has only two lone pairs of electrons (**Figure II.10**).[77d] This explains how the Chal-atom interacts with electron donors to form a non-covalent bond, which is similar to the halogen bond. Borrowing from the definitions of halogen and hydrogen bonds, we define chalcogen bonds (Chal···Y) as those in which chalcogens behave as acceptors of electron density.

(a)   **(b)**
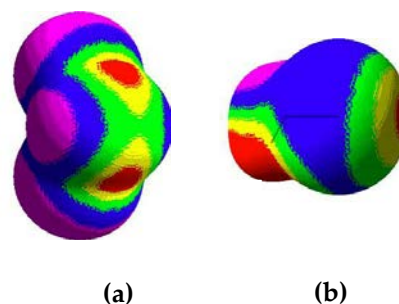
Figure II.10 Calculated electrostatic potential on the surface of (a) SCl_2 and (b) BrOH. Color ranges (kcal mol^{-1}): purple < –12, –12 < blue < 0, 0 < green < 10, 10 < yellow < 25, red >25.[77d]

3.1.2. Chalcogen bonding in crystal engineering

Chalcogen bonding have long been found as an important tool that brings together molecules in crystals. However, the real interest to chalcogen containing molecules[102] arose with the discovery of the superconducting properties of complexes of tetrathiafulvalene (TTF) and tetracyanoquinodimethane (TCNQ).[103]

In earlier studies, statistical analyses of crystal structures containing van der Waals contacts involving S- and Se-atoms (using the Cambridge Crystallographic Data Base) have been performed, aimed to reveal directional preferences of the non-covalent interactions.[104] For example, the interaction analysis of the contact between two divalent sulfurs (S···S) indicated the preferred and complementary directions of electrophilic and nucleophilic attacks of one sulfur by another. Later on, it was found that close Chal···Chal contacts, along with the C–H···S, C–H···π, and π–π stacking, play an important role in the formation of two- and three-dimensional networks in the solid state.[105]

Gleiter and co-workers in their studies of cyclic tetrachalcogenadiynes revealed a large variety of tubular structures in which chalcogen centers of the neighboring rings are involved in short contacts.[106,107] As a result, a zigzag arrangement arises between the stacks, as shown in **Figure II.11.** In some cases, this building motif is changed to a ladder-type arrangement (a << b). It was proved that even in saturated cyclic selenaethers, with the lack of π-π interactions, the Se···Se contacts are strong enough to stack the rather flexible cyclic systems upon each other and to form a tubular structure.[108]
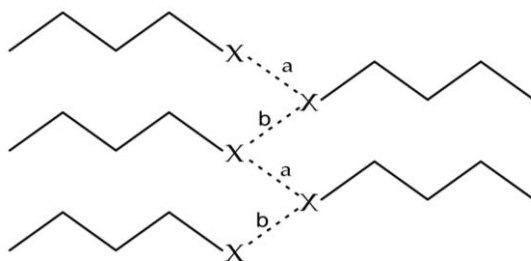
Figure II.11 Schematic drawing of a zigzag (a = b) or ladder (a << b) type arrangement of the chalcogen···chalcogen interaction in the solid state (X = S, Se, Te).[107a]

The synthesis of chalcogen-substituted macrocycles (24-33 members) leads to the formation of cavities in the solid state that are able to include various guest molecules (**Figure II.12**). Flexible enough, the rings allow the conformation to be alternated in such a way that even larger solvent molecules can be specifically hosted inside.

The latter-day application of the selenium containing compounds is in fabrication of well-defined azacalixarene nanosheets (applied to gas storage and catalysis) assisted by Se···N non-covalent interactions.[109] It is greatly anticipated that Se···N or Se···X (X=Cl, Br, I) intra/inter molecular interactions will act as new driving forces for controlling self-assembly, leading to functional supramolecular materials.

(a)   (b)
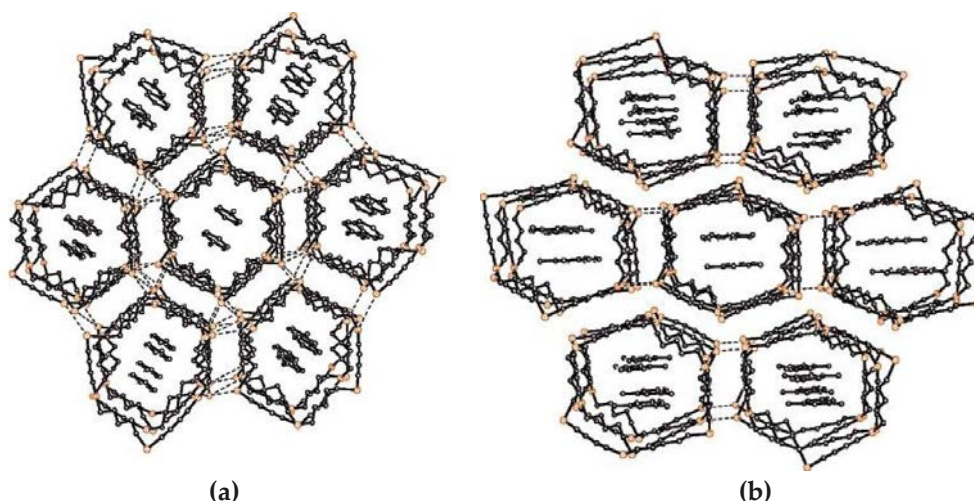
Figure II.12 Top view of columnar arrangement of (a) hexaselenacyclohexayne based self-assembling tube with inclusion of toluene and (b) mesitylene; short Se···Se interactions are indicated.[106c]

3.2. Theoretical and experimental studies

Despite an already large interest and an abundance of theoretical and experimental studies on chalcogen bonding, it doesn't seem that the discussion on its nature is likely to reach a point of agreement soon. The physical mechanism of these interactions is not yet completely clear. The nature of these interactions was already explained either as a pure electrostatic phenomenon[110] or as a pure second order orbital interaction phenomenon.[111] In the literature, explanations in between these two extreme cases can be found, especially as they actually do not exclude each other. However, the real nature of the interaction mechanism can not be simplified to only one of these extremes.

3.2.1. Chalcogen bond nature from theoretical investigations

Cozzolino et al.[112] investigated the nature of the supramolecular association of 1,2,5-chalcogenadiazoles containing Chal···N interaction by applying relativistic density functional theory (DFT). The interaction was interpreted in terms of charge transfer involving the delocalization of nitrogen lone pair electrons into the suitably aligned Chal–X antibonding orbital ($n_N \rightarrow \sigma^*_{Chal-X}$), although the importance of an electrostatic component was also marked out. **Figure II.13** illustrates the formation of the Se···S[113] bond as an interaction of the lone pair localized at the S atom of the PhS⁻ anion with the σ*-antibonding orbital of the Se–N bond in the heterocycle.[113a] This interchalcogen bond can be considered as a weak donor–acceptor bond.
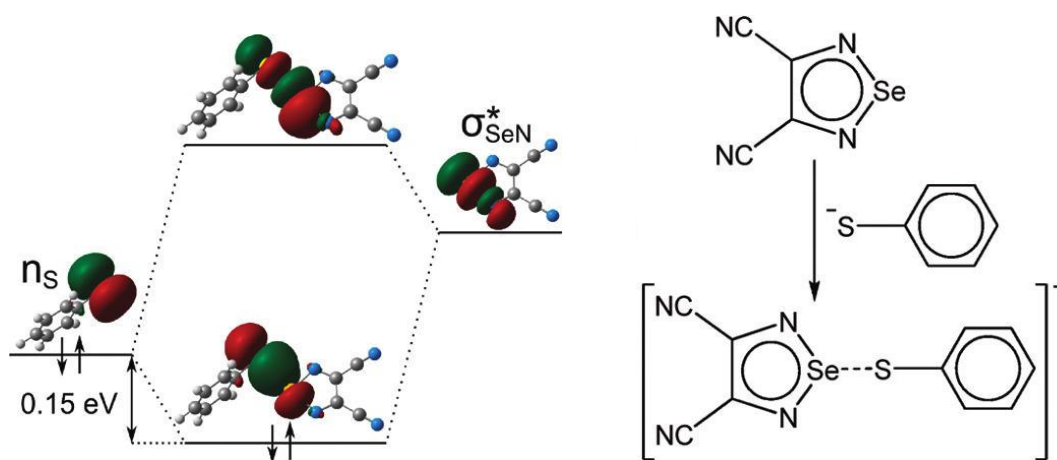
Figure II.13 NBO diagram for Se···S bond formation[113a]

Coulombic interaction between oppositely charged Se and S atoms in the series of substituted benzeneselenenyl derivatives also contributes to interchalcogen bonding. NBO and QTAIM analyses suggest that in several cases this interaction could bring a covalent character.[113b] Similar conclusions were made earlier concerning the Se···N interaction in seven 2-selenobenzylamine derivatives, studied by NMR technique.[114] Recently, computed interaction energies (NBO) for the same interaction in the series of *ortho*-substituted organoselenium compounds revealed that its

strength depends strongly on the nature of the substituent attached to selenium (i.e. on the nature of the Se–X acceptor orbital) and roughly follows the order $CH_2Ph < SPh < Br < Cl < I$.[115]

The Se⋯I–I intermolecular interactions between organoselenium compounds and diiodine were examined in the context of charge–transfer interaction.[116a] However, here the Se-atom acts as electron donor and therefore, the interaction can be rather defined as a halogen bond. Remarkable is the fact that based on the QTAIM topological analysis, this type of bond exhibits a more important covalent degree in comparison with the regular charge-transfer complexes with iodine. Similar results have been also previously observed for hydrogen-bonded complexes of organoselenium compounds.[116b]

Figure II.14 Views of the minimized geometries of the dimers $(CH_3)_2O$ (left) and $(CH_3)_2Te$, showing the geometrical preference for hydrogen (left) and chalcogen (right) bond formation. [117a]

Accordingly, it was assumed that these features may be rather common when selenium atoms act as electron donor.

Extended quantum chemical calculations on homo- and hetero-chalcogen model systems with different substituents were performed.[117] In all the cases, the interaction energy of Chal⋯Y increases along the series Chal = O < S < Se < Te. Despite this trend, the competition between weak hydrogen bonding and chalcogen interactions was observed (**Figure II.14**). Weak hydrogen bonding between methyl groups and Chal-atoms dominates in those compounds that contain lighter chalcogen centers in the accepting fragment (as for O⋯O systems). However, the importance of chalcogen⋯chalcogen interaction prevails with increased atomic weight of the accepting Chal-atom, dominating in the Te-containing systems. The correlation between the strength of hydrogen and chalcogen bonding in the intermediate cases (S- and Se-atoms) can be controlled by varying the Chal-atom substituents. Accordingly, the nature of these noncovalent interactions depends on the involved Chal-atom types. Theoretical perturbation analyses reveal that induction and dispersion forces dominate and contribute to the bonding in each case. The electrostatic contribution is involved in all hydrogen-bonded systems, while compounds involving chalcogen⋯chalcogen interactions exhibit a significant electrostatic contribution only if at least one of the atoms is O or S.

In the very recent studies, the theoretical investigations support previous conclusions for the HTeChalH (Chal = O, S, Se, Te) monomers and homodimers.[118] The authors underline the importance of the electrostatic contribution for interactions in which an O-atom is involved and of the dispersion contribution for the interactions involving heavier Chal-atoms.

Another attempt to investigate the competition between chalcogen, halogen, and hydrogen bonds in SCS–HOX and SeCSe–HOX (X = Cl, Br) complexes[119] demonstrates that the interaction strength is comparable for the two first interactions and a little weaker for the last one, pointing out the prevalence of its dispersion contribution.
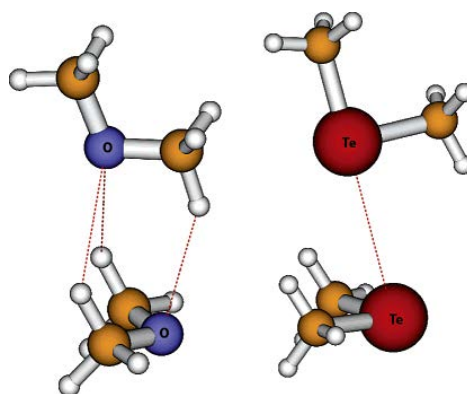
For the specific chalcogen-bond type C=Chal⋯Y,[120] it was found that charge-transfer along with the electrostatic, polarization, and dispersions contributions, plays an important role in its ground-state stabilization.

A new type of *σ-hole* bonding, namely chalcogen-hydride interaction,[121] was revealed and characterized with quantum-chemical and QTAIM approaches. In this interaction, the metal hydride acts as the *σ-hole* acceptor. This interaction exhibits some similar properties with hydrogen bonds in geometry and spectroscopy. The topological parameters at the S(Se)⋯H bond critical point have a linear relationship with the interaction energy. The energy decomposition indicates that the electrostatic interaction plays a dominant role in the chalcogen–hydride interaction with a significant dispersion contribution.

3.2.2.   Charge density analysis based studies

In contrast to the theoretical, experimental investigations concerning chalcogen bonding interactions are very sparse and excursive. Experimental and theoretical studies in the light of QTAIM approach were performed for several sulfur containing compounds in terms of local charge concentration and charge depletion of a Lewis acid-base concept.

A detailed analysis of the Laplacian topology in the VSCC region has been performed for the S- and N-atoms in heptasulfur imide (S_7NH) by periodic theoretical calculations.[122] The calculated atomic graph revealed the number and types of Laplacian CPs in the VSCC that satisfy the Euler's formula: V – E + F = 2. It was shown that the respective location of CC and CD regions is responsible for the Chal⋯Y interaction directionality and permits to define it as a Lewis acid-base pair. This can be illustrated on the example of the S⋯N intermolecular interaction in S_4N_4, that shows a *key-lock* arrangement (**Figure II.15a**).[123] The directionality of this interaction was supported by the structural angles in the corresponding intermolecular regions. Nice examples of directional binding interactions were also performed in a crown shape structure of S_7NH.[122] Here, S⋯N (**Figure II.15b**) and S⋯S (**Figure II.16**) intermolecular contacts are characterized as closed-shell interactions and visualized by the Laplacian distribution. The S⋯S interaction occurs also in agreement with the location of the CC and CD regions found in the atomic graph.

(a)   (b)
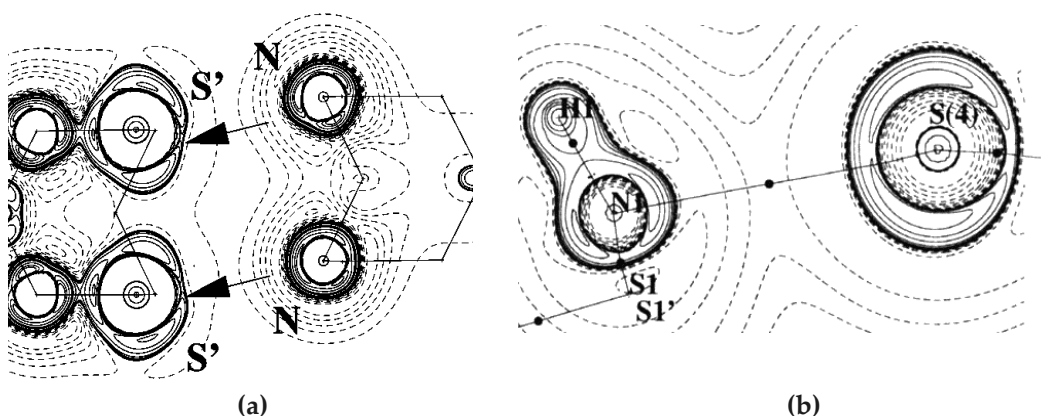
Figure II.15 The *key–lock* interaction illustrated on the $L(\mathbf{r}) = -\nabla^2\rho(\mathbf{r})$ maps: (a) NNS'S' plane in S_4N_4[123] and (b) $H_1N_1S_4$ plane in S_7NH.[122] $L(\mathbf{r})$ contours (eÅ^{-5}) are in logarithmic scale.

The experimental electron density analysis of L-cystine[24] was performed in the late 90's. In this structure, the S⋯S intermolecular contact presents a different from previously mentioned geometry: two S-atoms face each other along the interaction direction, reminding Type-I Hal⋯Hal contacts. This interaction was analyzed in terms of $\Delta\rho$ and the topology of $\rho(\mathbf{r})$, and was classified being of van der Waals type. In all the previously mentioned cases, the topological properties of the chalcogen bonding interactions characterize them as of closed-shell type.

(a)   **(b)**
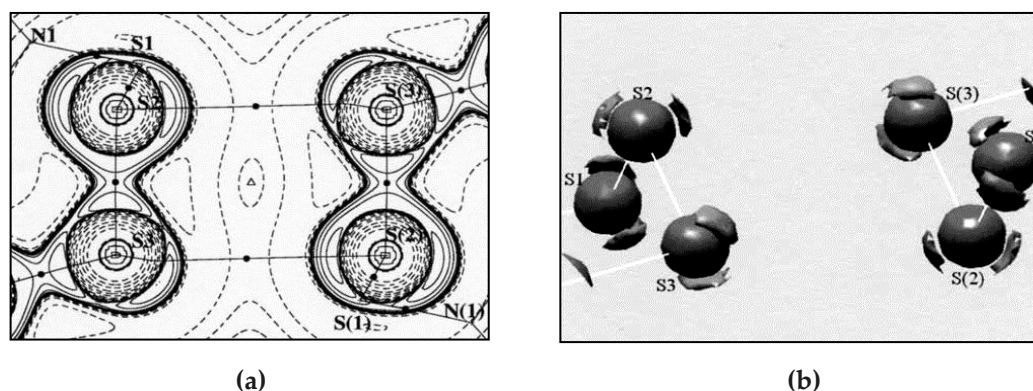
Figure II.16 Laplacian distribution in the intermolecular regions of S⋯S interactions observed in S7NH: (a) at 2D in the S2S3S(2) plane, (b) at 3D with the iso-value of –0.11 eÅ^{-5}. [122]

3.2.3. Interaction strength

To evaluate the strength of chalcogen bonding (Chal⋯Y) interaction and to classify it among other mentioned weak intermolecular interactions, some of the magnitudes calculated by different methods in different model compounds previously mentioned are summarized here.

In the series of works of Iwaoka et al., the strength of non-covalent interactions between Se and second-row atoms (N, O, and F) was calculated. Thus, on the basis of variable-temperature ^{1}H NMR analysis and molecular orbital (MO) calculations, the stabilization energies for Se⋯N were estimated at ~5-20 kcal mol^{-1} depending on the substituent at Se.[114] Stabilization energies in the case of Se⋯O interactions were found in the range of 1.9-6.8 and 6.1-16.6 kcal mol^{-1} for two series of studied compounds,[124,125] being smaller than in the Se⋯N case. Significantly smaller values were calculated for Se⋯F interactions (0.83-1.23 kcal mol^{-1}),[111] being consistent with the lower electron-donating ability of F lone pairs. The Se⋯Hal interactions, where the Hal-atom is involved as an electron donating group were also studied. On the basis of the NMR analysis of the model compounds, the strength of the Se⋯Hal interactions decreases in the order Se⋯F (1.9-7.0 kcal mol^{-1}) > Se⋯Cl (0.3-2.0 kcal mol^{-1}) > Se⋯Br (0.1-1.8 kcal mol^{-1}).[126]

The BSSE corrected binding interaction energies for S⋯N is estimated at 1.32 kcal mol^{-1},[122] while for S⋯S it is estimated at 0.75 and 1.4 kcal mol^{-1} for two geometrical cases.[122] The total stabilization energy for the S⋯N interactions were calculated to be ~3.2 and 2.5 kcal mol^{-1}. [127]

For the intermolecular interactions Te⋯Chal in HTeChalH (Chal = O, S, Se, Te) the interaction energy (BSSE corrected) decreases when going from O to Te, (3.34, 2.94, 2.75 0.60 kcal mol^{-1}).[118]

The interaction energy magnitudes for Chal···Chal homo- and hetero-chalcogen models are performed in the extended studies of Bleiholder et al.[117]

Most of the calculated values fall into the range, defined earlier for weak intermolecular interactions (0.5 – 5 kcal mol^{-1}), however, in some cases the strength of chalcogen bonding interaction is closer to the lower limit for covalent bonds (e.g. Se···N interaction).[114]

Summary

In summary, from the explicit literature investigation concerning intermolecular hydrogen, halogen, and chalcogen bonding were found to involve electrostatically positive region (*σ-hole*) which orientation defines the geometry of each contact. In terms of their main properties – namely strength, directionality, and distance fall-off – the three investigated types of contacts present varied characteristics. Therefore, more advanced criteria are needed in order to provide a deeper understanding of these intermolecular contacts.

Chapter III

Experimental processing & objects description

Chapter III presents a detailed description of the experimental processing that covers all the stages on the derivation of the experimental and the theoretical electron density models that are analyzed in the following chapters. For each of the studied compounds – namely, C_6Br_6, (and isostructural C_6Cl_6, discussed earlier), C_6Cl_5OH, C_6Br_5OH, $C_8H_4O_2Se$, and C_3HIOS_2 – an explicit description of the crystal growth experiment, of the high-resolution single crystal X-ray data collection and the structure determination, as well as the multipolar Hansen & Coppens electron density modeling, is performed. *Ab initio* periodic theoretical electron density calculations are described for C_6Br_6, $C_8H_4O_2Se$, and C_3HIOS_2, along with the gas-phase calculations on the optimized monomers. We also describe the molecular packing in the crystal structures in order to simplify the comprehension of the further discussions on intermolecular interactions. Based on the QTAIM methodology, the intramolecular interactions are characterized by using the topological analysis of the electron density distribution and compared with the corresponding data known from the literature.

1. Experimental & theoretical methods

The compounds studied in this work are hexabromobenzene (C_6Br_6), pentachlorophenol (C_6Cl_5OH), pentabromophenol (C_6Br_5OH), selenophtalic anhydride ($C_8H_4O_2Se$), and iododithiolone (C_3HIOS_2). The compound hexachlorobenzene (C_6Cl_6), discussed earlier, is isostructural with C_6Br_6 and will be used for comparison purposes.

1.1. Crystal growth

The powders of the halogenated compounds C_6Br_6, C_6Cl_5OH, and C_6Br_5OH were purchased from Aldrich; $C_8H_4O_2Se$ was prepared as previously described from phthaloyl chloride and LiAlHSeH in THF.[128] C_3HIOS_2 was synthesized from iododithiolthione in DMC and the solution of acetate of mercury with acetic acid as it was shown earlier.[129] The synthesis of the two later compaunds was performed by our collaborators from the team of *Condensed Matter and Electroactive Systems* (MaCSE) of the University of Rennes (France).

The sublimation method was used to obtain single crystals of good quality for all the studied compounds. A raw material in a vacuum-sealed Pyrex glass tube was placed in a bithermal electric furnace with the temperature gradient of 1°C. The temperature in the furnace was slowly increased (5-10°C/day) till the formation of the first crystal seeds, when the material was sublimated and its vapor was recondensed in a low-temperature area. Then, the observed temperature was kept constant (**Table III.1**) during several days for a desired crystal growth.

Table III.1 The sublimation temperatures for each of the studied compounds.

C_6Cl_6	C_6Br_6	C_6Cl_5OH	C_6Br_5OH	C_3HIOS_2	$C_8H_4O_2Se$
50 °C	110 °C	55 °C	80 °C	70 °C	50 °C

1.2. Experimental details of X-ray diffraction

Table III.2 gathers crystallographic data and experimental details for all the studied compounds. Spherical and multipolar refinement data are performed separately.

1.2.1. X-ray data collection

Low-temperature high-resolution single crystal X-ray diffraction (XRD) measurements were used to determine the crystal structures and to perform the charge density analysis of the investigated systems. Data collection strategies and data reduction were carried out with the CrysAlisPro CCD / RED.[130] After absorption correction,[131] the measured reflections were sorted, scaled and merged by using the SORTAV program.[132]

For C_6Cl_5OH and C_6Br_5OH, the experiments were carried out using laboratory Mo Kα radiation source (λ = 0.71073 Å) up to a maximum resolution of $(\sin \theta/\lambda)_{max}$ = 1.0 Å^{-1} in both cases. Single crystals of a very good XRD quality were fixed on a glass fiber and mounted on an Oxford Diffraction SuperNova four circle diffractometer equipped with Atlas-CCD detector with a crystal-to-detector distance of 55 mm. The crystals were cooled to 100 K with a liquid nitrogen stream using the Oxford Instruments Cryosystem cooling device.

Table III.2 Crystallographic data and experimental details for the crystal structures of C_6Br_6, C_6Cl_5OH, C_6Br_5OH, C_3HIOS_2, and $C_8H_4O_2Se$.

ID	C_6Br_6	C_6Cl_5OH	C_6Br_5OH	C_3HIOS_2	$C_8H_4O_2Se$	$C_8H_4O_2Se$
Crystal structure						
empirical formula	C_6Br_6	C_6Cl_5OH	C_6Br_5OH	C_3HIOS_2	$C_8H_4O_2Se$	$C_8H_4O_2Se$
formula weight (g/mol)	551.49	266.34	488.59	244.08	211.07	211.07
temperature (K)	100(2)	100(2)	100(2)	100(2)	100(2)	100(2)
source / wavelength (Å)	Synch / 0.45741	MoK$_\alpha$ / 0.71073	MoK$_\alpha$ / 0.71073	MoK$_\alpha$ / 0.71073	MoK$_\alpha$ / 0.71073	Synch / 0.45741
crystal system / space group	Monoclinic/ $P2_1/n$	Monoclinic / $C2/c$	Monoclinic / $P2_1$	Triclinic / $P1$	Monoclinic/ $P2_1/n$	Monoclinic/ $P2_1/n$
unit cell dimensions a (Å)	8.3000(1)	29.1212(5)	8.1997(5)	4.0925(1)	8.3167(1)	8.3029(1)
b (Å)	3.9332(1)	4.8906(1)	3.9469(3)	5.6345(1)	5.7518(1)	5.7383(2)
c (Å)	15.2342(1)	12.0702(2)	14.8097(10)	6.6474(1)	15.1598(2)	15.1336(1)
α (°)				104.019(2)		
β (°)	92.908(5)	93.775(2)	95.152(6)	91.088(2)	102.841(1)	102.934(1)
γ (°)				91.997(2)		
volume (Å^3)	496.69(2)	1715.39(6)	477.35(4)	148.568(5)	707.05(2)	702.74
Z	2	8	2	1	4	4
calculated density (g/cm^3)	3.688	2.063	3.399	2.728	1.983	0.998
absorption coefficient μ (mm^{-1})	7.58	1.63	20.99	5.96	5.24	0.83
crystal size (mm^3)	0.15 × 0.10 × 0.04	0.16 × 0.13 × 0.05	0.29 × 0.06 × 0.04	0.11 × 0.06 × 0.03	0.21 × 0.13 × 0.03	0.27 × 0.23 × 0.03
$F(000)$	492	1040	440	112	408	408
Data collection						
$(\sin\theta/\lambda)_{max}$ (Å^{-1}): exp/theor	1.0 / 1.0	1.0	1.0	1.28 / 1.0	1.0 / 1.0	1.0
index range	$-20 \leq h \leq 20$	$-58 \leq h \leq 58$	$-16 \leq h \leq 16$	$-10 \leq h \leq 10$	$-21 \leq h \leq 21$	$-17 \leq h \leq 15$
	$-11 \leq k \leq 11$	$-9 \leq k \leq 9$	$-7 \leq k \leq 7$	$-14 \leq k \leq 14$	$-14 \leq k \leq 14$	$-11 \leq k \leq 11$
	$-45 \leq l \leq 45$	$-24 \leq l \leq 24$	$-29 \leq l \leq 29$	$-16 \leq l \leq 17$	$-38 \leq l \leq 38$	$-45 \leq l \leq 45$
reflections collected	350 604	113 464	26 246	61 882	226 482	406 662

independent reflections	11 006	7 017	8 012	9 944	12 397	9 153
R_{int}	0.0622	0.0381	0.0440	0.0677	0.0520	0.0827
completeness to $(\sin \theta/\lambda)_{max}$ (%)	99.5	98.8	99.3	94.9	99.3	97.2
absorption correction	analytical	analytical	analytical	analytical	analytical	analytical
min/max transmission	0.53 / 0.75	0.78 / 0.92	0.07 / 0.54	0.51 / 0.94	0.75 / 0.98	0.50 / 0.77
Spherical refinement data						
refinement method	F^2	F^2	F^2	F^2	F^2	F^2
data/restrains/parameters	11 006 / 0 / 56	7 017 / 0 / 112	8 012 / 2 / 114	9 944 / 3 / 65	12 397 / 0 / 101	9 153 / 0 / 105
largest diff peak/hole (e$Å^{-3}$)	2.005 / –1.381	0.541 / –0.292	0.771 / –0.910	3.877 / –4.891	2.905 / –1.871	1.202 / –1.016
GOF on F^2	1.241	1.010	0.987	0.913	1.045	1.051
R (all data)	0.0235 (11006)	0.0244 (7017)	0.0382 (8012)	0.0396 (9944)	0.1007 (12397)	0.0250 (9153)
R ($I > 2\sigma (I)$)	0.0200 (9248)	0.0182 (6034)	0.0285 (6967)	0.0380 (9640)	0.0609 (6571)	0.0298 (7937)
wR(F)	0.0464	0.0312	0.0668	0.0516	0.1693	0.0673
Multipolar refinement data						
refinement method	F	F	F	F	F	F
data: $I> 3\sigma(I)$/total [a]	4015 / 4159	5815	6412	9701 / 2489	5927(total) / 5927	7528
N_{ref} / N_{var}	21.1 / 30.8	15.4	17.0	32.2 / 11.0	19.8/20.8	23.2
GOF on F [b]	1.145 / 0.069	1.093	0.974	0.859 / 0.023	0.981 / 0.059	1.490
R(F)	0.016 / 0.084	0.013	0.031	0.043/ 0.041	0.042 / 0.051	0.017
wR(F)	0.026 / 0.041	0.011	0.027	0.053 / 0.023	0.031 / 0.020	0.017

[a] First and second values for C_6Br_6, $C_8H_4O_2Se$, and C_3HIOS_2 correspond to experimental and theoretical (VASP calculations) data. [b] Low goodness-of-fit for theoretical calculations is due to the use of theoretical structure factors, for which the associated standard deviations are set to 1. In that case, the goodness-of-fit should go to 0 rather than to 1 at the convergence.

Despite the high absorption coefficient for C_6Br_5OH (μ(Mo-Kα) = 21 mm^{-1}), absorption effects were nicely corrected. To reduce the significant absorption effects observed for C_6Br_6 with the same source (μ(Mo-Kα) = 24 mm^{-1}), synchrotron radiation was used (μ = 7.4 mm^{-1}). The data collection was carried out at the CRYSTAL beamline (SOLEIL, Paris, λ = 0.45741 Å) up to a maximum resolution of (sin θ/λ)$_{max}$ = 1.0 Å^{-1}, reaching 97.9 % of completeness. The experiment temperature (T = 100 K) was reached with a gas streamer (CryoIndustries of America). The crystal-to-detector distance was set at 80 mm. Wavelength was selected with a double crystal monochromator (Si 111 crystals). The sagittal (horizontal) focalization was achieved by bending the second crystal of the monochromator, while the vertical focalization and harmonic rejections were carried out using mirrors. The beam attenuation was performed by using Al (or Cu) foils of different thicknesses inserted in the incident beam.

Due to the high absorption effect for Se-atom, X-ray diffraction measurements for $C_8O_2H_4Se$, were also carried out at the CRYSTAL beamline (SOLEIL, Paris, λ = 0.45741 Å), following the same strategy, described for C_6Br_6. The obtained data were compared with these from the laboratory Mo-Kα radiation source (λ = 0.71073 Å) of an Enraf-Nonius diffractometer with a Kappa-CCD detector up to a maximum resolution of (sin λ/θ)$_{max}$ = 1.28 Å^{-1}, T = 100(2) K (Oxford Cryosystems N$_2$ cooling device) with 226482 reflections collected.

For the C_3HIOS_2 compound, the X-ray diffraction measurements were performed in the same conditions as for $C_8O_2H_4Se$ up to a maximum resolution of (sin λ/θ)$_{max}$ = 1.28 Å^{-1}, T = 100(2) K with 61 882 reflections collected.

1.2.2. Structure refinement

The structures were solved by direct methods with SIR92[133] and refined in the spherical-atom approximation with the SHELXL-97[134] program by full-matrix least squares method (based on F^2), as interfaced in the WinGX software package.[135] All the non-hydrogen atoms were refined anisotropically. Hydrogen atoms were located in the difference Fourier map, refined isotropically and shifted to average distances observed from neutron diffraction.[136] The packing diagrams were generated using the Mercury 2.3 package.[137]

1.3. Computational electron density

As explained in **Chapter I**, periodic theoretical calculations can be used to resolve complicated experimental situations, arising when high-quality XRD data are difficult to obtain (this is for instance the case of C_6Br_6, for which the X-ray absorption effects may be severe depending on the wavelength of the incident beam (μ(Mo-Kα) = 24 mm^{-1})). Actually, periodic theoretical calculations can nicely approach the experimental electron density determination, as shown recently.[14] Hence, *ab initio* periodic DFT calculations have been performed on the crystal structure of C_6Br_6, $C_8H_4O_2Se$ and C_3HIOS_2 with the *Vienna Ab initio Simulation Package* (VASP).[13]

The Kohn-Sham equations have been solved in a plane-wave basis set using the *Projector Augmented Wave* (PAW) method of Blöchl.[12] The PAW method, as an all-electron frozen-core approach, is able to provide accurate complete charge densities that can be compared with those obtained from high-resolution X-ray diffraction experiments, either directly, through the visualization of deformation density maps $\Delta\rho(\mathbf{r})$ or *via* the quantitative analysis of the

topological features of $\rho(\mathbf{r})$ using the QTAIM methodology. For the DFT calculation, the functional of Perdew, Burke, and Ernzerhof (PBE)[138] was chosen. The wave function and the density in the augmentation spheres were described by standard PBE PAW atomic data sets. The plane wave cutoff of the calculation was set to a high value (900 eV) in order to ensure convergence. Experimental cell parameters (**Table III.2**) and atomic coordinates obtained from the experimental charge density refinement were used for the calculations. A reasonably dense sampling of the Brillouin zone has been ensured with a k-point mesh of (8, 14, 4) for C_6Br_6, (8, 12, 4) for $C_8H_4O_2Se$ and (16, 12, 8) for C_3HIOS_2. The valence electron density was represented on a regular grid comprising 336×180×600 (C_6Br_6), 336×224×600 ($C_8H_4O_2Se$) and 160×224×280 (C_3HIOS_2) points along the crystallographic axes, and was used to compute the structure factors corresponding to the valence electron density up to a resolution of 1 Å^{-1} for all the cases.

In addition to the periodic calculations, gas phase optimizations have been carried out for the monomers C_6Hal_6 and C_6Hal_5OH (Hal = Cl, Br) and $C_8O_2H_4Chal$ (Chal = O, S, Se, Te) at the Møller-Plesset second-order level (MP2) of theory using the Gaussian09 program package.[139] All electrons were included in the correlation calculation, and the aug-cc-pVTZ basis set was employed for all atoms. Topological analyses of $L(\mathbf{r})$ were performed with the AIMAll code.[140]

1.4. Multipolar electron density refinement

Multipolar refinement (based on F) was performed using the Hansen-Coppens model[18] (described in details in **Chapter I**) implemented in the MoPro package.[19] All the parameters were refined in the least-squares procedure against either experimental X-ray or theoretical VASP structure factors in order to fit the deformation of the atomic electron density.

Table III.3 The parameter ζ and n_l of Slater functions for the all the studied atoms.

Atom	ζ (bohr^{-1})	n_l (l = 1)	n_l (l = 2)	n_l (l = 3)	n_l (l = 4)
I	4.48	8	8	8	8
Br	4.9	4	4	6	8
Cl	4.4	4	4	6	8
Se	4.4	4	4	6 (ζ = 4.0)	8
S	3.9	4	4	6	8
O	4.5	2	2	3	—
C	3.0	2	2	3	—
C′^{a}	3.0	3	3	4	—
H	2.26	1	—	—	—
H′^{b}	2.0	1	—	—	—

^{a} C′ (n_l, ζ) definitions are used for carbon atoms bonded to Se in $C_8O_2H_4Se$. ^{b} H′ (n_l, ζ) definitions are used for hydrogen atoms bonded to C in $C_8O_2H_4Se$ and in C_3HIOS_2.

A local axial system is set for each atom to define the multipolar harmonic functions. Constrains of symmetry and chemical similarity are applied in the first stages of the refinement

of the multipolar parameters. The choice of the local axes depends on the crystallographic symmetry and the atom environment.[141] The local axes along with the multipolar parameters are supplied in Annex. The choice of the Slater-type radial function parameters (n_l, ζ) was based on the experimental electron density studies performed earlier.[142] These parameters for all the atoms in the studied structures are represented in **Table III.3**.

A slightly modified refinement strategy, proposed in the literature,[26,19a] for small unit cells was used for the multipolar modeling of the studied compounds. The following parameters were refined: scale factor (SCA), coordinates (xyz), thermal parameters (U_{ij} / U_{iso}), valence (P_{val}) and multipolar (P_{lm}) populations and expansion/contraction coefficients (κ, κ'). The strategy can be roughly divided into the refinement of the Independent Atom Model (IAM) and that of the multipolar model.

❖   IAM
  - xyz and U_{ij} of all non-hydrogen atoms are refined using all reflections;
  - Refinement of xyz and U_{ij} of non-hydrogen atoms at high order data (HO), e.g. $\sin \theta/\lambda > 0.7$ Å^{-1}. HO refinement strategy permits to obtain the best estimation of atomic positional and thermal parameters of non-hydrogen atoms (as HO reflections are mainly core electrons sensitive);
  - xyz and U_{iso} of hydrogen-atoms are refined at low order data (LO), e.g. $\sin \theta/\lambda < 0.7$ Å^{-1}. Restraints on distance, angles, and planarity are applied to hydrogen-atom positions.

❖   Multipolar model
  - P_{val} then κ;
  - P_{val} and κ refined together;
  - P_{lm}, followed by P_{val}, κ, and P_{lm} refined all together;
  - All the previously mentioned steps are cycled until convergence;
  - xyz and U_{ij} of non-hydrogen atoms, P_{val}, κ, and P_{lm};
  - κ';
  - All refined parameters (except κ');
  - κ'.

SCA was refined during each step. The initial κ and κ' of hydrogen atom were set to 1.16 instead of 1,[143] as this chemical species is expected to be electron depleted in the intermolecular region and its electron density around a nucleus is therefore contracted.

The refinement strategy is more complex for the structures containing heavy atoms (in this work Br, I, Se). In order to reduce the number of variables, and to produce physically meaningful parameters, local symmetry constraints and charge density parameters constraints for all chemically equivalent atoms were imposed. Afterward, the constrained refinement of the valence and multipole populations, together with the κ values, was performed for all atoms until convergence. In the following steps, all the charge density similarity constraints have been gradually replaced by restrains. By using this last model for the R_{free} calculations,[22] the most appropriate value of standard deviation for restraints was found. In most of the cases, the best multipolar refinement is the one with weak charge density restraints on all atoms of the molecule.

At each step, the residual and static deformation maps were calculated to monitor the refinement quality. The final values of statistical factors of all the studied structures as well as

these of other multipolar refinement parameters are gathered in **Table III.2** The values of the P_{val}, P_{lm}, κ, and κ' parameters of the converged models along with the local axes indications are available in **Annex**.

1.5. Topological analyses of $\rho(r)$ and $L(r)$ functions

The topological analyses of $\rho(\mathbf{r})$ and $L(\mathbf{r}) = -\nabla^2\rho(\mathbf{r})$ functions were performed within the framework of QTAIM as described in **Chapter I**.[2] The critical points (BCP's) between bonded and interacting atoms in the experimental and theoretical models were searched with the VMoPro module of the MoPro software.[19] The BCP position between a pair of atoms is found by minimizing the gradient norm of the total electron density, starting from the middle position between them. First, the minimization is done in one dimension on the segment between the two nuclei, and then a three-dimensional steepest descent is carried out. Intermolecular interactions, described throughout this work are defined by the existence of the BCP between the atoms.

1.5.1. The total interaction energy descriptor derived from the topology of $\rho(r)$

The phenomenological correlation between the interaction energy and the potential energy density at BCPs[144] was firstly proposed for hydrogen bonded systems X–H···O (X = C, N, O):[34a] $E_{int} \approx (1/2)V^{BCP}$. The strength of the hydrogen bonding interactions in the neutral complexes X–H···F–Y was analyzed in terms of topological and energetic properties of $\rho(\mathbf{r})$ at their BCP's.[34c] The estimated interactions energy permitted to distinguish between very weak ($E_{int} < 5$ kJ mol^{-1}), weak ($5 < E_{int} < 15$ kJ mol^{-1}), medium ($15 < E_{int} < 30$ kJ mol^{-1}) and medium-strong ($E_{int} > 30$ kJ mol^{-1}) interactions (**Table III.4**). This reported relationship has been also used in the experimental analysis of $\rho(\mathbf{r})$ as an estimation of the interaction energy when other types of *pure* closed-shell interactions are involved,[145] including halogen bonded systems,[89,92,95] and it will be extensively used throughout this work.

Table III.4 Interaction energies corresponding to the *pure* closed-shell neutral complexes.[34c]

neutral complex	E_{int} (kJ mol^{-1})	ρ (eÅ^{-3})	H/ρ (kJ mol^{-1}e^{-1})	$\lvert V\rvert/G$
NCH···FB	−2.2	0.033	509	0.79
FH···FNF$_2$	−6.9	0.089	515	0.81
NCH···FP	−14.9	0.089	437	0.83
NCH···FAl	−23.8	0.117	372	0.86
CNH···FAl	−36.4	0.184	218	0.92

1.5.2. Deriving an electrostatic interaction descriptor from the $L(\mathbf{r})$ function

As explained in **Chapter I**, the negative Laplacian function $L(\mathbf{r}) = -\nabla^2\rho(\mathbf{r})$ defines the charge concentration (CC) and charge depletion (CD) sites in the outer electron shell of an atom. Based on this knowledge, in the present work we develop the quantitative evaluation of CC/CD regions in interaction of the atom with the environment from the L magnitudes.

The nucleophilic power of the CC region increases with the positive value of L_{CC}, while the electrophilic one of the CD region parallels the decrease of L_{CD} from positive to negative values. As a result, the greater the difference $\Delta L = L_{CC} - L_{CD}$ in the face-to-face CC$\cdots$CD regions the more important the electrophilic–nucleophilic interaction is.

However, it is anticipated that this criterion is valid only for comparison of interactions involving the same types of atoms. The theory fails as soon as we try to apply it for the comparison of interactions between atoms that belong to different rows of the Periodic Table (e.g. Cl$\cdots$Cl vs Br$\cdots$Br). The reason stands in the participation of different outer electron shells in the formation of the interaction, leading to a different screening of the outer electrons. As a consequence, the values of L at CC and CD regions are not comparable in this case, indicating that the ΔL-parameter does not permit a straightforward comparison of intermolecular interactions involving atoms with different outer shells.

To overcome the problem, we introduce the normalized magnitude L/ρ (Å^{-2}), which measures the charge concentration ($L/\rho > 0$) or the charge depletion ($L/\rho < 0$) per charge density unit at the CC and CD sites located from the topology of $L(\mathbf{r})$. The $\Delta(L/\rho) = (L/\rho)_{CD} - (L/\rho)_{CC}$ criterion gives a reasonable quantitative evaluation of the electrophilic-nucleophilic power of the pairwise interaction. This would be illustrated in the following chapters based on the examples of weak intermolecular electrophilic–nucleophilic (electrostatic) interactions involving hydrogen, halogen, and chalcogen bondings.

2. Objects description

2.1. Hexabromobenzene C₆Br₆

2.1.1. Electron density modeling

Different X-ray diffraction conditions were tested for the single crystals obtained from several crystal growth batches of C_6Br_6 in order to obtain a good data: Mo Kα and synchrotron radiation source (λ = 0.71073 and 0.45741 Å, respectively), Atlas CCD and CMOS Photon100 (Brucker) detectors (the latter permits to rich higher resolution, but shows low dynamic range and high readout noise). However, all the experimental data sets proved to be of relatively low quality for charge density analysis (see residuals in **Figure III.1**). Therefore, the experimental data obtained with Mo sources were left and these with the synchrotron radiation were used for structure determination only. The charge-density analysis of C_6Br_6 was consequently performed based on the theoretical calculations.

(a)   (b)
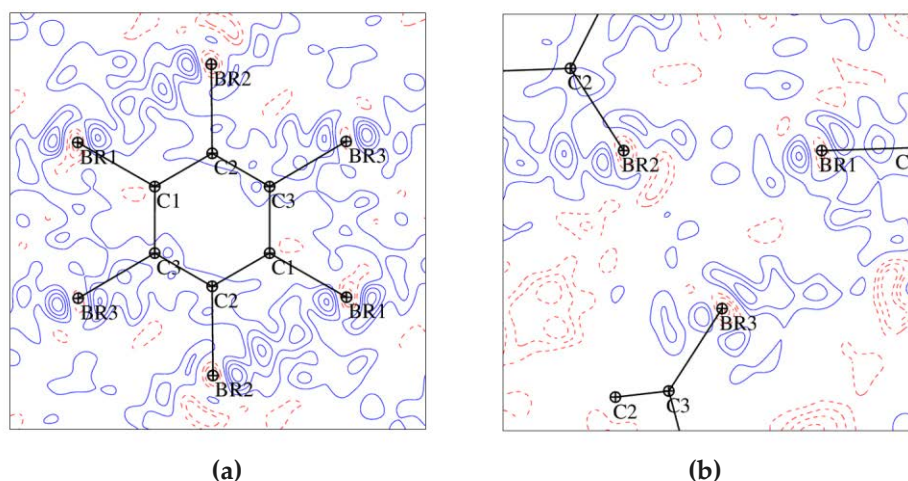
Figure III.1 Residual electron density maps for the experimental model of C_6Br_6 (synchrotron radiation) drawn (a) in the plane of the molecule and (b) in the plane of the Br_3-synthon. Contours are at ± 0.05 eÅ^{-3} level: full lines in blue – positive, dotted lines in red – negative. Resolution range is $0 \leq (\sin \theta/\lambda) \leq 0.9$ Å^{-1}.

The multipolar refinement against the theoretically calculated structure factors was initiated starting with the atomic positions obtained at the converged experimental multipolar model with synchrotron data, which were of better quality than those of the IAM model and were used for the calculation of the theoretical structure factors. The Slater-type radial functions were expanded up to the hexadecapolar level (l = 4) for Br-atoms and up to octapole level (l = 3) for carbon atoms (for n_l, ζ values see **Table III.3**). In the fitting against theoretical data, core electrons were omitted from MoPro atomic definitions, since the VASP structure factors correspond to valence electrons only. The theoretical multipolar model converged to the agreement factors $wR(F)$ = 0.041 and $R(F)$ = 0.084. The residual electron density maps drawn up to 0.9 Å^{-1} (**Figure III.2**) show peaks centered at the bromine nuclei (~0.25 eÅ^{-3}) and smaller features along the C–Br bonds. These trends, which correspond to the valence electron density

that was not taken into account by the multipolar atom model, come from different radial dependencies between ρ calculated from VASP (superimposition of plane waves and atom-centered numerical radial functions) and obtained from multipolar model (Slater-type radial functions).

(a)   (b)
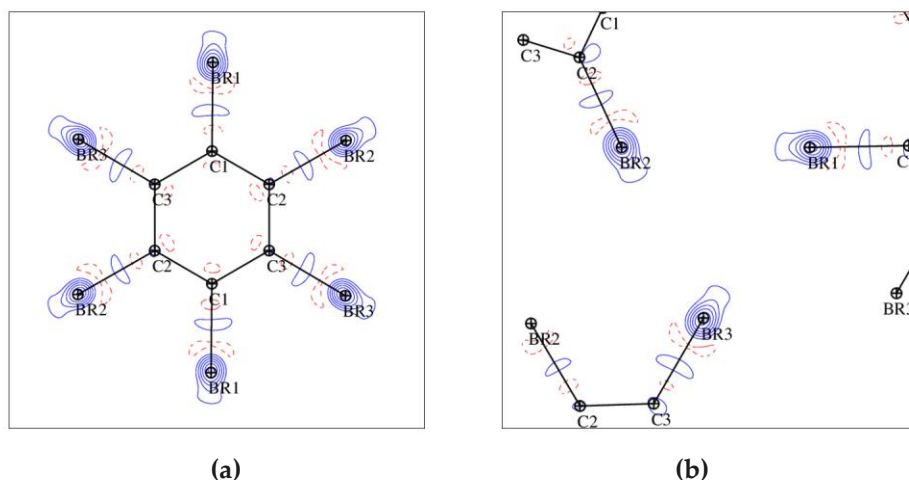
Figure III.2 Residual electron density maps for the theoretical model of C_6Br_6 drawn (a) in the plane of the molecule and (b) in the plane of the Br_3-synthon. Contours are at ±0.05 e$Å^{-3}$ level: full lines in blue – positive, dotted lines in red – negative. Resolution range is $0 \leq (\sin\theta/\lambda) \leq 0.9$ $Å^{-1}$.

The static deformation density maps in the C_6Br_6 molecular plane calculated from the refinement against the theoretical structure factors is shown in **Figure III.3a**. The observed deformation electron density is concentrated on the covalent bonds and around Br-atoms, associated with their lone pairs. The charge distribution in the phenyl ring is highly symmetric, as there is no additional functional group, with the values ~0.5 e$Å^{-3}$ on the C_{sp2}–C_{sp2} aromatic bonds. C–Br bonds are characterized by less pronounced values (~0.15 e$Å^{-3}$).

(a)   (b)
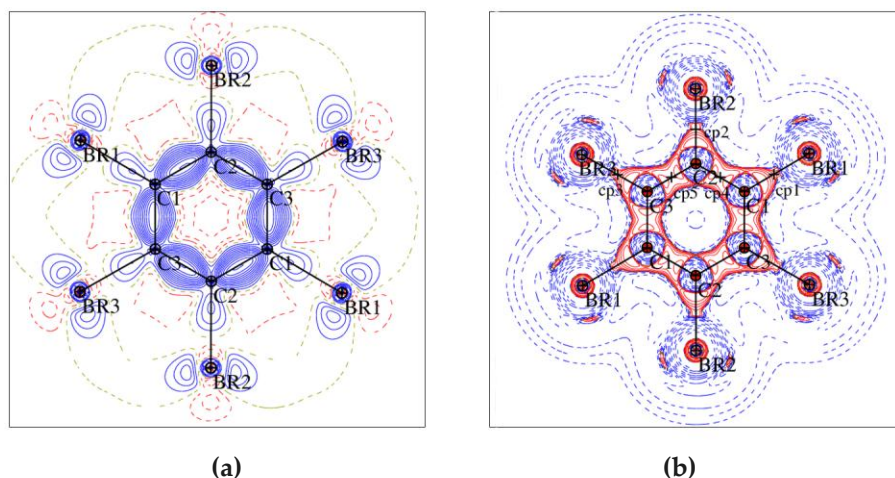
Figure III.3 (a) Static deformation density $\Delta\rho(\mathbf{r})$ and (b) negative Laplacian $L(\mathbf{r})$ maps for the theoretical multipolar model of C_6Br_6 drawn in the plane of the molecule. $\Delta\rho(\mathbf{r})$ contours are at ±0.05 e$Å^{-3}$ level: full lines in blue – positive, dotted lines in red – negative. $L(\mathbf{r})$ contours (e$Å^{-5}$) are in logarithmic scale, red – positive, blue – negative.

The regions along the C–Br bond directions at both sides of the bromine nuclei exhibit depleted $\Delta\rho$ distributions, while positive charge density regions are observed in the plane perpendicular to the bond axis direction. The C–Br bond is polarized, with a build-up of charge density close to the C-atom and depletion in the proximity of Br-atom. It should be noted that $\Delta\rho$ and L distributions around Br-atoms in the theoretical model exhibit highly symmetrical features. The map of negative Laplacian is shown in **Figure III.3b**. It reflects the anisotropic features of electron density around Br-atoms, observed on the deformation density map. The topological properties of $\rho(\mathbf{r})$ at the indicated BCP's will be discussed later on.

2.1.2.   Crystal structure description

Firstly determined by neutron powder diffraction at 300 K, C_6Br_6 crystallizes in the monoclinic system (space group $P2_1/n$)[146] and was found to be isostructural with C_6Cl_6, previously described.[147] According to the literature, these compounds were found to exist only in one polymorphic phase.

(a)   **(b)**
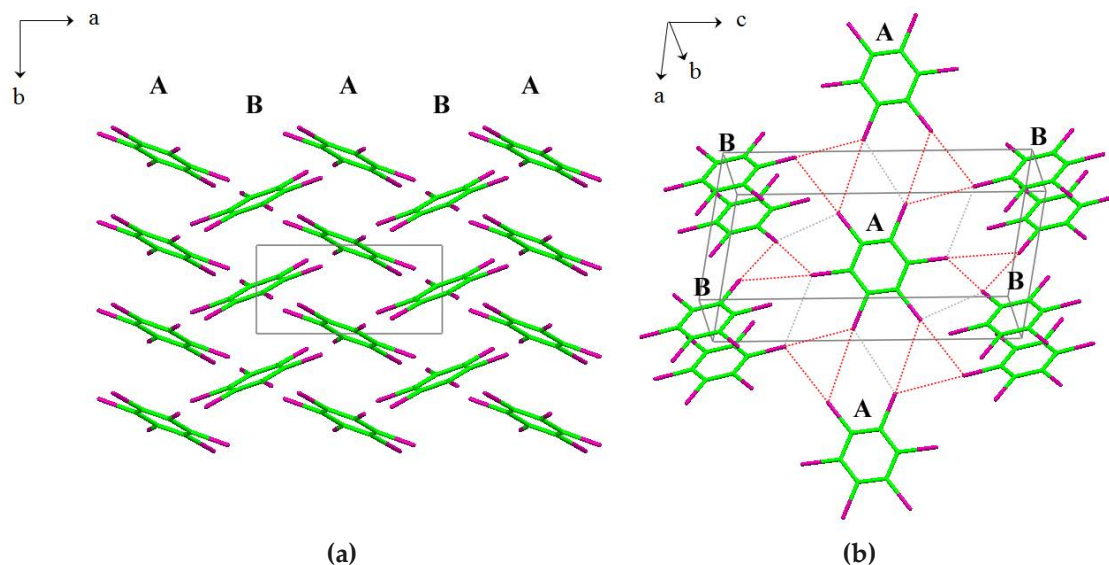
Figure III.4 Crystal structure of C_6Br_6. (a) Side view of the alternating columns A and B projected in the *ab*-plane; (b) down view of the A and B columns projected in the *ac* plane. Intercolumn Hal₃-synthon interactions are noted in red lines, while single Hal···Hal contacts are shown in grey. The columns are defined by symmetry operations (excluding lattice translations and inversion inside a molecule): A (x, y, z) and B (–x, 1/2+y, 1/2–z).

We have redetermined the C_6Br_6 crystal structure at low temperature (T = 100(2) K) by using X-ray diffraction data. As for the previously reported room temperature structure,[146] we also observed that C_6Br_6 crystallizes in the monoclinic system, space group $P2_1/n$ (see **Table III.2**). One-half of the molecule belongs to the asymmetric unit, the second half, being generated by an inversion center that is located in the middle of the molecular ring. In the crystal structure, C_6Br_6 molecules stack in columns along the *b*-axis direction. Molecules lying in alternated columns A and B (**Figure III.4a**) exhibit an interplanar angle of 130.1°. The columns alternate in such a way that each type A column is surrounded by six other columns – two of type A and

four of type B (**Figure III.4b**). This location allows for short Hal···Hal intercolumn interactions. Thus, six bromine atoms of a given molecule are involved in the bonding with the ten closest bromines belonging to neighboring molecules by means of cyclic three center halogen interactions (Hal$_3$-synthons) formation and single Hal···Hal contacts.

Along the *b*-axis direction the stacked molecules are close to each other with an interplanar distance of 3.583 Å and a slipping angle of 20.8 °. Interatomic contacts of type C···C, Br···Br, and Br···C are also found between each two adjacent stacked molecules, with the shortest Br···C distance of 3.6452(2) Å. It should be noted that the later contact exhibits an interatomic distance which is close to the sum of the van der Waals radii of the Br and C_{sp2} atoms (r_{vdw}(Br) + r_{vdw}(C_{sp2}) = 3.63 Å).[148] From the mechanical properties observed in the isostructural C_6Cl_6 compound,[149] π···π interactions seem to provide the rigidity of the columns, increasing the contact between the molecules along the *b*-axis direction.

2.2. Pentabromophenol C_6Br_5OH

2.2.1. Electron density modeling

The experimental data set for C_6Br_5OH was proved to be of appropriate quality for charge density analysis, however, the multipolar refinement procedure was much more extended than for the small organic molecules containing only light atoms. The R_{free} factor calculations[22] were used for the symmetry restraints and the most appropriate value for standard deviation for restraints (σ_{sym} = 0.02) was found.

(a)   **(b)**
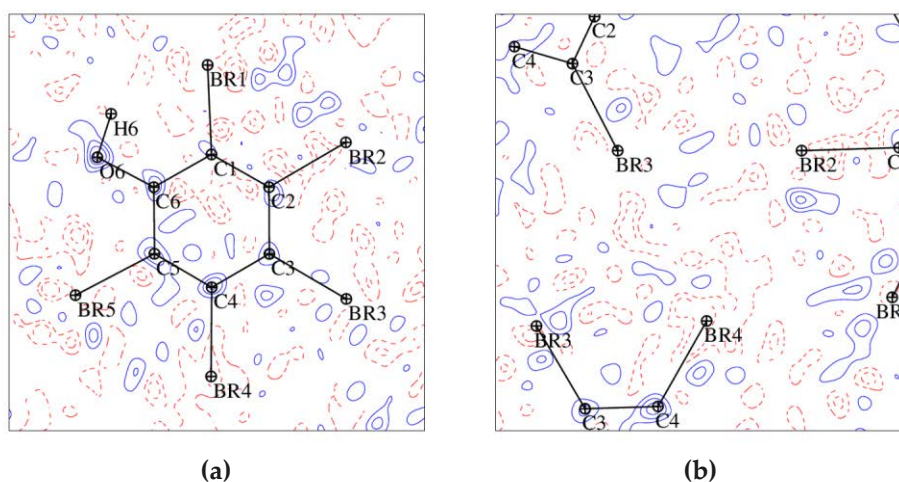
Figure III.5 Residual electron density maps for the experimental model of C_6Br_5OH drawn (a) in the plane of the molecule and (b) in the plane of the Br$_3$-synthon. Contours are at ±0.05 eÅ^{-3} level: full lines in blue – positive, dotted lines in red – negative. Resolution range is $0 \leq (\sin \theta/\lambda) \leq 0.9$ Å^{-1}.

The Slater-type radial functions were expanded up to the hexadecapolar level (l_{max} = 4) for Br-atoms, up to octapole level (l_{max} = 3) for carbon and oxygen atoms and up to dipole level (l_{max} = 1) for H-atoms (for n_l, ζ values see **Table III.3**). The refinement was performed for the reflections up to 1.0 Å^{-1} with $I > 3\sigma(I)$ cutoff, which gives a satisfying number of reflections-to

parameters ratio greater than 10 (see **Table III.2**). Due to the limitations in the quality of the diffraction data (resolution, Fourier series truncation effects, signal to noise ratio, etc.) and to high absorption effects induced by Br-atoms (μ = 21 mm^{-1}), constraints had to be applied in the first steps of the refinement. At the end of the refinement the agreement factors are $wR(F)$ = 0.027 and $R(F)$ = 0.031. The residual electron density maps show no significant features (**Figure III.5**) and the largest peak close to Br-atoms is 0.15 eA^{-3}. This indicates that the model used in the refinement is adequate. Its quality was also validated by the low values of the rigid bond test[30] (the largest difference of mean-square displacement amplitudes (DMSDA) along bonding directions were found to be 4.4·10^{-4} Å^2 at C_5–Cl_5 and 5.4·10^{-4} Å^2 at C_2–C_3).

The static deformation density map in the C_6Br_5OH molecular plane shows similar features than those found in the theoretical $\Delta\rho(\mathbf{r})$ map of the C_6Br_6 molecule (∼0.5 eÅ^{-3} on C_{sp2}–C_{sp2} bonds and 0.15-0.20 eÅ^{-3} on C–Br bonds (**Figure III.6a**). Very similar torus-shaped regions of charge accumulation around Br-atoms are observed, although it is less symmetrical for the experimental model. The $\Delta\rho$ maximum corresponding to the lone pair of the O-atom (∼0.4 eÅ^{-3}), is adjoin to the charge depletion region δ^+ (∼–0.6 eÅ^{-3}), which is placed in the prolongation of C_6–O_6 bond. The map of negative Laplacian $L(\mathbf{r})$ is shown in **Figure III.6b** with the indicated BCPs. The differences between the $L(\mathbf{r})$ maps of the two studied Br-containing compounds will be discussed in details in **Chapter IV**.

<center>(a)   (b)</center>
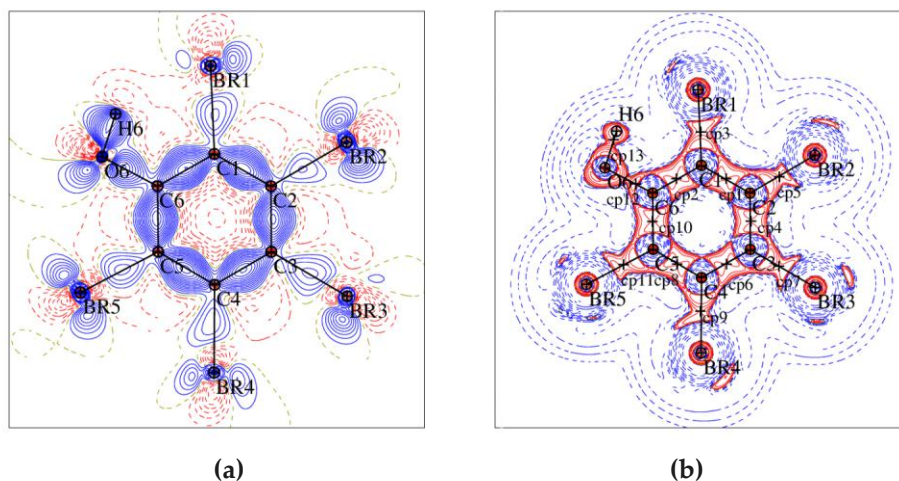
Figure III.6 (a) Static deformation density $\Delta\rho(\mathbf{r})$ and (b) negative Laplacian $L(\mathbf{r})$ maps for the experimental multipolar model of C_6Br_5OH drawn in the plane of the molecule. $\Delta\rho(\mathbf{r})$ contours are at ±0.05 eÅ^{-3} level: full lines in blue – positive, dotted lines in red – negative. $L(\mathbf{r})$ contours (eÅ^{-5}) are in logarithmic scale, red – positive, blue – negative.

2.2.2. Crystal structure description

While only one phase was observed for the isostructural C_6Cl_6 and C_6Br_6 compounds, the crystal structures of C_6Cl_5OH and C_6Br_5OH were found to crystallize in two polymorphic phases that are referred here as low- and high-temperature (LT and HT) phases. Indeed, investigating the thermodynamic behavior of C_6Br_5OH, Wójcik et al.[150] observed a first order phase transition at 441.5 K. The LT phase of C_6Br_5OH, determined by Betz *et al*. at 200(2) K,[151]

was found to crystallize in the monoclinic system, $C2/c$ space group ($Z = 8$, unit cell parameters: $a = 32.3058(15)$ Å, $b = 3.9957(2)$ Å, $c = 16.1887(8)$ Å, $\beta = 112.118(3)$ °, $V = 1935.93(17)$ Å³). On the other hand, Wójcik *et al.*[150] determined C_6Br_5OH at room temperature in the monoclinic system, $P2_1$ space group (with $Z = 2$ and unit cell parameters: $a = 8.238(8)$ Å, $b = 4.021(9)$ Å, $c = 14.822(8)$ Å, $\beta = 95.82(6)°$), similarly to C_6Br_6.[146] Probably, the existence of two C_6Br_5OH forms, both at low temperature conditions, is induced by the crystallization method – the crystals of the $C2/c$ phase were obtained upon recrystallization of the compound from boiling toluene, while for the $P2_1$ phase, the C_6Br_5OH crystals were obtained by slow evaporation from a benzene solution.

In C_6Br_5OH, the existence of the OH-group courses the formation of an infinite monodimensional chain of hydrogen bonds (O···O distance of 2.84/2.88 Å for LT/HT phases).[151,150] The existence of an intramolecular O–H···Br contact was observed in both C_6Br_5OH structures (the H···Br distance being 2.29 and 2.48 Å for the $P2_1$ and $C2/c$ phases, respectively). From the IR spectra of the LT and HT phases of C_6Br_5OH,[150] it was shown that the phase transition is associated to the breaking of the intermolecular hydrogen bonding interactions and the proceeding reorientation of the molecules. The broadening of the OH band in the HT phase of C_6Br_5OH indicates that the later intramolecular interaction remains, or even strengthens, during the phase transition. The C_6Br_5OH phase transition at 441.5 K is not reversible on cooling, so its HT phase has not been determined so far.

(a)   **(b)**
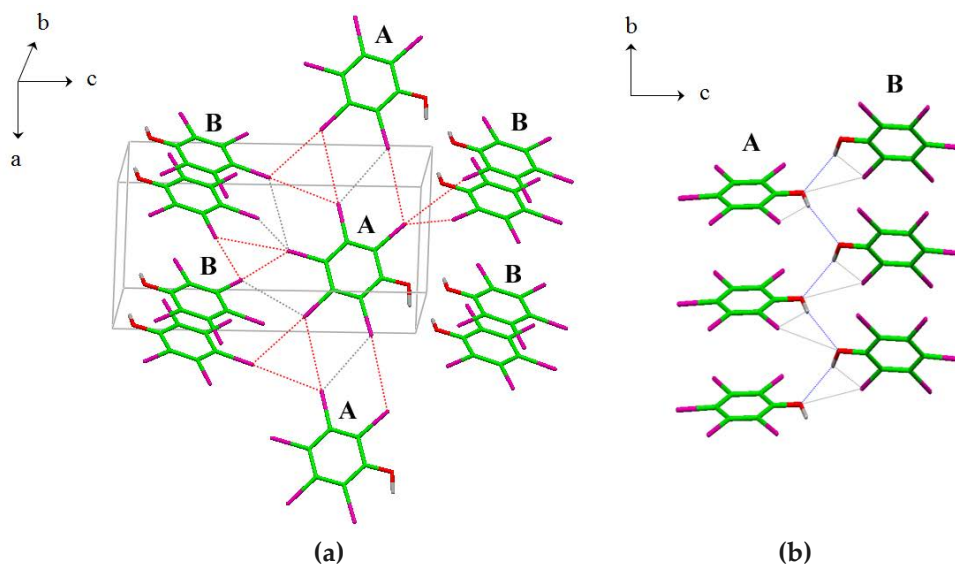
Figure III.7 Crystal structure of C_6Br_5OH ($P2_1$). (a) Down view of the A and B columns projected in the *ac*-plane. Intercolumn Hal₃-synthon interactions are noted in red, single Hal···Hal contacts are in grey. (b) Hydrogen bonding network along the *b*-axis direction is noted in blue, intramolecular O–H···Br and intermolecular O···Br are in grey dashed lines. The columns are defined by symmetry operations (excluding lattice translations): A (x, y, z) and B (–x, 1/2+y, –z).

In the present study, it was observed that the crystal structure of C_6Br_5OH seems to form an analogous molecular arrangement with the one of C_6Br_6 (and the isostructural C_6Cl_6), leading to similar molecular orientations and bonding networks (intra- and intermolecular interactions).

However, the substitution of one bromine atom by a phenol hydroxyl-group in C_6Br_5OH leads to the loss of the inversion centers, found in the crystal structure of C_6Br_6, lowering the space group symmetry. Though, C_6Br_5OH crystallizes in the monoclinic system ($P2_1$ space group) with one molecule in the asymmetric unit. As in C_6Br_6, the molecules stack along the b-axis direction forming columns, the interplanar distance and the slipping angle being equal to 3.568 Å and 29.5 °, respectively. The alternating columns A and B are assembled *via* hydrogen and halogen bonds (**Figure III.7**). As observed for C_6Br_6, each column here is also surrounded by six neighboring ones. The synthon formation in the intercolumn region involves only three bromine atoms of each molecule, placed in *meta-* and *para*-positions with respect to the hydroxyl group, while bromines in *ortho*-positions form short single contacts with adjacent molecules (**Figure III.7a**).

The presence of the OH-group leads to the hydrogen bond formation (O–H···O) that links the molecules into infinite chains along the b-axis direction (**Figure III.7b**), resembling several other mono and dihydric phenols.[152] While O···O and H···O distances are 2.8491(5) and 2.228 Å, the O–H···O angle is found to be quite low (120.95°).

From the crystal structure, the O- and H-atoms seem also to be involved in an inter- and intramolecular interaction with the adjacent *ortho*-Br atom, H_6···Br_1 and O_6···Br_1 distances being 2.285 and 3.4966(1) Å, respectively. Comparing to the previously investigated phenol groups,[152] the bifurcation of the hydrogen bond can be a reason of a low intermolecular hydrogen bond angle.

The C_6Br_5OH structure, that we determined at 100(2) K turned out to be different from the known one reported by Betz *et al.* at 200(2) K.[151] In both cases, the crystal system is monoclinic, but the crystal structures differ in their space groups ($P2_1$ *vs.* $C2/c$), number of molecules in the unit cell (2 *vs.* 8) and number and length of halogen and hydrogen bonding. Thereby, using the sublimation method, we obtained the LT phase, described by Wójcik *et al.*,[150] thus indicating that the crystallization method plays a conclusive role in phase determination even at low temperature.

Earlier studies showed that crystal structures with high Z values represent high energy minima in the crystallization pathway, therefore being less stable in comparison with the corresponding low-Z phases.[78,93,153] Based on these findings, it can be suggested that the $C2/c$ phase ($Z = 8$), obtained by recrystallization from the boiling toluene, corresponds to a less stable and kinetically formed structure, while the $P2_1$ phase ($Z = 2$), obtained by sublimation method, is thermodynamically stable.

2.3. Pentachlorophenol C_6Cl_5OH

2.3.1. Electron density modeling

Multipolar modeling for C_6Cl_5OH was performed according to the procedure described earlier. Due to a lower quantity of electrons in comparison with Br-atoms, in the multipolar modeling of Cl-atoms, the constraints were not needed.

(a) **(b)**
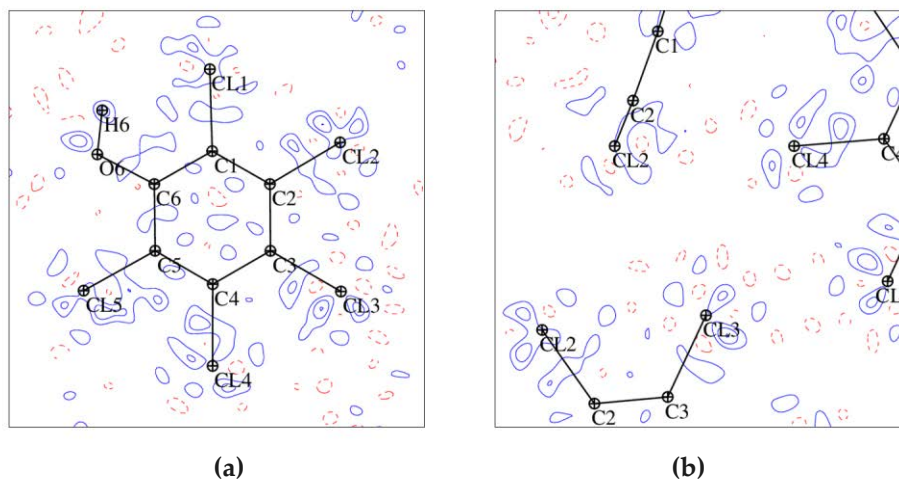
Figure III.8 Residual electron density maps for the experimental model of C_6Cl_5OH drawn (a) in the plane of the molecule and (b) in the plane of the Cl_3-synthon. Contours are at ± 0.05 eÅ^{-3} level: full lines in blue – positive, dotted lines in red – negative. Resolution range is $0 \leq (\sin \theta/\lambda) \leq 0.9$ Å^{-1}.

The multipole expansions level and (n_l, ζ) values are gathered in **Table III.3**. The refinement was performed for the reflections up to 1.0 Å^{-1} with $I > 3\sigma(I)$ cutoff; the agreement factors at convergence are w$R(F) = 0.011$ and $R(F) = 0.013$ (see **Table III.2)**. The quality of multipolar refinement was examined by the Hirshfeld rigid bond test[30] to all covalent bonds involving non-hydrogen atoms, and the largest DMSDA were found to be $3.6 \cdot 10^{-4}$ Å^2 at C_6–O_6, $3.2 \cdot 10^{-4}$ Å^2 at C_1–C_2 and $2.0 \cdot 10^{-4}$ Å^2 at C_1–Cl_1. In addition, the maximum residual electron density peak calculated (with $I > 3\sigma(I)$) over the asymmetric unit corresponds to 0.15 eA^{-3} (**Figure III.8**). The previous criteria indicate a good quality of the model used in the refinement.

The features observed at the static deformation density map of C_6Cl_5OH (**Figure III.9a**) are comparable to the ones reported earlier in the literature for Cl-containing compounds[83,154] – $\Delta\rho$ accumulation on C_{sp2}–C_{sp2} (~0.6 eÅ^{-3}) and C_{sp2}–Cl (~0.2 eÅ^{-3}) bonds. The deformation density around Cl-atoms is similar to the one observed for Br-atoms, clearly bringing out the features of the halogen lone pairs. The $\Delta\rho$ maximum and minimum around the O-atom correspond to its lone pair (~0.45 eÅ^{-3}) and its charge depletion region δ^+ (~–0.2 eÅ^{-3}). The typical Laplacian distribution for Cl-atoms is shown in **Figure III.9b**. Its features differ a lot from the ones observed for Br-atoms (**Figure III.3b, III.6b**) and will be discussed in the following chapter.

(a)   **(b)**
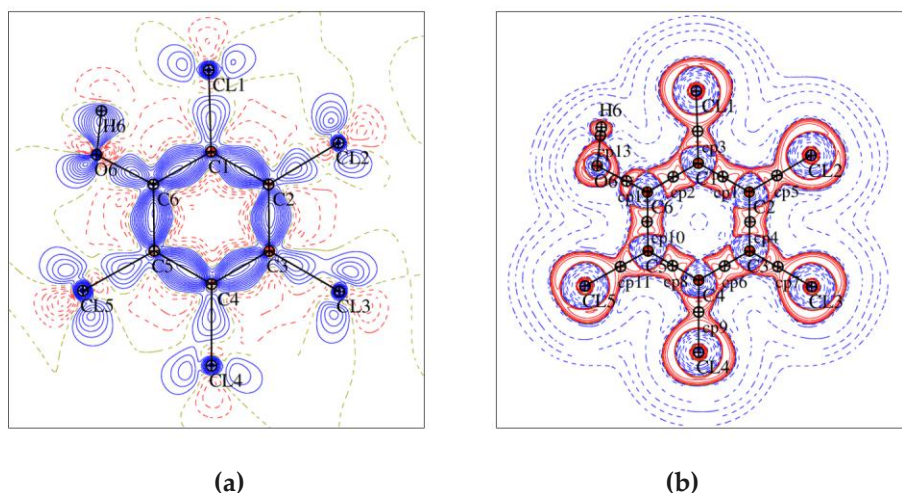
Figure III.9 (a) Static deformation density $\Delta\rho(\mathbf{r})$ and (b) negative Laplacian maps $L(\mathbf{r})$ for the experimental multipolar model of C_6Cl_5OH drawn in the plane of the molecule. $\Delta\rho(\mathbf{r})$ contours are at ±0.05 eÅ^{-3} level: full lines in blue – positive, dotted lines in red – negative. $L(\mathbf{r})$ contours (eÅ^{-5}) are in logarithmic scale, red – positive, blue – negative.

2.3.2.   Crystal structure description

According to Wójcik *et al.*,[150] the first order transition between the LT and HT phases of C_6Cl_5OH is observed at 341 K. In that case, the crystal structure of C_6Cl_5OH LT phase was solved by combining nuclear quadrupole resonance and X-ray diffraction data at room temperature[155] (monoclinic system, $C2/c$ space group, Z = 8, unit cell parameters: a = 29.11(3) Å, b = 4.93(5) Å, c = 12.09(2) Å, β = 93.38(4) °, V = 1732(5) Å^3). In this structure, the existence of OH-groups provides bifurcated intermolecular interactions involving a hydrogen bond, which links the molecules into infinite monodimensional chains (O···O distance of 2.97 Å), and a contact between the oxygen and a Cl-atom in *ortho*-position (O···Cl = 3.28 Å).[155] The crystal structure of C_6Cl_5OH HT phase was as well determined at room temperature. Indeed, while cooling, the HT phase remains for several hours as a metastable state, allowing the structure determination, until the stable LT phase is reconstructed. This allowed Wójcik and Rohleder[156] to conclude that the HT phase of C_6Cl_5OH, crystallizing in the monoclinic system, $P2_1$ space group, has similar structural characteristics with those observed in C_6Cl_6.[147] Similarly to the C_6Br_5OH structure, the phase transition in C_6Cl_5OH occurs while intermolecular hydrogen bonding interactions break.[150] Moreover, in comparison with the C_6Cl_5OH structure, the higher phase transition temperature of C_6Br_5OH was explained by its higher crystal density, which correlates with stronger intermolecular forces (also supported by shorter O···O distances) and the occurrence of an intramolecular O–H···Br interaction.

In the present study, the structure of C_6Cl_5OH, determined at 100(2) K (see **Table III.2**) is similar to the one obtained by Sakurai at room temperature.[155] **Figure III.10a,b** shows two different projections of the C_6Cl_5OH structure.

(a)

(b)

(c)

(d)
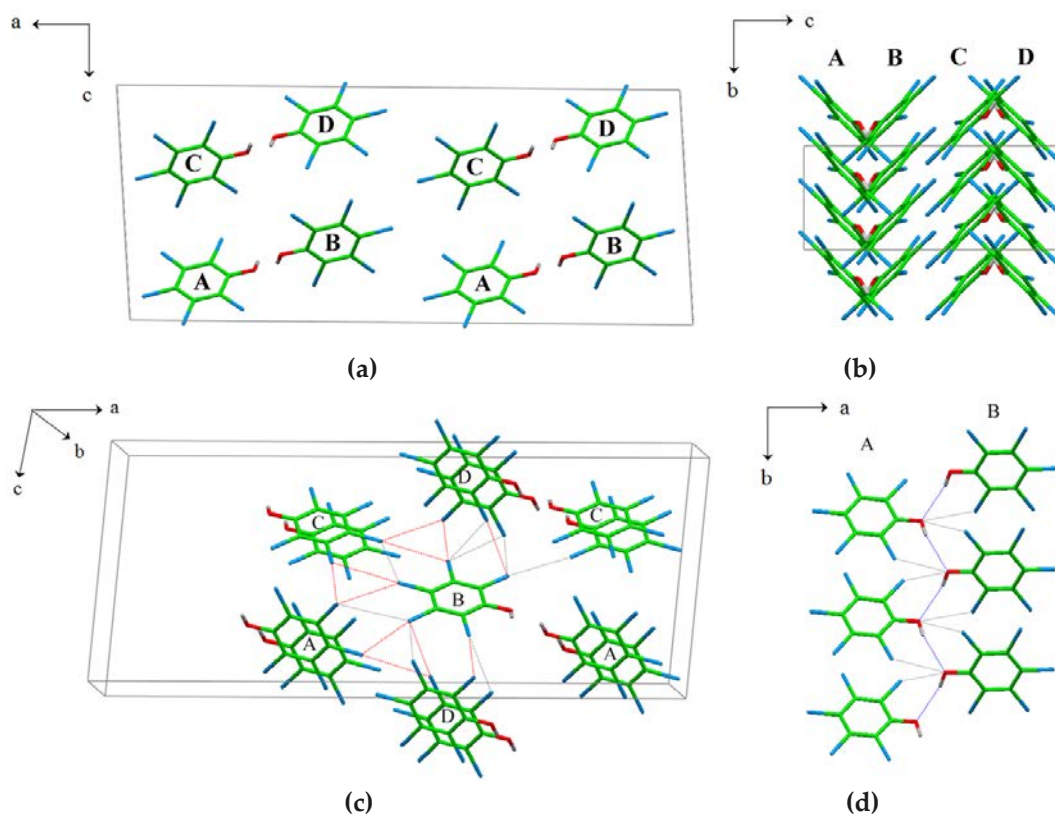
Figure III.10 Crystal structure of C_6Cl_5OH (*C2/c*). (a) Down view on the unit cell projected in the *ac*-plane. (b) Side view of alternating columns projected in the *bc*-plane. (c) Intermolecular interactions representation. Intercolumn Hal3-synthon interactions are noted in red, single Hal···Hal contacts are in grey dashed lines. (d) Hydrogen bonding network along the *b*-axis direction is noted in blue, intermolecular O···Cl contacts are in grey dashed lines. The columns are defined by symmetry operations (excluding lattice translations): A (*x*, *y*, *z*), B (−*x*, −*y*, −*z*), C (−*x*, *y*, 1/2−*z*), and D (*x*, −*y*, 1/2+*z*).

The molecules form columns by stacking along the *b*-axis direction, the interplanar distance and the slipping angle being equal to 3.389 Å and 31.5 °, respectively. Molecules lying in alternating columns A and B, C and D exhibit an interplanar angle of 91.8 °. As seen in **Figure III.10c**, each column (e.g. column B) is surrounded by six other columns, similarly to the previously described structures. However, in the case of the C_6Cl_5OH structure, the short interactions (synthons and single Hal···Hal contacts) are formed with nine instead of ten (C_6Br_5OH) neighboring molecules. The intermolecular hydrogen bond pattern of C_6Br_5OH is also present in the C_6Cl_5OH structure (**Figure III.10d**), with O···O and H···O distances of 2.9283(1) and 2.043 Å, respectively, and a O–H···O angle of 151.75°. The former distance is longer than the one observed for C_6Br_5OH (2.8491(5) Å). The O-atom seems to form short intermolecular contacts with the two neighboring chlorine atoms in *ortho*-position (the distances O···Cl being 3.2412(1) and 3.4763(1) Å, respectively), though indicating the formation of trifurcated, instead of bifurcated, O-involved interactions as reported previously.[155]

In general, the crystal structure of C_6Cl_5OH coincides with the one obtained by Sakurai.[155] Accordingly, C_6Cl_5OH does not show isostructural trends with C_6Br_5OH, however, it exhibits similar intermolecular halogen contacts that take place in C_6Br_5OH, as well as in C_6Br_6 and C_6Cl_6.

2.4. Selenophtalic anhydride $C_8H_4O_2Se$

2.4.1. Electron density modeling

X-ray diffraction measurements for $C_8H_4O_2Se$ were carried out using synchrotron and Mo Kα radiation sources (= 0.45741 and 0.71073 Å, respectively). Both data sets permit to obtain reasonable multipolar models, showing residual maps (**Figure III.11a,b**) almost featureless for the light atoms (C, O, and H). In the case of synchrotron radiation, the residuals around Se-atom and near Se–C bonds are however unaccountably large (0.3 and 0.25 eÅ^{-3}). Due to this fact, for the following intermolecular interactions analyses, the preference was given to the model based on the Mo Kα data. The presence of such a heavy atom as selenium stimulated us to perform periodic theoretical calculations in order to compare the obtained experimental and theoretical models and their features. Similarly to the C_6Br_6 case, the residual map drawn up to 0.9 Å^{-1} (**Figure III.11c**) shows a peak centered at the heavy atom nucleus (~0.4 eÅ^{-3} at selenium), corresponding to the valence electron density that was not taken into account by the multipolar atom model. Residues are in general due to experimental noise. In the case of Se-atom, they could be attributed to a defect of the Slater-type radial function used in the multipolar model.

(a)   (b)   (c)
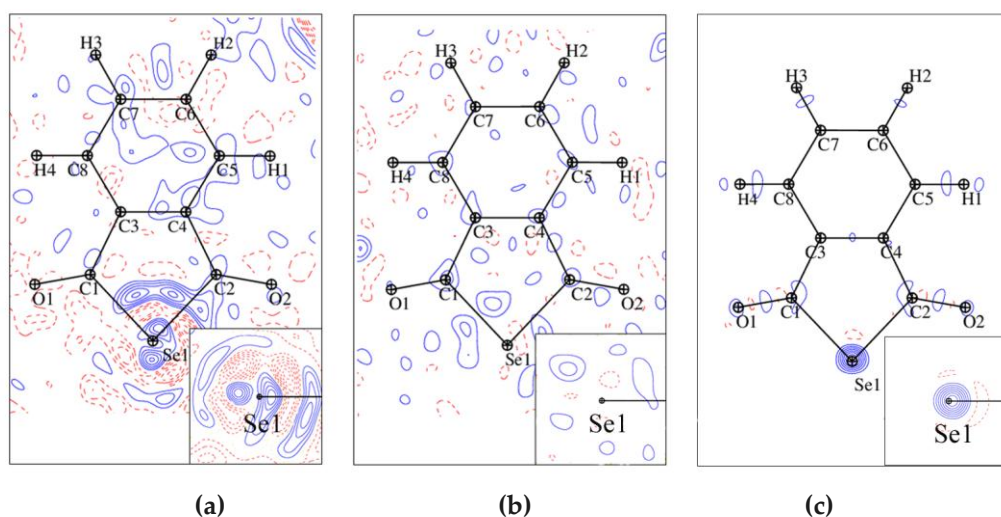
Figure III.11 Residual electron density maps for $C_8H_4O_2Se$ drawn in the plane of the molecule and in the perpendicular plane bisecting the C–Se–C angle: (a) experimental (synchrotron), (b) experimental (Mo Kα) and (c) theoretical models. Contours are at ±0.05 eÅ^{-3} level: full lines in blue – positive, dotted lines in red – negative. Resolution range is $0 \leq (\sin \theta/\lambda) \leq 0.8$ Å^{-1}.

In the multipolar refinements against the experimentally obtained and the theoretically calculated structure factors, identical Slater-type radial function parameters were used. Due to differing bond length, the carbon atoms in C–C and C–Se chemical bonds were differently defined (see the corresponding (n_l, ζ) values for C and C′ in **Table III.3**); for Se-atom, the (n_l, ζ) values were optimized by inspecting the residual maps. For the experimental multipolar refinement, 5 927 reflections were used up to resolution 1.0 Å^{-1}, leading to the agreement factors $R(F) = 0.042$ and $wR(F) = 0.031$ (for the theoretical model 5 927 reflections up to the same

experimental resolution 1.0 Å^{-1} were used leading to $R(F) = 0.051$ and $wR(F) = 0.020$).

The static deformation density maps for experimental and theoretical models of $C_8H_4O_2Se$ are shown in **Figure III.12**. While the experimental map reveals more pronounced electron accumulation on the bonds (e.g. in C–C bonds it shows ~0.6 eÅ^{-3} and ~0.5 eÅ^{-3} for the experimental and the theoretical models), qualitatively the two maps are very similar to each other. The most important difference is observed for Se-atom – at a similar contours level, a density accumulation in the direction bisecting the C_3-Se-C_4 angle is present just on the theoretical-model map, while in the perpendicular direction both of them show the δ^--regions, corresponding to the two lone pairs of Se-atom (the $\Delta\rho$ maxima being ~–0.05 and ~–0.1 eÅ^{-3} for experimental and theoretical models, respectively). Experimental and theoretical models reveal the regions of electron density depletion (δ^+) in the prolongations of C–Se bonds ($\Delta\rho$ minima ~ –0.05 and < 0.05 eÅ^{-3}).

The negative Laplacian maps for the experimental and theoretical models (**Figure III.13**) are qualitatively very similar – both of them represent two domains of Se lone pairs that are localized over and under the plane of the molecule. Quite similar features of the $L(\mathbf{r})$ distribution around Se-atom were obtained by the quantum-chemical calculations performed for the $Se(CH_3)_2$ molecule.[116b] In the latter, the CC regions were, however, characterized by the positive values of L, while in the present study both models show negative values of L. The detailed description of the Laplacian distribution around the Se-atom will be performed in Chapter V.

(a)   **(b)**
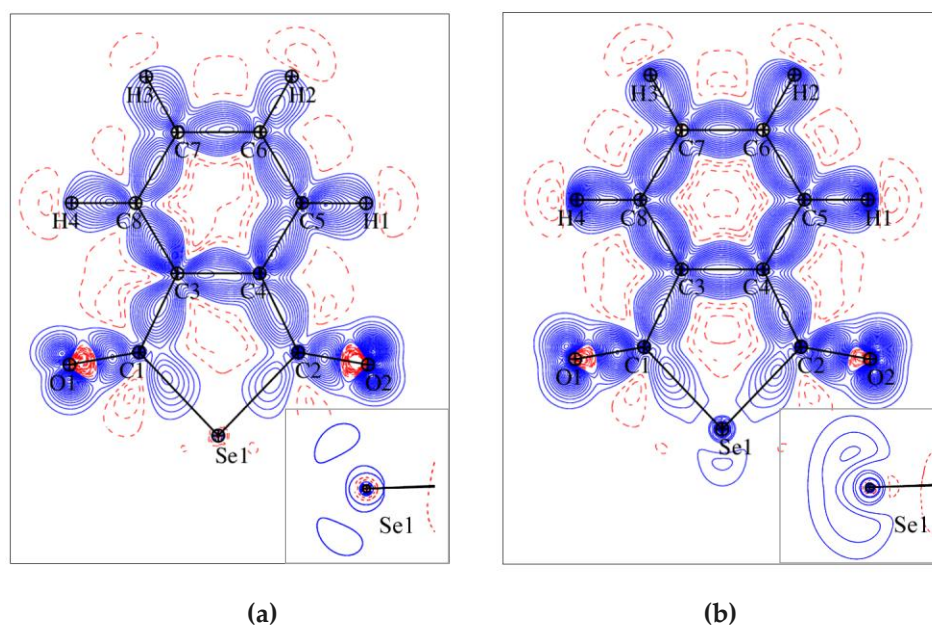
Figure III.12 Static deformation density $\Delta\rho(\mathbf{r})$ maps for $C_8H_4O_2Se$ drawn in the plane of the molecule and in a perpendicular plane bisecting the C–Se–C angle: (a) experimental and (b) theoretical models. Contours are at ±0.05 eÅ^{-3} level: full lines in blue – positive, dotted lines in red – negative.

(a)   **(b)**
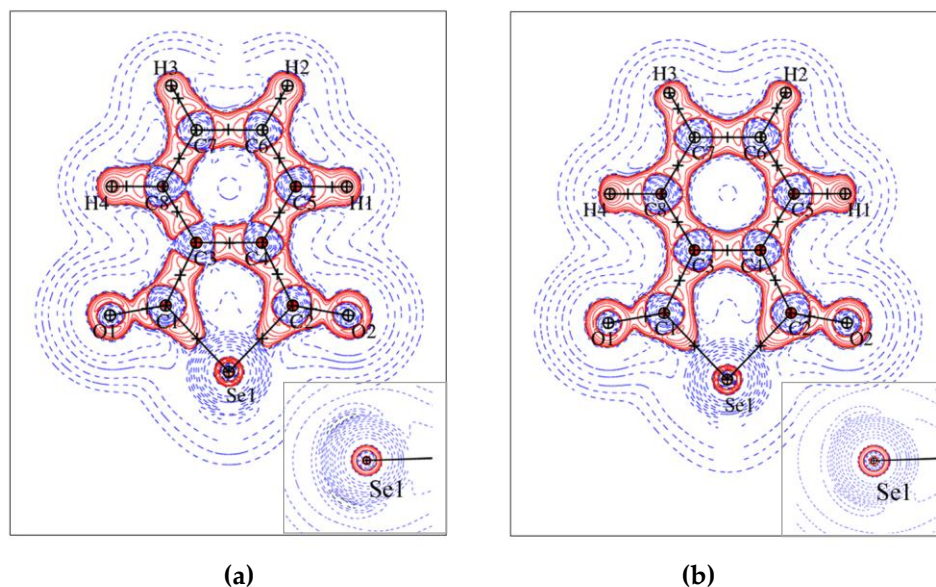
Figure III.13 $L(\mathbf{r})$ maps for $C_8H_4O_2Se$ drawn in the plane of the molecule and in a perpendicular plane bisecting the C–Se–C angle: (a) experimental and (b) theoretical models. Contours (eÅ^{-5}) are in logarithmic scale, red – positive, blue – negative.

2.4.2. Crystal structure description

(a)   **(b)**
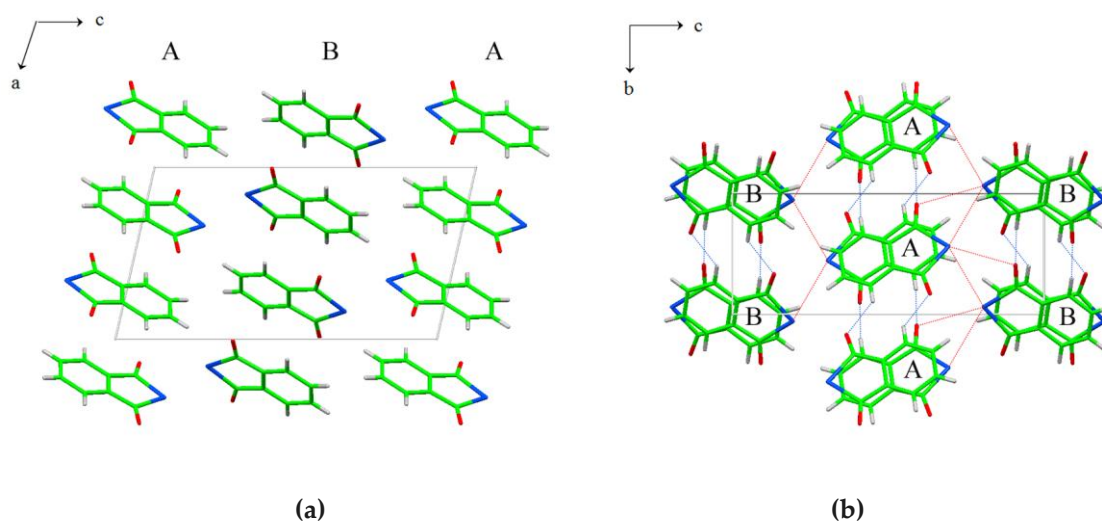
Figure III.14 Crystal structure of $C_8H_4O_2Se$. (a) Side view of the alternating columns A and B projected on the *ac*-plane; (b) down view of the A and B columns projected on the *bc*-plane. Intercolumn hydrogen bonding interactions are noted in red lines, chalcogen bondings are in blue lines.

$C_8H_4O_2Se$ crystallizes in the monoclinic system ($P2_1/n$ space group, Z = 4), with one molecule in the asymmetric unit (similarly to the one, reported earlier[157]). In the crystal structure, $C_8H_4O_2Se$ molecules form columns along the *a*-axis direction (**Figure III.14a**) with an interplanar distance of 2.986 Å and a slipping angle of 53.1 °; the angle between molecules from

neighboring columns is 62.2°. From the down view (**Figure III.14b**), it can be seen that molecules belonging to columns of the same type (A···A, and B···B) are linked by hydrogen bonding interactions involving O- and H-atoms, while those belonging to columns of different type (A···B) show quite short intermolecular contacts involving Se- and O-/Se-/H-atoms, the interatomic distances being close to the sum of the van der Waals radii of the interacting atoms.

2.5. Iododithiolone C_3HIOS_2

2.5.1. Electron density modeling

The experimental data set for iododithiolone C_3HIOS_2, obtained with Mo Kα (λ = 0.71073 Å) radiation, is of relatively low quality for charge density analysis due to the presence of several heavy atoms, such as two S and especially one I, in a small organic molecule that crystalizes in a non-centrosymmetric space group (*P*1). For this reason, periodic theoretical calculations were performed on the crystal structure of C_3HIOS_2 based on the experimental geometry. The obtained multipoles were used as a starting point in the multipolar refinement against the experimental structure factors. The residual density map of the best experimental model (**Figure III.15a**) shows numerous pronounced peaks near the heavy atoms (0.10 - 0.25 eÅ^{-3} near I, S, and O) and noise background, while the theoretical one shows peaks centered at I- and S-atoms (**Figure III.15b**).

(a)   (b)
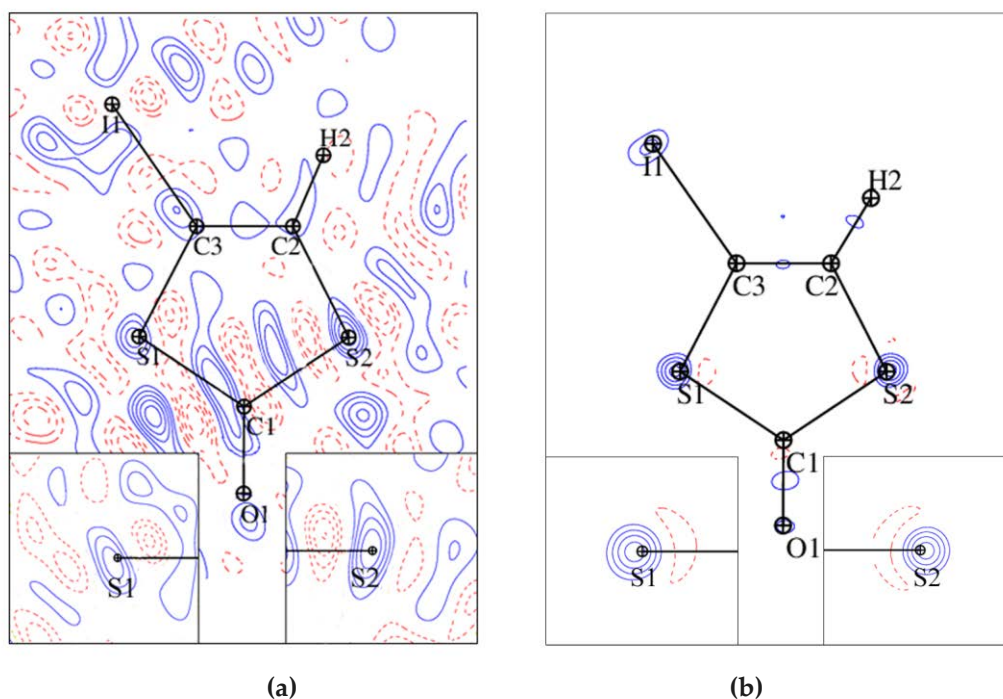
Figure III.15 Residual electron density maps for C_3HIOS_2 drawn in the plane of the molecule and in the two perpendicular planes bisecting the C–S–C angles: (a) experimental and (b) theoretical models. Contours are at ±0.05 eÅ^{-3} level: full lines in blue – positive, dotted lines in red – negative. Resolution range is $0 \le (\sin \theta/\lambda) \le 0.9$ Å^{-1}.

In the multipolar refinement against the experimentally obtained and theoretically calculated structure factors, the Slater-type radial functions were expanded up to the hexadecapole level (l = 4) for I-atom (n_l, ξ: 8,8,8,8 for l = 1,2,3,4; 4.84 bohr^{-1}), and up to octapole level (l = 3) for C-, O-, and S-atoms (**Table III.3**). In the fitting against theoretical data, core electrons were omitted from MoPro atomic definitions, as in the case of C_6Br_6. The multipolar models fitted against the experimental and theoretical structure factors converged to the agreement factors $wR(F) = 0.053$, $R(F) = 0.043$ and $wR(F) = 0.023$, $R(F) = 0.041$, respectively.

The static deformation density maps for experimental and theoretical models of C_3HIOS_2 are shown in **Figure III.16**. The two maps show qualitatively similar features with the highest density accumulation on the C_2–C_3 (~0.6 eÅ^{-3}) and C–S (up to 0.35 eÅ^{-3}) bonds. The contours, corresponding to the C_3–I_1 bond are less pronounced for the theoretical model than for the experimental one (0.1 and 0.45 eÅ^{-3}, respectively). At the lone-pairs positions, corresponding to the S_1- and S_2-atoms, $\Delta\rho$ is almost equal for the two atoms in the case of the experimental model and quite different for the theoretical one. In the latter, the lone-pairs separation is not observed for S_1-atom at any contour level. These differences could be explained by the participation of the two S-atoms in different intermolecular interactions. Both models clearly show the existence of the electron density depletion (δ^+) in the prolongations of C–S bonds ($\Delta\rho$ varies from –0.25 to –0.10 eÅ^{-3}). In general, the deformation density map of the S-atom shows very similar features to the ones observed for Se-atom in $C_8H_4O_2Se$.

On the other hand, the multipolar model of the I-atom in C_3HIOS_2 is qualitatively close to the ones previously described for Cl- and Br-atoms: the δ^+ region placed on the prolongation of the C_3–I_1 bond and δ^- regions in the perpendicular plane. The deviation of the δ^+ region from the C_3–I_1 bond direction is probably connected to the intermolecular interaction formation I···(lp)O and will be characterized in **Chapter IV**.

(a)   (b)
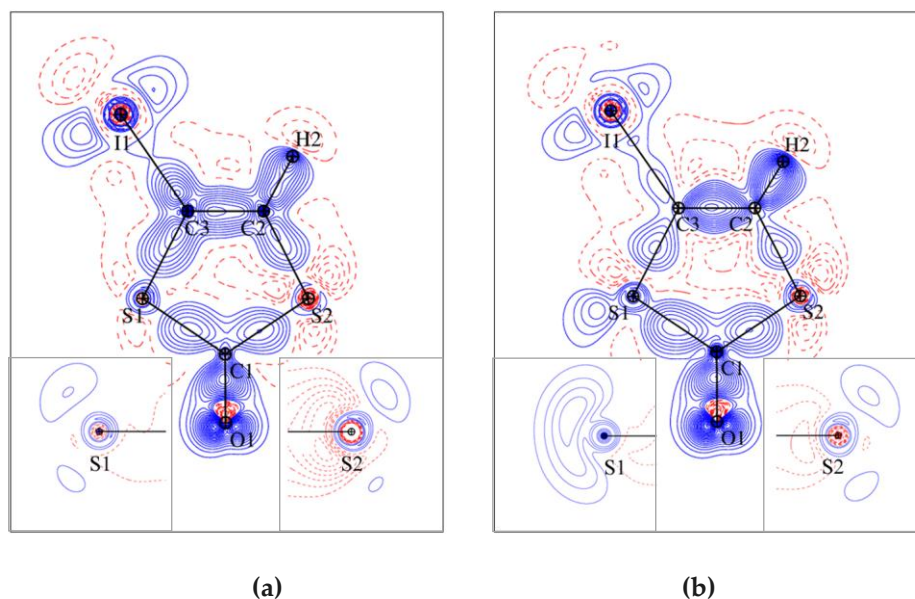
Figure III.16 Static deformation density $\Delta\rho(\mathbf{r})$ maps for C_3HIOS_2 drawn in the plane of the molecule and in the two perpendicular planes bisecting the C–S–C angles: (a) experimental and (b) theoretical models. Contours are at ±0.05 eÅ^{-3} level: full lines in blue – positive, dotted lines in red – negative.

The negative Laplacian maps for the experimental and theoretical models (**Figure III.17**) are qualitatively very similar between each other and comparable with the ones, described in the literature for S-atoms in sp^3 hybridization.[122,123] Unlike Se-, the valence shell of the S-atom presents a closed shape with positive L-values. The charge concentration (CC) regions of S-atoms are located at the δ^- positions defined from the $\Delta\rho(\mathbf{r})$ map. Qualitatively, the separation of the two CC-regions is less pronounced for S_2 and disappears for S_1 on the theoretical-model map (**Figure III.17b**). These regions will be characterized from the viewpoint of the topology of $L(\mathbf{r})$ function in **Chapter V**.

According to the previous comparison between experimental and theoretical models, in general, both of them show very close features. This is explained by the use of theoretical multipoles in the modeling against experimental structure factors. Thereby, in the following discussions, the two models will appear for the cases where the differences between them are important and only one model (experimental), when the difference is qualitatively negligible.

<div align="center">(a)   (b)</div>
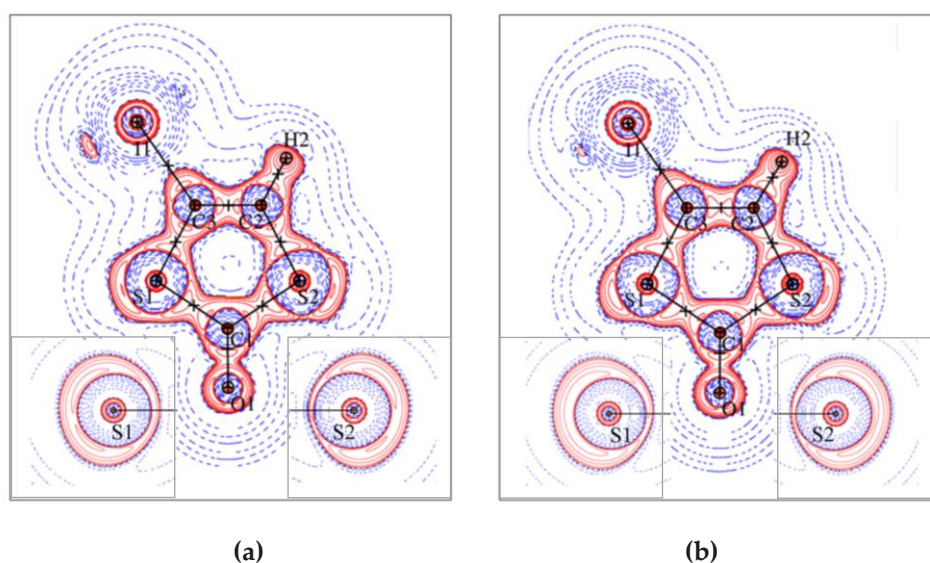
Figure III.17 $L(\mathbf{r})$ maps for C_3HIOS_2 drawn in the plane of the molecule and in the two perpendicular planes bisecting the C–S–C angles: (a) experimental and (b) theoretical models. Contours (eÅ^{-5}) are in logarithmic scale, red – positive, blue – negative.

2.5.2. Crystal structure description

C_3HIOS_2 crystallizes in the triclinic system ($P1$ space group) with only one molecule in the unit cell. In the crystal structure, C_3HIOS_2 molecules form layers in the ac-plane, where the molecules form chains connected by bifurcated interactions, involving hydrogen (H···O) and halogen (I···O) bonding (**Figure III.18a**) with distances (2.235 and 2.9312(1) Å, respectively) significantly shorter than the sum of the corresponding van der Waals radii (ω = 82.2 and 83.7%). The molecular arrangement allows for the formation of relatively short S···S and S···I chalcogen bonding between the neighboring molecules along the c-direction (3.8289(1) and 3.8031(3) Å, respectively). Along the a-direction, the distance between the layers is relatively short (2.541 Å), provided by the binding of the intracolumn S···I, S···O, S···C contacts (**Figure III.18b**).
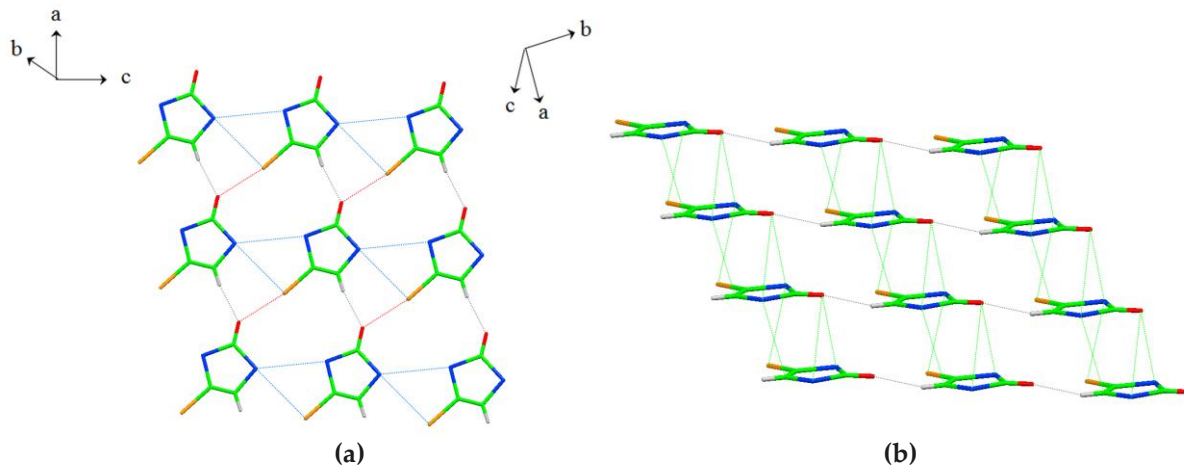
Figure III.18 Crystal structure of C_3HIOS_2. (a) Down view on the sheet in *bc* plane. (b) Side view of the sheets in the *ac* plane. Hydrogen, halogen, and chalcogen intracolumn interactions are displayed in red (I⋯O), grey (H⋯O), and green (S⋯S, S⋯I). Intracolumn interactions are noted in blue.

3. Characterization of intramolecular interactions

The analyzed structures exhibit a large variety of intramolecular interactions between different atoms of different hybridization. The topological analysis of the electron density at the (3,–1) bond critical points (BCP) permits to characterize these intramolecular interactions. **Table III.5** gathers the topological parameters for all the intramolecular interactions in the compounds analyzed in this work.

As discussed in details in Chapter I, the parameters ρ, $\nabla^2\rho$, λ_i, and ε are important to characterize the interactions. The magnitudes of λ_i (i = 1, 2) and λ_3 describe the tightening of $\rho(\mathbf{r})$, corresponding respectively to the local accumulation of charge in the plane perpendicular to the bonding direction and local charge depletion along the bond path. The ratio $|\lambda_1|/\lambda_3$ reflects the polarization effect of the interaction. The estimation of the energetic parameters G and V from the functional of Abramov and the local form of the virial theorem is not good to directly characterize the shared-shell interactions in chemical bonds.[34a,35] However, the ratio $|V|/G$, which permits to obtain a classification of interactions, could compensate for the errors of single V and G magnitudes as they are derived in the same way, giving us a possibility to compare interactions. According to this parameter, all the intramolecular interactions in the studied structures are of *pure* shared-shell (SS) type ($|V|/G > 2$), except the C—I interaction ($1 < |V|/G < 2$), which presents an intermediate character between *pure* CS and SS interactions. This is supported by the positive value of $\nabla^2\rho$ at the BCP of the C—I bond, in contrast to the other covalent interactions ($\nabla^2\rho < 0$). Whilst these qualitative results are coherent with the expected behaviors, a deeper analysis is needed to validate quantitatively the magnitudes of the $|V|/G$ descriptor, even if, in general, the increase of the latter parallels the negative magnitudes of the corresponding $\nabla^2\rho$ values.

The small RMSD magnitudes (see **Table III.5**) indicate that the topological values observed for the chemical bonds of the same type are very similar. Classifying the observed interactions

in the groups – X—H (X = O, C_{sp2}, C_{sp3}), C—C, C_{sp2}—Chal, and C_{sp2}—Hal – we expect the weakening of the interaction going down along this series, which is roughly reflected in the decrease of the charge concentration in the bonding region (see e.g. $\nabla^2\rho$ values). A very strong interaction is formed in the case of C_{sp2}—O_{sp2} for C_3HIOS_2, as measured from ρ. The low ellipticity value ε of these bonds indicates their σ character.

Among the studied compounds, the most frequent is C—C bond. Distinguishing between the three types, we observe the high ε-value for the aromatic bonds C_{sp2}—C_{sp2}, clearly indicating the π-character of this interaction in contrast to the lower ε-values for the single bonds C_{sp2}—C_{sp3} and C_{sp3}—C_{sp3}. The topological values for these interactions are in accordance with the previously reported by Cole *et al*.[158] The C—C bonds involving a C_{sp2}-atom are characterized by $|\lambda_1/\lambda_3| > 1$, being in accordance with the theoretical studies performed by R. Bader,[159] while the C_{sp3}—C_{sp3} covalent bond presents a more polarized character ($|\lambda_1/\lambda_3| < 1$).

The series of C_{sp2}—Chal and C_{sp2}—Hal bonds are characterized by lower charge concentration at the corresponding bcp's than the previously mentioned ones, decreasing from lighter to heavier Hal/Chal-atoms. The $|\lambda_1/\lambda_3|$ descriptor tends to decrease in the same order along the C_{sp2}—Chal/Hal series, indicating the increase of polarization. The result for C—Cl bonds are in accordance with the ones previously published[83,142b] with the highest value of λ_3 and the larger $|\lambda_1/\lambda_3|$ magnitude around C_{sp2}–Hal series.

Summary

In the present work, we have studied five halogenated and chalcogenated compounds along with the one described earlier (C_6Cl_6).

❖ We have performed the high-resolution XRD measurements (using laboratory equipment as well as synchrotron radiation) in order to obtain their crystal structures and carry out charge density modeling.

❖ We managed to solve the problem with multipolar modeling of molecules containing heavy atoms such as Br, I, and Se.

❖ We have demonstrated the possibility to use periodic theoretical calculations to resolve complicated experimental situations: (i) to replace experimental data of not appropriate quality (C_6Br_6); (ii) to support experimental results ($C_8H_4O_2Se$); (iii) to conduct experimental modeling starting from the theoretically obtained multipoles (C_3HIOS_2).

❖ We have performed topological analysis of electron density to characterize intramolecular interactions in the studied structures.

❖ Based on the topological analysis of $\rho(\mathbf{r})$ and $L(\mathbf{r})$ functions in the intermolecular regions (see the following chapters for detailed description), we have derived new criterion for evaluation of electrostatic interaction and have extended application of the one previously proposed for interaction energy estimation.

Table III.5 Experimentally obtained topological characteristics of intramolecular interactions in C_6Cl_6,[93] C_6Cl_5OH, C_6Br_6 (values from the theoretical model), C_6Br_5OH, $C_8H_4O_2Se$ and C_3HIOS_2. [a]

Interaction[b]	d (Å)	ρ	$\nabla^2\rho$	λ_1	λ_2	λ_3	$\mid\lambda_1\mid/\lambda_3$	ε	G	V	$\mid V\mid/G$	N
O_{sp3}—H	0.965 ± 0.002	2.46 ± 0.05	−33.67 ± 1.32	−36.81 ± 1.13	−35.75 ± 0.45	38.9 ± 0.27	0.95 ± 0.02	0.03 ± 0.01	793 ± 22	−2504 ± 79	3.16 ± 0.01	2
C_{sp2}—H	1.084 ± 0.002	1.73 ± 0.06	−16.69 ± 0.37	−17.65 ± 0.44	−16.96 ± 0.43	17.92 ± 0.87	0.99 ± 0.03	0.04 ± 0.01	475 ± 44	−1404 ± 84	2.96 ± 0.10	5
C_{sp3}—H	1.092 ± 0.001	1.71 ± 0.01	−12.05 ± 0.19	−16.28 ± 0.08	−15.47 ± 0.16	19.69 ± 0.03	0.83 ± 0.01	0.05 ± 0.01	544 ± 2	−1417 ± 10	2.60 ± 0.01	6
C_{sp2} — C_{sp2}	1.396 ± 0.011	2.10 ± 0.05	−18.56 ± 1.76	−16.38 ± 0.80	−12.87 ± 0.69	10.68 ± 1.15	1.56 ± 0.24	0.27 ± 0.04	741 ± 25	−1987 ± 74	2.68 ± 0.07	28
C_{sp2}—C_{sp2} [c]	1.484 ± 0.002	1.84 ± 0.03	−14.28 ± 2.02	−13.43 ± 0.78	−11.52 ± 0.45	10.67 ± 0.78	1.26 ± 0.10	0.17 ± 0.02	603 ± 12	−1596 ± 32	2.64 ± 0.10	2
C_{sp2}—C_{sp3}	1.505 ± 0.001	1.70 ± 0.06	−9.42 ± 0.64	−12.03 ± 0.61	−10.37 ± 0.23	12.98 ± 0.20	1.15 ± 0.03	0.16 ± 0.03	589 ± 30	−1434 ± 76	2.44 ± 0.01	2
C_{sp3}—C_{sp3}	1.559 ± 0.001	1.52 ± 0.01	−6.40 ± 0.34	−9.62 ± 0.19	−9.36 ± 0.08	12.57 ± 0.08	0.77 ± 0.02	0.03 ± 0.01	512 ± 1	−1200 ± 8	2.34 ± 0.02	2
C_{sp2}—O_{sp2}	1.204 ± 0.001	2.89 ± 0.03	−9.65 ± 7.57	−24.17 ± 0.97	−22.10 ± 0.93	36.62 ± 7.85	0.68 ± 0.14	0.10 ± 0.09	1660 ± 159	−3583 ± 117	2.16 ± 0.15	3
C_{sp2}—O_{sp3}	1.349 ± 0.001	2.09 ± 0.06	−15.23 ± 2.62	−15.98 ± 2.27	−14.04 ± 2.40	14.80 ± 2.04	1.08 ± 0.01	0.14 ± 0.03	792 ± 5	−1999 ±81	2.52 ± 0.09	2
C_{sp2}—S_{sp3}	1.746 ± 0.011	1.38 ± 0.04	−6.14 ± 0.89	−7.73 ± 0.36	−7.16 ± 0.75	8.75 ± 1.14	0.89 ± 0.13	0.09 ± 0.04	427 ± 24	−1020 ± 53	2.39 ± 0.06	12
C_{sp2}—Se_{sp3}	1.950 ± 0.006	1.00 ± 0.04	−1.41 ± 0.49	−4.73 ± 0.23	−3.93 ± 0.31	7.25 ± 0.04	0.65 ± 0.03	0.21 ± 0.04	288 ± 14	−615 ± 42	2.13 ± 0.04	2
C_{sp2}—Cl	1.714 ± 0.003	1.42 ± 0.01	−4.21 ± 0.34	−8.29 ± 0.27	−7.55 ± 0.23	11.62 ± 0.29	0.71 ± 0.02	0.10 ± 0.05	484 ± 8	−1083 ± 11	2.24 ± 0.02	8
C_{sp2}—Br	1.876 ± 0.004	1.14 ± 0.04	−2.48 ± 0.43	−5.89 ± 0.50	−5.22 ± 0.35	9.28 ± 0.24	0.64 ± 0.06	0.13 ± 0.03	354 ± 7	−758 ± 35	2.14 ± 0.07	8
C_{sp2}—I	2.076 ± 0.001	0.89 ± 0.06	0.57 ± 0.01	−4.43 ± 0.49	−3.91 ± 0.73	8.91 ± 1.21	0.50 ± 0.01	0.14 ± 0.08	266 ± 31	−517 ± 62	1.94 ±0.01	2

[a] For comparison some covalent bonds are taken from ref [93]. The parameters ρ (eÅ⁻³), $\nabla^2\rho$ (eÅ⁻⁵), λ_i (eÅ⁻⁵), G and V (kJ mol⁻¹ bohr⁻³) are calculated at the BCP's of $\rho(r)$. [b] For each topological property, the average value with the corresponding RMSD is represented for N interactions. [c] Two C_{sp2}—C_{sp2} interactions in $C_8H_4O_2Se$ are distinguished from the others, due to the different environment of the involved C_{sp2}-atoms, coursing the changes in the topological properties.

Chapter IV

Interactions involving halogen atoms

Chapter IV is devoted to the intermolecular interactions involving halogen atoms and responds the first objective of the present work. In the context of electrophilic–nucleophilic interactions, Hal···Hal contacts of Type-II geometry are analyzed in the crystal structures of C_6Br_6, $C6Cl_5OH$, and C_6Br_5OH, along with the previously investigated C_6Cl_6. The attention is paid to a particular geometrical case, formed by the association of three Type-II Hal···Hal contacts in a triangular motif, called synthon. The trends appearing for each Hal_3-synthon (Hal = Cl, Br) are characterized; the precise analysis is performed of the valence shell region of Cl- and Br-atoms, revealing their electrophilic and nucleophilic sites. Another type of electrophilic–nucleophilic halogen bonding – namely, the halogen···Lewis base (LB) interactions – are described in the crystal structure of C_3HIOS_2, and compared with previously investigated interactions of the same type. Other types of closed-shell interactions involving Hal-atoms, which cannot be clarified as of electrophilic–nucleophilic type, are discussed on the example of Type-I Hal···Hal and Hal···Cπ contacts. All the mentioned interactions are characterized from the structural point of view, from the X-ray multipole-refined electron density and from density functional theory (DFT) calculations on crystal phases and on monomers.

1. Electrostatically favoured halogen bonding interactions

1.1. Type-II Hal···Hal interactions in Hal₃-synthons

Triangular Hal₃-synthons appear as important intermolecular building units used for structure design. Originally, the cooperative effect in Hal₃-synthons, enhancing the strength of the Hal···Hal interaction, was noticed by Desiraju and co-workers in 1998.[160] Shortly after, Mak *et al.* examined the interactions for a series of tris(bromoaryl)triazines and showed how the Br₃ supramolecular synthon could be effectively utilized in the construction of host frameworks.[161] Bosch and Barnes explored the molecular packing in the crystal structure of trihalomesitylenes (Hal = Br, I) and concluded that the donor-acceptor Hal···Hal interactions must be considered as viable driving forces for making synthons to be used in crystal engineering.[162] In a more recent work, Nangia and co-workers have reported that the persistent crystallization of 2,4,6-tris(4-halophenoxy)-1,3,5-triazine host molecules *via* the Hal₃-synthon (Hal = Cl, Br or I) underscores the stability of this cyclic cooperative array for assembling host frameworks.[163]

From the geometries of Hal₃-synthons, it is easily anticipated that the relative positions of electrophilic and nucleophilic sites within these structural motifs are close to those formed in type-II interactions. Thus, a polar δ^+ region of one halogen atom points toward the equatorial δ^- region of an adjacent one in such a way that halogen atoms behave as donor and acceptor. As a result, the bonding picture of Hal₃-synthons is mainly achieved by electrostatics,[89,163] where cooperative contributions add to a gain in stabilization.[164] This has been recently revealed within Cl₃-synthons by performing the experimental electron density analysis of the crystal structure of C₆Cl₆,[83] from which type-II interactions in the Cl₃-synthon were characterized as electrophilic–nucleophilic in nature, involving oppositely polarized regions ($Cl^{\delta+}\cdots Cl^{\delta-}$) in front of each other. As a consequence, the type-II interaction was understood as attractive, corresponding to the Williams model.[90]

1.1.1. Structural characterization of Hal₃-synthons

In Chapter III, we have shown that C₆Cl₆, C₆Br₆, C₆Cl₅OH, and C₆Br₅OH share a significant degree of halogen bonding similarity; in all the cases type-II Hal···Hal interactions form Hal₃-synthons that behave as a structure-assembling motif. For C₆Cl₅OH and C₆Br₅OH, Hal₃-synthons co-exist with single type-II Hal···Hal contacts as a consequence of the substitution of one Hal-atom by the OH-group, avoiding the formation of additional Hal₃-synthons.

From the geometry of the Hal₃-synthon, the structural parameters characterizing the interaction are the intermolecular distances d_i (i = 1, 2, 3), and the geometrical angles, θ_i (i = 1, 2), which are defined around each halogen atom. The Hal···Hal distances are compared to the corresponding sum of the van der Waals radii (Σr_{vdw} (Br) = 3.7 Å, Σr_{vdw} (Cl) = 3.5 Å), which are used to calculate the penetration of the van der Waals spheres in **Table IV.1**:

$$\left(\omega = \frac{d_i}{\sum r_{vdw}(Hal)} 100\% \right)$$

From **Table IV.1** it is seen that bromines have the tendency to approach closer to each other (ω = 98.7 ± 2.9) than chlorines (ω = 100.6 ± 3.4). The geometry of the two closest Cl···Cl contacts (ω =

97.0 and 97.4 %) differs from the other Hal···Hal interactions as they are formed between almost perpendicularly placed molecules. In general, Hal_3-synthons are cyclic and geometrically similar to $(OH)_3$ trimers, a common aggregation motif in the crystal structure of alcohols.[165] The C–Hal···Hal angles (θ_1 and θ_2) are similar in the C_6Br_6, C_6Br_5OH, and C_6Cl_6 crystal structures (**Table IV.1**). Indeed, one interaction is almost linear (on average, θ_1 = 174.1 ± 1.7 °) and the other is oblique (on average, θ_2 = 120.7 ± 3.4 °). According to the geometrical features of these interactions, Hal_3-synthons could be classified as a particular case of type-II ($\theta_1 \approx 90$ °, $\theta_2 \approx 180$ °) Hal···Hal interactions.

Table IV.1 Halogen bonding geometry of Hal_3-synthons in C_6Cl_6, C_6Cl_5OH, C_6Br_6 and C_6Br_5OH along with the single type-II Hal···Hal contacts in C_6Cl_5OH and C_6Br_5OH.

		Interaction	d (Å)	ω (%)	θ_1(°)	θ_2(°)
C_6Cl_6	Cl_3-synt	Cl_1^i···Cl_2^{ii}	3.4466(1)	98.4	116.73(2)	175.03(2)
		Cl_2^{ii}···Cl_3^{iii}	3.4701(1)	99.1	124.17(2)	174.75(2)
		Cl_3^{iii}···Cl_1^i	3.6662(1)	104.7	123.30(1)	171.20(2)
C_6Cl_5OH	Cl_3-synt	Cl_4^i···Cl_2^{ii}	3.4095(1)	97.4	*78.28(2)*	175.10(0)
		Cl_2^{ii}···Cl_3^{iii}	3.6476(2)	104.2	126.45(1)	*110.26(2)*
		Cl_3^{iii}···Cl_4^i	3.6197(2)	103.4	122.14(2)	177.55(2)
	Cl···Cl	Cl_5^i···Cl_1^{iv}	3.3951(1)	97.0	78.09(3)	173.38(2)
		Cl_4^i···Cl_2^{iv}	3.6608(1)	104.6	92.55(5)	126.74(1)
		Cl_5^i···Cl_1^{ii}	3.7095(1)	106.0	93.46(3)	125.49(2)
C_6Br_6	Br_3-synt	Br_1^i···Br_2^{ii}	3.5412(2)	95.7	115.11(1)	174.18(1)
		Br_2^{ii}···Br_3^{iii}	3.5551(4)	96.1	123.83(1)	176.68(1)
		Br_3^{iii}···Br_1^i	3.7761(2)	102.1	122.77(1)	171.20(2)
C_6Br_5OH	Br_3-synt	Br_2^i···Br_3^{ii}	3.5066(2)	94.8	117.33(1)	173.35(1)
		Br_3^{ii}···Br_4^{iii}	3.6576(2)	98.8	122.58(1)	173.04(1)
		Br_4^{iii}···Br_2^i	3.7127(3)	100.3	120.73(1)	175.72(1)
	Br···Br	Br_5^i···Br_5^{iv}	3.6912(1)	99.8	124.54(3)	167.36(2)
		Br_1^i···Br_5^{iii}	3.7901(3)	102.4	119.13(2)	175.40(1)

[a] Distances (d_i, i = 1, 2, 3) and angles ($\theta_1 < \theta_2$,) are depicted in Figure II.2. The ω parameter measures the penetration of the van der Waals spheres ($\omega < 100$ %) or their separation ($\omega > 100$ %). The structural parameters correspond to the multipolar models described in Chapter III. The particular Hal_3-geometry found in C_6Cl_5OH is depicted by θ_1 and θ_2 values in italics. Symmetry codes: C_6Cl_6/C_6Br_6: (i) x, y, z; (ii) 1/2–x, –1/2+y, 1/2–z; (iii) 1–x, –y, –z; C_6Cl_5OH (i) x, y, z; (ii) x, 3–y, –1/2+z; (iii) –x, 3–y, –z; (iv) x, 2–y, –1/2+z; C_6Br_5OH: (i) x, y, z; (ii) 2–x, –1/2+y, 2–z; (iii) 2+x,–1+y, z; (iv) 1–x, y+1/2, 2–z

A special case concerns the three-center Hal_3-contact found in C_6Cl_5OH. Indeed, even if the three short Hal···Hal interactions seem to form a synthon (**Figure III.10**), two of its six structural contact angles (**Table IV.1**) deviated significantly from the expected ones in Hal_3-synthons ($\theta_1 \approx$ 120 ° and $\theta_2 \approx 180$ °), observed for C_6Br_6, C_6Cl_6, and C_6Br_5OH. The ability of C_6Cl_5OH to crystallize in two crystal phases (see section 2.3.2 in Chapter III) is at the origin of the observed differences.

1.1.2. Analysis of the Hal···Hal interaction in Hal$_3$-synthons from the $\rho(\mathbf{r})$ function

Figure IV.1a shows the geometries of two types of synthons with the corresponding BCP's in the intermolecular regions. Type-I interactions are also marked and will be discussed later on. The maps of the gradient of electron density for the two synthons (**Figure IV.1b**) clearly show the atomic basins, the zero-flux surfaces, and the BCP's positions between the atoms in the intermolecular regions.

(a)   (b)
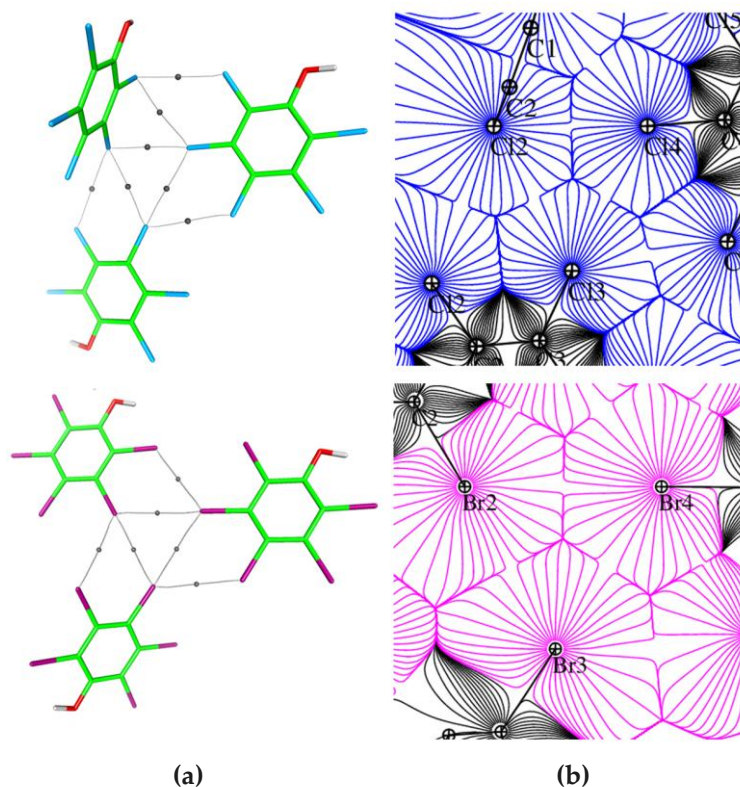
Figure IV.1 Geometrical representation and $\nabla\rho(\mathbf{r})$ map for the two types of synthons in (a) C_6Br_5OH (C_6Cl_6 and C_6Br_6 show a similar arrangement) and (b) C_6Cl_5OH. The BCP's corresponding to type-II Hal···Hal interactions in synthons, along with those of the accompanying type-I Hal···Hal contacts are represented as grey points.

Figure IV.2 shows 3D static deformation density maps plotted in the intermolecular region of Hal$_3$-synthons for the four halogenated compounds. In the case of C_6Cl_6 and C_6Cl_5OH, the $\Delta\rho(\mathbf{r})$ maps show a deficiency of electron density (δ^+) with respect to the spherical non-interacting atoms along the C–Cl bonding axes, behind the halogen atom, and a charge density excess (δ^-) in the planes perpendicular to the bonds around chlorine nuclei (**Figure IV.2a,c**).[83,93] The experimental model of C_6Cl_6 was recently compared with the one calculated against theoretical structure factors issued from periodic DFT calculations, showing a very good matching between them for most of the derived electron properties.[14] The main differences were found in the more contracted theoretical density close to the halogen nuclei. Theoretical calculations exhibit also a more symmetric deformation of the electron density around the chlorine nuclei, while keeping the same relative orientations of δ^- and δ^+ regions.

The $\Delta\rho(\mathbf{r})$ map of C_6Br_6, obtained from periodic theoretical calculations, discloses similar features than those found in the experimental $\Delta\rho(\mathbf{r})$ map of C_6Br_5OH molecule, while both of them exhibit very alike torus-shaped regions of charge accumulation around bromine nuclei (**Figure IV.2b,d**), as previously observed for chlorines in C_6Cl_6 and C_6Cl_5OH. Thereby, both experimental and theoretical $\Delta\rho(\mathbf{r})$ maps provide a good description of the aspherical nature of charge density distribution around bromine and chlorine atoms, clearly bringing out the *polar flattening* effect[79,83] at the intermolecular Hal···Hal regions in all the four compounds, the δ^- and δ^+ regions being situated in a similar way for all of them, as in those observed in chloranil.[142b]
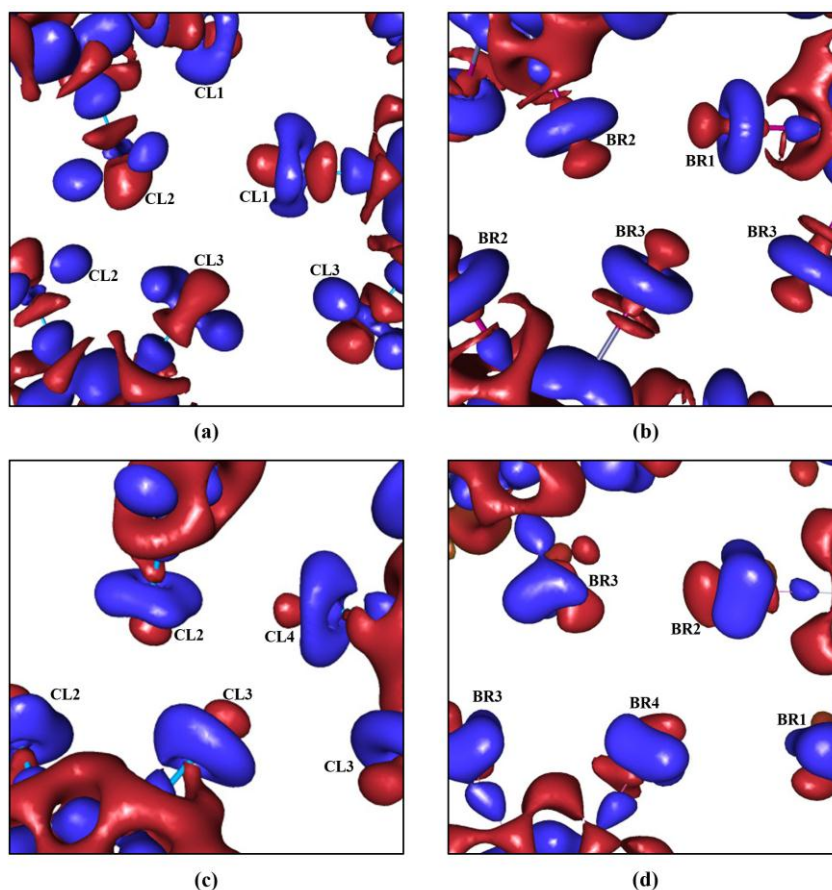
Figure IV.2 Static deformation density maps of the Hal$_3$-synthons in the crystal structures of (a) C_6Cl_6, (b) C_6Br_6 (theoretical calculations), (c) C_6Cl_5OH, and (d) C_6Br_5OH. The iso-surfaces are drawn at ±0.05 e$Å^{-3}$. Positive and negative values are represented in blue and red colors, respectively. For C_6Cl_6, the map corresponding to the theoretical calculations can be found in ref. 14.

From **Figure IV.2**, the four $\Delta\rho(\mathbf{r})$ maps representing the Hal$_3$-synthons, are qualitatively similar and specifically show that electron excess and electron deficient regions face each other along the three synthon edges, suggesting directional δ^- ··· δ^+ interactions. Despite the observed geometrical differences for the two types of synthons, these similarities allow us to discuss them together in a common framework of charge density analysis.

Table IV.2 Topological characteristics for each pairwise intermolecular interaction belonging to the Hal$_3$-synthons in C$_6$Cl$_6$, C$_6$Cl$_5$OH, C$_6$Br$_6$ and C$_6$Br$_5$OH along with the single type-II Hal···Hal contacts in C$_6$Cl$_5$OH and C$_6$Br$_5$OH.[a]

		Interaction	d (Å)	ρ	$\nabla^2\rho$	λ_1	λ_2	λ_3	G	V	E_{int}	$|V|/G$	H/ρ	ΔL	$\Delta(L/\rho)$
C$_6$Cl$_6$ [b]	Cl$_3$-synt	Cl$_1^i$···Cl$_2^{ii}$	3.4466(1)	0.049	0.63	−0.09	−0.08	0.79	13.3	−9.7	−4.9	0.73	496	11.4	5.6
				0.045	0.59	−0.10	−0.10	0.78	12.5	−8.9	−4.5	0.71	540	11.7	5.2
		Cl$_2^{ii}$···Cl$_3^{iii}$	3.4701(1)	0.057	0.57	−0.15	−0.14	0.87	12.8	−10.4	−5.2	0.82	284	10.3	4.5
				0.041	0.56	−0.09	−0.09	0.74	11.7	−8.1	−4.1	0.69	593	10.8	5.6
		Cl$_3^{iii}$···Cl$_1^i$	3.6662(1)	0.038	0.41	−0.09	−0.09	0.59	8.8	−6.4	−3.2	0.73	426	9.7	3.8
				0.028	0.38	−0.05	−0.05	0.48	7.7	−5.1	−2.6	0.66	627	10.7	5.4
C$_6$Cl$_5$OH	Cl$_3$-synt	Cl$_4^i$···Cl$_2^{ii}$	3.4095(1)	0.058	0.60	−0.13	−0.11	0.84	13.6	−10.9	−5.5	0.80	314	12.5	5.3
		Cl$_2^{ii}$···Cl$_3^{iii}$	3.6476(2)	0.039	0.47	−0.10	−0.09	0.66	10.0	−7.1	−3.6	0.71	502	11.3	5.0
		Cl$_3^{iii}$···Cl$_4^i$	3.6197(2)	0.039	0.41	−0.10	−0.08	0.59	8.8	−6.5	−3.3	0.74	398	10.7	4.4
	Cl···Cl	Cl$_5^i$···Cl$_1^{iv}$	3.3951(1)	0.062	0.67	−0.14	−0.12	0.93	15.2	−12.1	−6.0	0.80	337	12.8	5.6
		Cl$_4^i$···Cl$_2^{iv}$	3.6608(1)	0.038	0.46	−0.08	−0.08	0.63	9.7	−6.9	3.5	0.71	497	11.5	5.0
		Cl$_5^i$···Cl$_1^{ii}$	3.7095(1)	0.033	0.42	−0.07	−0.06	0.55	8.7	−5.9	3.0	0.68	573	9.3	4.1
C$_6$Br$_6$ [c]	Br$_3$-synt	Br$_1^i$···Br$_2^{ii}$	3.5412(2)	0.066	0.62	−0.15	−0.15	0.92	14.7	−12.5	−6.3	0.85	225	3.0	4.8
		Br$_2^{ii}$···Br$_3^{iii}$	3.5551(4)	0.064	0.61	−0.14	−0.14	0.89	14.3	−12.0	−6.0	0.84	243	2.9	4.8
		Br$_3^{iii}$···Br$_1^i$	3.7761(2)	0.042	0.41	−0.09	−0.09	0.59	9.1	−6.9	−3.5	0.76	353	2.8	4.6
C$_6$Br$_5$OH	Br$_3$-synt	Br$_2^i$···Br$_3^{ii}$	3.5066(2)	0.063	0.66	−0.15	−0.12	0.93	14.8	−12.4	−6.2	0.84	257	6.8	10.9
		Br$_3^{ii}$···Br$_4^{iii}$	3.6576(2)	0.051	0.53	−0.10	−0.10	0.73	11.7	−9.2	−4.6	0.79	331	6.5	8.5
		Br$_4^{iii}$···Br$_2^i$	3.7127(3)	0.047	0.47	−0.09	−0.09	0.65	10.5	−8.1	−4.1	0.77	345	5.2	6.9
	Br···Br	Br$_5^i$···Br$_5^{iv}$	3.6908(1)	0.051	0.54	−0.12	−0.11	0.76	11.9	−9.2	−4.6	0.77	364	6.3	8.1
		Br$_1^i$···Br$_5^{iii}$	3.7896(3)	0.041	0.43	−0.08	−0.07	0.58	9.3	−6.9	−3.5	0.74	395	4.9	6.7

[a] The parameters ρ (eÅ^{-3}), $\nabla^2\rho$ (eÅ^{-5}), λ_i (eÅ^{-5}), G and V (kJ mol^{-1} bohr^{-3}) are calculated at the BCP's of $\rho(\mathbf{r})$; H/ρ is in kJ mol^{-1}e^{-1}; $H = V + G$; ΔL (eÅ^{-5}) and $\Delta(L/\rho)$ (Å^{-2}) parameters are calculated as the difference between the values observed at the CD and CC sites of the interacting atoms. E_{int} (kJ mol^{-1}) values are estimated as $1/2V$, the constant being in bohr^3 units. See Table IV.1 for symmetry codes. [b] First and second lines correspond to experimental and theoretical (VASP calculations)[14] data. [c] Values are from theoretical (VASP calculations) data.

To characterize the type-II Hal···Hal interactions, we focus on the local properties of $\rho(\mathbf{r})$ at BCP's of the four given compounds obtained from both experimental and theoretical (the case of C_6Br_6) modeling (see Chapter I for their detailed description).

According to these properties (**Table IV.2**), all the mentioned Hal···Hal contacts exhibit typical features of *pure* closed-shell interactions: the values of ρ are relatively low (0.038 < ρ < 0.062 eÅ^{-3} for Cl···Cl; 0.042 < ρ < 0.066 eÅ^{-3} for Br···Br) and these of $\nabla^2\rho$ are positive and low (0.41 < $\nabla^2\rho$ < 0.67 eÅ^{-5} for Cl···Cl; 0.41 < $\nabla^2\rho$ < 0.66 eÅ^{-5} for Br···Br), both being typical of weak hydrogen bonds.[34c] Furthermore, the magnitudes of the kinetic energy density are greater than those of the potential energy density, leading to $|V|/G < 1$ and $H > 0$, therefore illustrating that these mainly electrostatic ($\delta^+\cdots\delta^-$) interactions are very weak.[165,34c] The phenomenological correlation between the interaction energy and the potential energy density at BCP's[34a] $E_{int} \approx (1/2)V^{CP}$ has been used as an estimation of the interaction energy in the experimental analysis of $\rho(\mathbf{r})$ for *pure* closed-shell type halogen bonded systems (see Chapter III for details).[89,92,95] Following this estimation, E_{int} has been evaluated for each type-II Hal···Hal interaction within and outside a synthon (**Table IV.2**), the average value being of 4.3 ± 1.1 kJ mol^{-1} for Cl···Cl and of 4.9 ± 1.2 kJ mol^{-1} for Br···Br (r.m.s. deviations are given to report statistical dispersion in the values). It is noteworthy that, at similar distances, the estimated E_{int} values for Cl···Cl interactions are very close to those recently reported for Cl···Cl type-II (4.8 kJ mol^{-1}) intermolecular contacts.[89]

Comparing the estimated E_{int} values for Cl···Cl and Br···Br interactions, the later was found to be 14 % more intense than the former. This observed tendency is in accordance with crystallographic and theoretical studies of Awwadi *et al.*,[101] showing that the strength of these contacts decreases in the order I···I > Br···Br > Cl···Cl. The calculated $|V|/G$ magnitudes (**Table IV.2**) also follow a similar trend, being on average 0.76 ± 0.04 and 0.81 ± 0.04 for Cl···Cl and Br···Br and showing 6 % difference.

1.1.3. Qualitative analysis of Hal-atoms in gas phase monomers from the *L*(**r**) function

Figure IV.3 shows a typical distribution of the $L(\mathbf{r})$ function, which is defined as the negative Laplacian of the electron density $-\nabla^2\rho(\mathbf{r})$, around Cl- and Br-atoms in C_6Cl_6, C_6Br_6, and $BrCH_2N(CH_3)_2$ optimized monomers from MP2 calculations. They also show the anisotropic nature of the charge distribution around halogen nuclei with charge concentration (CC) and charge depletion (CD) sites respectively located in δ^- and δ^+ regions, as experimentally shown in solid chlorine,[88a] chlorinefluoride,[88b] and hexachlorobenzene.[83] It should be noted that, experimental and both periodic and gas phase calculations performed for the halogenated compounds show a complex $L(\mathbf{r})$ topology, exhibiting a large number of cp's around the halogen nuclei. For the purpose of the present work, we focus only on those associated to the CC and CD sites in the valence shell of halogen atoms as they contain the main information needed for the analysis of the intermolecular interactions building the synthons.

For chlorine, both CC and CD sites, which correspond respectively to (3,–3) and (3,+1) CPs of the $L(\mathbf{r})$ function, belong to the *Valence Shell Charge Concentration* (VSCC) region of the atom. As a consequence, positive values of $L(\mathbf{r})$ exhibit for both of these regions (**Figure IV.3a**).
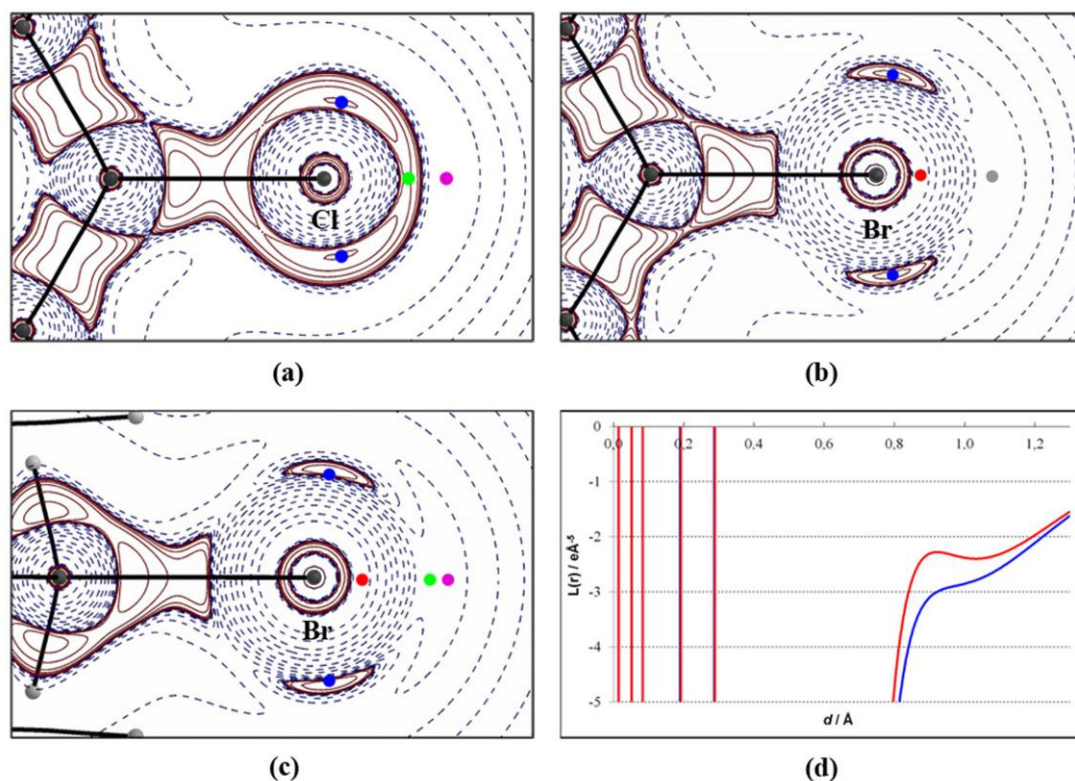
Figure IV.3 Contour maps of $L(r)$ around a Cl-atom in (a) C_6Cl_6 and around Br-atoms in (b) C_6Br_6 and (c) $BrCH_2N(CH_3)_2$, all of them obtained from MP2 calculations on optimized gas phase monomers. $L(r)$ contours ($e\text{Å}^{-5}$) are in logarithmic scale, red – positive, blue – negative. In the outer electron shell, CC sites are characterized by local maxima of $L(r)$ ((3,–3) CPs marked in yellow); the CD sites along the C–Hal bonding axis direction are characterized by either a couple of (3,+1) and (3,+3) CPs marked respectively in pink and violet (case of a and c) or a plateau with its characteristic site marked in gray (case of b). The minimum along the bonding axis direction ((3,–1) CP) of the closest inward shell is in green. (d) Plots of $L(r)$ along the C–Br bonding direction for C_6Br_6 (blue curve) and for $BrCH_2N(CH_3)_2$ (red curve). The inner electron shells of the Br-atom in both compounds almost exactly match, whereas in the outer region the existence of (3,+1) and (3, +3) CPs in the case of $BrCH_2N(CH_3)_2$, and their absence in the case of C_6Br_6, is observed.

This is not the case for bromine, for which the VSCC region is much more reduced, representing a 3D belt of negative Laplacian in the outer electron shell of the atom. Accordingly, only CC (3, –3) sites belong to the VSCC, while the CD site is found in the very extended $L(\mathbf{r}) < 0$ region, expanding from very close distances to the Br nucleus (**Figure IV.3b,c**). This is due to the overlap of charge depleted regions belonging to the outer electron shell and the closest inward one, which is characterized by a saddle point (i.e., a (3,–1) CP marked in green in **Figure IV.3b,c**) for the $L(\mathbf{r})$ function. The L magnitudes observed for Br atoms at these (3,–1) CPs are negatively pronounced and very close to each other ($-1836.9 < L < -1831.8 \ e\text{Å}^{-5}$) for the independent Br-atoms in C_6Br_6 and C_6Br_5OH. In all cases, the (3,–1) CP is placed at 0.35 Å from the bromine nucleus. These extremely similar features observed for all the bromine atoms analyzed in this work confirm that this (3,–1) CP belongs to a core electron shell that, in the multipolar modeling of $\rho(\mathbf{r})$, is similarly defined for all of them and considered to remain unperturbed. As a

consequence, the topological characteristics at the (3,–1) site can not be used to compare the particular electrophilic power of the CD region of bromines within different environments.

Compared to chlorine atoms, the important development of a very extended and significantly depleted electron density region in bromines is straightforwardly associated to the increasing intensity of the so-called *σ-hole*, firstly pointed out for heavier halogens.[77c,e] Indeed, this highly specific electron distribution is the primary origin of the well-known electrophilic region along the C–Hal bonding axis direction, which increases from lighter to heavier halogens and is chemically represented by the increase of both the *σ-hole* and its concomitant positive electrostatic potential ($\varphi_{CD} > 0$). Accordingly, the more depleted is $\rho(\mathbf{r})$ in that region, the more important are the *σ-hole* and the magnitude of $\varphi_{CD} > 0$.

Depending on the activation of the bromine atom by the neighboring chemical groups, its outer electron shell at the CD site is characterized by the presence of either a couple of successive (3,+1) and (3,+3) CPs or by a plateau, i.e. an area where the variation of $L(\mathbf{r})$ is locally the smallest but its gradient does not vanish. For example, **Figure IV.3c and d** display the $L(\mathbf{r})$ function in the case of the $BrCH_2N(CH_3)_2$ molecule: in this particular compound, the bromine atom is negatively charged due to the presence of the $-N(CH_3)_2$ electron donating group ($q_{Br} = -0.27e$) and the two CPs associated with the CD site exist. In the case of C_6Br_6 (**Figure IV.3b,d**), where the bromine atom is slightly positively charged ($q_{Br} = +0.03e$), these two CPs are coalesced, resulting in an area of soft variation of $L(\mathbf{r})$ without a presence of a true CP. In this last case, the location of the characteristic CD site in the plateau is determined by means of the derivative of the $L(\mathbf{r})$ function.

1.1.4. Quantitative analysis of the Hal···Hal from the $L(\mathbf{r})$ function

Passing from the isolated molecules to the crystal phase, **Figure IV.4** shows the maps of the negative Laplacian functions in the planes of the four synthons. They also show the anisotropic nature of the charge distribution around halogen nuclei. For Cl atoms, the charge concentration (CC) and charge depletion (CD) sites are respectively located in δ^- and δ^+ regions and correspond to nucleophilic and electrophilic sites around the halogen nuclei. From their relative positions within the four discussed synthons, CC and CD regions face to each other along the three directions of this structural motif, indicating attractive and directional electrophilic–nucleophilic (CD···CC) interactions.

As explained in **Chapter III**, different electron shells are involved in the outer electron distribution of Br- and Cl-atoms, leading to a more important screening of the outer electrons in bromines that significantly deplete their charge distribution. As a consequence, bromines reduce their VSCC region with respect to chlorines, inducing the concomitant decrease of L_{CC} magnitudes and therefore $L_{CC}(Br) < L_{CC}(Cl)$. The increased screening also depletes the electron distribution in the CD region of the bromines outer shell, leading to negative $L_{CD}(Br)$ values, in contrast to the positive ones observed for chlorines, and therefore to $L_{CD}(Br) < L_{CD}(Cl)$. As a result, $\Delta L(Br) < \Delta L(Cl)$ is systematically observed. Though, the ΔL parameter does not permit a straightforward comparison of the intermolecular interaction between different halogens.

On the other hand, applying the L/ρ criterion, the calculated difference $\Delta(L/\rho) = (L/\rho)_{CD} - (L/\rho)_{CC}$ for the three experimentally determined structures C_6Cl_6, C_6Cl_5OH, and C_6Br_5OH indicates the expected increase in intensity from Cl···Cl to Br···Br type-II interactions (**Table IV.2**).
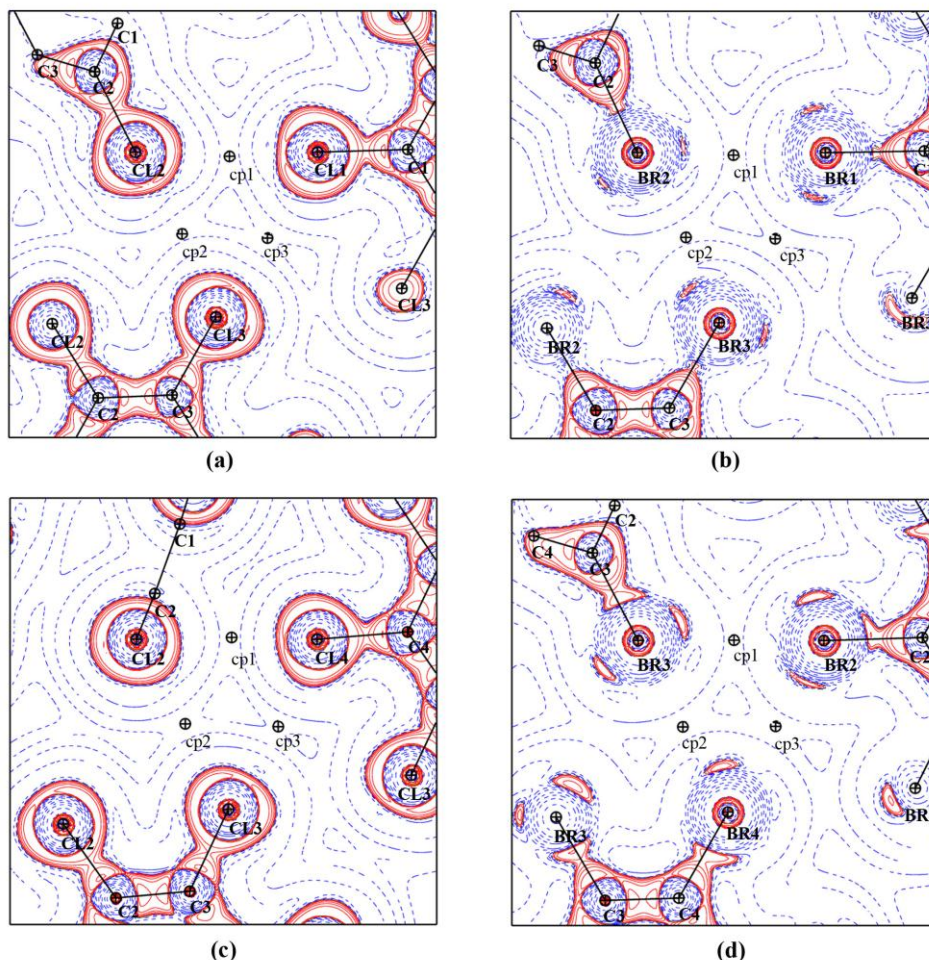
Figure IV.4 $L(\mathbf{r}) = -\nabla^2\rho(\mathbf{r})$ maps with the observed (3,–1) intermolecular bond critical points (cp) of $\rho(\mathbf{r})$ drawn in the plane of the Hal$_3$-synthon for (a) C_6Cl_6, (b) C_6Br_6 (theoretical calculations), (c) C_6Cl_5OH, (d) C_6Br_5OH. $\nabla^2\rho(\mathbf{r})$ contours (eÅ^{-5}) are in logarithmic scale. Red and blue contours denote positive and negative values, respectively. For C_6Cl_6, the map corresponding to theoretical calculations can be found in ref. 14.

In contrast, results coming from C_6Br_6 theoretical calculations show some differences. Indeed, while improving their ranking from ΔL to $\Delta(L/\rho)$ classifications, they do not reach values similar to the ones observed in C_6Br_5OH, as expected from the comparison between C_6Cl_6 and C_6Cl_5OH, where $\Delta(L/\rho)$ values are very close to each other ($<\Delta(L/\rho)> = 4.7 \pm 0.6$ Å^{-2}).

To reveal the origin of the observed difference between bromines in the experimental and theoretical crystal phases, theoretical calculations of the isolated molecules C_6Br_6 and C_6Br_5OH were performed. According to these calculations, the topological properties at CC and CD sites are extremely similar in both molecules, $\Delta(L/\rho)$ being 6.85 Å^{-2} for C_6Br_6 and on average 6.72 $\pm$ 0.02 Å^{-2} for C_6Br_5OH.

With respect to gas phase calculations, the topological values obtained for the corresponding crystal phases show lower magnitudes in the case of C_6Br_6 periodic theoretical calculations ($<\Delta(L/\rho)> = 4.74 \pm 0.11$ Å^{-2}) and greater magnitudes for the experimental C_6Br_5OH model

$(<\Delta(L/\rho)> = 8.77 \pm 2.00$ Å^{-2}). Thus, the case of C$_6$Br$_6$ repeats the same trend observed in the comparison of the gas and crystal phases of the Cl-containing compounds, for which the $<\Delta(L/\rho)>$ values are 6.87 and 4.62 ± 0.88 Å^{-2} (C$_6$Cl$_6$), and 6.68 and 4.87 ± 0.44 Å^{-2} (C$_6$Cl$_5$OH), for theoretical gas phase and experimental models, respectively (see **Table IV.2** and **Table IV.3**). Moreover, gas phase calculations earlier performed by different authors on other brominated molecules,[32,87,166] also present more pronounced CC regions around Br-nuclei than in the case of the theoretical crystal phase of C$_6$Br$_6$. On the other hand, experimental and theoretical multipolar models in crystal phase are expected to give similar results, as observed in the comparison of the $<\Delta(L/\rho)>$ values coming from the experimental and periodic theoretical data of C$_6$Cl$_6$,[14] which are found similar (4.62 ± 0.88 and 5.40 ± 0.22 Å^{-2}, respectively) even if the theoretical model exhibits slightly larger magnitudes. Overall, in spite of the high $<\Delta(L/\rho)>$C$_6$Br$_5$OH value that also shows a high statistical dispersion, $<\Delta(L/\rho)>$ decreases in most cases from gas to crystal phases. In addition to the intrinsic differences between the models used in gas and crystal phases (LCAO and multipolar) and to the effect of the basis used in the calculations, the pointed decrease of $<\Delta(L/\rho)>$ could be also brought closer to the screening of the electrophilic – nucleophilic interactions induced by the dielectric constant of the crystal environment.

Table IV.3 Calculated magnitudes $\Delta(L/\rho) = (L/\rho)_{CD} - (L/\rho)_{CC}$ (in Å^{-2}) for Hal···Hal interactions in C$_6$Cl$_6$, C$_6$Cl$_5$OH, C$_6$Br$_6$ and C$_6$Br$_5$OH, obtained from theoretical calculations performed for the optimized monomers in gas phase. Average values $< \Delta(L/\rho)>$ are given for C$_6$Cl$_5$OH and C$_6$Br$_5$OH.

	C$_6$Cl$_6$	C$_6$Cl$_5$OH	C$_6$Br$_6$	C$_6$Br$_5$OH
$\Delta(L/\rho)$	6.87	6.66	6.85	6.71
		6.67		6.72
		6.70		6.74
$< \Delta(L/\rho)>$	6.87	6.68	6.85	6.72

In summary, comparing Br- to Cl-atoms, $(L/\rho)_{CD}$ in the former exhibits a significant decrease from positive to negative values that overcomes the decrease of its positive $(L/\rho)_{CC}$ values, leading to a $\Delta(L/\rho)$ magnitude, and therefore to an electrostatic interaction, which is in general greater (in some cases is found comparable) than that found for chlorine atoms in type-II Hal···Hal interactions (see **Table IV.2**).

1.1.5. Cl$_3$- and Br$_3$-synthons from topological and energetic criteria

Considering the Hal$_3$-motif as a structure-determining unit, we characterize it as the addition of three Hal···Hal contributions. Thus, according to the topological properties calculated at the CPs of the $\rho(\mathbf{r})$ function (ρ_Σ, $\nabla^2\rho_\Sigma$, G_Σ, V_Σ, and $<|V|/G>$, see **Table IV.4**), all of them increase in magnitude from Cl$_3$- to Br$_3$-synthons indicating that Hal$_3$-synthons built with bromine atoms are stronger than those with chlorines. In addition to each Hal···Hal contact, the Hal$_3$-synthons can be also considered as pure closed-shell interactions ($<|V|/G> < 1$). Therefore, the interaction energy $E_{int,\Sigma}$ of the structure-determining unit has been calculated from the estimation:

$$E_{int\Sigma} \approx \frac{1}{2}\sum V^{BCP}$$

paralleling that used for interactions of *pure* closed-shell type.[89,92,95,144] However, it should be noted that $E_{int,\Sigma}$ is an approximation to E_{int} of the trimer, because other interactions that involve the latter and are external to the synthon can contribute to E_{int}. At the same time, it should be also kept in mind that $\rho(\mathbf{r})$ within the synthon reflects the influence of its environment. Accordingly, the $\rho(\mathbf{r})$ properties used to derive $E_{int,\Sigma}$ follow this effect, bringing closer the Hal$_3$-synthon contribution to E_{int} than the additional of three independent Hal⋯Hal interactions at the distances found in trimer. Thereby, applying the estimation, the interaction energy $E_{int,\Sigma}$ of Cl$_3$-synthons is on average 17 % lower than that of Br$_3$-synthons. Moreover, comparing C$_6$Cl$_6$ to C$_6$Cl$_5$OH, and C$_6$Br$_6$ to C$_6$Br$_5$OH, the crystal structures not involving hydrogen bonding interactions, exhibit Hal$_3$-synthons that are only slightly stronger (8 and 5) % than those involving hydrogen bonds.

Table IV.4 Topological characteristics of the Hal$_3$-synthon in each of the four compounds. [a]

Synthon	ρ_Σ	$\nabla^2\rho_\Sigma$	G_Σ	V_Σ	$<|V|/G>$	$|E_{int,\Sigma}|$	$\Delta(L/\rho)_\Sigma$
C$_6$Cl$_6$ [b]	0.144	1.60	34.9	−26.5	0.76	13.3	13.9
	0.143	1.59	34.7	−26.3	0.76	13.2	16.2
C$_6$Br$_6$ [c]	0.172	1.64	38.1	−31.4	0.82	15.7	14.2
C$_6$Cl$_5$OH	0.136	1.48	32.4	−24.5	0.76	12.3	14.6
C$_6$Br$_5$OH	0.161	1.66	37.0	−29.7	0.80	14.9	26.3

[a] The parameters ρ_Σ (eÅ^{-3}), $\nabla^2\rho_\Sigma$ (eÅ^{-5}), G_Σ, V_Σ (kJ mol^{-1} bohr^{-3}), $|E_{int,\Sigma}|$(kJ mol^{-1}) and $\Delta(L/\rho)_\Sigma$ (Å^{-2}) are calculated as the sum over the three pairwise interactions building the synthon, while $<|V|/G>$ is taken as an average of the three corresponding parameters at CP. [b] First and second lines correspond to experimental and theoretical (VASP calculations)[14] data. [c] Values are from theoretical data.

On the basis of the last considerations and on the definition of the L/ρ descriptor, the $\Delta(L/\rho)_\Sigma$ parameter measures the electrophilic–nucleophilic interaction that takes part in the Hal$_3$-synthon, being mainly assumed electrostatic. Accordingly, the strength of this contribution is on average ~30 % stronger in Br$_3$-synthons (C$_6$Br$_6$ and C$_6$Br$_5$OH) than in Cl$_3$-synthons (C$_6$Cl$_6$ and C$_6$Cl$_5$OH).

1.2. Halogen⋯Lewis Base interactions

An intermolecular interaction of type Hal⋯LB (LB = Lewis Base) is observed in the crystal structure of iododithiolone (C$_3$HIOS$_2$) between the atoms of iodine and oxygen (d(I⋯O)= 2.9312(1) Å, θ_1(C–I⋯O) = 170.38(1)°, θ_2(I⋯O–C) = 135.37(2)°). Together with the hydrogen bonding O⋯H, it is responsible for the formation of chains along *c*-direction.

1.2.1. Analysis of Hal⋯LB interaction from the $\rho(\mathbf{r})$ function

Charge density analysis discloses evidences of the I⋯O interaction: the bond path and the corresponding intermolecular BCP of type (3,–1) at the interatomic surface (**Figure IV.5**).

The 3D static deformation density map $\Delta\rho(\mathbf{r})$ (experimental and theoretical) plotted in the I⋯O intermolecular space (**Figure IV.6a**) clearly shows the aspherical distribution of the electron

density around the I-atom with δ^+ and δ^- regions perpendicularly placed to each other (similarly to the previously described Cl- and Br-atoms). The I···O interaction is formed by putting face-to-face the δ^+-region of I and the δ^--region of O. It is remarkable, that the electrophilic region (δ^+) of the I-atom is shifted from the C–I bond direction and turned towards the O-atom (in accordance with the bond geometry, which slightly deviates from linearity θ_1 = 170.38(1) °). Qualitatively similar observation can be made from the experimental model, plotted in the intermolecular I···O space.

The electron density and its Laplacian were analyzed by applying the QTAIM methodology. The topological characteristics at the BCP of the I···O interaction obtained from experimental and theoretical modeling are reported in **Table IV.5**, along with the corresponding properties of other experimentally studied Hal···LB interactions available from the literature. These properties vary in a large range of values (e.g. $0.032 < \rho < 0.201$ eÅ^{-3}, $0.45 < \nabla^2\rho < 2.08$ eÅ^{-5}), indicating their similarity with Type-II Hal···Hal interactions at the lower limit and coming closer to interactions of partial covalent character at the upper limit. The latter case is also evidenced from the $|V|/G$ and H/ρ parameters – the first one exceeds unity, while the second becomes negative – indicating the prevalence of the potential energy density.

| (a) | (b) |
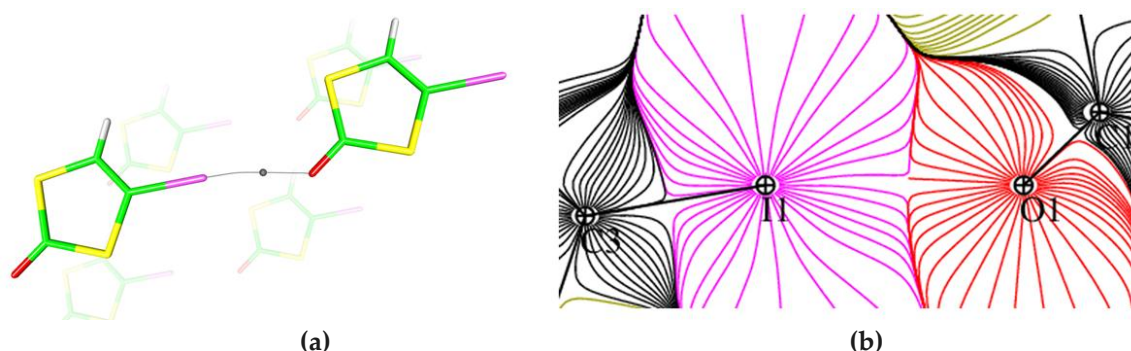
Figure IV.5 (a) Intermolecular halogen bonding interaction (I···O) in the crystal structure of C$_3$HIOS$_2$ with the corresponding bond path and BCP. (b) $\nabla\rho(\mathbf{r})$ map for the same interaction displaying the existence of the BCP by the zero value of $\nabla\rho(\mathbf{r})$.

Though, depending on the involved Lewis base and Hal-atom, the character of the Hal···LB interaction varies from a *pure* closed shell to a *transit* interaction that presents a partial covalence degree. The latter seems more possible when the I-atom is involved as an electron density acceptor and depends on the Lewis base activation and interaction geometry. Indeed, from the collected experimental data (**Table IV.5**), the interaction strength decreases for the less linear interactions.

Comparing the I···O interactions in the crystal structures of C$_3$HIOS$_2$ and in the halogen bonded complex characterized earlier (bpNO·F$_4$dIb)[92b] we observe the decreased covalent character for the first interaction. These differences are supported by the E_{int} values – 14.6 kJ mol^{-1} (averaged over experimental and theoretical values) *vs* 30.8 kJ mol^{-1} – and can be due to the different activation of the interacting atoms in the two systems.

Table IV.5 Topological characteristics of the I···O interaction in the crystal structure of C_3HIOS_2 compared with the experimental results for the Hal···LB interactions available in the literature. [a]

Interaction	d	ω	θ_1	ρ	$\nabla^2\rho$	λ_1	λ_2	λ_3	G	V	E_{int}	$|V|/G$	H/ρ	$\Delta L/\rho$	ref
$I^{ii}···O^{i}$ [b]	2.9309(1)	83.7	170.38(1)	0.099	1.30	−0.24	−0.19	1.73	30.2	−25.1	−12.6	0.83	348	33.8	C_3HIOS_2
				0.117	1.38	−0.34	−0.29	2.01	33.8	−29.9	−15.0	0.84	225	32.6	
$CI···N_{ar}$	2.7804(8)	78.8	179.3	0.236	1.96	−0.68	−0.66	3.30	63.8	−74.3	−37.2	1.16	−300		92a
$CI···O=N$	2.7253(10)	77.9	—	0.201	2.04	−0.61	−0.57	3.22	58.8	−61.5	−30.8	1.05	−91		92b
$CBr···N_{ar}$	2.8219(6)	83.0	179.2	0.183	2.08	—	—	—	56.4	−56.0	−28.0	0.99	15		92c
$CBr···N_{ar}$	2.8800(9)	84.7	177.2	0.156	1.86	—	—	—	47.9	−45.5	−22.8	0.95	104		92c
$CBr···N_{ar}$	2.9785(9)	87.6	176.3	0.123	1.47	—	—	—	36.2	−32.3	−16.2	0.89	214		92c
$CCl···O=N$	3.0774(7)	94.1	158.1	0.063	0.85	−0.16	−0.15	1.16	18.5	−13.9	−7.0	0.75	493		93
$CCl···O=C$	3.0562(3)	93.5	164.7	0.054	0.80	—	—	—	16.2	−10.8	−5.4	0.67	675		94
$CCl···O=N$	3.4186(8)	104.5	145.0	0.032	0.45	−0.08	−0.08	0.61	9.2	−6.1	−3.05	0.66	654		93

[a] The parameters ρ (eÅ⁻³), $\nabla^2\rho$ (eÅ⁻⁵), λ_i (eÅ⁻⁵), G and V (kJ mol⁻¹ bohr⁻³) are calculated at the BCP's of $\rho(\mathbf{r})$; H/ρ is in kJ mol⁻¹e⁻¹ ($H = V + G$); $\Delta(L/\rho)$ (Å⁻²) is calculated as the difference between the values observed at the CD and CC sites of the interacting atoms. E_{int} (kJ mol⁻¹) values are estimated as $1/2V$, the constant being in bohr³ units; structural parameters d (Å), ω (%) and θ_1 (°) are performed for each contact. [b] First and second lines for C_3HIOS_2 correspond to experimental and theoretical (VASP calculations) data. Symmetry codes: C_3HIOS_2 (i) x, y, z; (ii) 1+x, 1+y, 1+z.

(a)   **(b)**
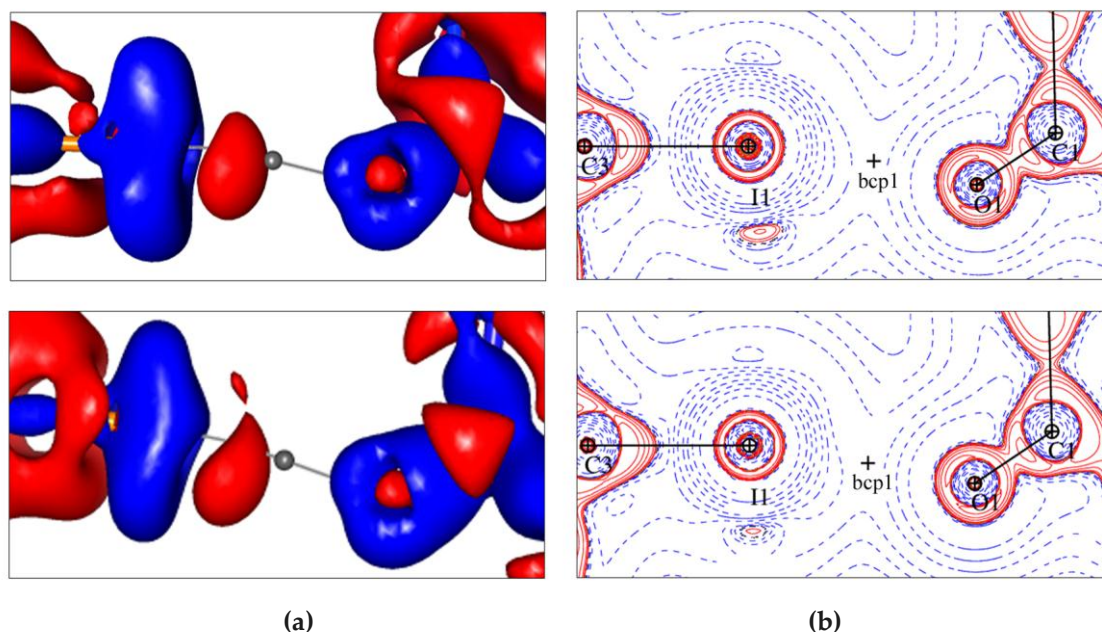
Figure IV.6 Experimental (top) and theoretical (bottom) maps in the intermolecular region of the I···O interaction in C_3HIOS_2. (a) 3D static deformation density maps, iso-surface at ±0.05 e$Å^{-3}$, blue – positive, red – negative; (b) $L(\mathbf{r})$ maps, contours (e$Å^{-5}$) are in logarithmic scale, red – positive, blue – negative.

1.2.2.   Analysis of Hal···LB interaction from the $L(r)$ function

Figure IV.6b shows the experimental and theoretical $L(\mathbf{r})$ maps plotted in the intermolecular I···O region. The aspherical nature of the I-atom is evident from the shape of the $L(\mathbf{r})$ contours. The relative location of CC and CD sites is close to the one observed for Br-atoms obtained either experimentally or theoretically: CC sites belong to the VSCC region ($L(\mathbf{r}) > 0$), while the CD site corresponds to the VSCD region ($L(\mathbf{r}) < 0$). Qualitatively similar features were observed on Laplacian maps of the I-atom in previous experimental works.[92a,b]

With the aim to perform a quantitative evaluation of the electrophilic and nucleophilic power of CD and CC sites and to estimate the electrostatic CD···CC interaction, hereafter we check the criterion, introduced in Chapter III, namely $\Delta(L/\rho)$. For experimental and theoretical calculations we obtain the following magnitudes of these parameters in the interacting sites: L/ρ_{CC1} (O) = 19.68/19.13 $Å^{-2}$ and L/ρ_{CD} (I) = –14.12/–13.51 $Å^{-2}$, resulting in $\Delta(L/\rho)$ = 33.8/32.6 $Å^{-2}$. These results show an increase of the electrophilic power of the Hal-atom going down the group (Cl, Br, I), albeit the differences in the considered systems. The total interaction energy of the I···O interaction is comparable to the one calculated for Hal_3-synthons (**Table IV.4**).

2. Other closed-shell interactions involving Hal-atoms

While the Hal_3-synthon behaves as a main structural unit in the crystal structures of C_6Hal_6 and C_6Hal_5OH, other interactions involving Hal-atoms provide packing efficiency. Thus, intercolumn Type-I Hal···Hal interactions are the satellites of the synthon arrangement, while intracolumn Hal···Hal of Type I, Hal···C, and C···C contacts allow for connectivity between adjacent stacking molecules along the b-axis direction (see structures descriptions in **Chapter III**).

2.1. Type-I Hal···Hal interactions

2.1.1. Structural characterization

In the crystal structures of C_6Hal_6 and C_6Hal_5OH one halogen atom forms up to seven intermolecular contacts with the surrounding atoms (Hal, C, O). The number of Hal···Hal interactions of Type-I in each of the four discussed structures is almost twice greater than these of Type-II. Similarly to Type-II, we characterize the Type-I Hal···Hal interactions by the intermolecular distances d, the corresponding penetration parameter ω and the geometrical angles, θ_1 and θ_2 ($\theta_1 \leq \theta_2$), which are defined around each halogen atom (Table IV.6).

Almost all the interactions exceed the sum of the van der Waals radii, however, it can be noticed that, in general, bromines are able to approach closer to each other than chlorines, similarly to Type-II interactions. This can be demonstrated by the Type-I Hal···Hal contacts in iso-structural C_6Br_6 and C_6Cl_6 compounds, for which $\omega_{Br···Br} = 104.3 \pm 2.5$ % and $\omega_{Cl···Cl} = 106.8 \pm 3.0$ %. The shortest contact for chlorines ($Cl_5···Cl_5$, $\omega = 98.1$ %) corresponds to an almost linear geometry ($\theta_1 = \theta_2 = 163.24(1)$).

Table IV.6 Structural characteristics of Type-I Hal···Hal interactions in C_6Cl_6, C_6Cl_5OH, C_6Br_6 and C_6Br_5OH. [a]

	Interaction [b]	d	ω	θ_1	θ_2
C_6Cl_6	*Cl_1^i···Cl_1^{iv}	3.8221(2)	109.2	107.40(1)	131.65(2)
	*Cl_2^i···Cl_2^v	3.6238(2)	103.5	119.34(1)	126.32(4)
	*Cl_3^i···Cl_3^{vi}	3.6355(2)	103.9	124.61(1)	124.63(1)
	*Cl_3^i···Cl_1^{vii}	3.9026(1)	111.5	99.07(1)	129.10(1)
	*Cl_3^i···Cl_3^{viii}	3.6531(2)	104.4	104.31(1)	104.33(1)
	**Cl_2^i···Cl_2^{ix}	3.7626(2)	107.5	84.34(1)	95.66(1)
	**Cl_3^i···Cl_3^{ix}	3.7626(2)	107.5	72.02(2)	107.99(1)
C_6Cl_5OH	*Cl_2^i···Cl_2^{vi}	3.7492(2)	107.1	123.01(2)	123.01(2)
	*Cl_3^i···Cl_3^{iii}	3.5116(1)	100.3	125.77(3)	125.77(3)
	*Cl_4^i···Cl_1^v	3.7743(3)	107.8	72.45(1)	123.99(2)
	*Cl_4^i···Cl_1^{iv}	3.7721(1)	107.8	72.66(1)	122.21(3)
	*Cl_5^i···Cl_5^{vii}	3.4349(2)	98.1	163.24(1)	163.24(1)
	*Cl_3^i···Cl_3^{viii}	3.9144(2)	111.8	125.77(3)	125.77(3)

C₆Br₆	* Br$_1$^{i}···Br$_1$^{iv}	3.9351(2)	106.4	106.24(1)	123.81(1)
	* Br$_2$^{i}···Br$_2$^{v}	3.7445(3)	101.2	118.35(1)	126.72(2)
	* Br$_3$^{i}···Br$_3$^{vi}	3.7359(1)	101.0	124.62(1)	124.62(1)
	* Br$_3$^{i}···Br$_3$^{viii}	3.8197(1)	103.2	103.30(1)	103.30(1)
	** Br$_2$^{i}···Br$_2$^{ix}	3.9332(2)	106.3	83.28(1)	96.72(4)
	** Br$_3$^{i}···Br$_2$^{ix}	3.9177(3)	105.9	72.58(1)	83.98(1)
	** Br$_3$^{i}···Br$_3$^{ix}	3.9332(2)	106.3	71.56(2)	108.44(4)
C₆Br₅OH	* Br$_1$^{i}···Br$_4$^{iii}	3.6212(2)	97.9	122.48(1)	125.31(1)
	* Br$_3$^{i}···Br$_3$^{v}	3.7126(2)	100.3	120.90(1)	125.65(2)
	* Br$_2$^{i}···Br$_2$^{ii}	3.9642(2)	107.1	107.01(2)	131.32(1)
	* Br$_1$^{i}···Br$_4$	3.9720(3)	107.4	98.02(1)	100.27(1)
	** Br$_1$^{i}···Br$_1$^{vi}	3.9469(1)	106.7	69.37(2)	110.63(1)
	** Br$_3$^{i}···Br$_3$^{vi}	3.9469(1)	106.7	86.26(1)	93.74(2)
	** Br$_4$^{i}···Br$_4$^{vi}	3.9469(1)	106.7	69.46(3)	110.54(2)
	** Br$_3$^{i}···Br$_4$^{vi}	3.9833(1)	107.6	69.69(2)	86.20(2)
	** Br$_5$^{i}···Br$_5$^{vi}	3.9469(1)	106.7	67.53(1)	112.47(1)

[a] Distance (d, Å) and angles ($\theta_1 \leq \theta_2$, °) are depicted in Figure II.2. The ω penetration parameter is in %. The structural parameters correspond to the multipolar models described in Chapter III. [b] (*) intercolumn interactions, (**) intracolumn interactions. Symmetry codes: C₆Cl₆/C₆Br₆: (i) x, y, z; (iv) 1/2–x, 1/2+y, 1/2–z; (v) –1/2–x, 1/2+y, 1/2–z; (vi) –1–x, 2–y, –z; (vii) –1+x, y, z; (viii) –1–x, 1–y, –z; (ix) x, –1+y, z. C₆Cl₅OH: (i) x, y, z; (ii) x, 3–y, –1/2+z; (iii) –x, 3–y, –z; (iv) x, 2–y, –1/2+z; (v) x, 3–y, 1/2+z; (vi) –x, y, 1/2–z; (vii) –x+1/2, 7/2–y, –z; (viii) –x, 2–y, –z; C₆Br₅OH: (i) x, y, z; (ii) 2–x, –1/2+y, 2–z; (iii) 2+x,–1+y, z; (iv) 1–x, y+1/2, 2–z; (v) 2–x, –1/2+y, 1–z; (vi) x, –1+y, z;

2.1.2. Interaction analyses from ρ(r) and L(r) functions

In accordance with the structural parameters ω, θ_1 and θ_2, and with the anisotropic distribution of the electron density around Hal-atoms, we can define two geometrical arrangements for type-I Hal···Hal contacts – *head-on* and *side-side*. In the first type, the δ^+ regions of Hal-atoms face each other (**Figure IV.7a** – the case of Cl$_5$···Cl$_5$ in C₆Cl₅OH), leading to a short interactions with an almost linear geometry. The second geometrical type – *side-side* – is characterized by the interaction between two δ^- regions, which is possible either in the case of two oblique angles of close magnitudes (e.g. the satellite Hal···Hal contacts around the synthons, **Figure IV.7b**) or with the two angles close to 90 ° (e. g. intracolumn interactions, **Figure IV.7c,d**). The longer radius of the Hal-atom in the direction of the δ^- region is the reason of longer interatomic distances for these types of contacts.

Topological properties of ρ(**r**) at BCP's (**Table IV.7**) show the numerical difference between the two geometrical arrangements of Type-I Hal···Hal contacts. *Side-side* arrangement shows the highest topological values (in accordance with the other experimental studies for *side-side* contacts[93]), which are actually typical for those of Type-II Hal···Hal contacts (ρ = 0.055 eÅ^{-3}, $\nabla^2\rho$ = 0.54 eÅ^{-5}, $|V|/G$ = 0.80). The energetic criterion $|V|/G$ for all the studied cases characterize the type-I Hal···Hal interactions as *pure* closed-shell ones (0.64 <$|V|/G$ < 0.73 for *side-side* Cl···Cl

contacts and $0.69 < |V|/G < 0.79$ for Br⋯Br contacts), being lower than the corresponding Type-II interactions ($0.66 < |V|/G < 0.82$ for Cl⋯Cl contacts and $0.74 < |V|/G < 0.85$ for Br⋯Br contacts). The values of the interaction energy, $E_{int} \sim V/2$, follow the same behavior and, except several short interactions, can be also comparable to the very weak hydrogen bonding (< 5 kJ mol^{-1}).

From the Laplacian viewpoint, the *head-on* and *side-side* type of contacts can be understood as repulsive electrostatic CD⋯CD (**Figure IV.7a**) and CC⋯CC (**Figure IV.7b,c,d**) interactions, respectively.

The possibility of applying the $\Delta(L/\rho)$ criterion for describing the electrostatic contribution of these interactions was considered. However, from the Laplacian maps, it can be seen, that the regions, involved in the interaction formation, are equivalent; thereby the values of L/ρ are almost equal in the two regions, resulting in a negligible value of the electrostatic descriptor. For example, for Br$_1$⋯Br$_4$ interaction in C$_6$Br$_5$OH (**Figure IV.7c**), L/ρ(Br$_1$)$_{CC}$= 3.63 Å^{-2} and L/ρ(Br$_4$)$_{CC}$ = 3.49 Å^{-2}, resulting in $\Delta(L/\rho)$ = 0.14 Å^{-2}.

In general, the variety of the observed Hal⋯Hal contacts of Type-I suggest their non-directional character, which nature should be studied experimentally and theoretically in more details using a specially developed approach.

(a)   **(b)**   **(c)**   **(d)**
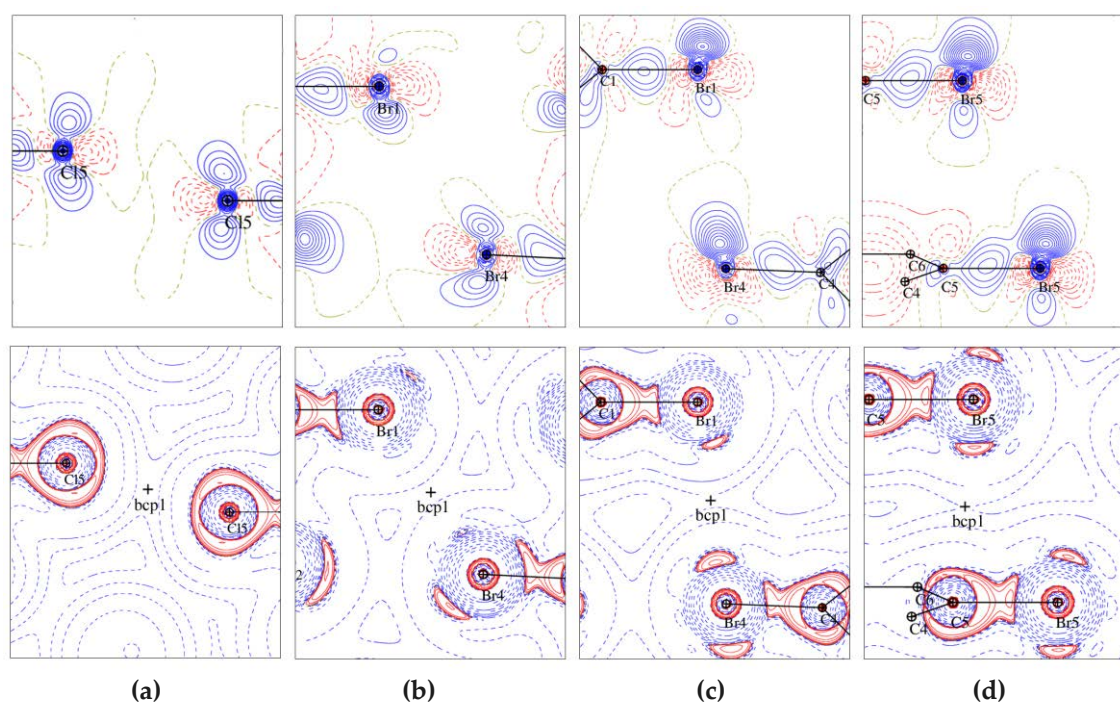
Figure IV.7 Static deformation density (top) and $L(\mathbf{r})$ maps (bottom) for Type-I Hal⋯Hal interactions (a) *head-on* and (b), (c), (d) the variations of *side-side* geometrical arrangements. $\Delta\rho(\mathbf{r})$ contours are at ±0.05 eÅ^{-3}, blue – positive, red – negative; $L(\mathbf{r})$ contours (eÅ^{-5}) are in logarithmic scale, red – positive, blue – negative.

2.2. Hal···Cπ interaction

The last interaction that we consider in this chapter occurs between Hal-atom (Hal = Cl, Br) and the π electrons. This type of contacts was noticed to play an important role in the crystal packing of organic compounds.[149] It also appears to influence generation of molecular motifs in crystalline lattices along with other intermolecular interactions. The π electrons are supposed to be delocalized on the aromatic ring in the crystal structures of C_6Hal_6 and C_6Hal_5OH (Hal = Cl, Br). Despite their delocalized character, the bonding character of these interactions can be well recognized through the existence of a bond path, linking the Hal- and C-atoms, and a corresponding BCP's. For each Hal-atom, several contacts with carbon atoms were found in the studied halogenated structures. All of them occur between the parallel molecules of the same column along the *b*-axis direction, though, these interactions support the rigidity of the columns along with the previously discussed intracolumn type-I Hal···Hal and Cπ···Cπ interactions.[149]

(a) **(b)** **(c)**
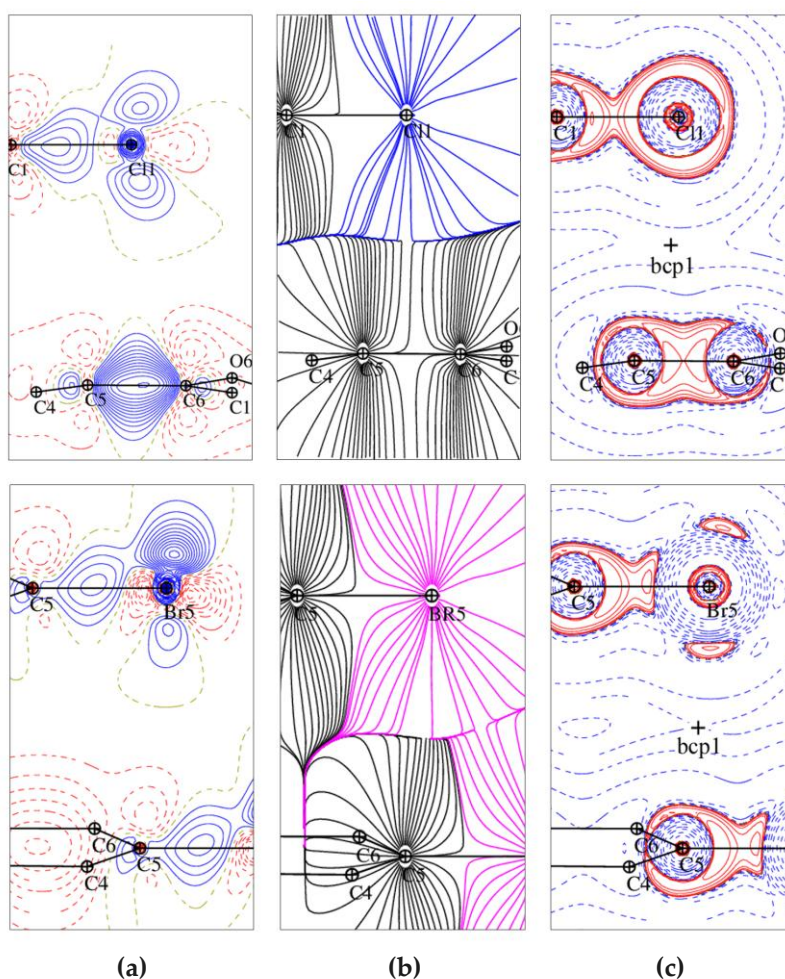
Figure IV.8 Intermolecular interactions $Cl_1···C_5$ in C_6Cl_5OH (top) and $Br_5···C_5$ in C_6Br_5OH (bottom): (a) static deformation density maps, contours are at ±0.05 eÅ⁻³, blue – positive, red – negative, (b) $\nabla\rho(\mathbf{r})$ map and (c) $L(\mathbf{r})$ maps, contours (eÅ⁻⁵) are in logarithmic scale, red – positive, blue – negative.

2.2.1. Structural characterization

The distance of the Cl⋯Cπ and Br⋯Cπ contacts can be compared with the corresponding average values for these intermolecular interactions obtained from the statistical analysis of structural data from the Cambridge Structural Database (CSD) – 3.525 ± 0.007 Å for Cl⋯Cπ and 3.625 ± 0.009 Å for Br⋯Cπ.[167] The shortest Cl⋯Cπ contact is of 3.4751(2) Å (ω = 100.7 %), while the shortest Br⋯Cπ contact is of 3.6452(2) Å (ω = 102.7 %). Though, according to the ω-magnitude, Cl-atom is able to form shorter contacts with Cπ than the Br-atom.

2.2.2. Interaction analyses from $\rho(r)$ and $L(r)$ functions

According to the local topological properties of $\rho(\mathbf{r})$ at BCP's (**Table IV.8**), Hal⋯Cπ interactions exhibit very close magnitudes to the ones obtained for type-I Hal⋯Hal interactions (type CC⋯CC) and can be also classified as *pure* closed-shell interactions ($0.67 < |V|/G < 0.75$). The values of the interaction energy, estimated from the potential energy density ($E_{int} \sim V/2$), are comparable to the very weak hydrogen bonding (< 5 kJ mol^{-1}). For the Hal⋯Cπ interactions, the already observed tendency of the topological properties increase with the distance shortening is also valid.

Figures IV.8 shows experimental $\Delta\rho(\mathbf{r})$, $\nabla\rho(\mathbf{r})$ and $L(\mathbf{r})$ maps for the two typical contact arrangements. From $\Delta\rho(\mathbf{r})$ and $\nabla\rho(\mathbf{r})$ maps, it can be seen that the interaction occurs between the δ^- regions of Hal-atoms and electron density deficient region around C-atoms. Thereby, the electrostatic character of these interactions cannot be excluded. However, the precise experimental and theoretical investigations are needed for the exact conclusions.

Table IV.7 Topological characteristics of Type-I Hal···Hal pairwise intermolecular interactions in C_6Cl_6, C_6Cl_5OH, C_6Br_6 and C_6Br_5OH.[a]

	Interaction[d]	d (Å)	ρ	$\nabla^2\rho$	λ_1	λ_2	λ_3	G	V	E_{int}	$|V|/G$	H/ρ
C_6Cl_6[b]	*Cl1[i]···Cl1[iv]	3.8221(2)	0.029	0.35	−0.06	−0.05	0.46	7.3	−4.9	−2.5	0.68	542
			0.026	0.33	−0.05	−0.04	0.42	6.7	−4.4	−2.2	0.66	597
	*Cl2[i]···Cl2[v]	3.6238(2)	0.040	0.50	−0.10	−0.06	0.66	10.5	−7.4	−3.7	0.70	523
			0.038	0.48	−0.08	−0.07	0.63	10.0	−7.0	−3.5	0.70	533
	*Cl3[i]···Cl3[vi]	3.6355(2)	0.035	0.48	−0.06	−0.05	0.59	9.8	−6.7	−3.4	0.68	598
			0.037	0.46	−0.08	−0.07	0.61	9.7	−6.7	−3.4	0.69	547
	*Cl3[i]···Cl1[vii]	3.9026(1)	0.024	0.29	−0.04	−0.04	0.37	5.9	−3.9	−2.0	0.66	562
			0.026	0.28	−0.04	−0.04	0.36	5.7	−3.7	−1.9	0.65	519
	*Cl3[i]···Cl3[viii]	3.6531(2)	0.037	0.45	−0.08	−0.06	0.60	9.5	−6.7	−3.4	0.71	511
			0.038	0.47	−0.09	−0.08	0.64	9.9	−7.0	−3.5	0.71	515
	**Cl2[i]···Cl2[ix]	3.7626(2)	0.033	0.38	−0.07	−0.05	0.50	7.9	−5.5	−2.8	0.70	491
			0.032	0.38	−0.06	−0.06	0.51	8.0	−5.5	−2.8	0.69	527
	**Cl3[i]···Cl3[ix]	3.7626(2)	0.037	0.41	−0.07	−0.03	0.51	8.7	−6.2	−3.1	0.71	456
			0.034	0.40	−0.06	−0.01	0.47	8.3	−5.8	−2.9	0.70	496
C_6Cl_5OH	*Cl2[i]···Cl2[vi]	3.7492(2)	0.028	0.36	−0.05	−0.05	0.46	7.3	−4.9	−2.5	0.66	578
	*Cl3[i]···Cl3[iii]	3.5116(1)	0.049	0.62	−0.12	−0.11	0.85	13.3	−9.7	−4.9	0.73	496
	*Cl4[i]···Cl1[v]	3.7743(3)	0.032	0.39	−0.05	−0.02	0.46	8.1	−5.5	−2.8	0.68	566
	*Cl4[i]···Cl1[iv]	3.7721(1)	0.033	0.39	−0.06	−0.05	0.49	8.0	−5.6	−2.8	0.70	491
	*Cl5[i]···Cl5[vii]	3.4349(2)	0.055	0.54	−0.13	−0.12	0.79	12.3	−9.8	−4.9	0.80	307
	*Cl3[i]···Cl3[viii]	3.9144(2)	0.020	0.28	−0.05	−0.03	0.35	5.5	−3.5	−1.8	0.64	675
C_6Br_6[c]	* Br1[i]···Br1[iv]	3.9351(2)	0.032	0.36	−0.06	−0.04	0.47	7.6	−5.3	−2.7	0.70	485
	* Br2[i]···Br2[v]	3.7445(3)	0.045	0.51	−0.09	−0.08	0.68	11.1	−8.2	−4.1	0.74	435
	* Br3[i]···Br3[vi]	3.7359(1)	0.046	0.52	−0.10	−0.08	0.70	11.3	−8.5	−4.3	0.75	411
	* Br3[i]···Br3[viii]	3.8197(1)	0.043	0.45	−0.10	−0.08	0.63	9.8	−7.4	−3.7	0.76	377

106

	d (Å)	ρ	$\nabla^2\rho$	λ_1	λ_2	λ_3	G	V	E_{int}		
**Br$_2^i$···Br$_2^{ix}$	3.9332(2)	0.036	0.36	−0.08	−0.07	0.50	7.8	−5.7	−2.9	0.73	394
**Br$_3^i$···Br$_2^{ix}$	3.9177(3)	0.035	0.37	−0.06	−0.04	0.47	7.9	−5.7	−2.9	0.72	424
**Br$_3^i$···Br$_3^{ix}$	3.9332(2)	0.034	0.37	−0.06	−0.03	0.46	7.8	−5.5	−2.8	0.71	456
C$_6$Br$_5$OH *Br$_1^i$···Br$_4^{iii}$	3.6212(2)	0.056	0.60	−0.12	−0.11	0.83	13.6	−10.7	−5.4	0.79	349
*Br$_3^i$···Br$_3^v$	3.7126(2)	0.049	0.54	−0.11	−0.09	0.75	11.9	−9.0	−4.5	0.76	399
*Br$_2^i$···Br$_2^{ii}$	3.9642(2)	0.031	0.34	−0.06	−0.05	0.45	7.2	−5.0	−2.5	0.69	479
*Br$_1^i$···Br$_4$	3.9720(3)	0.032	0.36	−0.07	−0.06	0.49	7.6	−5.3	−2.7	0.70	485
**Br$_1^i$···Br$_1^{vi}$	3.9469(1)	0.035	0.39	−0.08	−0.02	0.49	8.3	−5.9	−3.0	0.71	463
**Br$_3^i$···Br$_3^{vi}$	3.9469(1)	0.029	0.31	−0.05	−0.04	0.40	6.5	−4.6	−2.3	0.71	442
**Br$_4^i$···Br$_4^{vi}$	3.9469(1)	0.032	0.34	−0.05	−0.03	0.42	7.1	−5.1	−2.6	0.72	422
**Br$_3^i$···Br$_4^{vi}$	3.9833(1)	0.033	0.38	−0.07	−0.05	0.49	7.9	−5.6	−2.8	0.71	470
**Br$_5^i$···Br$_5^{vi}$	3.9469(1)	0.033	0.36	−0.07	−0.03	0.46	7.6	−5.4	−2.7	0.71	450

[a]The parameters ρ (eÅ^{-3}), $\nabla^2\rho$ (eÅ^{-5}), λ_i (eÅ^{-5}), G and V (kJ mol^{-1} bohr^{-3}) are calculated at the BCP's of $\rho(\mathbf{r})$. E_{int} (kJ mol^{-1}) values are estimated as $-1/2V$, the constant being in bohr^3 units. See Table IV.6 for symmetry codes. [b] First and second lines correspond to experimental and theoretical (VASP calculations)[14] data. [c] Values are from theoretical (VASP calculations) data.[d] (*) intercolumn interactions, (**) intracolumn interactions.

Table IV.8 Topological characteristics of Hal···C intermolecular interactions in C_6Cl_6, C_6Cl_5OH, C_6Br_6 and C_6Br_5OH.[a]

	Interaction	d, ω	ρ	$\nabla^2\rho$	λ_1	λ_2	λ_3	G	V	E_{int}	$|V|/G$	H/ρ
$C_6Cl_6^b$	$Cl_1^i···C_1^{ix}$	3.5081(2), 101.7	0.043	0.47	−0.06	−0.04	0.58	10.2	−7.6	−3.8	0.75	408
			0.040	0.47	−0.07	−0.04	0.57	9.9	−7.2	−3.6	0.73	455
	$Cl_3^i···C_3^x$	3.6211(2), 104.9	0.040	0.50	−0.10	−0.06	0.66	10.5	−7.4	−3.7	0.70	523
			0.039	0.48	−0.09	−0.06	0.63	10.4	−7.1	−3.6	0.68	571
C_6Cl_5OH	$Cl_1^i···C_5^{ix}$	3.4751(2), 100.7	0.044	0.51	−0.09	−0.04	0.65	10.9	−8.0	−4.0	0.73	445
	$Cl_2^i···C_3^{ix}$	3.5337(2), 102.4	0.038	0.43	−0.08	−0.04	0.65	9.1	−6.6	−3.3	0.73	444
	$Cl_5^i···C_6^x$	3.5180(1), 102.0	0.039	0.45	−0.08	−0.04	0.57	9.6	−6.9	−3.5	0.72	467
$C_6Br_6^c$	$Br_1^i···C_1^{ix}$	3.6452(2), 102.7	0.039	0.41	−0.06	−0.03	0.51	8.9	−6.5	−3.3	0.73	415
C_6Br_5OH	$Br_1^i···C_1^{vi}$	3.7266(2), 105.0	0.038	0.41	−0.08	−0.03	0.52	8.8	−6.5	−3.3	0.74	408
	$Br_2^i···C_2^{vi}$	3.6914(2), 104.0	0.040	0.42	−0.08	−0.03	0.54	9.1	−6.7	−3.4	0.74	405
	$Br_5^i···C_5^{vii}$	3.6660(2), 103.3	0.031	0.40	−0.07	−0.02	0.49	8.2	−5.5	−2.8	0.67	588

[a] The parameters ρ (eÅ^{-3}), $\nabla^2\rho$ (eÅ^{-5}), λ_i (eÅ^{-5}), G and V (kJ mol^{-1} bohr^{-3}) are calculated at the BCP's of $\rho(\mathbf{r})$. E_{int} (kJ mol^{-1}) values are estimated as $-1/2V$, the constant being in bohr^3 units. [b] First and second lines correspond to experimental and theoretical (VASP calculations)[14] data. [c] Values are from theoretical (VASP calculations) data. Symmetry codes: C_6Cl_6/C_6Br_6: (i) x, y, z; (ix) x, −1+y, z; (x) x, 2+y, z; C_6Br_5OH: (i) x, y, z; (vi) x, −1+y, z; (vii) x, 1+y, z.

Summary

In this chapter, we have characterized intermolecular interactions involving Hal-atoms in the crystal structures of C_6Br_6, C_6Cl_5OH, C_6Br_5OH, and C_3HIOS_2 along with the previously investigated C_6Cl_6. Based on the experimental and theoretical charge density analysis, we distinguished between the electrostatically favoured halogen bondings (Type-II Hal···Hal and Hal···LB interactions) and other interactions with participation of Hal-atoms (Type-I Hal···Hal and Hal···Cπ contacts).

We have performed a comparative study of Cl_3- and Br_3-synthons and established the main differences between them coming from the particular structure of the *Valence Shell Charge Concentration* region in Cl- and Br-atoms. The electrophilic–nucleophilic interactions within the intermolecular regions of Hal_3-synthons were pointed by putting face-to-face charge depletion and charge concentration regions belonging to the valence-shell of the halogen atoms. The estimated value of the total interactions energy at BCP was found to be 17 % stronger for Br_3- than for Cl_3-synthons, while based on the electrostatic descriptor $\Delta(L/\rho)$, this difference increases up to 30 %. The interactions energy for I···O interaction in C_3HIOS_2 was found to be comparable to the ones, defined for Hal_3-synthons.

Chapter V

Interactions involving chalcogen atoms

In Chapter V, we present a detailed analysis of intermolecular interactions involving chalcogen atoms, which complies the second objective of this work. First, on the basis of *ab initio* calculations on the series of monomers $C_8O_2H_4Chal$ (Chal = O, S, Se, Te), where Chal-atom is represented in its sp^3 hybridization, we show the evolution of the electron density distribution along the series of chalcogen atoms. Then, from a highly accurate analysis of the experimental and theoretical electron density $\rho(\mathbf{r})$ and its negative Laplacian function $L(\mathbf{r})$, we characterize directionality and strength of chalcogen bonding Chal$\cdots$X (X = Chal, Hal, Lewis Base) in the crystal phases of $C_8O_2H_4Se$ and C_3HIOS_2. Other closed-shell interactions involving chalcogen atoms in the crystal structures of $C_8O_2H_4Se$, C_3HIOS_2, and C_6Hal_5OH (Hal = Cl, Br) are also characterized from the $\rho(\mathbf{r})$ and $L(\mathbf{r})$ functions.

1. Chalcogen atoms from gas-phase calculations

The details of gas-phase calculations are described in **Chapter III** (section 1.3). For the analysis of electron density distribution along the series of chalcogen atoms, we have chosen chalcogenophtalic anhydrides $C_8O_2H_4Chal$ (Chal = O, S, Se, Te) as model systems, where the two electron-withdrawing carbonyl groups are expected to enhance the *σ-hole* structure of the central chalcogen atom in its sp^3 hybridization. Indeed, for the known structures with Chal = S,[168] Se,[157] and Te,[157] these crystal structures show a recurrent structural motif with C=O···Chal angles that describe the geometry of the carbonyl-group lone pair pointing towards the Chal-atom (**Table V.1**).

Table V.1 Crystal structure characteristics of chalcogen bonding for $C_8O_2H_4Chal$ (Chal = S, Se, and Te): distance Chal···O (d_1 /Å), penetration parameter (ω /%), defined as the Chal···O distance over the sum of van der Waals radii, and angles C_1–Chal···O, Chal···O=C and θ (ζ_1, ζ_2 and θ /°); $\sin\theta = d_2/d_1$.
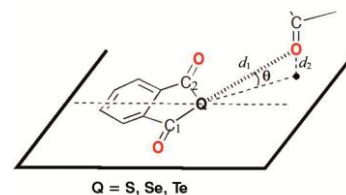
Chal···O	d_1	ω	ζ_1	ζ_2	θ
S···O	3.47(1)	104.5	139.6(4)	115.05(3)	23.5
Se···O	3.413(5)	99.7	144.5(1)	111.5(3)	19.8
Te···O	3.376(4)	99.3	145.8(2)	109.1(4)	17.0

Although the O···Chal distances are not significantly shorter than the sum of the van der Waals radii, a strengthening is observed going down in the chalcogen series, as shown by the ω parameter. The small θ-values (see scheme in **Table V.1** caption) indicate that the oxygen atom is close to the basal plane of the neighboring molecule, whereas the O···Chal–C_1 angle of ~140 ° shows that the electron-rich oxygen atom is not located in the prolongation of the C–Chal bonds, as anticipated from earlier models. These structures might indicate that the *σ-hole* can be much more diffuse than described earlier and that a more precise parameter is needed to characterize the interaction directionality.

1.1. Deformation electron density

The deformation electron density $\Delta\rho(\mathbf{r})$ characterizes the charge redistribution with respect to the superposition of spherically averaged non-interacting atomic densities, showing the formation of lone pairs and chemical bonds. The sp^3 hybridization of chalcogen atoms is observed in the $\Delta\rho(\mathbf{r})$ maps (**Figure V.1**), where the electron distribution associated to the lone pairs (δ^- regions) is grouped in the plane bisecting the α(C–Chal–C) angle. The progressive separation of the chalcogen lone pairs (*lp*) along the series O < S < Se < Te (β(*lp*$_1$–nucleus–*lp*$_2$) = 0, 114, 120, and 130°, **Figure V.1 bottom**) follows the decrease of α (109.9, 92.3, 88.2, and 82.4 °, respectively) and is accompanied by more extended and less concentrated δ^- regions. Simultaneously, electron deficient (δ^+) regions along the C–Chal directions are reduced and shifted towards the external part of chalcogen atom through the series from S- to Te-atoms (**Figure V.1 top**).
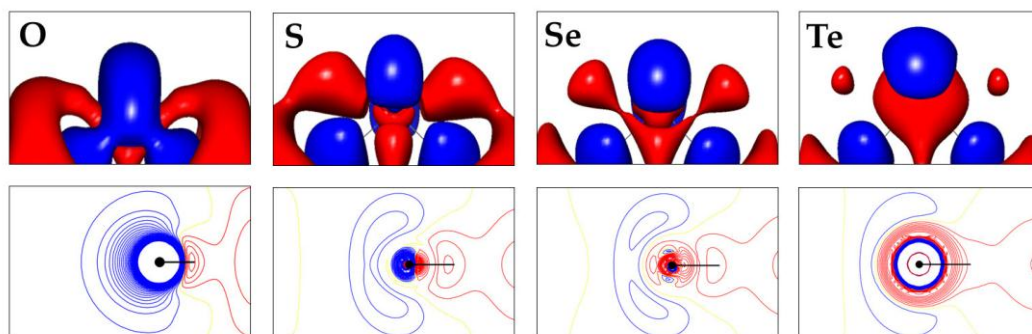
Figure V.1 Deformation density $\Delta\rho(\mathbf{r})$ maps around chalcogen atoms in $C_8O_2H_4Chal$ monomers (C-Chal-C plane (top) and perpendicular plane bisecting the α(C-Chal-C) angle (bottom), obtained from gas-phase calculations. Iso-surfaces and contours are drawn at ±0.05 eÅ^{-3} levels: blue – positive, red – negative.

1.2. Electrostatic potential

Figure V.2 shows the electrostatic potential $V(\mathbf{r})$ maps for the optimized monomers $C_8O_2H_4Chal$ (Chal = O, S, Se, Te) in gas phase. The positive and negative regions of $V(\mathbf{r})$ on the molecular $\rho(\mathbf{r})$ iso-surface of 0.001 a.u. (0.0067 eÅ^{-3}, which can be considered as the molecular envelope) follow the disposition and the intensity of the δ^+ (blue) and δ^- (red) regions found around the chalcogen atoms in the $\Delta\rho(\mathbf{r})$ maps. Thus, along the C–Chal direction the value of $V(\mathbf{r})$ is 0.61, 1.66, and 3.25 ($\times10^{-2}$ eÅ^{-1}) for S, Se, and Te, while at the lone-pairs position $V(\mathbf{r})$ is –7.52, –2.10, –2.15, and –2.15 ($\times10^{-2}$ eÅ^{-1}) for O, S, Se, and Te.
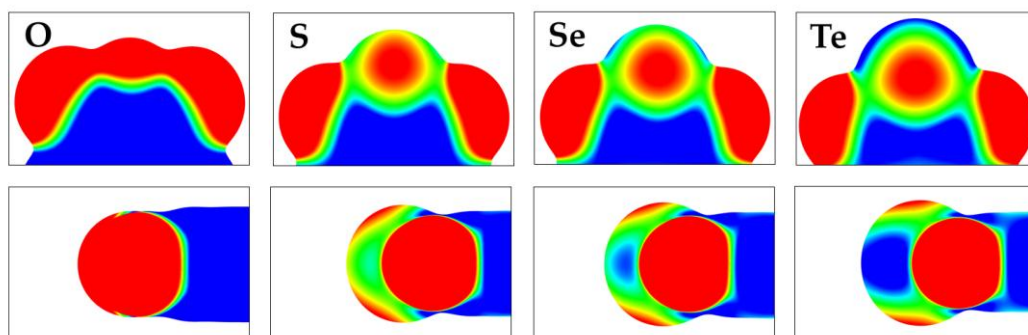
Figure V.2 Electrostatic potential $V(\mathbf{r})$ maps around chalcogen atoms in $C_8O_2H_4Chal$ monomers (C-Chal-C plane (top) and perpendicular plane bisecting the α(C-Chal-C) angle (bottom), obtained from gas-phase calculations. $V(\mathbf{r})$ (eÅ^{-1}) displayed on the molecular $\rho(\mathbf{r})$ iso-surface of 0.001 a.u. (from most positive - blue to most negative - red values).

1.3. Laplacian of electron density

The Laplacian function $L(\mathbf{r})$ indicates the molecular regions where the charge density is locally concentrated ($L(\mathbf{r}) > 0$) or depleted ($L(\mathbf{r}) < 0$). δ^+ and δ^- distributions rising from $\Delta\rho(\mathbf{r})$ find

their physical interpretations in the charge depletion (CD) and charge concentration (CC) regions of $\rho(\mathbf{r})$, which are pointed by $L(\mathbf{r})$.
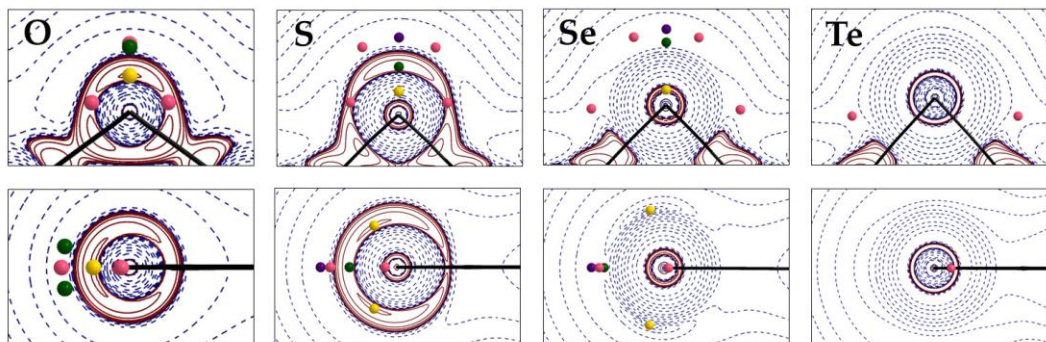
Figure V.3 Laplacian $L(\mathbf{r}) = -\nabla^2\rho(\mathbf{r})$ maps around chalcogen atoms in $C_8O_2H_4Chal$ monomers (C-Chal-C plane (top) and perpendicular plane bisecting the α(C-Chal-C) angle (bottom), obtained from gas-phase calculations. $L(\mathbf{r})$ contours (eÅ^{-5}) are in logarithmic scale, red – positive, blue – negative. The topology of $L(\mathbf{r})$ of the atomic valence shell is marked in colored circles: (3,–3) – yellow, (3,–1) – green, (3,+1) – pink, (3,+3) – violet.

According to the topological analysis of $L(\mathbf{r})$ in the atomic valence shell charge concentration (VSCC) of light atoms,[2,169] such as O, F, S, or Cl, saddle and local maxima distributions permit to locate atomic electrophilic and nucleophilic sites from the observation of (3,+1) and (3,–3) critical points (CPs). For heavier atoms, such as Se, Br, Te, or I, the whole valence shell of the atom (including its charge depletion region, VSCD) is needed (see **Chapter IV**) and additional (3,+3) and (3,–1) CPs must be considered. Thereby, (3,–3) and (3,+3) CPs of $L(\mathbf{r})$ always indicate a local maximum (CC region) and a local minimum (CD region) of electron density along the three main directions, while (3,–1) and (3,+1) CPs depending on the interaction geometry can correspond to a local minimum (CD region) along one and two main directions or to a local maximum (CC region) along two and one main directions. Paralleling the separation of the lone pairs observed in $\Delta\rho(\mathbf{r})$ and $V(\mathbf{r})$ maps, the angular disposition of the CC sites around the chalcogen atoms (**Figure V.3 bottom**) follows the series O < S < Se (β(CC–nucleus–CC) = 0, 122.4, 151.2 °). Due to the highly diffuse lone pairs of Te-atom in $C_8O_2H_4Te$, no (3,–3) CPs of $L(\mathbf{r})$ are found in its valence shell. They are however present in $Te(CH_3)_2$ (β(CC–nucleus–CC) = 157.2 °), where the valence shell of Te-atom is activated by the influence of the intramolecular chemical environment (**Figure V.4**). It should be noted that in regions where $L(\mathbf{r}) < 0$ (i.e. a depleted *region* of electron density), CC *sites* are rather associated to local regrouping of depleted charge than to, strictly speaking, charge concentration.
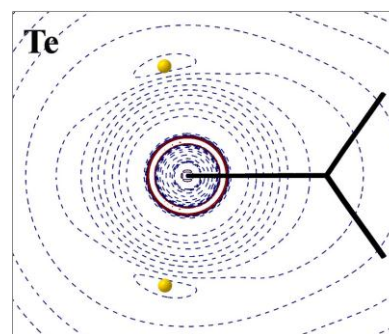
Figure V.4 $L(r) = -\nabla^2\rho(r)$ map of Te-atom in $Te(CH_3)_2$ (plane bisecting the α(C-Te-C) angle). $L(r)$ contours (eÅ^{-5}) are in logarithmic scale, red – positive, blue – negative. (3,–3) CPs (CC sites) are marked in yellow.

Within the C–Chal–C plane, a first couple of (3,+1) CPs (**Figure V.3 top**) was found for all the four chalcogen atoms. Placed in δ^+ regions (see $\Delta\rho(\mathbf{r})$ maps in **Figure V.1**), these points can be associated with the charge depletion and will be notated as CD_1 hereafter. The angular separation for each couple is $\gamma(CD_1\text{–nucleus–}CD_1)$ = 153.1, 152.0, 173.6, and 204.7 ° for O, S, Se, and Te respectively. In the case of O and S, the CD_1 sites belong to a positive area of $L(\mathbf{r})$ (*i.e.* the VSCC), while for Se and Te to a negative one (*i.e.* the VSCD), showing a larger angular separation. For S- and Se-atoms, an additional pair of (3,+1) CPs (CD_2) was found, placed closer to the bisector direction ($\gamma(CD_2\text{–nucleus–}CD_2)$ = 57.3 and 51.6 °, respectively). Similarly to halogen atoms, the origin of the σ-hole in chalcogens is found in the development of the electron CD region in the atomic valence shell, the increase of the σ-hole paralleling the extension of the CD region.

For O-, S-, and Se-atoms a (3,–1) CP was found along the bisector direction of the C–Chal–C angle. At this site, $\rho(\mathbf{r})$ is minimum (i.e it behaves as a CD site) along the direction linking the two maxima and maximum (i.e it behaves as a CC site) along the two perpendicular directions. Depending on the molecular environment this region can be considered as a CD or CC site. Both possibilities will be demonstrated later, when we will analyze the intermolecular interactions taking place in the crystal phase.

In **Chapter IV**, on the example of Hal···Hal interactions, it was shown that the electrophilic/nucleophilic power of the CD/CC sites can be quantified in a common scale by using the normalized descriptor L/ρ, where L and ρ values are calculated at the critical points of $L(\mathbf{r})$. **Table V.2** shows the L/ρ values at the CD/CC sites of chalcogen atoms in $C_8O_2H_4Chal$ monomers. The electrophilic/nucleophilic power of these sites increases with the more negative/positive magnitudes of L/ρ. Accordingly, the nucleophilic power of CC sites decreases along O > S > Se > Te, whereas the electrophilic power averaged over the CD sites increases along the same series. In the crystal phase, the L/ρ magnitudes are expected to be influenced by a redistribution of $\rho(\mathbf{r})$ due to the interaction of Chal-atom with the molecular environment.

Table V.2 Electrophilic and nucleophilic power (L/ρ in Å^{-2}) of CD and CC sites in the electron valence shell of the chalcogen atoms for the monomers $C_8O_2H_4Chal$ (Chal = O, S, Se, and Te) in gas phase.

CP	Site	O	S	Se	Te
(3, –3)	CC	16.89	8.64	–0.09	—
(3, +1)	CD_1	8.64	2.19	–6.71	–6.13
(3, +1)	CD_2	—	–4.95	–4.26	—
(3, –1)	CD_3 or CC_2	—	7.85	–1.65	—

1.4. Comparison with halogen atoms

In **Chapter IV** we represented the gas phase calculations for the monomers of C_6Hal_6 and C_6Hal_5OH (Hal = Cl, Br), calculated at the same level of theory as $C_8O_2H_4Chal$. The average of $(L/\rho)_{CD}$ values found for Cl- and Br-atoms are 4.35 ± 0.07 and –5.59 ± 0.12 Å^{-2}, respectively (the statistical dispersion is represented by RMSD magnitudes). The average of $(L/\rho)_{CC}$ values for the same atoms are 10.95 ± 0.09 and 1.10 ± 0.13 Å^{-2}, respectively. Within the context of the considered molecules, the comparison of S- to Cl-atoms, and of Se- to Br- atoms indicates that the

electrophilic power of sulphur is more pronounced than this of chlorine (both L/ρ_{CDi} values are lower for the former), while those of Se- and Br-atoms values are approximately similar to each other. According to the $(L/\rho)_{CC}$ values, the nucleophilic power increases from chalcogens to halogens. These features can not be straightforwardly generalized to any interaction involving chalcogen and halogen atoms; the modification of the electrophilic/nucleophilic power of the CD/CC sites by different intramolecular environment being in cause.

2. Electrostatically favoured chalcogen bonding interactions

Hereafter, we characterize $Se_1 \cdot \cdot Se_1$ and $Se_1 \cdots O_2$ chalcogen bonding in $C_8O_2H_4Se$ and $S_1 \cdots S_2$ and $S_2 \cdots I_1$ chalcogen boding in C_3HIOS_2 from their geometrical criteria (distance and angles) and topological characteristics. The comparison of these interactions becomes possible due to a similar hybridization state (sp^3) of the involved Chal-atoms.

2.1. Structural characterization

From the viewpoint of chalcogen bonding, the two investigated chalcogenated structures show similar features. Indeed, both of them exhibit similar types of intermolecular contacts – one involving two Chal-atoms and another involving a Chal-atom and a Lewis base. In **Table V.3** we list the observed $Chal \cdots X$ (X = Chal, Hal, LB) distances, which are compared to the corresponding sum of the van der Waals radii by means of the penetration parameter ω, and angles ζ_1, ζ_2 and θ, which help to evaluate the directionality of each contact.

Table V.3 Structural characteristics of chalcogen bonding in C_3HIOS_2 and $C_8O_2H_4Se$. [a]

Chal(δ^+)$\cdots$(δ^-)X	d	ω	ζ_1	ζ_2
$S_1^i \cdots S_2^{iii}$	3.8289(1)	106.4	161.38 / 97.98	126.61 / 135.44
$Se_1^i \cdots Se_1^{ii}$	3.8220(2)	100.6	166.31 / 79.11	87.47 / 121.95
$S_2^{iii} \cdots I_1^i$	3.8031(3)	100.6	170.90 / 84.97	92.87
$Se_1^i \cdots O_2^{ii}$	3.3552(1)	98.1	119.03 / 145.38	111.17

[a] Distance $Chal \cdots X$ (X = Chal, Hal, LB) (d/Å), penetration parameter (ω /%), defined as the $Chal \cdots X$ distance over the sum of van der Waals radii and angles ζ_1 (C_1/C_2–$Chal \cdots X$) (°), ζ_2 ($Chal \cdots X$– C_1/C_2) (°). Symmetry codes: C_3HIOS_2: (i) x, y, z; (iii) x, y, -1+z; $C_8O_2H_4Se$: (i) x, y, z; (ii) 1/2-x, -1/2+y, 3/2-z.

From the ω-parameter it is seen that the contacts involving the Se-atom approach closer to each other than those with S-atom – this was already noticed for halogen atoms (**Chapter IV**) where heavier bromines approach closer to each other than lighter chlorines.

The angles ζ_1 and ζ_2 permit to assume the location of δ^+ and δ^- regions of Chal-atoms involved in the interaction formation. The angular magnitudes show several differences in the interaction geometries. For the interactions $S_1 \cdots S_2$, $Se_1 \cdots Se_1$ and $S_2 \cdots I_1$, one of the two ζ_1 angles tends to be close to 180 ° (linearity) predicting the location of the δ^+ region placed close to the prolongation of the C_1–Chal bond. In contrast, the two ζ_1 values for $Se_1 \cdots O_2$ are quite close to each other, pointing on the δ^+ location close to the bisecting C–Se–C angle direction. Inverse situation is

observed for the ζ_2 parameter. Here, $Se_1\cdots Se_1$, $S_2\cdots I_1$ and $Se_1\cdots O_2$ show ζ_2 close to 90 °, which corresponds to the location of the δ^- region of I- and O-atoms and predicts one for Se-atom. In the case of the $S_1\cdots S_2$ contact, the two ζ_2 values are close to each other, indicating that the δ^- region is roughly located along the bisecting C–S–C angle direction.

The observed 'disagreements' in the positions of δ^+/δ^-, assumed from the geometrical considerations, can be resolved by the following analysis of $\rho(\mathbf{r})$ and $L(\mathbf{r})$ functions. However, despite different relative positions of the interacting molecules and different atoms involved in the interactions, the bifurcated chalcogen bonding contacts form geometrically similar cyclic motifs – synthon-type fragments. Based on this, we can assume that the interactions are formed also in a similar way.

2.2. Analysis of Chal⋯X interactions from the $\rho(\mathbf{r})$ function

The chalcogen bonding interactions were identified by the observed BCP's associated to the $Se_1\cdots O_2$, $Se_1\cdots Se_1$, $S_2\cdots I_1$, and $S_1\cdots S_2$ bond paths. (**Figure V.5a**). The gradient maps illustrate the atomic basins and zero-flux surfaces between the interacting atoms (**Figure V.5b**).

(a)   (b)
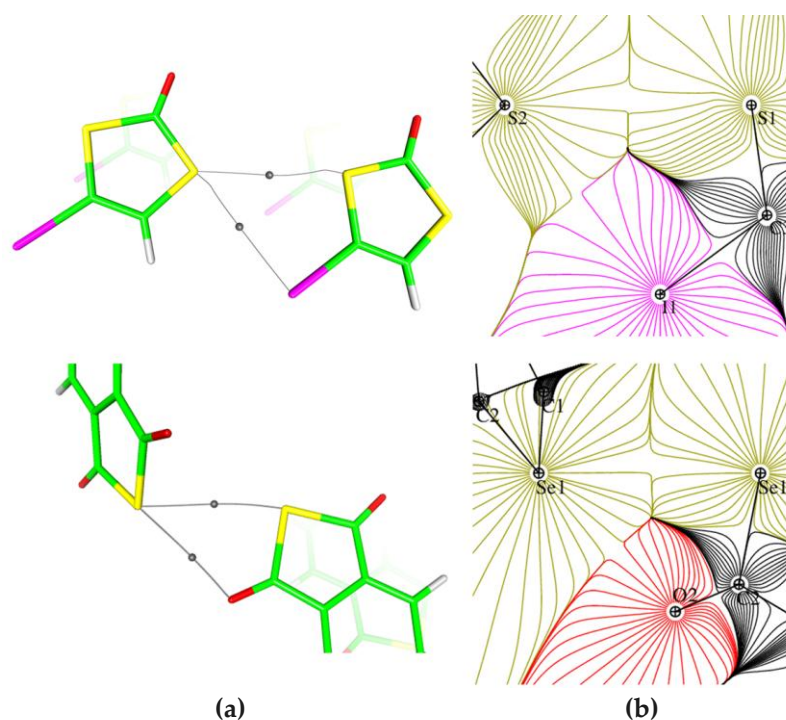
Figure V.5 Chalcogen bonding interactions in C_3HIOS_2 (top) and $C_8O_2H_4Se$ (bottom): (a) bond paths and the corresponding BCP's between the interacting atoms; (b) $\nabla\rho(\mathbf{r})$ maps in the intermolecular regions indicating the gradient lines and zero-flux surfaces.

Figure V.6 shows experimental and theoretical 3D static deformation density $\Delta\rho(\mathbf{r})$ maps plotted in the intermolecular region for the two compounds. In the case of C_3HIOS_2, the plots of $\Delta\rho(\mathbf{r})$ for both models suggest $S_2(\delta^-)\cdots(\delta^+)S_1$ and $S_2(\delta^+)\cdots(\delta^-)I_1$ chalcogen bonding interactions (**Figure V.6a**).

(a)   **(b)**
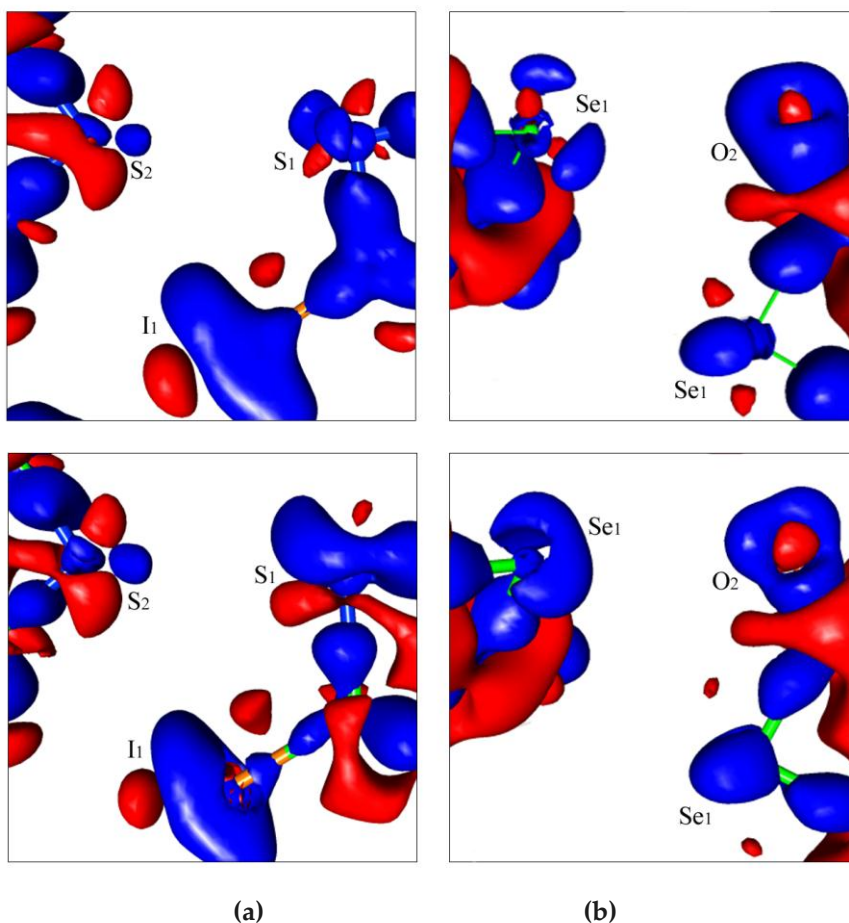
Figure V.6 Experimental (top) and theoretical (bottom) static deformation density maps in the intermolecular region for (a) C_3HIOS_2 and (b) $C_8O_2H_4Se$. Iso-surfaces and contours are drawn at ±0.05 eÅ^{-3} levels: blue – positive, red – negative.

In the case of $C_8O_2H_4Se$, experimental and theoretical models (**Figure V.6b**) provide a good description of the aspherical nature of charge density distribution around the Se-atom and show $Se(\delta^+)\cdots(\delta^-)Se$ and $Se(\delta^+)\cdots(\delta^-)O$ chalcogen bonding interactions. The observed differences in the deformation density shape around the Se-atom were explained in **Chapter III**. Overall, the $\Delta\rho(\mathbf{r})$ maps for Chal$\cdots$Chal and Chal$\cdots$LB are qualitatively similar despite the observed geometrical differences and specifically show δ^- and δ^+ regions facing each other along the interaction directions.

In order to give a quantitative characteristic for the observed pairwise interactions, we concentrate on the local properties of $\rho(\mathbf{r})$ at BCP's, obtained from both experimental and theoretical modeling (see **Chapter I** for the properties description). **Table V.4** gathers the values of the electron density ρ, the Laplacian $\nabla^2\rho$ with the three eigenvalues λ_i and the local electron kinetic G and potential V energy densities at the BCP's. For all the four intermolecular interactions, the values of ρ and $\nabla^2\rho$ are close to each other ($0.034 < \rho < 0.059$ eÅ^{-3}, $0.33 < \nabla^2\rho < 0.62$ eÅ^{-5}) and fall into the range determined theoretically and experimentally for weak hydrogen bonds,[34bc,59c,60] Hal$\cdots$Hal,[89] and weak Hal$\cdots$O (Hal = Cl, Br) interactions.[14,83,92b,94,98d]

Table V.4 The topological parameters for the Chal···X (X = Chal, Hal, LB) chalcogen bonding in the crystal structures of C_3HIOS_2 and $C_8O_2H_4Se$. [a]

Chal···X [b]	d, ω	ρ	$\nabla^2\rho$	λ_1	λ_2	λ_3	G	V	E_{int}	$|V|/G$	H/ρ	$\Delta(L/\rho)$
$S_1^i \cdots S_2^{iii}$	3.8289(1), 106.4	0.038	0.35	−0.07	−0.07	0.48	7.7	−5.9	−3.0	0.76	325	6.5
		0.034	0.33	−0.05	−0.04	0.42	7.1	−5.2	−2.6	0.74	377	6.7
$Se_1^i \cdots Se_1^{ii}$	3.8220(2), 100.6	0.051	0.37	−0.10	−0.09	0.56	9.0	−7.8	−3.9	0.83	146	2.5
		0.047	0.37	−0.09	−0.09	0.54	8.6	−7.2	−3.6	0.84	201	3.1
$S_2^{iii} \cdots I_1^i$	3.8031(3), 100.6	0.061	0.53	−0.14	−0.12	0.80	12.5	−10.6	−5.3	0.85	210	0.8
		0.059	0.51	−0.14	−0.12	0.77	12.1	−10.3	−5.1	0.85	206	0.7
$Se_1^i \cdots O_2^{ii}$	3.3552(1), 98.1	0.049	0.62	−0.11	−0.11	0.84	13.3	−9.8	−4.9	0.74	482	20.4
		0.049	0.62	−0.11	−0.11	0.85	13.3	−9.7	−4.9	0.73	498	22.1

[a] The parameters ρ (e$Å^{-3}$), $\nabla^2\rho$ (e$Å^{-5}$), λ_i (e$Å^{-5}$), G and V (kJ mol^{-1} $bohr^{-3}$) are calculated at the BCP's of $\rho(\mathbf{r})$; H/ρ is in kJ $mol^{-1}e^{-1}$ ($H = V + G$); $\Delta(L/\rho)$ ($Å^{-2}$) is calculated as the difference between the values observed at the CD and CC sites of the interacting atoms. E_{int} (kJ mol^{-1}) values are estimated as $1/2V$, the constant being in $bohr^3$ units; structural parameters d (Å) and ω (%) are repeated from Table V.3 for clarity. [b] First and second lines correspond to experimental and theoretical (VASP calculations) data. See Table V.3 for symmetry codes.

The ratio $|V|/G < 1$ classifies the four contacts as *pure* closed-shell interactions of weak intensity,[34c] allowing the use of the potential energy density for the estimation of the interaction energy ($E_{int} \sim V/2$).[34b,144] Accordingly, the four interaction energies are small and close to each other ($|E_{int}| \sim 3\text{-}5$ kJ mol^{-1}), being quite similar to those found in the theoretical calculations, involving Chal···Chal and weak Chal···LB chalcogen bonding.[117,122]

Comparing the estimated E_{int} values derived for interactions involving homochalcogens, the Se···Se interaction is about 30 % more intense than S···S (3.8 kJ mol^{-1} *vs* 2.7 kJ mol^{-1}, as average between experimental and theoretical values). The observed tendency, supported by the calculated $|V|/G$ magnitudes (**Table V.4**), is in accordance with theoretical studies of Bleiholder *et al.*,[117a] showing that the strength of these contacts decreases in the order Te···Te > Se···Se > S···S > O···O, and reflects the tendency discussed in **Chapter IV** for Hal···Hal interactions ($|E_{int}|$ for Br···Br is 4.9 ± 1.2 kJ mol^{-1} and for Cl···Cl is 4.3 ± 1.1 kJ mol^{-1}). Remarkable, is the fact that, along the row from chalcogen to halogen atoms, the estimated value of E_{int} increases probably due to a higher dispersion contribution.

The $|E_{int}|$ magnitudes are quite similar to those found in the theoretical calculations (MP2/aug-cc-pVTZ level of theory, BSSE corrected) of three $(C_8O_2H_4Se)_2$ dimers at the experimental geometries, for which the calculated E_{int} and the estimated $E_{int} \sim V/2$ values (in kJ mol^{-1}) are 11.1/9.1 (Se···Se and Se···O interactions in dimer 1), 7.6/5.0 (Se···H interaction in dimer 2) and 19.3/21.3 (two O···H and one O···O interactions in dimer 3). The interaction energy of the corresponding trimer, approximated by the addition of the contributions of the three dimers, is 38.0/35.4 kJ mol^{-1}. As observed in a calculation employing a smaller basis set required for the large trimer size (MP2/6-311++G(d,p), see **Annex**), the interaction energy of the trimer (26.3 kJ mol^{-1}) is very close to the addition of the interaction energies of the three dimers (5.9, 4.8 and 15.5 kJ mol^{-1}), indicating that the effects of cooperativity can be neglected.

2.3. Analysis of Chal···X interactions from the $L(r)$ function

Compared to the $C_8O_2H_4Chal$ (Chal = S, Se) monomers (**Figure V.3**), the topological analysis of $L(\mathbf{r})$ in the crystal phase (experimental and theoretical) shows a smaller number of critical points in the valence shell of the S- and Se-atoms (**Figure V.7**). Indeed, only one pair of CD sites is observed, being located between the CD$_1$ and CD$_2$ sites determined for the isolated monomer (for S$_2$-atom γ(CD$_a$–nucleus–CD$_b$) = 137.9/138.1° and for Se-atom γ(CD$_a$–nucleus–CD$_b$) = 152.0/154.5° for experimental and theoretical models). The angular separation of the CC sites decreases from gas to crystal phases (in the latter, for S-atom β(CC$_a$–nucleus–CC$_b$)= 108.6/111.1° and for Se-atom β(CC$_a$–nucleus–CC$_b$)=118.3/119.9° for experimental and theoretical models). The observed differences can be caused by the influence of the molecular environment on $\rho(\mathbf{r})$ in the crystal phase or linked to the calculation method, used for the monomers.

Based on the Laplacian topology of chalcogen atoms in crystal phase, the geometry of atomic graphs for S- and Se-atoms are very similar and can be defined as a slightly distorted tetrahedron (**Figure V.7c**). There are four vertices: two non-bonded CCs and two bonded CCs, five edges and three faces. The atomic graphs of S$_1$ and S$_2$ in C$_3$HIOS$_2$ are essentially the same and for both atoms the topological analysis permits to distinguish between the two (3,–3) CP's (this was not clear from the qualitative description of the $L(\mathbf{r})$ maps of S-atoms in the perpendicular planes (**Figure III.17**)).

With this knowledge, it becomes possible to define the atomic sites that take part in the formation of intermolecular interactions and explain the geometrical differences observed between the two structures. Thus, in the crystal structure of C_3HIOS_2, the $S_2 \cdots I_1$ contact is obviously formed between a (3,+1) CP (CD site) of S_2, and a (3,–3) CP (CC site) of I_1, while the $S_1 \cdots S_2$ interaction involves a (3,+1) CP (CD site) of S_1, and a (3,–1) CP of S_2. The later critical point, having a saddle topology, can be considered here as a region of charge concentration in respect to the neighboring sites in the plane of the molecule. Thereby both chalcogen bondings in C_3HIOS_2 are of CD$\cdots$CC type (**Figure V.8a**). A different pattern is observed in $C_8O_2H_4Se$ (**Figure V.8b**). In this structure $Se_1 \cdots Se_1$ contact clearly shows a CD$\cdots$CC interaction (involving (3,+1) and (3, –3) CPs). However, the $Se_1 \cdots O_2$ is formed between a (3,–3) CP (CC site) of the O-atom and a (3, –1) CP of the Se-atom. Thereby, in this case, the (3,–1) CP behaves as a site of depletion of charge in the region between the two $\rho(\mathbf{r})$ maxima of Se. This example clearly demonstrates the dual nature of a type (3,–1) saddle point, behaving according to the molecular environment.

(a)   **(b)**   **(c)**
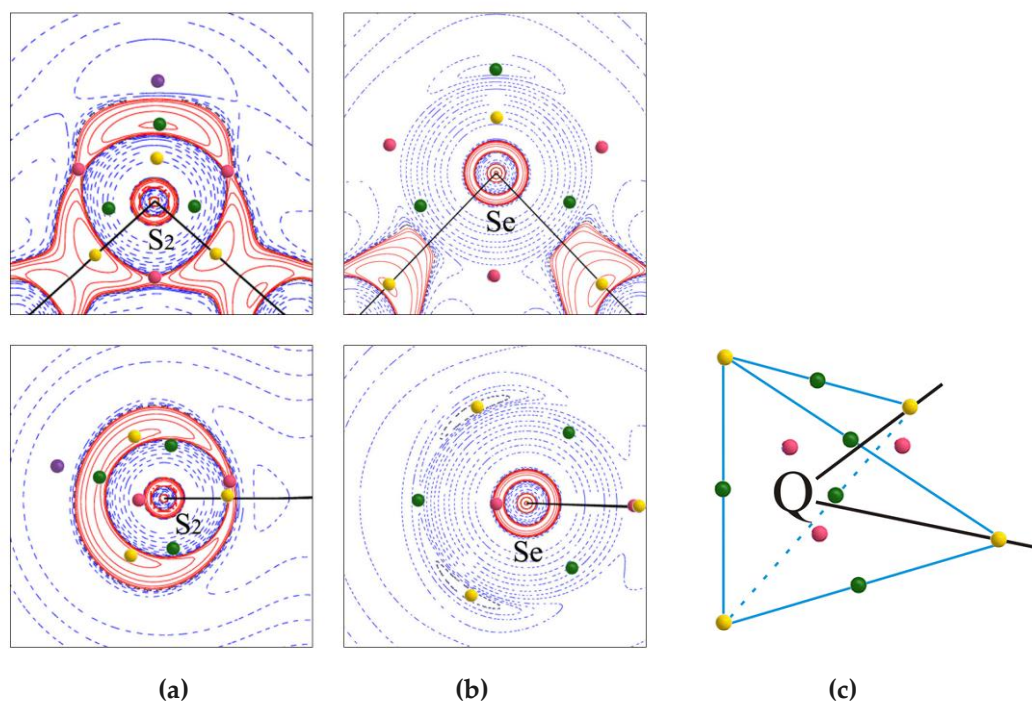
Figure V.7 Experimental $L(\mathbf{r}) = -\nabla^2\rho(\mathbf{r})$ maps around chalcogen atoms in (a) C_3HIOS_2 and (b) $C_8O_2H_4Se$. (C-Chal-C plane (top) and perpendicular plane bisecting the α(C-Chal-C) angle (bottom). $L(\mathbf{r})$ contours (eÅ^{-5}) are in logarithmic scale, red – positive, blue – negative. Laplacian critical points of the valence shell are represented: (3,–3) - yellow; (3,–1) - green, (3,+1) - pink, (3,+3) - violet. Theoretical calculation of $L(\mathbf{r})$ shows the same number and location of critical points for S- and Se-atoms. (c) Atomic graph of Chal-atom (Q) in the shape of tetrahedron with the CP's corresponding to vertices – yellow, edges – green and faces – pink.

The previous discussions confirm the suggested CD$\cdots$CC nature of the $S_1 \cdots S_2$, $Se_1 \cdots Se_1$ and $S_1 \cdots S_1$, $S_2 \cdots I_1$ interactions, while the relative location of the involved CC and CD sites can specify their directionality, which is not obvious from geometrical considerations only. The geometrical parameters, listed in **Table V.5** show that the angles formed between CD$\cdots$CC and internuclear

Chal⋯X directions are, on average 9.6±4.2°, whereas the BCP's of $\rho(\mathbf{r})$ and therefore the bond paths are placed nearby the CC–CD line (distances 0.21±0.11 Å). A very similar description is found for the theoretical multipolar model.

Though, the CD and CC sites face each other in the four intermolecular regions, indicating directional electrophilic–nucleophilic interactions where the Chal-atom interacts with the molecular environment by involving simultaneously its electrophilic and nucleophilic sites – situation already observed for halogen atoms (see **Chapter IV**). In particular, the S(CC)⋯(CD)S and Se(CC)⋯(CD)Se interactions can be considered as the analogue of type-II Cl⋯Cl and Br⋯Br interactions, respectively as studied in solid-Cl_2,[88a] and Hal_3-synthons (Hal = Cl, Br).

(a)   (b)
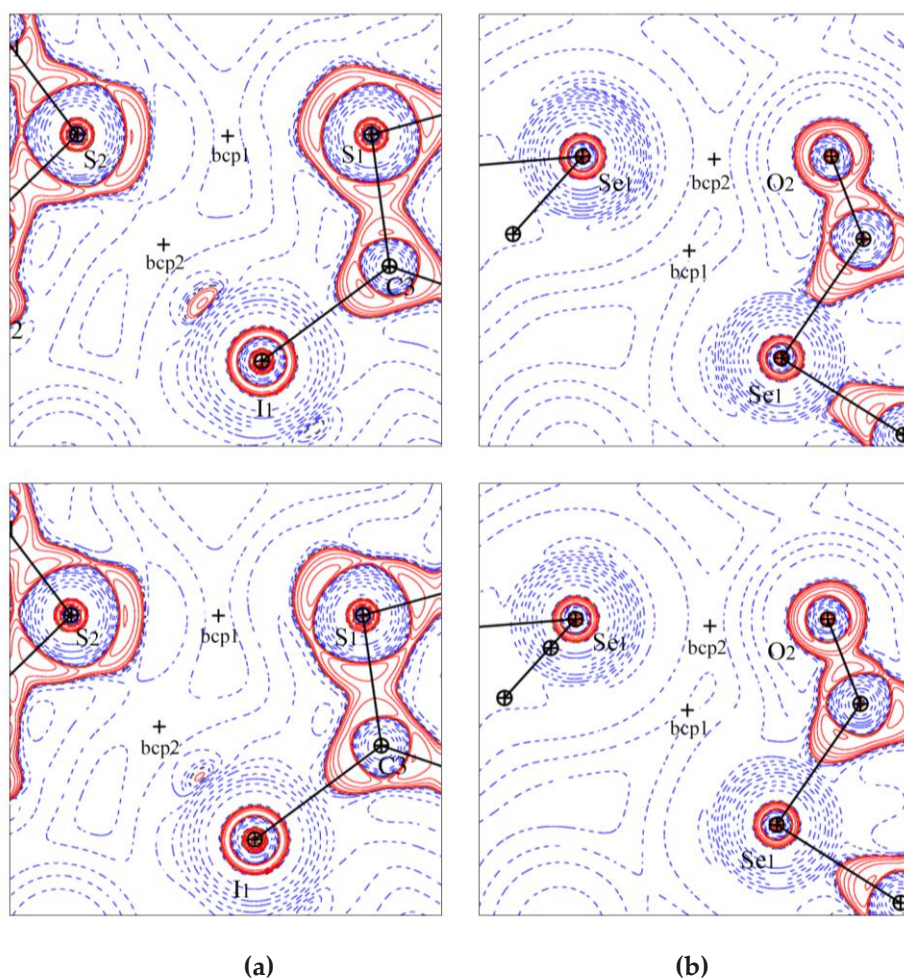
Figure V.8 Experimental (top) and theoretical (bottom) $L(\mathbf{r}) = -\nabla^2\rho(\mathbf{r})$ maps in the intermolecular region for (a) $C_8O_2H_4Se$ and (b) C_3HIOS_2. $L(\mathbf{r})$ contours (e$Å^{-5}$) are in logarithmic scale, red – positive, blue – negative.. Intermolecular bcp's and CD/CC sites (see **Figure V.6** for colors description), involved in the intermolecular interaction are depicted.

The quantitative analysis of the CC/CD sites of the chalcogen atoms can be performed with the L/ρ parameter calculated in these points. In accordance with the $L(\mathbf{r})$ map of S_1-atom, that do

not permit to distinguish between its two maxima ((3,–3) CP's) and a saddle point ((3,–1) CP), the values of the L/ρ parameter at these points are very close.

In general, the electrophilic/nucleophilic power of the CC/CD sites decreases from gas (**Table V.2**) to crystal (**Table V.6**) phases. This feature, already noted for halogen atoms (see **Chapter IV**), can be understood as a consequence of the dielectric screening in the crystal.

Table V.5 Geometrical parameters showing the directionality of the CC···CD interactions in the crystal phases of C_3HIOS_2 and $C_8O_2H_4Se$.[a] Experimental (left) and theoretical (right) values.

$Chal_{CD}$···X_{CC}	d_{CD}	d_{CC}	d_{BCP}	ξ_1	ξ_2	θ
S_{CD}···S_{CC}	0.28/0.35	0.10/0.07	0.13/0.18	161.3/165.6	159.1/162.3	5.1/13.2
Se_{CD}···Se_{CC}	0.21/0.35	0.39/0.41	0.21/0.37	105.6/106.5	112.8/123.5	15.7/13.9
S_{CD}···I_{CC}	0.41/0.33	0.08/0.05	0.06/0.12	155.6/158.9	162.0/165.3	7.5/6.0
Se_{CD}···O_{CC}	0.35/0.42	0.15/0.18	0.34/0.29	105.8/112.6	121.2/123.4	5.2/10.1

[a] d_{CC}/d_{CD} (Å) are the distances from the CC/CD sites to the bonding line between the interacting atom nuclei; d_{BCP} is the distance from the BCP of $\rho(\mathbf{r})$ to the CC–CD direction. The angles ξ_1/ξ_2 (°) are defined as (C–$Chal_{nucl}$···$Chal_{CP}$) and (C–$Chal_{nucl}$···X_{CP}, X = Chal, Hal, LB); θ (°) is the angle defined between the CC–CD and Chal–X directions. For symmetry codes see **Table V.3**.

Comparing S- and Se-atoms between each other in a crystal phase, we observe an increased electrophilic and much more decreased nucleophilic power for the heavier chalcogen, resulting in a weaker electrostatic contribution in the case of Se···Se than in the case of S···S interaction. These observations are in accordance with the theoretical calculations that show significant electrostatic contribution only for lighter chalcogens (O and S), while for the heavier atoms (Se and Te), induction and dispersion forces dominate.[117,122]

Table V.6 Electrophilic and nucleophilic power (L/ρ in Å^{-2}) of CD and CC sites in the electron valence shell of the S- and Se-atoms in the crystal phase of C_3HIOS_2 and $C_8O_2H_4Se$. [a]

CP notation	Site	S_1	S_2	Se
(3,–3)	CC_a	9.11/9.23	8.37/8.73	–0.22/–0.28
(3,–3)	CC_b	8.92/9.33	3.03/9.45	–0.23/–0.38
(3,+1)	CD_a	1.33/1.24	0.79/1.08	–2.76/–3.52
(3,+1)	CD_b	0.86/1.17	1.09/0.98	–2.88/–3.54
(3,–1)	CD or CC	8.70/9.21	7.83/7.98	–0.35/–0.91

[a] First and second values correspond to the experimental and theoretical data, respectively.

A close comparative look to Br···Br interactions in the crystal structures of C_6Br_6 and C_6Br_5OH indicates that the electrophilic/nucleophilic power of CD/CC sites of the Se-atom in $C_8O_2H_4Se$ is less pronounced than those found for Br-atoms (–7.7 < $(L/\rho)_{CD}$ < –4.1 Å^{-2} and 0.5 < $(L/\rho)_{CC}$ < 4.1 Å^{-2}). As measured from $\Delta(L/\rho)$, the resulting electrostatic interaction is greater for Br···Br ($\Delta(L/\rho)$ = 6.8 ± 2.6 Å^{-2}) than for Se···Se (**Table V.4**). Along with the electrostatic descriptor $\Delta(L/\rho)$, the estimated interaction energy E_{int} for Se···Se is also lower in magnitude than that of Br···Br (<E_{int}> = 5.1 ± 1.2 kJ mol^{-1} with <$d_{Br···Br}$> = 3.62 ± 0.11 Å). An inverse situation is observed comparing the Cl- and S-atoms – the nucleophilic power of CC regions is very close, but the electrophilic power of CD regions are much more important for S, coursing the greater electrostatic power of S···S

interaction. These disagreements could be explained by the different environment and hybridization of the compared Hal- and Chal-atoms.

Thereby, on the example of chalcogen bonding interactions we have illustrated that the synthon arrangement can be formed not only involving similar atoms, like in Hal_3-synthons, but also involving similar sites in contact formation (CC⋯CD).

3. Other close-shell interactions involving Chal-atoms

As it was shown in the previous section, chalcogen bonding Chal⋯X in $C_8O_2H_4Se$ and C_3HIOS_2, being numerous and directional, contribute to the connectivity in the crystal packing. At the same time, other closed-shell intermolecular contacts involving Chal-atoms in the two compounds, being by itself quite weak and non-directional, allow the packing efficiency when combined together. For example, in the C_3HIOS_2 crystal structure, the stacking of the columns along the a-direction is provided by the intracolumn S⋯I, S⋯C, and two S⋯O contacts (all together reflecting π⋯π interaction); they permit the neighboring molecules to approach to each other with an intramolecular distance of 2.541 Å. In the crystal structure of $C_8O_2H_4Se$, the O_2⋯O_2 contact between the molecules in the same plane provides the formation of the layers along with the numerous hydrogen bonding. In addition,, the intercolumn contacts are provided by several C⋯C and O_2⋯O_1, Se⋯C contacts, with greater intermolecular distance than in the previous case (2.986 Å). In the crystal structure of C_6Cl_5OH, intermolecular Cl⋯O interactions follow the hydrogen bonding chain along the b-axis direction. In the crystal structure of C_6Br_5OH, the BCP is observed between the atoms O_6 and Br_1 of the facing molecules (interatomic distance being 103.7 % from the sum of the van der Waals radii of O and Br atoms), in contrast to the previously reported structure,[150] where this contact was not described.

Hereafter these intermolecular contacts will be characterized from the $\rho(\mathbf{r})$ and $L(\mathbf{r})$ functions.

3.1. Structural characterization

Table V.7 gathers geometrical characteristics of the observed interactions. The penetration parameter ω shows the disperse character of the interaction distances, varying from very short (99.1% for O_6⋯Cl_1) to very long (114.4% for S_1⋯O_1) ones. Most of the interactions are between adjacent molecules placed parallel to each other (intracolumn); for the others, θ_1 and θ_2 angles permit to characterize their geometry. According to these angles, the contact O_2⋯O_2 resembles the Type-I Hal⋯Hal interaction created between electrostatically identical regions of the adjacent atoms. The θ_2-angles for O⋯Br and O⋯Cl contacts are far from 180°, showing that δ^+ regions of Cl- and Br-atoms are not involved in the interactions formation.

Table V.7 Structural characteristics of intermolecular interactions involving Chal-atoms in $C_8O_2H_4Se$, C_3HIOS_2, C_6Br_5OH and C_6Cl_5OH.[b]

	Chal⋯X[a]	d	ω	θ_1	θ_2
C_3HIOS_2	**$S_1{}^i$⋯$O_1{}^{iv}$	3.7995(3)	114.4	—	—
	**$S_2{}^i$⋯$O_1{}^{iv}$	3.7434(2)	112.7	—	—
	**$S_1{}^{iv}$⋯$I_1{}^i$	3.8189(1)	101.0	—	—
	**$S_2{}^{iv}$⋯$C_2{}^i$	3.5944(1)	105.5	—	—

C$_8$O$_2$H$_4$Se	*O$_2^i$···O$_2^{iii}$	3.4096(1)	112.2	120.14(2)	120.14(2)
	**O$_2^i$···O$_1^{iv}$	3.2125(2)	105.7	—	—
	**Se$_1^i$···C$_6^v$	3.8505(2)	105.5	—	—
C$_6$Cl$_5$OH	*O$_6^i$···Br$_1^{viii}$	3.4966(1)	103.7	149.14(1)	97.99(2)
C$_6$Cl$_5$OH	*O$_6^i$···Cl$_1^{xi}$	3.2412(1)	99.1	151.56(1)	105.47(2)
	*O$_6^i$···Cl$_5^{xii}$	3.4763(1)	106.3	96.39(2)	137.31(2)

[a] (*) intercolumn interactions, (**) intracolumn interactions. [b] Distance Chal···X (d /Å), penetration parameter (ω /%) listed for all the interaction; angles θ_1 (C–Chal···X) (°), θ_2 (Chal···X–C) (°) are performed just for the intercolumn interactions. The structural parameters correspond to the multipolar models described in Chapter III. Summetry codes: C$_3$HIOS$_2$: (i) x, y, z; (iv) -1+x, y, z; C$_8$O$_2$H$_4$Se: (i) x, y, z; (iii) -x, 2-y, 1-z; (iv) x, 1+y, z; (v) –x, 1-y, 1-z. C$_6$Cl$_5$OH (i) x, y, z; (xi) 1/2–x, 1/2+y, 1/2–z; (xii) 1/2–x, –1/2+y, 1/2–z; C$_6$Br$_5$OH (i) x, y, z; (viii) 2–x, 1/2+y, 2–z.

3.2. Interaction analysis from $\rho(r)$ and $L(r)$ functions

The existence of bonding interactions at the distances discussed here was stated from the presence of bond paths and concomitant intermolecular BCP's. The gradient maps show the interatomic surfaces of the atoms in interaction for the four chalcogenated crystal structures (**Figures V.9, V.10, V.11**).

(a) **(b)** **(c)**
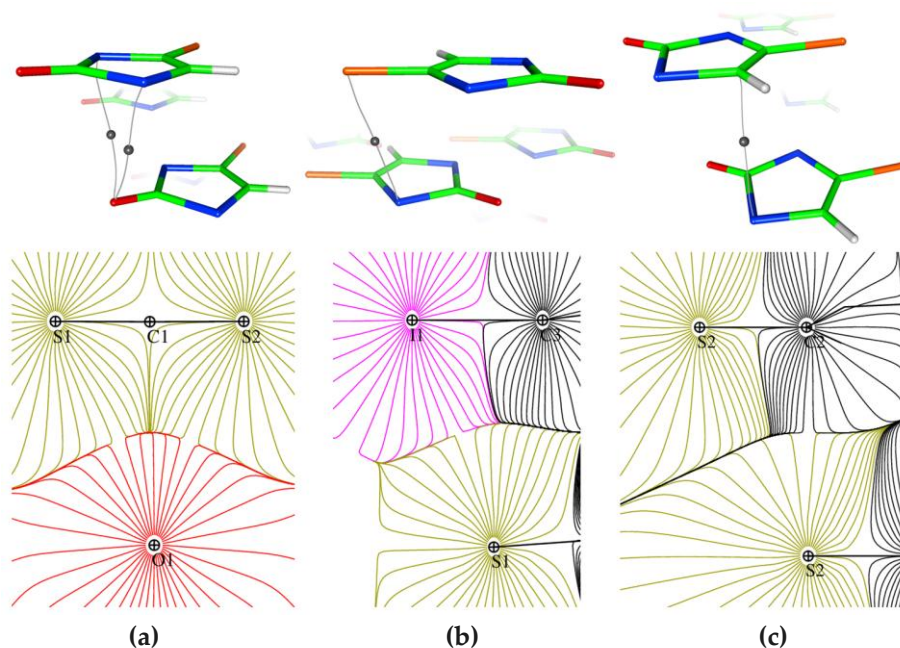
Figure V.9 Intermolecular interactions involving S-atoms in the crystal structure of C$_3$HIOS$_2$ (experimental model, theoretical one show similar features), represented by the bond paths and the corresponding BCP's between the interacting atoms (top) and by the gradient $\nabla\rho(\mathbf{r})$ maps (bottom): (a) S$_1$···O$_1$ and S$_1$···O$_1$, (b) S$_1$···I$_1$ and (c) S$_2$···C$_2$ contacts.
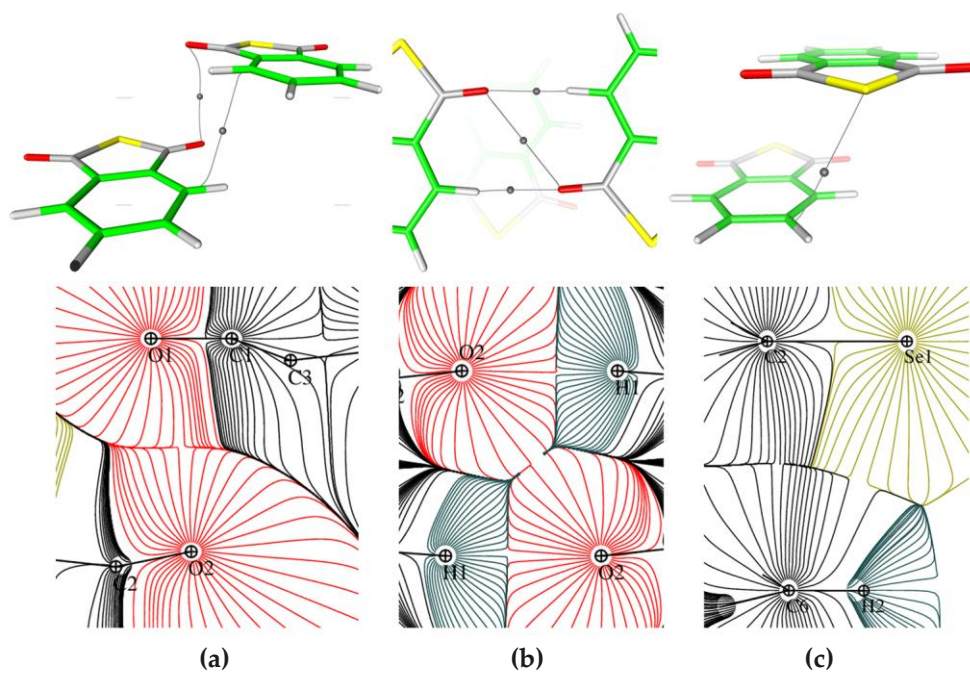
Figure V.10 Intermolecular interactions involving O- and Se-atoms in the crystal structure $C_8O_2H_4Se$ (experimental model), represented by the bond paths and the corresponding BCP's between the interacting atoms (top) and by the gradient $\nabla\rho(\mathbf{r})$ maps (bottom): (a) $O_2{\cdots}O_1$, (b) $O_2{\cdots}O_2$, (c) $Se{\cdots}C_6$.
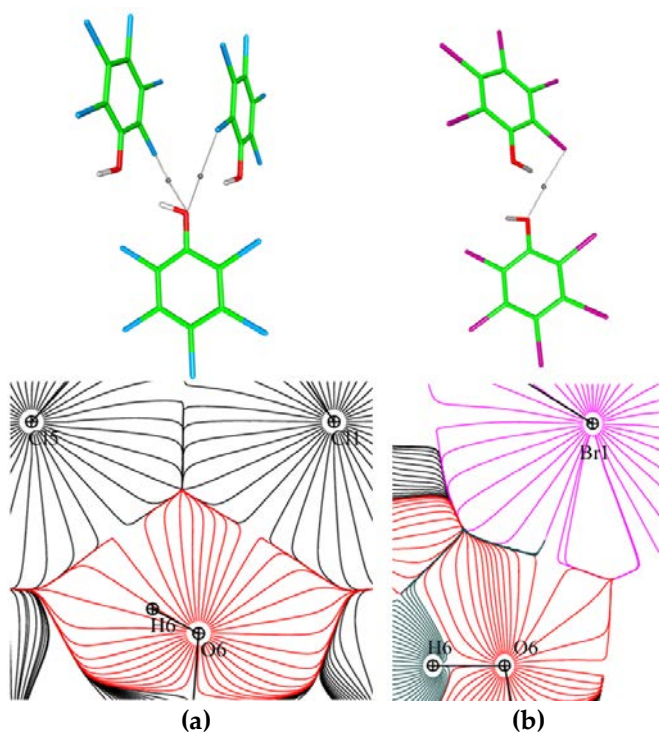
Figure V.11 Intermolecular interactions involving O-atoms in the crystal structures of (a) C_6Cl_5OH ($O_6{\cdots}Cl_1/Cl_5$) and (b) C_6Br_5OH ($O_6{\cdots}Br_1$), represented by the bond paths and the corresponding BCP's between the interacting atoms (top) and by the gradient $\nabla\rho(\mathbf{r})$ maps (bottom).

Figures **V.12, V.13, V.14** show the experimental static deformation density $\Delta\rho(\mathbf{r})$ and Laplacian $L(\mathbf{r})$ maps for each contact. In the crystal structure of C_3HIOS_2, O-atom forms intermolecular interactions simultaneously with the two S-atoms above (**Figures V.12a**). Being located just between these two atoms, it results in the longest and weakest (according to the topological properties) intermolecular interactions in the crystal structure. From the viewpoint of the $L(\mathbf{r})$ topology, the two interactions probably occur between the (3,–1) CP of S-atom (see **Figure V.7a**) and the (3,–3) CPs of O-atom. These interactions between the parallel molecules, along with the S···Cπ contact (**Figures V.12c**), provide such a short interplane distance and support the columns rigidity. They could be also a reason of rather short interaction distance between I_1 and S_1–atoms (**Figure V.7b**) with the strongest topological parameters (see **Table V.8**).

(a)   **(b)**   **(c)**
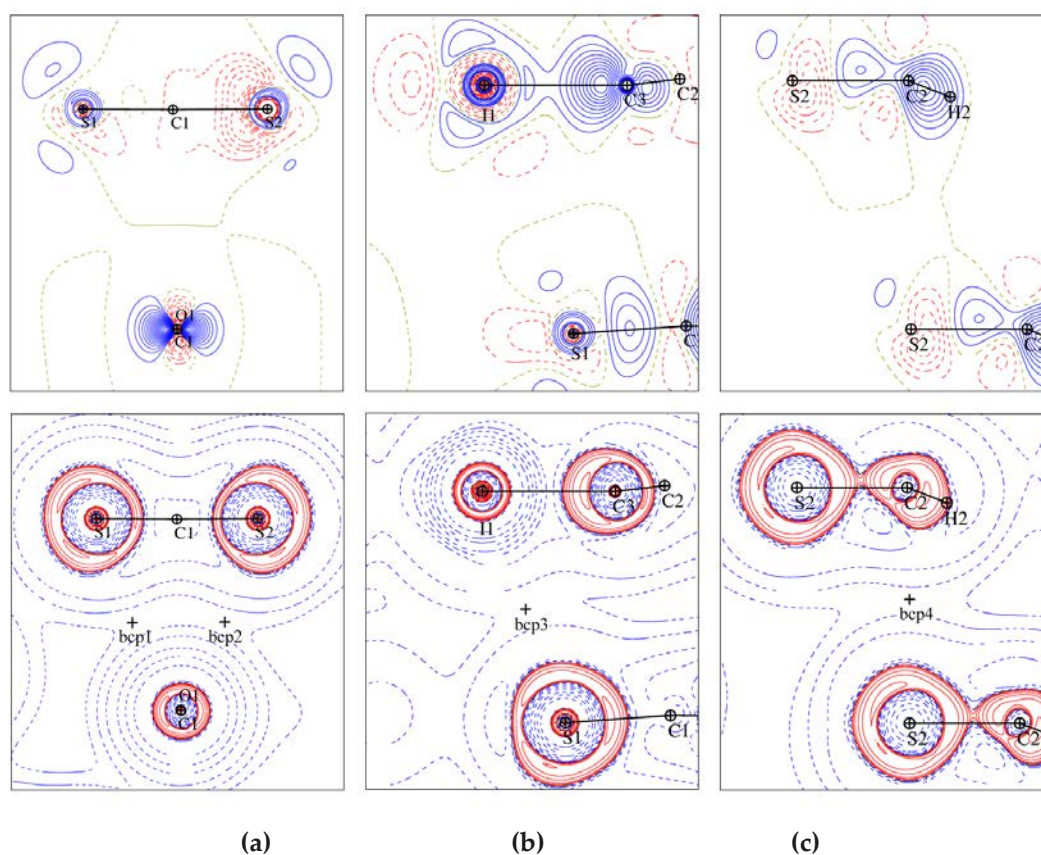
Figure V.12 Experimental static deformation density maps $\Delta\rho(\mathbf{r})$ (top) and Laplacian maps $L(r)$ (bottom) in the intermolecular regions of interactions involving S-atoms in the crystal structure of C_3HIOS_2: (a) S_1···O_1 and S_1···O_1, (b) S_1···I_1 and (c) S_2···C_2 contacts. $\Delta\rho(\mathbf{r})$ contours are at ±0.05 eÅ^{-3}, blue – positive, red – negative; $L(\mathbf{r})$ contours (eÅ^{-5}) are in logarithmic scale, red – positive, blue – negative. Theoretical model show similar features.
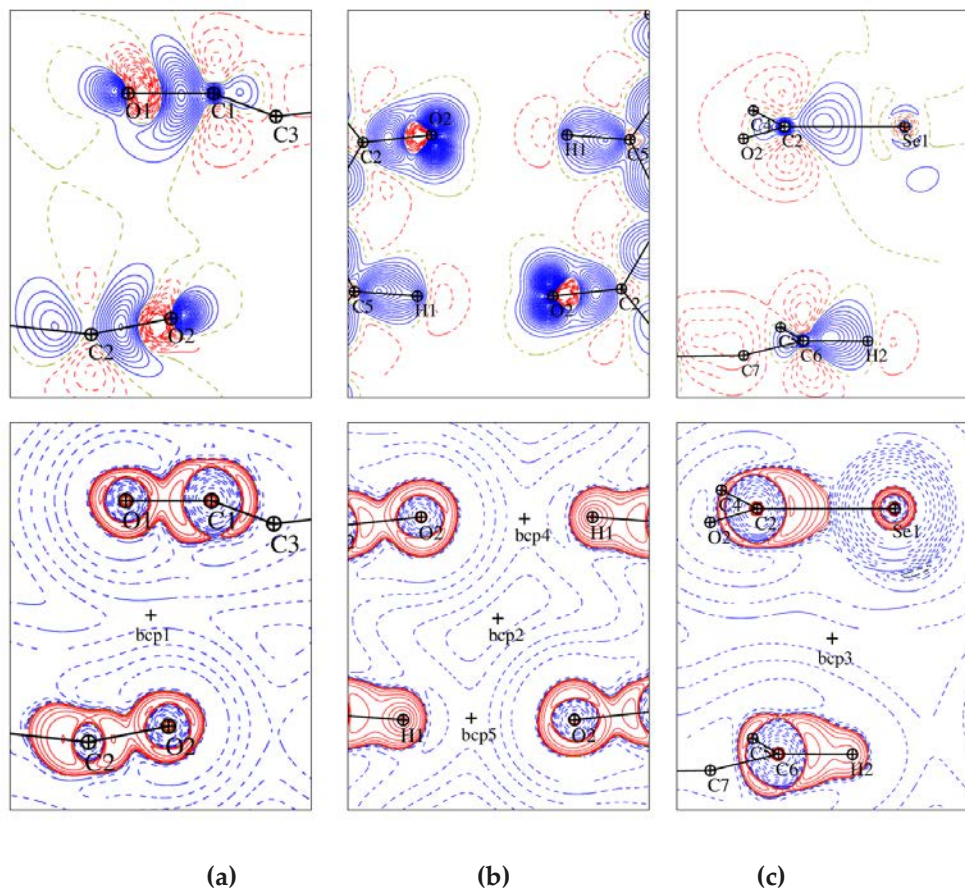
Figure V.13 Experimental static deformation density maps $\Delta\rho(\mathbf{r})$ (top) and Laplacian maps $L(\mathbf{r})$ (bottom) in the intermolecular region of interactions involving O- and Se-atoms in the crystal structure $C_8O_2H_4Se$: (a) $O_2\cdots O_1$ (b) $O_2\cdots O_2$, (c) $Se\cdots C_6$ contacts. $\Delta\rho(\mathbf{r})$ contours are at ±0.05 eÅ^{-3}, blue – positive, red – negative; $L(\mathbf{r})$ contours (eÅ^{-5}) are in logarithmic scale, red – positive, blue – negative.

For defining the real origin of the pointed contacts in $C_8O_2H_4Se$, a deeper investigation is needed. However, in general, in the interactions observed here the atoms tend to approach to each other mostly with their δ^- regions. Accordingly, the classification applied for Type-I Hal$\cdots$Hal contacts (**Figure IV.7**) is also valid here, even if for the considered cases only *side-side* type can be observed. It can be clearly seen on the $O_2\cdots O_2$ interaction in $C_8O_2H_4Se$ (**Figure V.13**), which is formed thanks to the hydrogen bond $H_1\cdots O_2$ – the strongest one in this structure, and $O_6\cdots$Hal contacts in C_6Hal_5OH (**Figure V.14**), Maps plotted from the theoretical model for $C_8O_2H_4Se$ and C_3HIOS_2 qualitatively disclose very similar features.

(a)   **(b)**
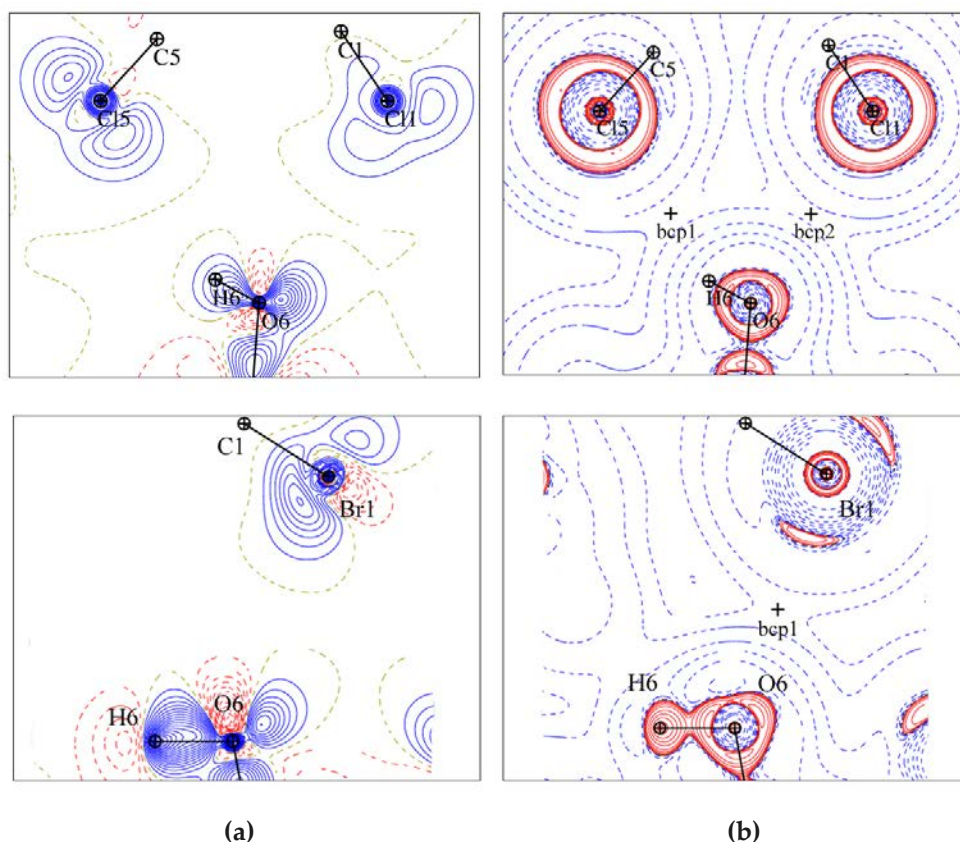
Figure V.14 (a) Experimental static deformation density $\Delta\rho(\mathbf{r})$ and (b) Laplacian $L(\mathbf{r})$ maps in the crystal structure of C_6Cl_5OH ($O_6\cdots Cl_1/Cl_5$) (top) and C_6Br_5OH ($O_6\cdots Br_1$) (bottom). $\Delta\rho(\mathbf{r})$ contours are at ± 0.05 eÅ^{-3}, blue – positive, red – negative; $L(\mathbf{r})$ contours (eÅ^{-5}) are in logarithmic scale, red – positive, blue – negative.

Local topological properties of $\rho(\mathbf{r})$ at BCP's, obtained from both experimental and theoretical modeling (**Table V.8**) show a wide range of parameter-magnitudes (which is actually in accordance with the high dispersion of interaction distances). From the ratio $|V|/G$ all the contacts can be classified as *pure* closed-shell interactions ($0.58 < |V|/G < 0.83$), allowing the estimation of the interaction energy from the potential energy density ($E_{int} \sim V/2$). These values ($-5.3 < E_{int} < -1.5$ kJ mol^{-1}) are comparable wih the very weak hydrogen bonding (< 5 kJ mol^{-1}). The observed Chal$\cdots$C$_\pi$ contacts for Se- and S-atoms show the same penetration of the van der Waals radii and accordingly very close interactions energies ($E_{int} = -2.7$ and -2.4 kJ mol^{-1}), as well as $|V|/G$ ($|V|/G = 0.72$ in both cases) and H/ρ ($H/\rho = 425$, 392 kJ mol^{-1}e^{-1}) values. Based on these parameters, Chal$\cdots$C$_\pi$ contacts are slightly weaker than those already characterized for Hal-atoms ($E_{int} = -3.6$ and -3.2 kJ mol^{-1} for Cl$\cdots$C$_\pi$ and Br$\cdots$C$_\pi$, respectively). In general, for these interactions, the topological properties tend to increase with the distance shortening, like for all the interactions investigated in this work.

Table V.8 The topological parameters for the interactions involving Chal-atom in the crystal structures of C_3HIOS_2, $C_8O_2H_4Se$, and C_6Cl_5OH. [a]

	Interaction [c]	d, ω	ρ	$\nabla^2\rho$	λ_1	λ_2	λ_3	G	V	E_{int}	$|V|/G$	H/ρ
C_3HIOS_2 [b]	**$S_1^i \cdots O_1^{iv}$	3.7995(3),114.4	0.025	0.29	−0.04	−0.02	0.34	5.8	−3.9	−1.9	0.67	526
			0.023	0.27	−0.03	−0.01	0.31	5.5	−3.6	−1.8	0.66	549
	**$S_2^i \cdots O_1^{iv}$	3.7434(2), 112.7	0.026	0.31	−0.04	−0.03	0.37	6.3	−4.2	−2.1	0.67	542
			0.024	0.29	−0.04	−0.03	0.36	6.0	−3.9	−2.0	0.66	568
	**$S_1^{iv} \cdots I_1^i$	3.8189(1), 101.0	0.053	0.46	−0.09	−0.08	0.63	10.8	−8.9	−4.5	0.83	237
			0.051	0.47	−0.08	−0.05	0.60	10.7	−8.6	−4.3	0.81	273
	**$S_2^{iv} \cdots C_2^i$	3.5944(1). 105.5	0.033	0.35	−0.04	−0.03	0.41	7.33	−5.3	−2.7	0.72	425
			0.036	0.35	−0.06	−0.05	0.46	7.54	−5.6	−2.8	0.74	366
$C_8O_2H_4Se$ [b]	*$O_2^i \cdots O_2^{iii}$	3.4096(1), 112.2	0.015	0.26	−0.04	−0.01	0.30	5.0	−2.9	−1.5	0.58	945
			0.016	0.27	−0.04	−0.01	0.31	5.2	−3.1	−1.6	0.60	945
	**$O_2^i \cdots O_1^{iv}$	3.2125(2), 105.7	0.040	0.57	−0.11	−0.06	0.74	11.8	−8.1	−4.1	0.68	624
			0.036	0.52	−0.08	−0.03	0.64	10.7	−7.2	−3.6	0.67	656
	**$Se_1^i \cdots C_6^v$	3.8505(2), 105.5	0.031	0.31	−0.06	−0.03	0.40	6.5	−4.7	−2.4	0.72	392
			0.029	0.28	−0.05	−0.04	0.49	5.7	−4.0	−2.0	0.70	396
C_6Br_5OH	*$O_6 \cdots Br_1^{viii}$	3.4966(1), 103.7	0.034	0.48	−0.08	−0.06	0.62	9.8	−6.6	3.3	0.67	365
C_6Cl_5OH	*$O_6^i \cdots Cl_1^{xi}$	3.2412(1), 99.1	0.049	0.71	−0.13	−0.12	0.97	15.0	−10.6	−5.3	0.71	606
	*$O_6^i \cdots Cl_5^{xii}$	3.4763(1), 106.3	0.043	0.57	−0.11	−0.10	0.78	11.9	−8.4	−4.2	0.71	549

[a] The parameters ρ (eÅ^{-3}), $\nabla^2\rho$ (eÅ^{-5}), λ_i (eÅ^{-5}), G and V (kJ mol^{-1} bohr^{-3}) are calculated at the BCP's of $\rho(\mathbf{r})$; H/ρ is in kJ mol^{-1}e^{-1} ($H = V + G$); E_{int} (kJ mol^{-1}) values are estimated as $1/2V$, the constant being in bohr^3 units; structural parameters d (Å) and ω (%) are repeated from Table V.7 for clarity. [b] First and second lines correspond to experimental and theoretical (VASP calculations) data. [c] (*) intercolumn interactions, (**) intracolumn interactions. See Table V.7 for symmetry codes.

Summary

In accordance with the second objective of our work, this chapter is dedicated to the investigation of intermolecular interactions involving chalcogen atoms in the crystal structures of C_3HIOS_2, $C_8O_2H_4Se$, and C_6Cl_5OH. Based on their main characteristics – directionality and strength – we distinguish between chalcogen bonding (*σ-hole* interaction) and other Chal-involved contacts.

Chalcogen bonding was established as a directional electrophilic–nucleophilic interaction, with facing each other $CD(\delta^+)/CC(\delta^-)$ regions. As a consequence of the $\rho(\mathbf{r})$ polarization in the chemical bond and the sp^3 hybridization of the chalcogen atom, CD/δ^+ regions are observed approximately along the C–Chal directions and give rise to two σ-holes in the electrostatic potential, while CC/δ^- regions are in the perpendicular plane bisecting the C–Chal–C group and coincide with the location of the lone pairs. The electrophilic/nucleophilic intensity of the CD/CC regions is quantitatively monitored by the L/ρ parameter. The concerted increase/decrease of the extension of CD/CC regions along the series O < S < Se < Te follows the progressive depletion of $\rho(\mathbf{r})$ in the chalcogen valence shell. In this process, topological CD sites dominate a progressively enlarged electrophilic region within the C-Chal-C plane, while two nucleophilic regions significantly separate and weaken in a perpendicular disposition to the former.

The electrostatic power of CD···CC interactions, estimated from the electrostatic descriptor $\Delta(L/\rho) = (L/\rho)_{CC} - (L/\rho)_{CD}$, is more pronounced for S···S than for Se···Se interactions. Last trend is actually in accordance with results observed in the literature coming from theoretical calculations. In contrast, according to interaction energy estimations E_{int}, Se···Se (3.8 kJ mol^{-1}) appears to be stronger than S···S (2.7 kJ mol^{-1}).

On the example of the studied bifurcated chalcogen bonding interactions it is shown that the synthon arrangement can be formed not only involving similar atoms, like in Hal$_3$-synthons, but also involving similar sites in contact formation (CC···CD).

On the other hand, Chal-atoms tend to form intermolecular contacts displaying a wide distance range. The topological analysis of $\rho(\mathbf{r})$ characterizes the Chal···X (X = Hal, Chal, LB) contacts as pure closed-shell interactions of very weak strength. Being numerous, they provide packing efficiency in the studied compounds.

Chapter VI

Compromise arrangement of different intermolecular interactions in crystal structures

In the final chapter of our work, we analyze the hydrogen bonding interactions in the crystal structures of C_6Hal_5OH (Hal = Cl, Br), C_3HIOS_2, and $C_8O_2H_4Se$ from the $\rho(\mathbf{r})$ and $L(\mathbf{r})$ functions. The interactions are characterized qualitatively, based on the structural characteristics and on the analysis of the $\Delta\rho(\mathbf{r})$ and $L(\mathbf{r})$ maps in the intermolecular regions, as well as quantitatively, based on the estimated interaction energy criterion E_{int} and the calculated electrostatic descriptor L/ρ. The attention is paid to the comparison of the halogen and chalcogen intermolecular interactions, investigated in the previous chapters, with the hydrogen bonding within the same crystal structure. The conclusions are made on the effectiveness of these interactions in driving specific crystal packing and their use for crystal engineering purposes. Finally, the analysis of the topological properties at BCP's of all intermolecular interactions studied in this work is performed, permitting to classify them into different families and to reveal universal features for all families together.

*Any crystal structure is the result of a compromise
between the demands of many weak
intermolecular interactions.*
G.R. Desiraju

Introduction

In complex systems with the presence of several types of non-covalent interactions, a competition occurs among them. For certain cases, the knowledge about their structural advantages permit to control the cocrystallization reactions.[170] It was pointed out that, exhibiting many similarities, *σ-ho*le bonding (halogen and chalcogen interactions) and hydrogen bonding can certainly compete with each other.[77f,78,171] Alkorta et al. studied the competition of hydrogen bonds and halogen bonds in complexes of hypohalous acids with nitrogenated bases (NH_3, N_2, and NCH).[171d] In $H_2CO–HOX$ (X = F, Cl, and Br) complexes, it was shown that the hydrogen bond is stronger than the halogen bond.[172] In $H_2SO–HOX$ complexes, the difference in the strength of both interactions is decreased for the system where X = Cl, while the Br-involved halogen bond is even stronger than the hydrogen bond.[173] A theoretical evidence for the competition of hydrogen bond and *σ-hole* interactions in $CS_2–HF$ were found.[174] The most recent theoretical studies concerning the competing interactions were performed by Q.-Z. Li and co-workers, showing the close strength of hydrogen and halogen bonding interactions.[119]

In the present work, the studied crystal structures are organized by a compromise arrangement of different intermolecular contacts; four of them, showing the competition of halogen or chalcogen bonding with hydrogen bonding, will be discussed in details hereafter.

1.   Intermolecular interactions in C_6Hal_5OH

A particular feature of the structures containing the OH-group (C_6Cl_5OH and C_6Br_5OH) is the existence of hydrogen bondings linking the molecules into an infinite chain along the *b*-axis direction at the opposite side of the molecule where halogens form Hal_3-synthons (**Figures III.7b and III.10d**). As a consequence, hydrogen bondings play a significant role in directing the packing of the molecules in the crystal lattice of these compounds. A first assumption about the existence and the significance of the hydrogen bonding in the present crystal structures was based on IR spectra.[150] Actually, the charge density approach and the associated topological analysis at the hydrogen bonding critical points (3,–1) allow us to evaluate quantitatively the strength of the interactions and to put it in comparison with that of Hal_3-synthons.

1.1. Structural characterization of hydrogen bonding

The geometry of hydrogen bonding in the crystal structures of C_6Cl_5OH and C_6Br_5OH, which contain Hal_3-synthons of different types, is also different (**Figure VI.1**). Indeed, additional intramolecular hydrogen bonding is formed between H- and Br-atoms in C_6Br_5OH. This

intramolecular interaction can be a reason for the observed lower intermolecular hydrogen-bond angle (see θ(O–H···X) values). The longer distance between oxygen atoms in C_6Cl_5OH is probably due to the formation of other O-involved interactions with the two *ortho*-Cl-atoms of adjacent molecules in contrasted to only one O···Br interaction in C_6Br_5OH (as discussed in **Chapter V**).

Table VI.1 Geometry of hydrogen bonding interaction in the structures of C_6Cl_5OH and C_6Br_5OH.

compound	interaction	d(O–H), Å	d(H···X), Å	d(O···X), Å	$\omega_{H···X}$ / $\omega_{O···X}$, %	θ(O–H···X), °
C_6Cl_5OH	O_6–H_6^{xi}···O_6^i	0.964	2.043	2.9283(1)	75.1/ 96.3	151.75
C_6Br_5OH	O_6–H_6^{viii}···O_6^i	0.967	2.228	2.8491(5)	81.9/93.7	120.95
C_6Br_5OH	O_6–H_6^i···Br_1^i	0.967	2.285	3.0302(1)	74.9/89.9	133.25

Summetry codes: C_6Cl_5OH (i) x, y, z, (xi) 1/2–x, 1/2+y, 1/2–z; C_6Br_5OH (i) x, y, z, (viii) 2–x, 1/2+y, 2–z.

1.2. Hydrogen bonding from the topology of ρ(r) and L(r)

Figure VI.1 shows hydrogen bonding chains along the *b*-axis direction in C_6Cl_5OH and C_6Br_5OH crystal structures with the corresponding BCP's. The existence of the BCP's is also evident from the gradient lines.
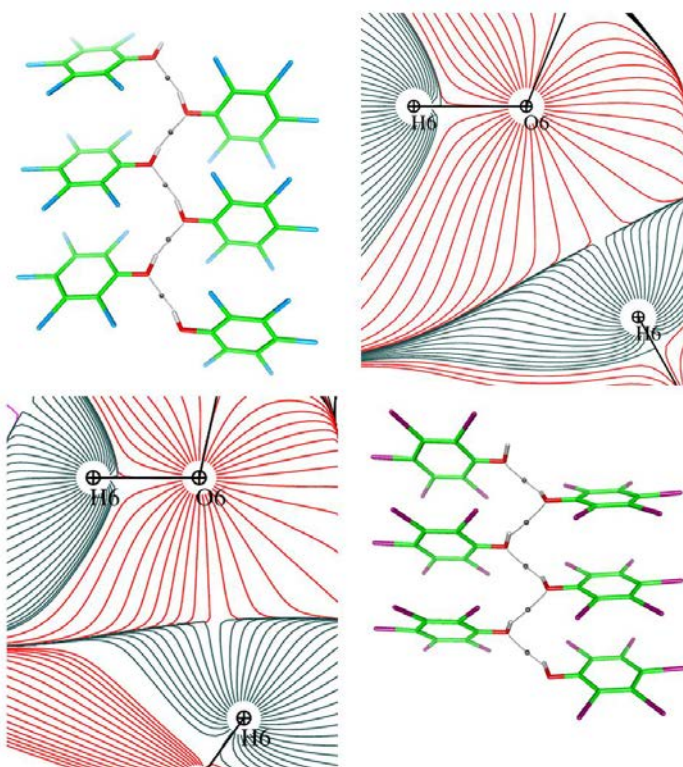
Figure VI.1 Geometrical representation of hydrogen bonding chains and $\nabla\rho(\mathbf{r})$ maps in the intermolecular region in C_6Cl_5OH (top) and C_6Br_5OH (bottom). The BCP's corresponding to H···O interactions are represented as grey points.

The plots of the experimental deformation density maps in the hydrogen bond regions (**Figure VI.2top**) suggest the interactions of type $H(\delta^+)\cdots(\delta^-)X$, (X = O, Br). However, the geometrical differences for the three observed interactions are reflected in their different relative orientation of δ^- and δ^+ regions. The location of the interacting charge concentration (CC) and charge depletion (CD) regions can be clearly seen from the Laplacian maps (**Figure VI.2bottom**). CD and CC regions, facing each other for $H_6\cdots O_6$ in C_6Cl_5OH and being in relative proximity to each other for $H_6\cdots O_6$ and $H_6\cdots Br_1$ in C_6Br_5OH, indicate an attractive electrophilic –nucleophilic (CD$\cdots$CC) interactions.

The topological parameters for the intermolecular and intramolecular hydrogen bondings are given in **Table VI.2** and correspond to the interactions shown on **Figures VI.1, VI.2**. All of them are characterized as *pure* closed-shell interactions ($|V|/G < 1$). According to the previous studies, the intermolecular O–H$\cdots$O hydrogen bonding in C_6Cl_5OH and C_6Br_5OH can be classified within those of weak strength ($5 < |E_{HB}| < 15$ kJ mol^{-1}).[34c] On the other hand, the intramolecular O–H$\cdots$Br interaction exhibits a greater strength than the intermolecular ones, its interaction energy being estimated from the value of the potential energy density at BCP as 20 kJ mol^{-1}. Accordingly, the characterized energies, which indicate weak intermolecular interactions in C_6Cl_5OH and C_6Br_5OH, as well as an interaction of medium strength in C_6Br_5OH, parallel the IR features observed in both C_6Cl_5OH and C_6Br_5OH structures, indicating a LT to HT phase transition associated to the breaking of intermolecular and the preservation of intramolecular hydrogen bonding in the HT phase of C_6Br_5OH.

(a)   **(b)**   **(c)**
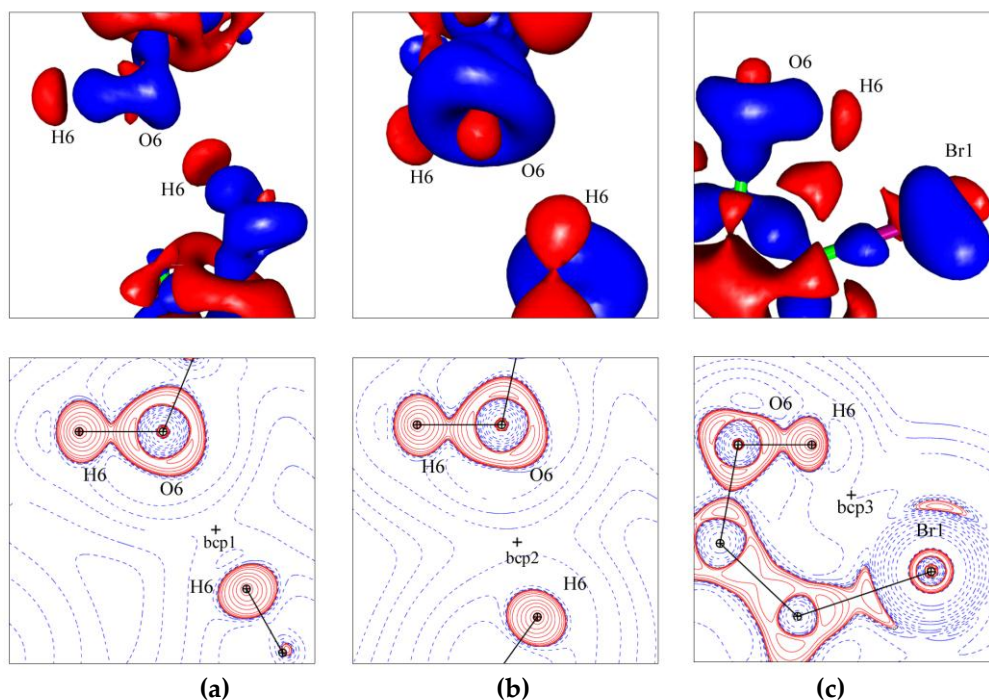
Figure VI.2 Static deformation density $\Delta\rho(\mathbf{r})$ (top) and $L(\mathbf{r})$ (bottom) maps showing the intermolecular hydrogen bonding for C_6Cl_5OH (a) and C_6Br_5OH (b), and the intramolecular hydrogen bonding for C_6Br_5OH (c). $\Delta\rho(\mathbf{r})$ iso-surfaces are drawn at ±0.05 eÅ^{-3}: blue – positive, red – negative. $L(\mathbf{r})$ contours (eÅ^{-5}) are in logarithmic scale, red – positive, blue – negative.

Table VI.2 Comparison of the topological characteristics of Hal3-synthons and inter- and intramolecular hydrogen bondings in C_6Cl_5OH and C_6Br_5OH.

Hal3-synthon [a]	ρ_Σ	$\nabla^2\rho_\Sigma$	$\lambda_{1\Sigma}$	$\lambda_{2\Sigma}$	$\lambda_{3\Sigma}$	G_Σ	V_Σ	$E_{int,\Sigma}$	$<|V|/G>$	H/ρ	$\Delta(L/\rho)_\Sigma$
C_6Cl_5OH	0.136	1.48	–0.33	–0.28	2.09	32.4	–24.5	–12.3	0.76	392	14.6
C_6Br_5OH	0.161	1.66	–0.34	–0.31	2.31	37.0	–29.7	–14.9	0.80	306	26.3
hydrogen bonding	ρ	$\nabla^2\rho$	λ_1	λ_2	λ_3	G	V	E_{int}	$|V|/G$	H/ρ	$\Delta(L/\rho)$
C_6Cl_5OH: $O_6–H_6^{xi}\cdots O_6^{i}$	0.092	2.07	–0.46	–0.41	2.94	43.5	–30.5	–15.3	0.70	953	29.9
C_6Br_5OH: $O_6–H_6^{viii}\cdots O_6^{i}$	0.105	1.63	–0.43	–0.34	2.40	37.0	–29.5	–14.8	0.80	482	32.0
C_6Br_5OH: $O_6–H_6^{i}\cdots Br_1^{i}$	0.134	2.08	–0.46	–0.43	2.98	48.8	–40.9	–20.5	0.84	398	13.8

[a] The parameters ρ_Σ (eÅ^{-3}), $\nabla^2\rho_\Sigma$ (eÅ^{-5}), G_Σ, V_Σ (kJ mol^{-1} bohr^{-3}), $E_{int,\Sigma}$ (kJ mol^{-1}) and $\Delta(L/\rho)_\Sigma$ (Å^{-2}) are calculated as the sum over the three pairwise interactions building the synthon, H/ρ (kJ mol^{-1}e^{-1}) is calculated from the obtained parameters, $<|V|/G>$ is taken as the average of the three corresponding parameters at BCP. See Table VI.1 for symmetry codes.

Table VI.3 Comparison of the topological characteristics of hydrogen (O$\cdots$H) and halogen (O$\cdots$I) bonding in the crystal structure of C_3HIOS_2. [a]

	ρ	$\nabla^2\rho$	λ_1	λ_2	λ_3	G	V	E_{int}	$|V|/G$	H/ρ	$\Delta(L/\rho)$
$H_2^{v}\cdots O_1^{i}$	0.072	1.13	–0.26	–0.25	1.65	24.5	–18.0	–9.0	0.74	607	29.5
	0.064	1.14	–0.23	–0.23	1.60	23.9	–16.7	–8.4	0.70	684	32.5
$I_1^{ii}\cdots O_1^{i}$	0.099	1.30	–0.24	–0.19	1.73	30.2	–25.1	–12.6	0.83	348	33.8
	0.117	1.38	–0.34	–0.29	2.01	33.8	–29.9	–15.0	0.84	225	32.6

[a] The parameters ρ (eÅ^{-3}), $\nabla^2\rho$ (eÅ^{-5}), λ_i (eÅ^{-5}), G and V (kJ mol^{-1} bohr^{-3}) are calculated at the BCP's of $\rho(\mathbf{r})$; H/ρ is in kJ mol^{-1}e^{-1}; $H = V + G$; $\Delta(L/\rho)$ (Å^{-2}) is calculated as the difference between the values observed at the CD and CC sites of the interacting atoms. E_{int} (kJ mol^{-1}) values are estimated as $1/2V$, the constant being in bohr^3 units. First and second lines correspond to experimental and theoretical (VASP calculations) data. Symmetry codes: (i) x, y, z; (ii) 1+x, 1+y, 1+z; (v) 1+x, 1+y, z.

1.3. Comparison between Hal$_3$-synthons and hydrogen bonding interactions

From the estimated interaction energies, the intermolecular hydrogen bonding in C$_6$Cl$_5$OH is more energetic than the Cl$_3$-synthon by only 3 kJ mol^{-1}, while in C$_6$Br$_5$OH it is almost equivalent to the Br$_3$-synthon. This small comparative difference between C$_6$Cl$_5$OH and C$_6$Br$_5$OH crystal structures is mainly due to the small increase in $E_{int,\Sigma}$ of the Br$_3$-synthon with respect to that of the Cl$_3$-synthon, while for the intermolecular hydrogen bonding E_{int} remains almost unchanged from C$_6$Cl$_5$OH to C$_6$Br$_5$OH in spite of a less favorable orientation between the H- and O-atoms in C$_6$Br$_5$OH, as observed by both δ-/ δ+ and CC/CD regions in $\Delta\rho$ and $\nabla^2\rho$ maps, respectively (**Figure VI.2**).

Comparing the electrostatic component in hydrogen bondings and in synthons, as monitored from $\Delta(L/\rho)$ and $\Delta(L/\rho)_\Sigma$, we observe that whereas in C$_6$Br$_5$OH the magnitude is only 20 % greater in hydrogen bonding than in the Hal$_3$-synthon, in C$_6$Cl$_5$OH the difference rises up to 50 %. The differences fall down respectively to ~ 0% and 20% when considering the estimation of the total interaction energy. Overall, it indicates that the electrostatic contribution to the total interaction is greater in hydrogen bondings than in Hal$_3$-synthons, and that the observed differences between them reduce in the total interaction energy due to other energetic contributions, probably linked to the significant dispersion effects characterizing Hal···Hal interactions. A similar trend has been detected with the PIXEL energy decomposition[175] of C–H···X (X = N, O) and Br···Br interactions observed in the crystal structure of a polyhalogenated bipyridine compound,[176] where the dispersion contribution to the stabilization energy was found predominant for Hal···Hal. In contrast, it did not exhibit in the observed hydrogen bondings. Furthermore, as in the present work, the electrostatic contribution (Coulombic plus polarization components) in hydrogen bondings was shown to be larger than in Hal···Hal interactions.

2. Intermolecular interactions in C$_3$HIOS$_2$

2.1. Structural characterization of hydrogen bonding

In the crystal structure of C$_3$HIOS$_2$, hydrogen bonding O···H together with the halogen bonding O···I is responsible for the chains formation along the *c*-direction. The structural characteristics of these interactions are listed in **Table VI.4**. Here, the O-atom forms a bifurcated interaction with H- and I-atoms, showing almost similar θ_2 angles that are greater than those typically observed for the location of the oxygen lone pairs (~ 110°). This can be explained by the necessity of responding to the arrangement of two neighboring molecules. In respect to the penetration parameter ω, both interactions present similar values. The angle θ_1 for O···I is closer to the linear geomatry than the one for the O···H contact.

Table VI.4 Geometry of hydrogen and halogen bonding in the crystal structure of C_3HIOS_2 [a]

C–X···O–C	d(C–X)	d(X···O)	d(C···O)	$\omega_{X···O}$ / $\omega_{C···O}$	θ_1(C–X···O)	θ_2(X···O–C)
C_2–H_2^v···O_1^i– C_1	1.089	2.235	3.274	82.2/ 101.7	158.76	137.75
C_3–I_1^{ii}···O_1^i– C_1	2.0753(1)	2.9312(1)	4.9891(2)	83.7/—	170.38(1)	135.37(2)

[a] The structural parameters d (Å), θ_1 and θ_2 (°) correspond to the multipolar models described in Chapter III. The penetration parameter ω (%) permits to compare the interaction distances with the corresponding sum of the van der Waals spheres. See Table VI.3 for symmetry codes.

2.2. Hydrogen bonding from the topology of $\rho(r)$ and $L(r)$

The geometry of the two bifurcated interactions of the O-atom is evident from the representation of interacting molecules with the corresponding bond paths and BCP's and from the gradient map with the interatomic surfaces (**Figure IV.3**).

(a)   **(b)**
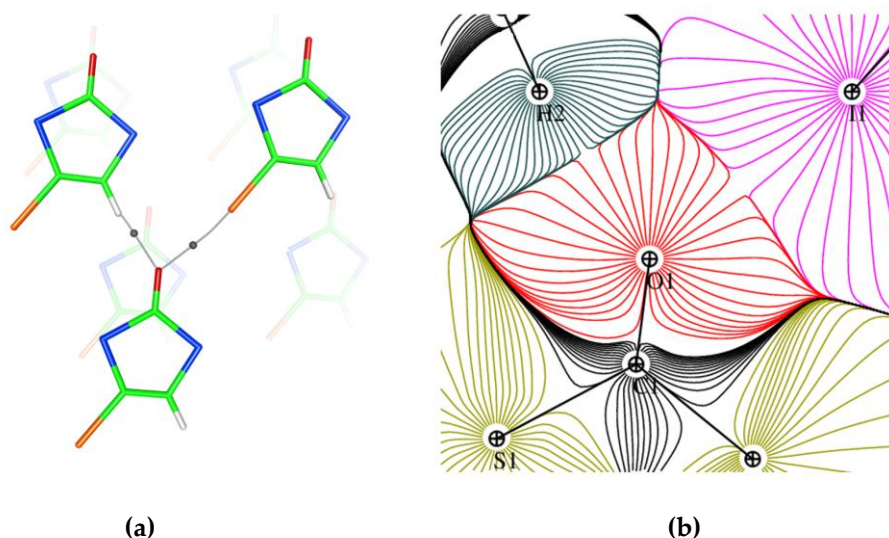
Figure VI.3 (a) Halogen (O···H) and hydrogen (O···I) bonding in the crystal structure of C_3HIOS_2 with the corresponding bond paths and BCP's, (b) Experimental $\nabla\rho(\mathbf{r})$ map for the same interactions indicating the interatomic surfaces.

The experimental and theoretical deformation maps $\Delta\rho(\mathbf{r})$ in the interatomic region display very similar features of hydrogen and halogen bonding – the two δ^- regions of the O-atom (which correspond to its lone pairs) point towards the δ^+ regions of I- and H-atoms.

The topological parameters of $\rho(\mathbf{r})$ for the intermolecular hydrogen bonding in C_3HIOS_2 are given in **Table VI.3** and correspond to the BCP's indicated in **Figures VI.3,VI.4**. Similarly to the previously described hydrogen bondings, this interaction is also characterized as *pure* closed-shell ($|V|/G$ < 1) of weak strength (on average between experimental and theoretical values, $|E_{HB}|$= 8.7 kJ mol^{-1}). Being longer than the previously described interactions, it shows lower magnitudes of the topological parameters at BCP.
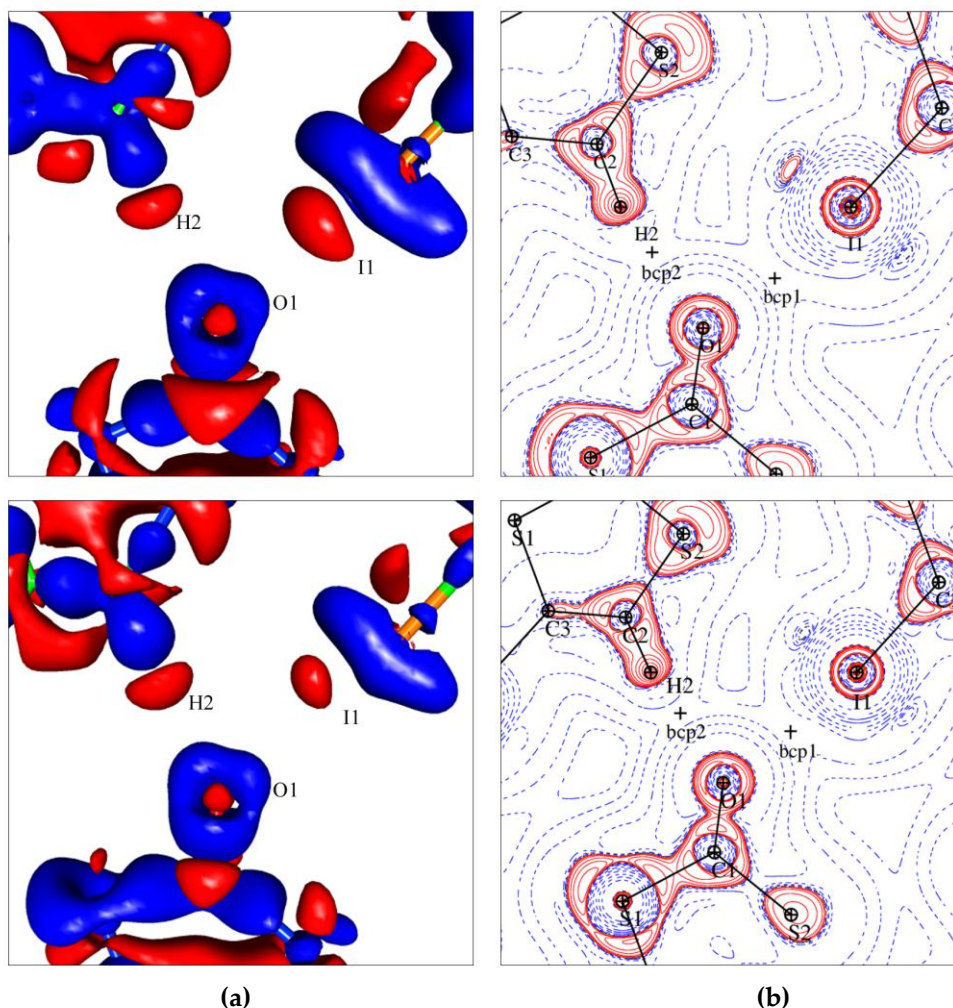
Figure VI.4 Experimental (top) and theoretical (bottom) maps in the intermolecular space of the competing halogen (O⋯H) and hydrogen (O⋯I) bondings in the crystal structure of C_3HIOS_2: (a) 3D static deformation density maps $\Delta\rho(\mathbf{r})$, iso-surface are drawn at ±0.05 eÅ^{-3}, blue – positive, red – negative; (b) $L(\mathbf{r})$ maps, contours (eÅ^{-5}) are in logarithmic scale, red – positive, blue – negative.

These characteristic features observed on $\Delta\rho(\mathbf{r})$ maps are reflected on the Laplacian maps $\nabla^2\rho(\mathbf{r})$. The hydrogen bonding directionality, which is not clear from the interactions angles, becomes evident from the relative locations of Laplacian CP's, where a (3,–3) CP of the O-atom (charge concentration region) face a (3,+3) CP of the H-atom (charge depletion region). These regions are characterized by the values L/ρ = 19.8/19.9 and –9.7/–12.6 Å^{-2}, giving rise to $\Delta(L/\rho)$ = 29.5/32.5 Å^{-2} for experimental and theoretical models, respectively. These values are extremely similar to the ones calculated for the O–H⋯O intermolecular interactions in C_6Hal_5OH, meaning that albeit the different interactions energy of these contacts, the electrostatic interaction remains mostly the same between the interacting CD and CC sites.

141

2.3. Comparison between Hal···LB halogen and H···O hydrogen bonding interactions

In the crystal structure of C_3HIOS_2, the topological properties at the intermolecular BCP are greater for the O···I than for the O···H interaction. Therefore, from the estimated interaction energies, the intermolecular hydrogen bonding is less energetic than the halogen bonding with a Lewis base (O…I), in contrast to the previously discussed C_6Br_5OH, where hydrogen bonding and the Br_3-synthon are almost equivalent in strength.

However, the quantitatively defined electrophilic–nucleophilic interactions are similarly formed, implementing the two CC ((3,–3) CPs) sites of the O-atom and the CD sites of the I- and H-atoms ((3,+3) CP for H-atom and (3,+1) CP for I-atom), both located in a negative region of $L(\mathbf{r})$. These similitudes are displayed on the very close values of the electrostatic descriptors $\Delta(L/\rho)$ (on average between experimental and theoretical values, 31 and 33.2 Å^{-2} for O···H and O…I, respectively). It seems to indicate that if the electrostatic component is similar, halogen interactions will be of greater energy than hydrogen bonding, most probably due to the dispersion effects.

3. Intermolecular interactions in $C_8O_2H_4Se$

3.1. Structural characterization of hydrogen bonding

In the crystal structure of $C_8O_2H_4Se$, hydrogen interactions are numerous and play an important role. They provide layers formation in the *bc* plane and, along with the previously described chalcogen bonding, support the intercolumn connectivity. Thereby, these intermolecular interactions are characterized by various geometries and different electron donating atoms (O and Se). In **Table VI.5** the characterizing interatomic distances and angles are represented and estimated in respect to the corresponding van der Waals radii by the penetration parameter ω.

Table VI.5 Geometry of hydrogen bonding interaction in the structure of $C_8O_2H_4Se$.

C–H···X	d(H···X)	d(C···X)	$\omega_{H···X} / \omega_{C···X}$	θ_1 (C–H···X)	θ_2 (H···O–C)
C_5–H_1^{iv}···O_2^{i}	2.295	3.3641(1)	84.4/104.5	169.02	165.59
C_8–H_4^{vi}···O_1^{i}	2.359	3.2523(2)	86.7/100.9	138.64	130.45
C_6–H_2^{vii}···O_1^{i}	2.528	3.3394(2)	92.4/103.7	149.38	132.56
C_7–H_3^{vii}···O_1^{i}	2.929	3.5230(1)	107.7/109.4	114.78	109.01
C_6–H_2^{viii}···Se_1^{i}	2.974	3.8461(3)	95.9/106.8	137.76	—
C_7–H_3^{vii}···Se_1^{i}	3.567	4.1597(1)	115.1/115.5	116.07	—

[a] The structural parameters d (Å), θ_1 and θ_2 (°) correspond to the multipolar models described in Chapter III. The penetration parameter ω (%) permits to compare the interaction distances with the corresponding sum of the van der Waals spheres. The angle θ_2 is given only for the H···O contacts to compare the interaction direction with the location of the O-atom lone pairs. $C_8O_2H_4Se$: (i) x, y, z; (iv) x, 1+y, z; (vi) 1–x, -y, 1-z; (vii) 1/2+x, 1/2-y, 1/2+z; (viii) 1/2+x, 3/2-y, 1/2+z

The first two interactions ($H_1 \cdots O_2$ and $H_4 \cdots O_1$) occur twice involving two molecules of the same plane (**Figure VI.5**). Being the shortest among all the $H \cdots O$ contacts in the structure of $C_8O_2H_4Se$ they are formed with the similar θ_1 and θ_2 angles. For the $H_4 \cdots O_1$ contact, θ_2 angle is closer to the value corresponding to the approximate location of the O-atom lone pair, while for $H_1 \cdots O_2$ it is close to 180° in an almost linear geometry. The next two contacts ($H_2 \cdots O_1$ and $H_3 \cdots O_1$) are formed with the same O-atom on one side and two H-atoms belonging the same molecule on the other, thus creating a bifurcated interaction.

(a)   (b)
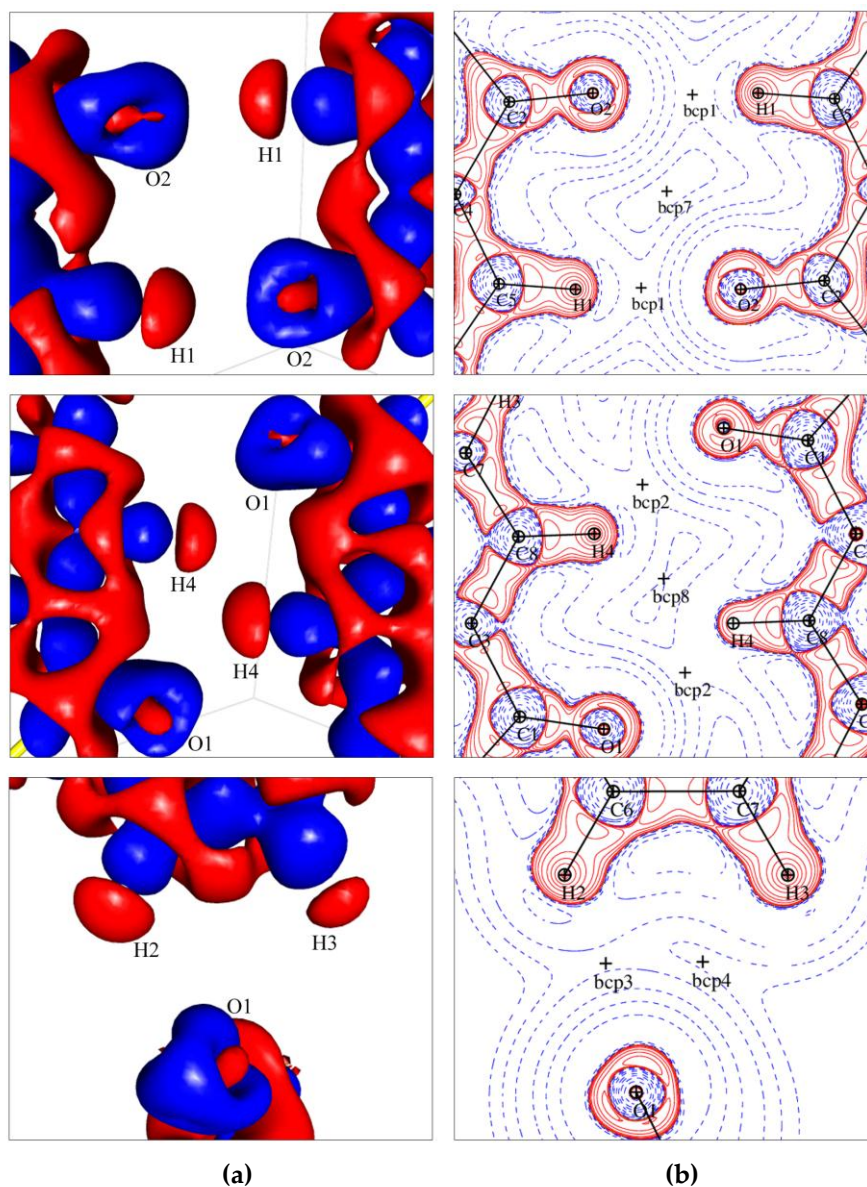
Figure VI.5 Experimental maps in the intermolecular space of the hydrogen bonding in $C_8O_2H_4Se$: (a) 3D static deformation density maps $\Delta\rho(\mathbf{r})$, iso-surface are drawn at ±0.05 e$Å^{-3}$, blue – positive, red – negative; (b) $L(\mathbf{r})$ contours (e$Å^{-5}$) are in logarithmic scale, red – positive, blue – negative.

143

3.2. Hydrogen bonding from the topology of ρ(r) and L(r)

All the hydrogen bonding interactions can be qualitatively analyzed by plotting the deformation density and Laplacian maps in the interaction regions. **Figure VI.5** illustrates $\Delta\rho(\mathbf{r})$ and $L(\mathbf{r})$ for the hydrogen bonding of type H···O. All the interactions can actually be classified as electrostatically favoured with the region of electron density deficiency δ^+ of the H-atom always facing electron density excess δ^- of the O-atom on the $\Delta\rho(\mathbf{r})$ maps. However, for the H_1···O_2 contact, the latter doesn't coincide with the location of the oxygen lone pair (which is also evident from the structural angles of this interaction). From the $L(\mathbf{r})$ map, it could be suggested that the interaction in this case occurs not with the L local maximum of O-atom ((3,–3) CP), but with its saddle point ((3,+1) CP), which could act here as a CC site, however, a more detailed investigation is needed to evaluate this feature. On **Figure VI.6**, the same kind of maps represent for the hydrogen bonding of type H···Se are plotted. They also denote an electrophilic–nucleophilic interaction, involving a CC site ((3,–3) CP) of the Se-atom and a CD site ((3,+3) CP) of the H-atom. It has to be noted, that both hydrogen bonds involve the same CC sites (CC_b), opposite to the one involved in the Se···Se chalcogen bond discussed in **Chapter V**. Accordingly, we can say that the CC_b region of the Se-atom is involved in a bifurcated hydrogen bonding interaction.

(a)   **(b)**
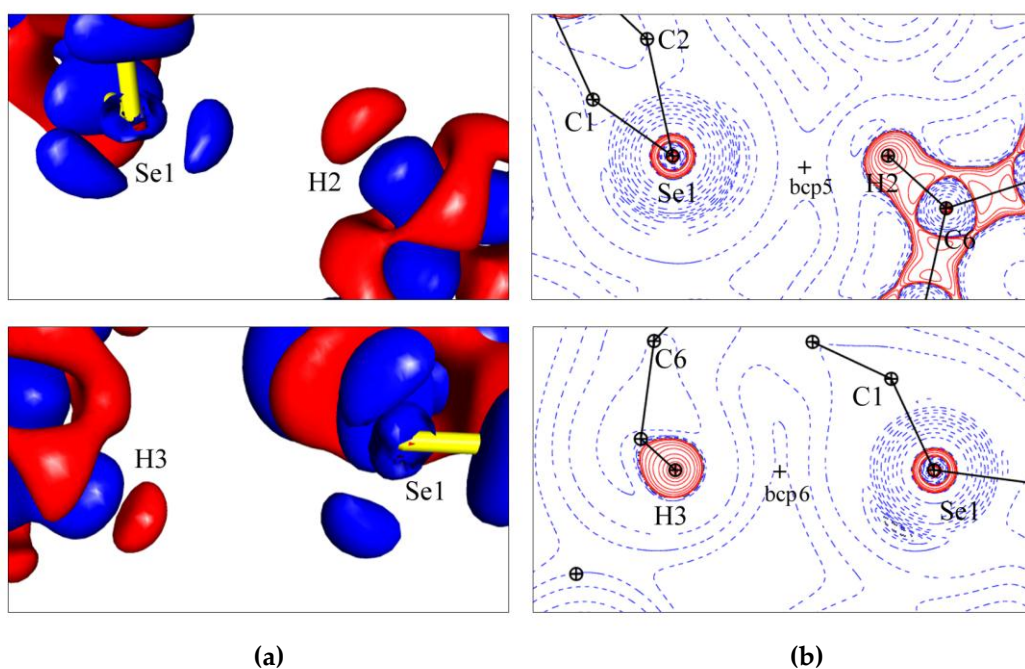
Figure VI.6 Experimental maps in the intermolecular space of the hydrogen bonding in $C_8O_2H_4Se$: (a) 3D static deformation density maps $\Delta\rho(\mathbf{r})$, iso-surface are drawn at 0.05 e$Å^{-3}$, blue – positive, red – negative; (b) $L(\mathbf{r})$ contours (e$Å^{-5}$) are in logarithmic scale, red – positive, blue – negative.

From the topological properties of $\rho(\mathbf{r})$, hydrogen bonding of type C–H⋯O and C–H⋯Se in the $C_8O_2H_4Se$ crystal structure (**Table VI.6**) can be also characterized as *pure* closed-shell interactions ($|V|/G < 1$), being of very weak and weak strength ($1.3 < |E_{HB}| < 7.7$ kJ mol^{-1}).[34c]

For all the hydrogen bonds observed in this work, the differences in the interaction distances and in the involved donors (Br-, O-, or Se-atoms) are reflected in the values of the topological properties at the BCP's (**Table VI.6**). It can be seen that the hydrogen bond strength, estimated from $|E_{int}|$, increases with the distance shortening.

The electrostatic interaction monitored from the $\Delta(L/\rho)$ descriptor depends on the activation of the interacting δ^+ and δ^- regions, and therefore on the atomic environment, as well as on the interaction geometry. Consequently, it is difficult to observe any tendency from this descriptor. However, it is underlined that for all the studied hydrogen bonding interactions, this parameter can vary by a factor of 6, e.g. from 5.8 Å^{-2} for the weakest $Se_1 \cdots H_3$ to 32.0 Å^{-2} for the strongest $H_6 \cdots O_6$ interaction.

3.3. Comparison of chalcogen and hydrogen bonding

Experimental end theoretical electron density modeling around the Se-atom in $C_8O_2H_4Se$ provide an evidence of chalcogen bonding $(Se(\delta^+)\cdots(\delta^-)O$ and $(Se(\delta^-)\cdots(\delta^+)Se)$ and hydrogen bonding $(Se(\delta^-)\cdots(\delta^+)H)$ interactions (**Figures V.6, VI.6**, the $Se \cdots H_3$ contact is not considered here, being of different distance range with $\omega = 115.1\%$). The topological analysis of the $L(\mathbf{r})$ function reveals the electrophilic–nucleophilic nature of the four interactions. The CD and CC sites face each other in the four intermolecular regions, where the Se-atom interacts with the molecular environment by involving simultaneously its electrophilic and nucleophilic sites – situation already observed for halogen atoms in the Hal$_3$-synthons formation.

As it was shown throughout this work, the electrostatic interaction increases with the electrophilic/nucleophilic power of the CD/CC sites, monitored by their L/ρ values. Accordingly, the quantity $\Delta(L/\rho) = (L/\rho)_{CC} - (L/\rho)_{CD}$ estimates its strength. The $\Delta(L/\rho)$ values in the crystal phase decrease abruptly along the interaction series Se⋯O, Se⋯H$_2$, and Se⋯Se (the experimental values being 20.4, 14.8, and 2.8 Å^{-2}), while the estimated total interaction energy values are close to each other (4-5 kJ mol^{-1}). This significant difference for the three CC⋯CD interactions points out the presence of an important energetic contribution that brings closer the Se⋯Se interaction energy to those of Se⋯O and Se⋯H. As for halogen atoms (see **Chapter IV**), the dispersion component could be invoked to explain this trend,[118] expected to be more significant in the former than in the two latter Se-interactions. On the other hand, the estimated values of total interaction energy indicate that chalcogen bonding can compete with weak hydrogen bonding for driving molecular packing.

Table VI.6 The topological parameters for hydrogen bonding in the crystal structure of $C_8O_2H_4Se$. [a]

hydrogen bonding [b]	d, ω	ρ	$\nabla^2\rho$	λ_1	λ_2	λ_3	G	V	E_{int}	$|V|/G$	H/ρ	$\Delta(L/\rho)$
$H_1^{iv}\cdots O_2^{i}$	2.295, 84.4	0.058	1.10	–0.21	–0.21	1.52	22.6	–15.4	–7.7	0.68	838	19.1
		0.068	1.01	–0.24	–0.24	1.50	22.0	–16.3	–8.2	0.74	566	20.2
$H_4^{vi}\cdots O_1^{i}$	2.359, 86.7	0.061	1.03	–0.22	–0.22	1.48	21.7	–15.3	–7.7	0.71	708	26.6
		0.071	1.04	–0.26	–0.25	1.56	22.8	–17.1	–8.5	0.75	542	28.7
$H_2^{vii}\cdots O_1^{i}$	2.528, 92.4	0.045	0.69	–0.15	–0.14	0.98	14.3	–9.8	–4.9	0.69	675	27.1
		0.048	0.74	–0.16	–0.16	1.05	15.4	–10.8	–5.4	0.70	647	27.0
$H_3^{vii}\cdots O_1^{i}$	2.929, 107.7	0.024	0.36	–0.06	–0.03	0.45	7.2	–4.5	–2.3	0.63	759	23.8
		0.026	0.38	–0.08	–0.05	0.51	7.9	–5.0	–2.5	0.63	753	25.9
$H_2^{viii}\cdots Se_1^{i}$	2.974, 95.9	0.050	0.51	–0.13	–0.12	0.77	11.5	–8.9	–4.5	0.77	351	14.8
		0.052	0.50	–0.14	–0.13	0.77	11.4	–9.1	–4.6	0.80	298	11.4
$H_3^{vii}\cdots Se_1^{i}$	3.567, 115.1	0.019	0.18	–0.04	–0.03	0.25	3.8	–2.5	–1.3	0.66	462	5.8
		0.018	0.18	–0.03	–0.02	0.24	3.7	–2.4	–1.2	0.65	487	6.5

[a] The parameters ρ (e$Å^{-3}$), $\nabla^2\rho$ (e$Å^{-5}$), λ_i (e$Å^{-5}$), G and V (kJ mol^{-1} $bohr^{-3}$) are calculated at the BCP's of $\rho(\mathbf{r})$; H/ρ is in kJ $mol^{-1}e^{-1}$ ($H = V + G$); $\Delta(L/\rho)$ ($Å^{-2}$) is calculated as the difference between the values observed at the CD and CC sites of the interacting atoms. E_{int} (kJ mol^{-1}) values are estimated as $1/2V$, the constant being in $bohr^3$ units; structural parameters d (Å) and ω (%) are repeated from Table VI.5 for clarity. [b] First and second lines correspond to experimental and theoretical (VASP calculations) data. See Table VI.5 for symmetry codes.

4. General discussion on hydrogen, halogen & chalcogen bonding

As it was shown throughout this work, electron properties at the BCP can be used to characterize the intermolecular interactions from the electron density distribution, which can be experimentally determined from single crystal X-ray diffraction or theoretically obtained from the quantum chemistry calculations. The topological and energetic properties of $\rho(\mathbf{r})$ at BCP, reported in the previous chapters for the interactions involving Hal-, Chal-, and H-atoms are: i) the total electron density ρ, ii) the three main curvatures (λ_i, i = 1, 2, 3) that correspond to the eigenvalues of the Hessian matrix of $\rho(\mathbf{r})$, iii) the Laplacian $\nabla^2\rho = \sum_i \lambda_i$ and iv) the local electron kinetic G, potential V and total H energy densities ($H = G + V$). It would be noted that while the former can be experimentally determined from high-resolution X-ray diffraction data, the latter are not straightforwardly accessible from experiments and can be calculated for closed-shell interactions by using the Abramov functional and the local form of the virial theorem.

Previously, it was shown that the set of dependences between the topological and energetic properties of $\rho(\mathbf{r})$ at BCP, as well as between each of them and the bonding distances, permit to distinguish between different families of intermolecular interactions and to reveal universal features of $\rho(\mathbf{r})$ in their bonding regions. Dependencies between topological properties and bonding distances were first observed for hydrogen bondings,[177a] and some other interactions,[177b] by means of theoretical calculations on molecules and complexes in gas phase. Since then, many dependencies involving $\rho(\mathbf{r})$ properties at BCP have been reported and used in theoretical analyses of complexes in the gas phase, such as those given in the detailed study of N–H⋯N interactions interactions.[178] Similar dependencies for hydrogen bondings have been observed in crystals from experimental electron density distributions determined by using high-resolution X-ray diffraction data[34a,59a,b,179] or from theoretical calculations.[180]

In the analysis of these dependencies, the values of the properties at BCP present some degree of dispersion around the fitting curves. When using experimental data, this dispersion is usually attributed to observational errors, which correspond to the difference between the experimentally determined and the exact magnitude of $\rho(\mathbf{r})$ and affect the derived topological and energetic properties at BCP. These errors can be pronounced, in particular for properties involving the second derivative of $\rho(\mathbf{r})$, because of the difficult modeling of the electron distribution in the intermolecular regions, where $\rho(\mathbf{r})$ is flat within molecules and the relevance of the experimental noise is relatively more important. On the other hand, theoretical calculations of properties at BCP carried out on large families of complexes presenting H⋯F and H⋯N hydrogen bonding strongly suggest that deviations from the expected dependencies are also related to the effect of the environment on the atoms directly involved in the interaction.[34c,41] However, as far as this dispersion is small enough, the set of dependencies associated to these families of complexes appears well defined. Accordingly, the set of dependencies obtained for a given family can be taken as fundamental descriptors of the interaction, and can be used for its characterization, independently of the individual systems used for the derivation of the dependencies. It has been shown that these dependencies are a consequence of the electronic shell structure of the involved atoms, their existence being hence a universal trait of the interatomic interaction.[181]

During our work we have collected quite enough experimental data for the following types of interactions: Cl···Cl, Br···Br, Hal···LB, H···O that permit us to analyze the topological and energetic properties dependences in order to reveal the typical features of these contacts. In the case of Hal···LB contacts, the data is used from the analysis of the I···O interaction in C_3HIOS_2 performed in **Chapter IV** and from the ones available in the literature. Chal···Chal interactions will not be characterized as the quantity of data in the present study and in the literature is not large enough to make the general conclusions about the properties behavior.

4.1. BCP topological properties dependence on intermolecular bond distances

The ρ, $\nabla^2\rho$, λ_3, $|\lambda_1+\lambda_2|$, G, and $|V|$ values calculated for all the studied intermolecular interactions are represented against the bonding distance d in **Figure VI.7**. All topological and energetic properties exhibit data clustering for the following families – Cl···Cl, Br···Br (the families of Hal···Hal interactions include Type-I and Type-II geometries), Hal···LB, and H···O. This feature is most probably related to the fact that all the represented properties depend mainly on the atoms involved in the pairwise interaction. Log-linear plots were preferred to underline the observed exponential behaviors. Thus, linearized exponential fitting functions were applied. In most cases, the statistical results show good fittings (see R^2-values in **Table VI.7**), permitting to conclude exponential dependences between these parameters and the interaction distance. The best fitting corresponds to the H···O interactions, while the data for Hal···LB exhibit more dispersion than those of Cl···Cl, Br···Br and H···O. The latter is most probably due to the fact that the plot includes data from different Hal- and LB-atoms, (see **Table IV.5**), which normally should be separated. For this reason, Hal···LB contacts show the widest range of parameter magnitudes. From the represented topological properties, greater dispersions are observed for the $|\lambda_1+\lambda_2|$ versus d plots, in particular for Hal···Hal interactions. This was already observed for H···O interactions.[60]

The set of data for Hal···Hal interactions is the greatest among all the studied interactions. Regardless the geometry (Type-I or Type-II), all the interactions for the same Hal-atom can be described by the same fitting function. The distance dependence for all the studied properties is described by very similar but shifted equations for Cl···Cl and Br···Br contacts, so as for the same distance, the topological properties are always greater in magnitudes for the latter (however, standard uncertainties should be taken into account, being rather high in some cases). A very similar trend was firstly observed for hydrogen bonding interactions,[60] indicating the classification of H···X (X = H, C, N, O, F, S, Cl, π) interactions by the type of the last unfilled electron shell, then by number of electrons inside in it. The R^2-values are almost always lower for the Cl···Cl interaction set, mainly due to its long-distance Type-I contacts that spread around the fitting function.

(a)

(b)

(c)

149
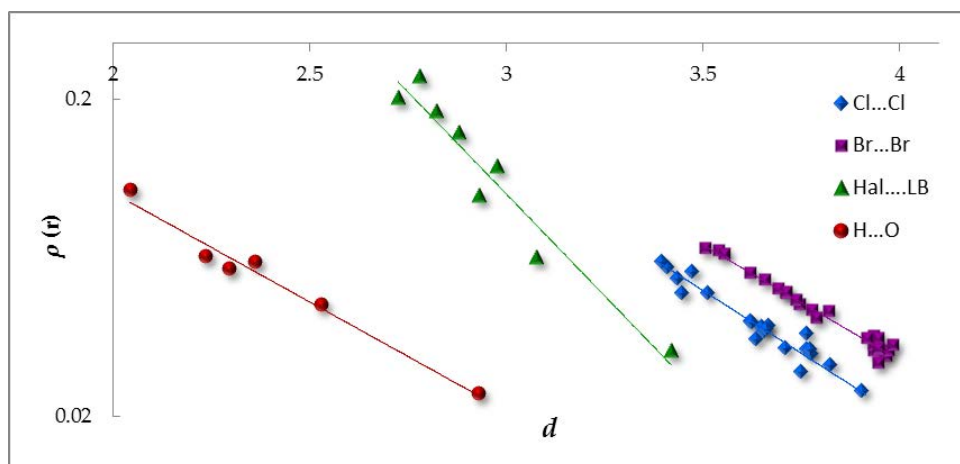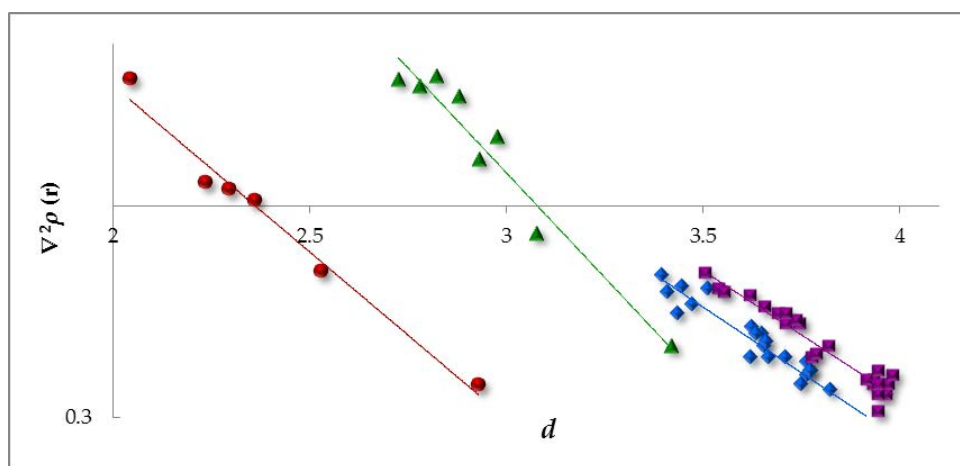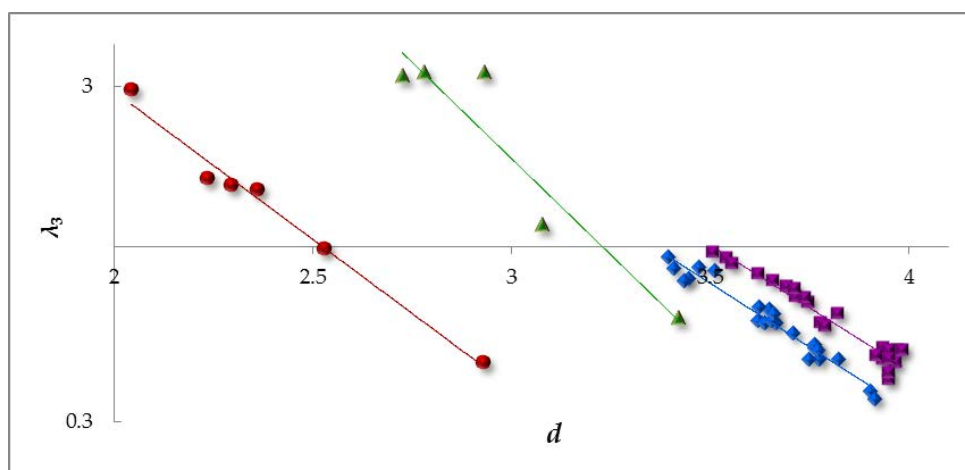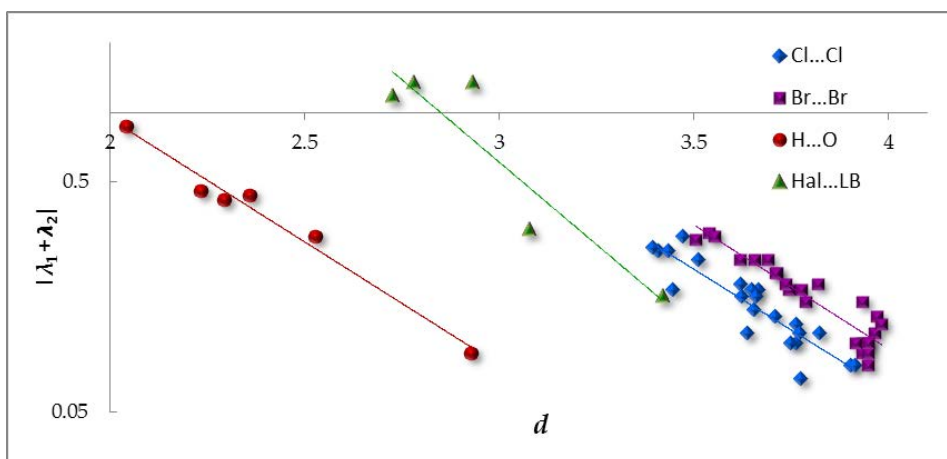
(d)
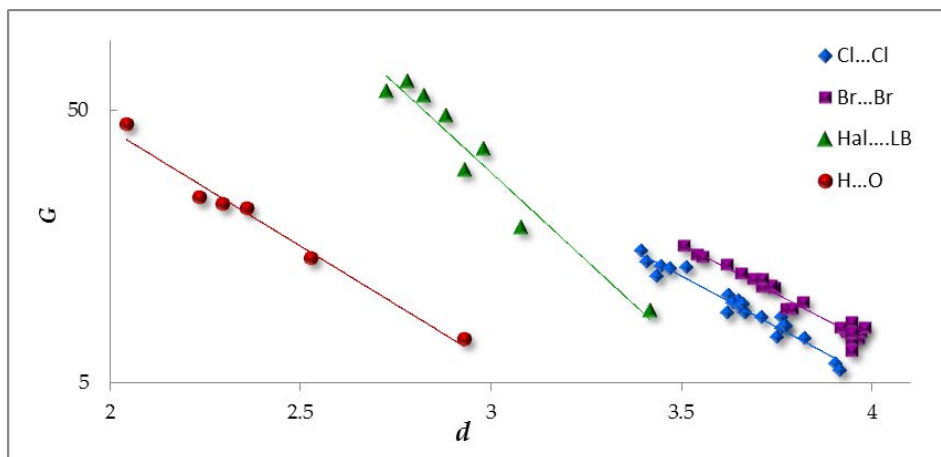
(e)
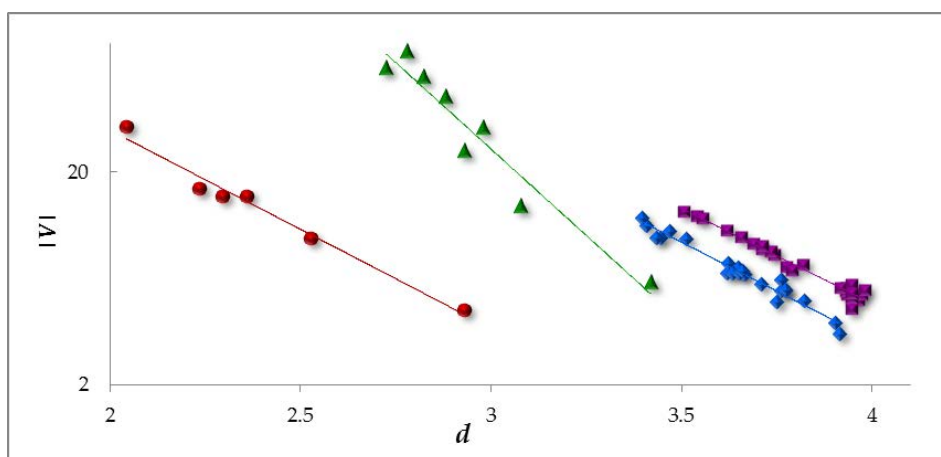
(f)

Figure VI.7 BCP topological properties dependence versus interaction distance d (Å): (a) ρ (eÅ^{-3}), (b) $\nabla^2\rho$ (eÅ^{-5}), (c) λ_3 (eÅ^{-5}), (d) $|\lambda_1+\lambda_2|$ (eÅ^{-5}), (e) G (kJ mol^{-1} bohr^{-3}), (f) V (kJ mol^{-1} bohr^{-3}). For these properties, the families are classified along the series Cl···Cl (blue diamonds), Br···Br (purple squares), Hal···LB (green triangles), H···O (red circles).

150

(a)

(b)
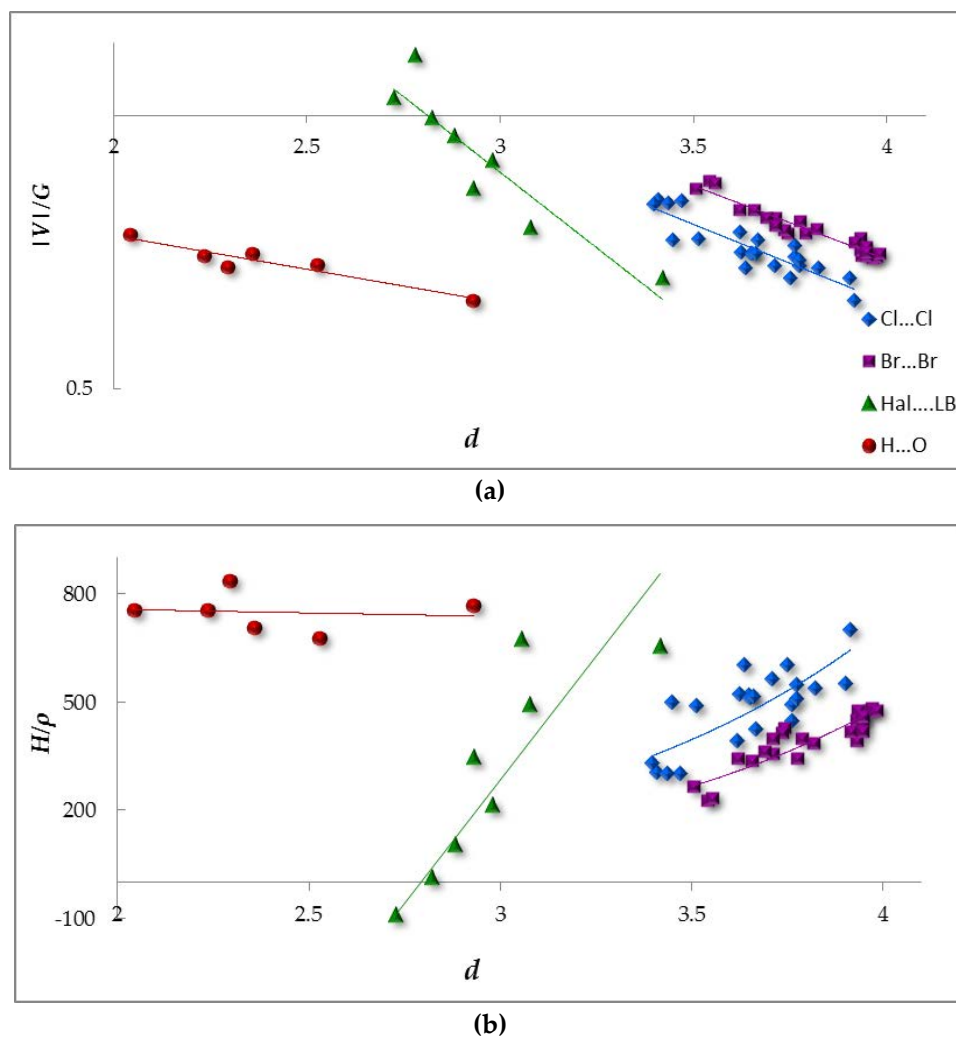
Figure VI.8 Distance dependence for the parameters (a) $|V|/G$ and (b) H/ρ (kJ mol^{-1}e^{-1}). For the interaction notation see Figure VI.7.

Figure VI.8 shows data of the normalized parameters $|V|/G$ and H/ρ against the interaction distance. Both properties follow quite a general monotonic dependence ($|V|/G$ increases and H/ρ decreases with the distance shortening). A particular behavior is observed for Hal···LB contacts – the parameters $|V|/G$ and H/ρ respectively increase and decrease much faster with distance shortening than for the other series. This indicates the fact that $|V|$ becomes closer to G, making the covalent character more pronounced, probably due to the effect of a more important charge transfer that is expected to take place in these contacts between the lone pairs orbital (n_O) of the Lewis base lone pair and the anti-bonding σ^* orbital of C-I ($n_O \rightarrow \sigma^*_{C-I}$).

Table IV.7 Fitting parameters a and b, and correlation coefficient (R^2) for the exponential regressions from Figures VI.7 and VI.8 for the four interaction families – Cl···Cl, Br···Br, Hal···LB and H···O. [a]

$\ln(y) = \ln(a) - bx$	Cl···Cl, $n = 22$	Br···Br, $n = 24$	Hal···LB, $n = 8$ [b]	H···O, $n = 7$
		ρ vs d		
$\ln(a)$	3.38(13)	3.19(9)	6.59(27)	0.88(12)
a	29.55(16)	24.25(15)	727(53)	2.41(8)
b	1.83(10)	1.67(9)	2.96(16)	1.59(18)
R^2	0.9321	0.9758	0.9364	0.9771
		$\nabla^2\rho$ vs d		
$\ln(a)$	4.66(9)	4.74(7)	7.34(24)	4.47(15)
a	105(7)	114(9)	$1.5(9)10^3$	87(32)
b	1.49(8)	1.46(4)	2.38(13)	1.89(21)
R^2	0.9255	0.9397	0.9451	0.8909
		λ_3 vs d		
$\ln(a)$	5.9(5)	6.0(7)	8.55(25)	5.1(3)
a	362(38)	420(42)	$5.2(7)10^3$	170(21)
b	1.76(5)	1.72(7)	2.65(16)	2.04(10)
R^2	0.9553	0.9470	0.8948	0.9849
		$\|\lambda_1 + \lambda_2\|$ vs d		
$\ln(a)$	6.9(7)	7.6(9)	9.41(17)	4.6(8)
a	$1.0(4)10^3$	$1.9(7)10^3$	$1.2(9)10^4$	129(38)
b	2.43(8)	2.48(5)	3.30(12)	2.46(8)
R^2	0.8219	0.8723	0.8578	0.9790
		G vs d		
$\ln(a)$	8.55(5)	8.68(6)	12.32(9)	7.71(7)
a	$5.1(4)10^3$	$5.9(2)10^3$	$2.24(4)10^5$	$2.2(4)10^3$
b	1.73	1.69	2.98	1.97
R^2	0.9509	0.9551	0.9446	0.9799
		$\|V\|$ vs d		
$\ln(a)$	9.66(13)	9.81(9)	14.52(21)	7.73(7)
a	$1.6(3)10^4$	$1.8(2)10^4$	$2.1(3)10^6$	$2.3(4)10^3$
b	2.12(3)	2.06(3)	3.74(11)	2.14(14)
R^2	0.9593	0.9695	0.9343	0.9790
		$\|V\|/G$ vs d		
$\ln(a)$	1.11(13)	1.13(4)	2.22(10)	0.04(4)
a	3.02(9)	3.09(5)	8.63(9)	1.03(12)
b	0.39(3)	0.37(6)	0.77(15)	0.17(9)
R^2	0.7866	0.9266	0.8478	0.8904
		H/ρ vs d		
$\ln(a)$	1.86(33)	1.29(26)	–2.20(61)	6.68(61)
a	6.45(23)	3.62(16)	0.11(47)	798(82)
b	–1.18(16)	–1.23(9)	–2.64(18)	0.03(53)
R^2	0.5774	0.7825	0.4837	0.0124

[a] n indicates the number of data by the linear functions fitting. [b] For the parameters λ_i (1 = 1, 2, 3) of Hal···LB interactions, $n = 5$ in accordance with data available in the literature (Table IV.5).

4.2. Interdependences between the electron density properties at BCP

Data correlations in the representations of $|\lambda_1 + \lambda_2|$ versus λ_3 and of $|V|$ versus G are shown in **Figure IV.9a,b** for the four defined intermolecular interaction families. In both figures, the data distributions show, in general, good linear dependencies. Along the three families – H⋯O, Cl⋯Cl and Br⋯Br – the positive slope of the linear fitting function slightly increases, indicating that $|\lambda_1 + \lambda_2|$ and $|V|$, which are related to the stabilization of the interaction by grouping charge in the internuclear region become more important as the values of λ_3 and G, which are related to the depletion of charge due to the overlapping of the electron clouds in a closed-shell interaction, increase along the series. However, for very weak interactions, these parameters are very similar for the three sets, so they can be actually described by the unique fitting function (e.g. for $|\lambda_1 + \lambda_2|$ vs λ_3, $a = 0.32$, $b = 0.04$, $R^2 = 0.9805$). The values of the corresponding fitting parameters for the Hal⋯LB contacts are not comparable with the other three sets. Indeed, in this case, data show a very large spread due to the variety of Hal- and LB-atoms included in the dataset. However, it is noticed that, even in this case, data show a remarkable linearity in both cases ($R^2 = 0.9892$, 0.9817 for $|\lambda_1 + \lambda_2|$ vs λ_3 and $|V|$ vs G respectively).

The linear dependencies between the curvatures and the energetic (G vs. λ_3 and $|V|$ vs. $|\lambda_1 + \lambda_2|$) and topological (ρ vs. λ_3) properties are shown in **Figure IV.9c,d,e**. In the case of G versus λ_3 the separation of the families datasets is very small, so that a single linear function can be fitted for the three families H⋯O, Cl⋯Cl and Br⋯Br ($a = 14.84$, $b = 0.68$, $R^2 = 0.9968$), indicating that this correlation is mostly independent of the involved atoms and molecular environment, at least for the weak interactions studied here, exhibiting rather low G and λ_3 values. As it was noticed earlier,[60] this feature can be particularly interesting for the problems detection in the modeling of $\rho(\mathbf{r})$, either experimentally determined or theoretically calculated, if significant outliers with respect to the fitting function appear. In the case of $|V|$ versus $|\lambda_1 + \lambda_2|$ and of ρ versus λ_3 dependences, the later clearly shows the interactions separation into the four already defined families, while the former represents rather high dispersion for Cl⋯Cl, Br⋯Br and particularly Hal⋯LB data that doesn't make possible to distinguish between the different types of interactions. Data corresponding to the representation of $|V|/G$ versus $|\lambda_1 + \lambda_2|/\lambda_3$ are shown in **Figure IV.9f.** Even if the dispersion is too large for all the families to conclude any dependence, a general tendency of the $|V|/G$ to increase along the series H⋯O, Cl⋯Cl and Br⋯Br is viewed.

The properties $|V|/G$ and H/ρ evaluate the strength of an intermolecular interaction (see **Table I.2** in Chapter I). The $|V|/G$ (($|V|/\rho$)/(G/ρ)) descriptor introduces the classification of any intermolecular interaction permitting to pick out a region of intermediate strength ($1 < |V|/G < 2$), where the interaction has a partially covalent character between these of *pure* closed-shell ($|V|/G < 1$) and *pure* shared-shell ($|V|/G > 2$) character, while the bond degree parameter H/ρ ($|V|/\rho + G/\rho$) permits to distinguish between the *softness degree* ($H/\rho > 0$) and the *covalence degree* ($H/\rho < 0$) of an interaction as it can be interpreted as the total energy per electron at BCP. According to the parameters definition, an increase of $|V|/G$ must be accompanied by a decrease of H/ρ and *vice versa*. This is reflected in **Figure IV.10** for all the studied intermolecular interactions of closed-shell type. The fitting is rather good for all the interactions, except hydrogen bondings, for which different types were considered (H⋯O, H⋯Br, H⋯Se).

Figure IV.9 Interdependences between the electron density properties: (a) $|\lambda_1+\lambda_2|$ vs λ_3 (eÅ^{-5}), (b) $|V|$ vs G, (c) G vs λ_3, (d) $|V|$ vs $|\lambda_1+\lambda_2|$, (e) ρ vs λ_3, (f) $|V|/G$ vs $|\lambda_1+\lambda_2|/\lambda_3$. For the interaction notation see Figure VI.7,

Table IV.8 Fitting parameters a and b, and correlation coefficient (R^2) for the linear regressions from Figure VI.9 for the four interaction families – Cl···Cl, Br···Br, Hal···LB, H···O. [a]

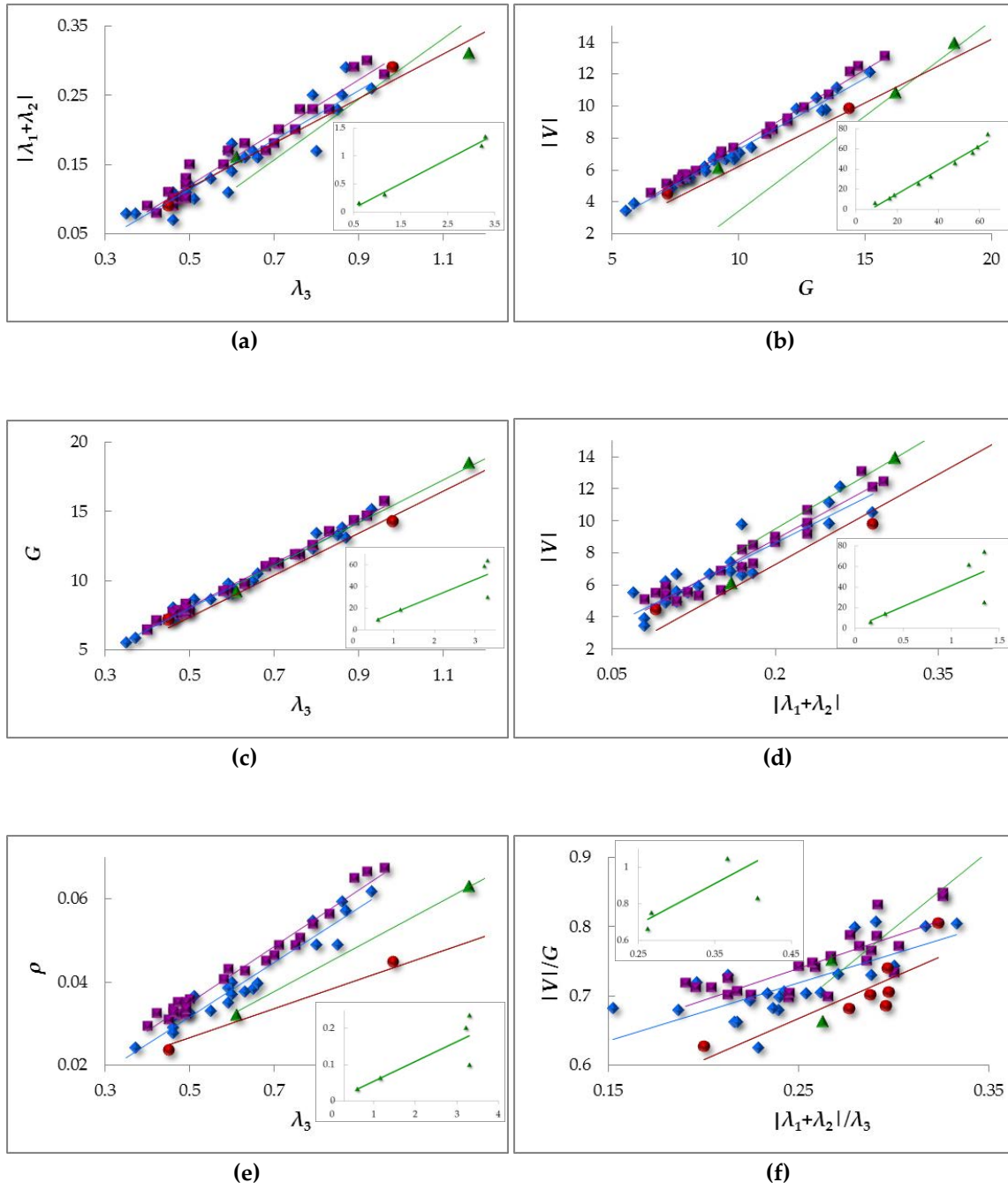| $y = a + bx$	Cl···Cl, $n = 22$	Br···Br, $n = 24$	Hal···LB, $n = 8$ [b]	H···O, $n = 7$
$|\lambda_1 + \lambda_2|$ vs λ_3				
a	–0.04(16)	–0.07(13)	–0.15(11)	–0.05(3)
b	0.32(2)	0.38(5)	0.44(5)	0.32(7)
R^2	0.9897	0.9556	0.9892	0.9897
$|V|$ vs G				
a	–1.60(10)	–1.75(3)	–8.53(3)	–1.73(7)
b	0.89(4)	0.93(3)	1.19(2)	0.80(7)
R^2	0.9830	0.9924	0.9817	0.9899
G vs λ_3				
a	0.20(4)	0.17(3)	0.27(11)	–0.26(1)
b	15.60(3)	15.85(3)	15.46(9)	15.19(2)
R^2	0.9797	0.9932	0.7115	0.9989
$|V|$ vs $|\lambda_1 + \lambda_2|$				
a	1.82(7)	1.46(5)	1.43(8)	–0.21(3)
b	34.08(6)	37.02(6)	40.13(18)	37.51(7)
R^2	0.8435	0.9402	0.6032	0.9934
ρ vs λ_3				
a	–0.0012(3)	0.0012(8)	–0.0005(9)	0.0092(14)
b	0.0658(18)	0.0676(5)	0.055(14)	0.035(3)
R^2	0.9461	0.976	0.6692	0.9478
$|V|/G$ vs $|\lambda_1 + \lambda_2|/\lambda_3$				
a	0.51(31)	0.51(23)	0.13(20)	0.37(12)
b	0.84(12)	0.91(9)	2.22(23)	1.20(11)
R^2	0.5393	0.6371	0.5888	0.7356

[a] n indicates the number of data by the linear functions fitting. [b] For the parameters λ_i (1 = 1, 2, 3) of Hal···LB interactions, $n = 5$ in accordance with data available in the literature (Table IV.5).

Accordingly, these normalized energetic properties allow us to compare interactions involving atoms of different nature and based on them we can estimate the intensity of the closed-shell interactions, studied in this work. Their classification proposed earlier for the closed-shell interactions Cl···X and C_π ···X (X = Cl, O, H, C_π)[93] permitted to distinguish between the interactions of different intensity.

The weak intermolecular interactions studied in this work can be classified as following: the most intense ($H/\rho < 400$ kJ mol^{-1} e^{-1} and $|V|/G > 0.82$) are Hal···LB, chalcogen bonding (ChalB: Se···Se and S···I), and Br···Br (Type-II), the interactions of intermediate intensity ($400 < H/\rho < 500$ kJ mol^{-1} e^{-1} and $0.68 < |V|/G < 0.82$) are Br···Br (Type-I), Cl···Cl (Type-II), Hal···Cπ (Hal = Cl, Br), and the interactions of very weak intensity ($H/\rho > 500$ kJ mol^{-1} e^{-1} and $|V|/G < 0.68$) are Cl···Cl (Type-I), hydrogen bonding (HB), Chal···X.
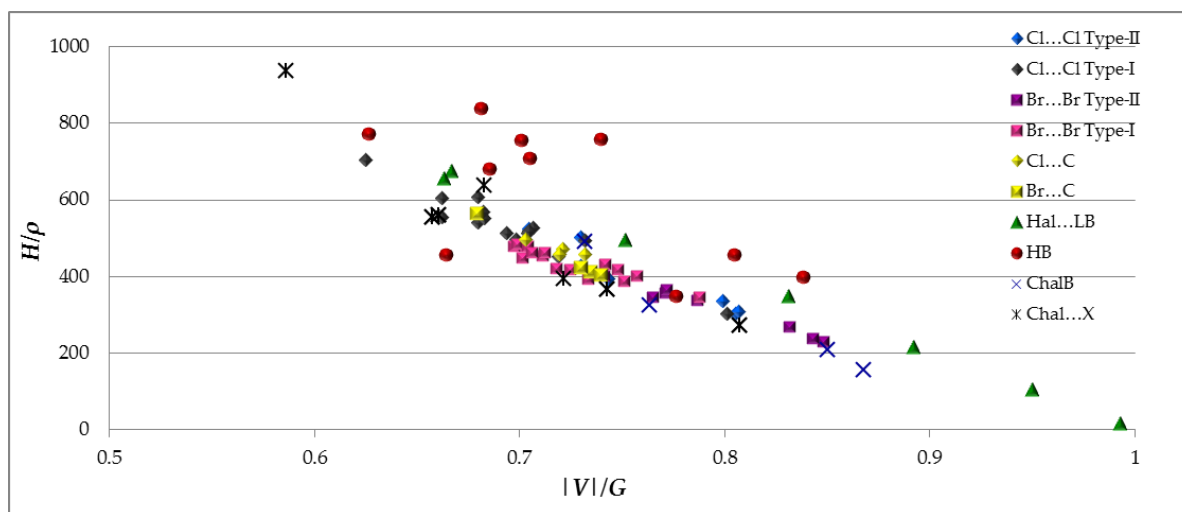
Figure IV.10 Interdependence between the parameters H/ρ (kJ mol^{-1}e^{-1}) and $|V|/G$. All the studied interactions are included.

Summary

In this chapter we have performed a comparative study of different intermolecular interactions within the crystal structures of C_6Hal_5OH (Hal = Cl, Br), C_3HIOS_2, and $C_8O_2H_4Se$ from the $\rho(\mathbf{r})$ and $L(\mathbf{r})$ functions. The effectiveness of halogen and chalcogen bonding for driving molecular packing was shown, based on the estimated interaction energy at BCP and the calculated electrostatic power of each interaction. Halogen bonding interactions, when forming Hal_3-synthons, show similar E_{int} magnitudes to those found for hydrogen bonding of small-medium strength. However, halogen bonding, formed between a Hal-atom and a Lewis base (I···O in our case) is more energetic than the competing hydrogen bonding, while showing very close electrostatic interactions as measured from $\Delta(L/\rho)$. The comparison between hydrogen and chalcogen bonding in the crystal structure of $C_8O_2H_4Se$ revealed the close to each other interaction energy values. In this case, the electrostatic descriptor shows much more pronounced values for hydrogen bonding. From these results, it seems to appear that, interaction energy contributions other than electrostatic can overcompensate for the contribution of the latter in halogen and chalcogen interactions, permitting to be more energetic (case of Hal···LB) or similar in energy (case of chalcogen bonding) than weak hydrogen bonding interactions. This trend is brought closer to the dispersion component to the total interaction energy, which is expected to be more important in halogen and chalcogen bondings.

The analysis of the topological properties of weak intermolecular interactions, involving Hal, Chal-, and H-atoms reveals that these interactions can be classified in families: Cl···Cl, Br···Br, Hal···LB, H···O. Each family is characterized by a set of dependencies between the electron properties at the intermolecular BCP and the bonding distance, along with the cross-correlation between those properties. A very good correlation found for H/ρ *vs.* $|V|/G$ parameters can be used to quantify the *softness degree* ($H/\rho > 0$) or the *covalence degree* ($H/\rho < 0$) of any closed-shell interaction, in particular for halogen and chalcogen bondings.

GENERAL CONCLUSION & PERSPECTIVES

1. General conclusion

Understanding and control of intermolecular interactions play a crucial role in molecular recognition, crystal engineering, and biological systems. For this reason, the central goal of this work was the investigation of the three very frequent weak contacts linking the molecules in organic solids – halogen, chalcogen and weak hydrogen bonding.

Data obtained from accurate single-crystal high-resolution low-temperature X-ray diffraction measurements for the isostructural hexabromobenzene (C_6Br_6) and hexachlorobenzene (C_6Cl_6, discussed earlier), pentachlorophenol (C_6Cl_5OH), pentabromophenol (C_6Br_5OH), iododithiolone (C_3HIOS_2), and selenophtalic anhydride ($C_8H_4O_2Se$) permitted to perform their charge density modeling.

Nowadays, charge density analysis based on experimental measurements and periodic theoretical calculations have reached a stage where parameters derived from both the electron density distribution $\rho(\mathbf{r})$ and its topology allow for obtaining the electron properties that characterize the features associated to chemical bonding and intermolecular interactions. To this end, the analysis of $\rho(\mathbf{r})$ based on the *Quantum Theory of Atoms in Molecule* (QTAIM) methodology, developed by R. F. Bader and collaborators, has provided the framework for quantitative characterization of the weak intermolecular interactions studied in the mentioned crystal structures. Based on this methodology, the interaction energy (E_{int}) and electrostatic (L/ρ and $\Delta(L/\rho)$) criteria have been proposed. The E_{int} descriptor, being calculated from the potential energy density at bond critical point (BCP), gives an estimation of the interaction energy of a pairwise interaction. The L/ρ parameter permits to evaluate qualitatively the strength of charge concentration (CC) and charge depletion (CD) regions. It is considered that the nucleophilic power of the CC region increases with the L/ρ_{CC} value, while the electrophilic one of the CD region parallels the decrease of L/ρ_{CD} value. As a result, the greater the difference $\Delta(L/\rho) = (L/\rho)_{CD} - (L/\rho)_{CC}$ in the face-to-face CC···CD regions the more pronounced electrophilic–nucleophilic interaction character is.

Responding the first objective of this work, formulated in *General Introduction*, we have carried out a comparative study of the intermolecular interactions involving Hal-atoms (Hal = Cl, Br, I) in different geometries using the described methodology. A special attention has been paid to cyclic trimers based on Hal···Hal interactions (Cl_3- and Br_3-synthons) analyzed in terms of experimental and theoretical charge density analysis, followed by a careful topological evaluation of properties. The functions $\Delta\rho(\mathbf{r})$ and $L(\mathbf{r}) = -\nabla^2\rho(\mathbf{r})$ have revealed the anisotropic nature of the charge distribution around the halogen atoms giving rise to local charge concentration (CC/δ^-) and charge depletion (CD/δ^+) regions, which correspond to nucleophilic and electrophilic sites around the halogen nuclei. As a result, CC and CD face to each other along the interaction direction of type II Hal···Hal contacts, indicating both an electrostatically favoured electrophilic–nucleophilic interaction and a highly directional contact driven by these electrostatic sites. According to the topological and energetic properties at BCP, all the studied Hal···Hal Type-II contacts exhibit as *pure* closed-shell interactions. Hal_3-synthons were analyzed

157

as a unique structural motif, being characterized by the topological and energetic properties resulting from the addition of the contributions at the three bond critical points (*i.e.*, each property P of the Hal$_3$-synthon was calculated as $P_\Sigma = \Sigma_i\ P_i^{BCP}$, i = 1, 2, 3). In particular, the interaction energy of the Hal$_3$-synthon ($E_{int,\Sigma}$) was experimentally estimated as: $E_{int,\Sigma} \sim \dfrac{1}{2}\sum_i V_i^{BCP}$

This expression follows similar evaluations used for other *pure* closed-shell interactions and is being assumed to be the most important contribution to the trimer interaction energy E_{int}. Based on this estimation, the interaction energy is, on average, 17 % greater in Br$_3$- than in Cl$_3$-synthons (15 and 13 kJ mol^{-1}, respectively). Moreover, the $E_{int,\Sigma}$ magnitudes of Cl$_3$- and Br$_3$-synthons are comparable to those of small-medium strength hydrogen bonds, while single Cl$\cdots$Cl and Br$\cdots$Br interactions within the synthon exhibit a very weak strength (~4 and 5 kJ mol^{-1}, respectively).

The present study brings out, for the first time, the main difference between Cl$_3$- and Br$_3$-synthons, based on the topological analysis of the function $L(\mathbf{r}) = -\nabla^2\rho(\mathbf{r})$ and on the L/ρ magnitudes. The intensity of the electrostatic interactions, measured from the electrophilic and nucleophilic power of the involved CD and CC regions, has been quantified by the difference in the Laplacian values normalized to charge density unit ($\Delta(L/\rho)$) at the topological critical points of the $L(\mathbf{r})$ function in these regions. The $\Delta(L/\rho)$ magnitudes in Cl$_3$- and Br$_3$-synthons, which reflect the electrostatic interaction in these structural motifs, parallel the calculated $E_{int,}$ magnitudes, supporting our suggestion about a stronger interaction in the case of Br$_3$-synthons, not only from the interaction energy point of view but also from the electrostatic strength between the CC and CD regions. As a consequence of their particular electron density distribution, Hal$_3$-synthons are structurally recovered motifs in crystal environments due to a very important directional electrostatic recognition between δ^+/CD and δ^-/CC regions, thanks to their very well adopted dispositions in triangular motifs.

In accordance with the second objective of this work, we have investigated intermolecular interactions involving chalcogen atoms (Chal). We have proved that directionality is one of the most important characteristics of chalcogen bonding Chal$\cdots$X (X = Chal, Hal, LB). As previously observed with halogen bonding, chalcogen bonding is also controlled by electrostatic electrophilic–nucleophilic interactions, which are established by placing face-to-face CD$\cdots$CC regions and are quantitatively monitored by $\Delta(L/\rho)$ magnitudes. As a consequence of the charge density polarization in the chemical bond and of the sp^3 hybridization of the chalcogen atom, CD/δ^+ regions are observed approximately along both C–Chal directions and give rise to two σ-holes, while CC/δ^- regions are in the perpendicular plane bisecting the C–Chal–C group due to the location of the lone pairs. The concerted increase/decrease of the extension of CD/CC regions along the series O < S < Se < Te follows the progressive depletion of $\rho(\mathbf{r})$ in the chalcogen valence shell. In this process, topological CD sites dominate a progressively enlarged electrophilic region within the C-Chal-C plane, while two nucleophilic regions significantly separate and weaken in a perpendicular disposition to the former.

On the example of the studied bifurcated chalcogen bonding interactions it is shown that the synthon arrangement can be formed not only involving similar atoms, like in Hal$_3$-synthons, but also involving similar sites in contact formation (CC$\cdots$CD).

Chalcogen and halogen bonding exhibit many similarities between each other as both of them are induced from the interaction between the atomic CD/δ^+ and CC/δ^- regions. These interactions are directional and increase in strength with the atom size.

From the results of this study, the series Chal = O, S, Se, Te could be put in front of Hal = F, Cl, Br, I to expect roughly similar interaction energies when comparing chalcogen (Chal···X) to halogen (Hal···X) bonding interactions at similar penetrations (Chal and Hal by pairs of closest atoms). However, as the dispersion component is expected to be slightly larger in halogen than in chalcogen bonding, interaction energies are expected to be somewhat larger for the former. Main differences between chalcogen and halogen bonding can be attributed to the particular orientation of CD and CC regions in chalcogen and halogen atoms, leading to specific directionalities in their electrophilic–nucleophilic interactions. This important trend indicates that chalcogen and halogen bonding can drive different geometrical preferences of molecular packing and therefore they can be put in perspective to design specific molecular arrangements in supramolecular chemistry and crystal engineering.

Responding the third purpose of our work, we have investigated the competition between halogen- or chalcogen- and hydrogen-bonding interactions inside a crystal structure. Competing halogen bonding (Hal_3-synthons) and hydrogen bonding coexist in the crystal structures of C_6Hal_5OH (Hal = Cl, Br). All the topological properties calculated for Cl_3- and Br_3-synthons, as well as their estimated $E_{int,\Sigma}$ values, show similar magnitudes than those observed for hydrogen bonding of small-medium strength. The comparison of Hal_3-synthons to intermolecular hydrogen bonding indicate that while the $E_{int,\Sigma}$ magnitudes are mostly equivalent in C_6Br_5OH, the hydrogen bond in C_6Cl_5OH is ~ 20 % stronger than the Cl_3-synthon. Comparing the corresponding $\Delta(L/\rho)$ magnitudes, hydrogen bonding exhibits electrostatic interactions ~ 20 % and 50 % more intense than Br_3- and Cl_3-synthons. Accordingly, the electrostatic contribution increases from chlorine to bromine based synthons. On the other hand, a further contribution adds to the electrostatic one in the total interaction energy to bring closer $E_{int,\Sigma}$ values from hydrogen bonding and Hal_3-synthons. Most probably, this contribution is coming from dispersion effects that have not been analyzed in this work. Even though it is considered that halogen bonding interactions play a secondary role with respect to the more dominant hydrogen bonding capabilities, the present results show that, when forming Hal_3-synthons, they could be as effective as hydrogen bonding for supramolecular chemistry and crystal engineering purposes.

The competing halogen (Hal···LB) and hydrogen bonding were described in the crystal structure of C_3HIOS_2. In contrast to weaker Hal···Hal interactions, halogen bonding formed with a Lewis base are found to be stronger in comparison with the neighboring hydrogen bonding (on average between experimental and theoretical values, 13.8 and 9.1 kJ mol^{-1}, respectively).

In the crystal structure of $C_8H_4O_2Se$, the chalcogen atom of each molecule is involved in chalcogen (Se···O and Se···Se) and hydrogen (Se···H) bonding interactions. Based on the interaction energy evaluation, the three interactions perform very similar and low values (4.9, 3.8 and 4.6 kJ mol^{-1}, respectively), while the electrostatic descriptor reveals a much more pronounced electrostatic contribution in the case of hydrogen bonding comparing with chalcogen bonding ($\Delta(L/\rho)$ = 13.1, 21.3 and 2.8 Å^{-2} on average between experimental and theoretical values for the Se···H, Se···O and Se···Se interactions, respectively).

The dependencies of the topological and energetic properties of $\rho(\mathbf{r})$ at BCP on the intermolecular distance, along with the cross-correlation between those properties, were represented for all the studied intermolecular interactions. Having good exponential fittings, the representations of the topological values at BCP (ρ, $\nabla^2\rho$, λ_i, G and V) against the interaction distances distinguish between the families of intermolecular interactions – Cl···Cl (Type-I and II), Br···Br (Type-I and II), Hal···LB, H···X (X = O, Br, Se). On the other hand, the representations of $|\lambda_1+\lambda_2|$ *vs.* λ_3, G *vs.* λ_3, $|V|$ *vs.* $|\lambda_1+\lambda_2|$, $|V|$ *vs.* G, and H/ρ *vs.* $|V|/G$ data show that families regroup, and a unique function could be used for fitting all the interactions together in each representation. This feature indicates (i) similar correlations hold for all the studied interactions and (ii) they can be used to retrieve a good estimation of one property from the magnitude of the other. Moreover, from the very good correlation found for H/ρ *vs.* $|V|/G$ data, the $|V|/G$ descriptor, which permits to classify interactions in *pure* closed-shell ($|V|/G < 1$), shared-shell ($|V|/G > 2$), and those of intermediate character ($1 < |V|/G < 2$), can be used to quantify the *softness degree* ($H/\rho > 0$) or the *covalence degree* ($H/\rho < 0$) of any closed-shell interaction.

Finally, the dependences of the topological and energetic properties on the intermolecular distance, and the cross-correlation between the topological and energetic properties, parallel those previously observed for hydrogen bonding, indicating that weak interactions behave similarly from topological descriptors at BCP independently of their nature.

2. Perspectives

The present work, which is aimed to investigate weak intermolecular interactions and, based on the QTAIM methodology, to create new approaches for understanding their nature, can be developed in the two principal directions.

The first one concerns the proposed methodological approaches. As it was shown, the analysis of the experimental and theoretical charge density and of topological properties of electron density $\rho(\mathbf{r})$, and Laplacian $\nabla^2\rho(\mathbf{r})$ functions permits to compare different intermolecular interactions between each other. In this context, the energetic descriptor – interaction energy (E_{int}) – derived earlier for hydrogen bonding, was tested on the other weak intermolecular interactions, involving Hal- and Chal-atoms. Characterizing a pairwise interaction and being derived from the corresponding potential energy density at BCP, it was shown to work qualitatively well for the comparison between halogen and chalcogen bondings. However, the correlation coefficient between the interaction energy and the potential energy density (derived for hydrogen bonding as 0.5) seems to slightly vary depending on the interaction type. Therefore, precise theoretical calculations are needed in order to define the exact magnitude of this coefficient for each interaction.

The second criteria – electrostatic descriptors L/ρ and $\Delta(L/\rho)$ – were proposed for evaluation of the electrostatic interaction in the intermolecular contacts, involving the common for organic structures light atoms (such as O, S, Cl, and H), as well as heavier halogen and chalcogen atoms (Br, I, Se). On this stage of development, the $\Delta(L/\rho)$ parameter permits to compare different intermolecular interactions thanks to the normalization of L by ρ. In this work, L/ρ was calculated at the electrophilic (CD) and nucleophilic (CC) sites involved in the directional CD···CC interactions, showing good agreement with the predictions made from the theoretical

calculations in the literature. For the interactions of type CD⋯CC, in which the location of interacting sites deviates significantly from the interaction direction (typical in the case of bifurcated interactions), the choice of interacting sites should be probably changed to the ones placed exactly along the corresponding bond path. In order to confirm quantitatively the obtained L/ρ and $\Delta(L/\rho)$ values, the precise theoretical calculations should be performed.

Another methodological aspect concerns the possibility to distinguish between different intermolecular-interaction families by observing the correlation between the topological and energetic properties of the electron density at BCP, as well as between each of them and the bonding distance. In this work, several tendencies were pointed out and the best correlation parameters were defined. It was noticed, that a dispersion of values around the expected dependencies is more pronounced for some properties than for others. To which extent this larger dispersion is due to experimental errors or to the complex effect of the crystal environment is an important issue that should be investigated. Also the defining the exact fitting functions parameters can be useful to predict the properties of a certain contact. For this purpose, a large statistical sampling should be investigated for each interaction series.

In general, the dependencies between the electron properties at the BCP, as well as between them and the bonding distance, for all kind of intermolecular interactions can be used in the analysis of experimental electron densities.

As the second research direction we outline the practical application of the developed methodology. Working quite well on halogen and chalcogen bonding interactions, the electrostatic and interaction energy descriptors can be applied for the other types of intermolecular interactions of Lewis acid–base type when highly accurate charge density model is available. For example, it was noticed, that the elements of nitrogen family (pnictogens: N, P, As, Sb, Bi) in some cases form the discussed here *key-lock* arrangement – the contacts As⋯S and As⋯O in arsenates As_xChal_y (Chal = O, S), characterized by the electron density distributions and local-energy density properties, were defined as Lewis acid-base-directed van der Waals interactions. [182]

The developed approach for the halogen bonding interactions can be extended to the compounds that are considered to be promising from the viewpoint of material science. It can concern the halogenated charge-transfer complexes that are known as organic conductors.[183] For example, the series of cation radical salts derived from the iodinated tetrathiafulvalene with different oxo anions are linked by very short halogen bonding interaction I⋯O. An attempt in this direction was done in the framework of this PhD thesis with the $(TM\text{-}TTF\text{-}I)_2/ClO_4$ compound. However, experimental data were of too low quality to study the role of halogen bonding (I⋯O) in the control of the anion-cation charge transfer, governing the physical properties of the material. Accordingly, further work should be therefore done in the future application of charge density analysis on these relevant materials.
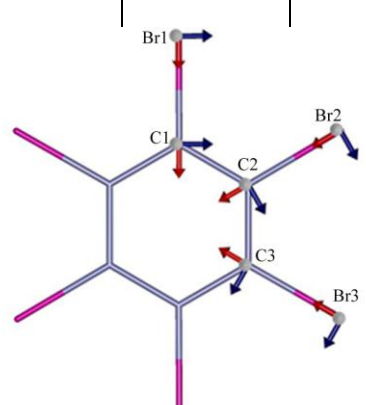
Based on the knowledge about the nature and geometrical preferences of the intermolecular interactions, different growth mechanism for molecular crystals can be proposed. This knowledge is also important for the development of molecules with biological activity.

Annexes

Annex 1. Multipolar parameters

Table 1. Electron density multipolar parameters for Br- and C-atoms belonging to the asymmetric unit of C_6Br_6 – theoretical model The directions of the X and Y axis are marked in red and blue arrows respectively. Z axis is orthogonal to X and Y and marked in grey.

	Br_1	Br_2	Br_3	C_1	C_2	C_3
κ	1.0141	1.0140	1.0141	1.0071	1.0077	1.0080
κ'	0.8194	0.8294	0.8252	0.9641	0.9803	0.9743
P_v	7.007	7.012	7.013	4.002	3.983	3.984
$D_{1,1+}$	-0.044	-0.043	-0.043	0.065	0.061	0.064
$D_{1,1-}$	0.001	-0.001	-0.002	-0.001	0.001	-0.003
$D_{1,0}$	-0.002	0.002	-0.004	0.002	0.002	-0.002
$Q_{2,0}$	0.056	0.056	0.054	-0.121	-0.116	-0.117
$Q_{2,1+}$	0.006	0.001	0.002	-0.004	0.001	0.003
$Q_{2,1-}$	-0.001	0.005	0.005	0.001	0.003	-0.001
$Q_{2,2+}$	-0.115	-0.114	-0.112	-0.076	-0.075	-0.078
$Q_{2,2-}$	0.004	-0.002	-0.002	0.001	-0.001	-0.001
$O_{3,0}$	0.007	0.001	0.004	-0.003	0.002	0.003
$O_{3,1+}$	-0.074	-0.074	-0.075	-0.003	0.002	-0.001
$O_{3,1-}$	0.001	0.002	0.001	0.001	0.003	0.001
$O_{3,2+}$	-0.005	0.005	-0.003	0.004	-0.002	-0.001
$O_{3,2-}$	-0.003	-0.003	-0.002	0.002	-0.001	-0.001
$O_{3,3+}$	0.090	0.090	0.091	-0.228	-0.224	-0.223
$O_{3,3-}$	0.002	-0.003	-0.001	0.001	-0.001	0.002
$H_{4,0}$	0.031	0.034	0.031			
$H_{4,1+}$	0.010	-0.001	0.009			
$H_{4,1-}$	0.001	0.006	0.003			
$H_{4,2+}$	-0.033	-0.039	-0.032			
$H_{4,2-}$	0.005	-0.004	0.004			
$H_{4,3+}$	-0.002	0.004	-0.001			
$H_{4,3-}$	-0.001	0.005	-0.001			
$H_{4,4+}$	0.037	0.037	0.038			
$H_{4,4-}$	0.005	0.003	0.001			

Table 2. Electron density multipolar parameters for Cl-, C-, O- and H-atoms of C_6Cl_5OH. For the axis description see Table 1.

	Cl_1	Cl_2	Cl_3	Cl_4	Cl_5	C_1	C_2	C_3	C_4	C_5	C_6	O_6	H_6
κ	1.0001	1.0054	1.0075	1.0005	0.9972	1.0147	1.0048	1.0215	1.0208	1.0115	1.0166	0.9928	1.1103
κ'	1.0186	1.0321	0.9767	0.9723	1.0316	0.9686	0.9804	0.9713	0.9785	0.9758	0.9709	0.9534	1.1602
P_v	7.100	7.128	7.091	7.059	7.096	3.948	3.946	3.950	3.918	3.919	3.972	6.036	0.834
$D_{1,1+}$	-0.023	-0.028	-0.036	-0.021	-0.011	0.056	0.053	0.056	0.080	0.048	0.049	-0.046	0.158
$D_{1,1-}$	0.002	0.002	0.038	-0.032	-0.008	0.021	0.029	-0.006	-0.024	-0.002	-0.018	0.049	
$D_{1,0}$	0.004	0.014	-0.009	0.002	0.016	0.020	-0.007	0.002	0.018	0.012	-0.005	-0.023	
$Q_{2,0}$	0.071	0.061	0.070	0.062	0.071	-0.126	-0.168	-0.157	-0.166	-0.128	-0.200	0.053	
$Q_{2,1+}$	-0.003	-0.038	-0.026	0.009	0.032	-0.002	-0.029	-0.004	-0.002	0.022	0.010	0.009	
$Q_{2,1-}$	-0.046	-0.020	0.023	0.054	0.009	-0.008	-0.011	-0.001	0.014	-0.009	-0.028	0.024	
$Q_{2,2+}$	-0.076	-0.129	-0.124	-0.087	-0.136	-0.049	-0.104	-0.060	-0.088	-0.107	-0.042	-0.053	
$Q_{2,2-}$	0.003	-0.024	0.042	-0.012	-0.010	0.005	0.009	-0.003	-0.015	-0.011	0.014	0.003	
$O_{3,0}$	-0.001	0.004	-0.006	-0.001	-0.004	-0.014	-0.007	-0.007	-0.028	0.005	0.002	-0.012	
$O_{3,1+}$	-0.084	-0.079	-0.091	-0.089	-0.083	0.020	0.002	0.030	0.003	0.023	0.060	0.005	
$O_{3,1-}$	-0.018	-0.022	0.006	-0.001	-0.012	-0.002	-0.004	0.005	0.013	0.001	-0.007	0.009	
$O_{3,2+}$	-0.024	0.005	-0.014	0.009	-0.019	0.012	-0.009	0.034	0.018	-0.004	0.007	-0.010	
$O_{3,2-}$	-0.022	0.007	-0.007	0.016	-0.004	-0.010	-0.010	-0.012	-0.004	-0.020	0.004	0.018	
$O_{3,3+}$	0.102	0.082	0.102	0.114	0.121	-0.260	-0.307	-0.301	-0.283	-0.267	-0.355	0.065	
$O_{3,3-}$	0.012	0.013	-0.016	0.006	0.018	0.003	-0.018	-0.017	0.004	-0.30	-0.020	-0.009	
$H_{4,0}$	0.002	0.020	0.031	0.038	0.011								
$H_{4,1+}$	0.002	0.014	0.002	0.012	0.006								
$H_{4,1-}$	0.007	0.015	-0.014	-0.011	-0.007								
$H_{4,2+}$	-0.015	-0.076	-0.056	-0.045	-0.048								
$H_{4,2-}$	0.015	-0.001	0.008	-0.006	0.010								
$H_{4,3+}$	0.007	0.002	0.027	-0.019	0.017								
$H_{4,3-}$	0.016	0.006	-0.001	0.001	-0.027								
$H_{4,4+}$	0.036	0.029	0.027	0.030	0.050								
$H_{4,4-}$	-0.008	0.007	-0.021	0.017	-0.008								
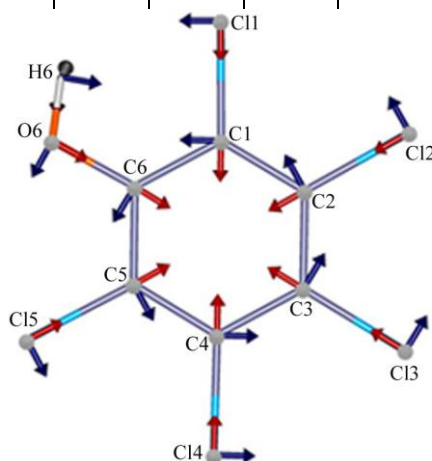
Table 3. Electron density multipolar parameters for Br-, C-, O- and H-atoms of C_6Br_5OH. For the axis description see Table 1.

|	Br$_1$	Br$_2$	Br$_3$	Br$_4$	Br$_5$	C$_1$	C$_2$	C$_3$	C$_4$	C$_5$	C$_6$	O$_6$	H$_6$
κ	1.0155	1.0188	1.0187	1.0106	1.0202	0.9929	0.9948	0.9919	0.9986	0.9970	0.9951	0.9749	1.1611
κ'	1.0333	1.0335	1.0356	1.0335	1.0351	0.8357	0.8326	0.8326	0.8317	0.8329	0.8344	0.8686	1.1597
Pv	7.065	7.064	7.065	7.066	7.065	3.874	3.877	3.875	3.882	3.882	3.879	6.505	0.900
D$_{1,1+}$	-0.038	-0.018	-0.015	-0.027	-0.035	0.067	0.070	0.050	0.053	0.079	0.071	0.032	0.154
D$_{1,1-}$	-0.053	-0.030	-0.049	-0.018	0.006	0.015	0.010	-0.003	-0.011	0.012	0.026	-0.003	
D$_{1,0}$	-0.186	-0.163	-0.131	-0.171	-0.134	0.111	0.093	0.094	0.084	0.080	0.086	0.001	
Q$_{2,0}$	0.115	0.104	0.085	0.078	0.098	-0.197	-0.149	-0.172	-0.170	-0.186	-0.170	0.096	
Q$_{2,1+}$	0.038	0.056	0.023	0.048	0.032	0.038	0.041	0.025	0.022	0.009	0.014	0.006	
Q$_{2,1-}$	0.002	-0.014	-0.039	-0.046	-0.001	0.004	0.002	-0.008	0.004	-0.003	-0.007	0.004	
Q$_{2,2+}$	-0.101	-0.170	-0.087	-0.111	-0.141	-0.129	-0.125	-0.133	-0.118	-0.125	-0.134	-0.072	
Q$_{2,2-}$	0.011	-0.008	0.043	-0.008	0.021	-0.002	0.007	0.010	-0.001	-0.003	0.012	0.001	
O$_{3,0}$	-0.024	0.003	-0.024	-0.008	0.001	0.036	0.038	0.035	0.047	0.029	0.021	-0.008	
O$_{3,1+}$	-0.088	-0.070	-0.054	-0.072	-0.060	0.002	-0.007	-0.002	-0.022	-0.015	-0.015	-0.067	
O$_{3,1-}$	-0.006	0.023	-0.009	-0.031	0.005	0.006	-0.002	-0.008	0.026	0.008	-0.005	0.005	
O$_{3,2+}$	-0.006	-0.023	-0.007	-0.28	-0.043	0.003	0.004	0.008	-0.008	0.009	-0.001	0.001	
O$_{3,2-}$	0.009	0.044	0.019	0.009	-0.007	-0.001	0.012	-0.002	0.008	0.005	-0.003	-0.004	
O$_{3,3+}$	0.085	0.065	0.112	0.082	0.112	-0.433	-0.414	-0.422	-0.427	-0.436	-0.431	0.143	
O$_{3,3-}$	0.002	-0.010	-0.028	0.005	0.012	0.001	0.001	0.013	0.013	0.014	-0.010	0.011	
H$_{4,0}$	0.003	0.010	0.042	0.032	0.031								
H$_{4,1+}$	-0.010	-0.072	-0.036	0.033	0.005								
H$_{4,1-}$	0.056	0.084	0.078	0.081	0.069								
H$_{4,2+}$	-0.061	-0.034	-0.071	-0.047	-0.056								
H$_{4,2-}$	0.061	0.049	0.052	0.073	0.052								
H$_{4,3+}$	0.001	0.005	0.024	-0.008	-0.012								
H$_{4,3-}$	-0.033	-0.024	-0.021	-0.025	-0.049								
H$_{4,4+}$	0.010-	0.013	-0.020	-0.022	0.046								
H$_{4,4-}$	0.014	-0.021	0.015	-0.028	-0.034								
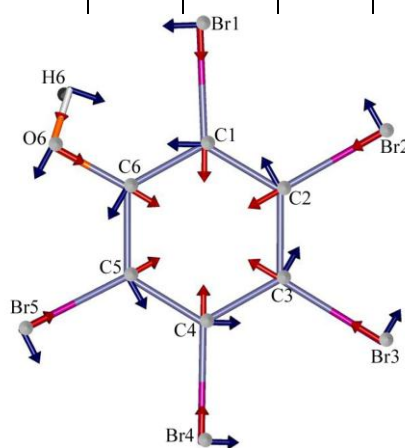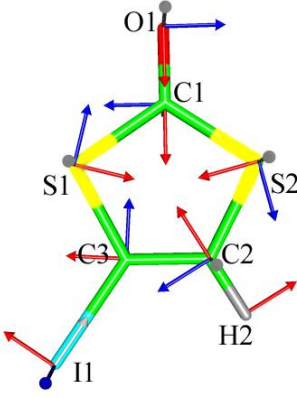
Table 4. Experimental electron density multipolar parameters for the atoms belonging to the asymmetric unit of selenophtalic anhydride ($C_8H_4O_2Se$). For the axis description see Table 1.

	Se$_1$	O$_1$	O$_2$	C$_1$	C$_2$	C$_3$	C$_4$	C$_5$	C$_6$	C$_7$	C$_8$	H$_1$	H$_2$	H$_3$	H$_4$
κ	0.9904	1.0097	1.0100	0.9865	0.9918	0.9995	1.0190	1.0151	1.0097	1.0132	1.0024	1.1544	1.1429	1.1347	1.1583
κ'	0.9479	1.1711	1.2686	1.0698	1.0787	1.1471	1.1029	1.0105	0.9774	1.0452	1.0452	1.1889	1.2384	1.2005	1.1248
Pv	6.051	5.862	5.888	4.3253	4.367	4.048	4.012	4.128	4.156	4.113	4.042	0.776	0.719	0.796	0.751
D$_{1,1+}$	-0.064	-0.147	-0.147	-0.193	-0.194	-0.032	-0.031	-0.052	-0.018	-0.102	-0.055	0.091	0.079	0.068	0.085
D$_{1,1-}$	0.001	-0.002	-0.002	0.029	-0.039	0.051	0.004	0.018	-0.021	-0.053	0.028				
D$_{1,0}$	-0.000	-0.002	-0.002	-0.012	-0.055	0.008	-0.029	0.021	0.005	-0.032	-0.027				
Q$_{2,0}$	0.058	-0.057	-0.057	-0.325	-0.306	-0.173	-0.117	-0.241	-0.234	-0.225	-0.161				
Q$_{2,1+}$	-0.001	0.003	0.003	-0.041	0.001	-0.015	0.009	-0.001	-0.012	0.026	-0.025				
Q$_{2,1-}$	-0.002	0.004	0.004	0.021	-0.016	0.018	0.008	-0.010	-0.015	-0.053	0.027				
Q$_{2,2+}$	0.022	-0.095	-0.095	0.241	0.198	0.068	0.073	0.073	-0.016	0.003	0.032				
Q$_{2,2-}$	0.002	-0.002	-0.002	0.025	-0.066	0.022	-0.037	-0.033	-0.031	0.022	0.016				
O$_{3,0}$	0.005	0.032	0.032	-0.022	0.007	-0.07	0.020	0.049	-0.027	-0.007	0.043				
O$_{3,1+}$	-0.054	0.019	0.019	-0.045	0.026	0.044	-0.021	0.046	0.039	0.051	0.058				
O$_{3,1-}$	-0.001	0.032	0.032	-0.013	0.037	0.021	0.019	0.011	0.043	0.059	0.021				
O$_{3,2+}$	0.002	-0.007	-0.007	0.019	-0.028	0.029	-0.006	-0.033	0.067	-0.037	-0.025				
O$_{3,2-}$	0.001	-0.007	-0.007	0.001	-0.038	0.043	-0.039	-0.021	0.003	-0.012	0.008				
O$_{3,3+}$	-0.104	0.001	0.001	-0.432	-0.395	-0.271	-0.188	-0.241	-0.241	-0.285	-0.265				
O$_{3,3-}$	-0.003	-0.026	-0.026	0.036	-0.006	-0.001	0.010	-0.053	0.195	-0.001	-0.30				
H$_{4,0}$	0.030														
H$_{4,1+}$	-0.003														
H$_{4,1-}$	-0.001														
H$_{4,2+}$	0.004														
H$_{4,2-}$	-0.001														
H$_{4,3+}$	0.004														
H$_{4,3-}$	0.001														
H$_{4,4+}$	-0.068														
H$_{4,4-}$	0.002														
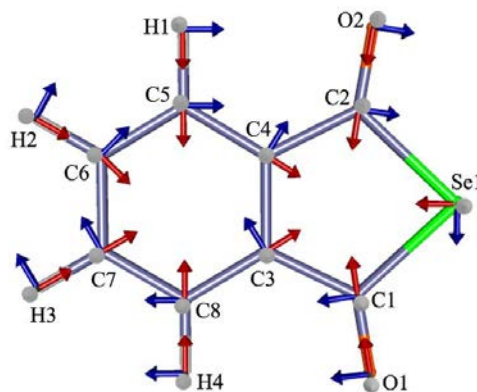
Table 5. Electron density multipolar parameters for I-, S-, O-, C-, and H-atoms belonging to the asymmetric unit of iododithiolone (C_3HIOS_2) – theoretical model. For the axis description see Table 1.

	I_1	S_1	S_2	O_1	C_1	C_2	C_3	H_2
κ	1.0343	0.9834	0.9737	1.0005	0.9770	1.0147	1.0044	1.3000
κ'	0.9527	1.0975	1.1888	1.1885	0.8531	0.9431	0.8532	1.4847
P_v	6.7239	6.4043	6.0765	5.9181	4.4311	3.8474	3.9497	0.6491
$D_{1,1+}$	-0.020	-0.063	-0.008	-0.102	-0.184	-0.139	-0.126	0.090
$D_{1,1-}$	0.016	0.104	-0.023	-0.013	-0.003	0.049	-0.012	
$D_{1,0}$	-0.076	-0.021	-0.013	-0.002	0.036	0.020	0.012	
$Q_{2,0}$	0.255	0.017	0.038	-0.047	-0.322	-0.148	-0.154	
$Q_{2,1+}$	-0.005	0.000	0.006	0.000	0.018	-0.028	-0.010	
$Q_{2,1-}$	-0.002	-0.014	0.000	0.001	0.006	0.001	-0.006	
$Q_{2,2+}$	0.044	0.046	0.017	-0.054	0.206	0.072	0.144	
$Q_{2,2-}$	0.010	0.002	0.017	0.004	-0.021	0.076	-0.032	
$O_{3,0}$	0.093	0.000	0.005	0.000	-0.006	0.007	-0.005	
$O_{3,1+}$	-0.068	-0.112	-0.080	-0.010	0.055	0.037	0.000	
$O_{3,1-}$	0.008	0.035	-0.022	0.000	0.011	0.021	-0.004	
$O_{3,2+}$	0.055	-0.035	-0.019	-0.001	0.008	-0.003	-0.010	
$O_{3,2-}$	0.014	-0.001	-0.007	0.000	-0.006	-0.018	0.015	
$O_{3,3+}$	0.009	-0.259	-0.173	0.012	-0.308	-0.261	0.239	
$O_{3,3-}$	-0.039	-0.018	0.007	0.004	-0.032	0.015	-0.006	
$H_{4,0}$	0.111	0.038	0.018					
$H_{4,1+}$	0.023	0.004	0.004					
$H_{4,1-}$	-0.008	0.015	-0.013					
$H_{4,2+}$	-0.064	0.022	-0.016					
$H_{4,2-}$	0.018	0.041	-0.009					
$H_{4,3+}$	-0.004	-0.005	0.016					
$H_{4,3-}$	-0.022	0.005	0.017					
$H_{4,4+}$	-0.008	-0.072	-0.104					
$H_{4,4-}$	-0.009	-0.059	-0.000					

Annex 2. Characterization of the CC1 and CD regions of Hal-atoms

that take part in the synthon formation in C_6Cl_6, C_6Cl_5OH, C_6Br_6, and C_6Br_5OH.[a]

	Atom	Region	L/ρ (Å^{-2})	d (Å)	Angle (°)
C_6Cl_6	Cl_1	CC_1	10.07	0.630	106.2
		CC_2	10.18	0.635	105.6
		CD	4.71	0.654	174.2
	Cl_2	CC_1	10.26	0.635	105.0
		CC_2	10.35	0.636	104.8
		CD	6.10	0.646	173.2
	Cl_3	CC_1	10.61	0.625	95.4
		CC_2	9.60	0.630	101.4
		CD	6.28	0.649	171.2
C_6Cl_5OH	Cl_4	CC_1	10.38	0.627	104.0
		CC_2	10.31	0.626	103.2
		CD	4.89	0.636	177.9
	Cl_2	CC_1	10.17	0.625	103.5
		CC_2	10.21	0.629	104.9
		CD	5.25	0.643	173.1
	Cl_3	CC_1	10.20	0.626	104.0
		CC_2	10.24	0.627	103.3
		CD	5.99	0.637	178.2
C_6Br_6[b]	Br_1	CC_1	0.53	0.857	107.5
		CC_2	0.59	0.861	105.3
		CD	−4.23	0.996	177.6
	Br_2	CC_1	0.60	0.859	103.6
		CC_2	0.57	0.860	108.1
		CD	−4.22	0.972	176.6
	Br_3	CC_1	0.55	0.858	111.5
		CC_2	0.55	0.862	109.8
		CD	−4.09	0.909	172.9
C_6Br_5OH	Br_2	CC_1	2.74	0.839	120.5
		CC_2	3.89	0.837	111.0
		CD	−7.72	0.998	173.3
	Br_3	CC_1	3.16	0.830	95.3
		CC_2	3.52	0.853	109.6
		CD	−5.23	0.975	173.0
	Br_4	CC_1	3.30	0.847	130.0
		CC_2	4.05	0.865	105.9
		CD	−4.16	0.999	175.7

[a] CC and CD regions are characterized by their positions (distance from the nucleus and angle C–Hal–CC1/CD) and L/ρ values. Characteristics of CC2 sites, not involved in the Hal3-synthons, are given for comparison with the CC1 ones. [b] Theoretical calculations

Annex 3. Gas-phase calculations
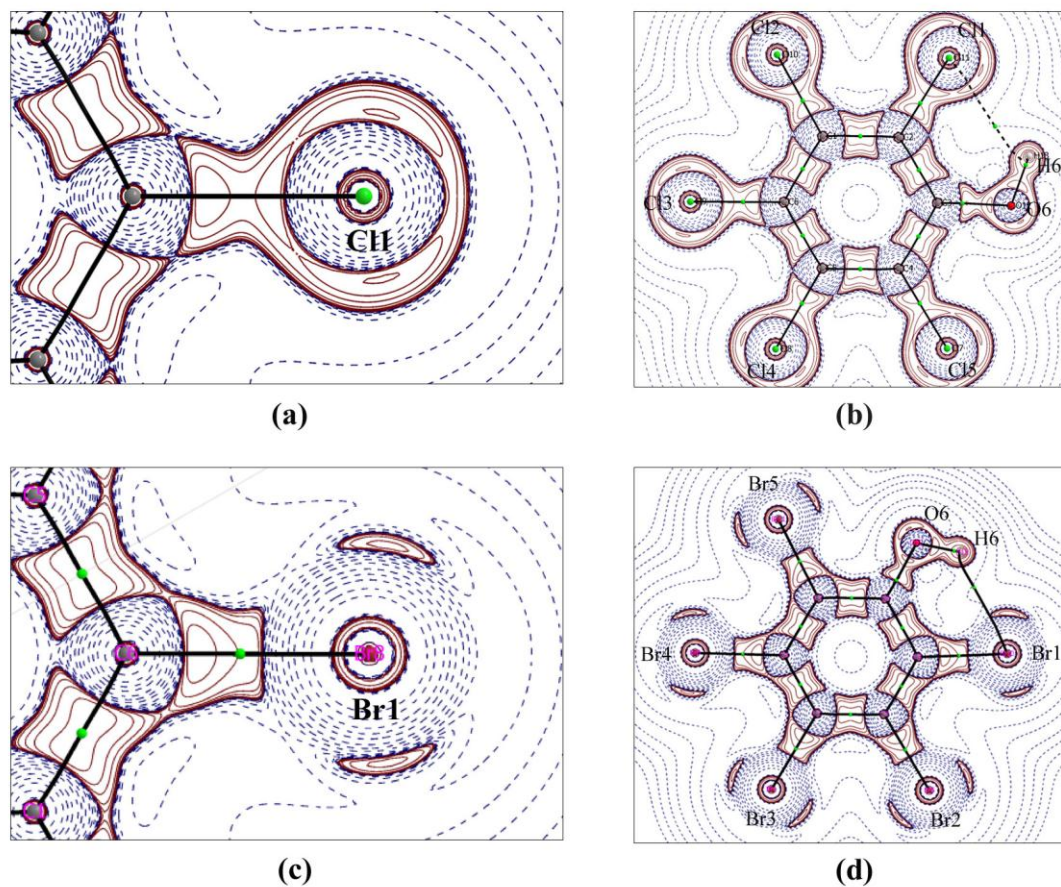
Figure 1. Contour maps of $L(\mathbf{r})$ drawn in the plane of the molecule obtained from the theoretical calculations performed for the isolated molecules in the gas phase for (a) C_6Cl_6 (b) C_6Cl_5OH (c) C_6Br_6 and (d) C_6Br_5OH. Contours are (in a.u.): $0, \pm1\cdot10^{-3}, \pm2\cdot10^n, \pm4\cdot10^n, \pm8\cdot10^n$, with n=-3,-2,-1, 0, 1, 2. Positive contours: red lines, negative contours: blue dashed lines.

Table 6. Magnitudes of L/ρ_{calc} parameter at CC and CD sites, obtained from the theoretical calculations performed for the isolated C_6Cl_6, C_6Cl_5OH, C_6Br_6 and C_6Br_5OH molecules in gas phase. The sites are also characterized by the distance d from the nuclei and the angle C–Hal–CC/CD.

	Atom	Region	d (Å)	Angle (°)	ρ (e Å^{-3})	L (e Å^{-5})	L/ρ_{calc} (Å^{-2})
C_6Cl_6	Cl_1	CC_1	0.624	140.7	1.86	20.47	11.02
		CD	0.652	180.0	1.36	5.87	4.33
C_6Cl_5OH	Cl_1	CC_1	0.627	130.0	1.85	20.16	10.91
		CC_2	0.625	153.4	1.83	19.70	10.76
		CC_3	0.625	153.4	1.83	19.70	10.76
		CD	0.651	180.0	1.37	6.12	4.48
	Cl_2	CC_1	0.625	139.0	1.86	20.38	10.99
		CC_2	0.624	142.4	1.85	20.33	10.97
		CD	0.652	180.0	1.36	5.87	4.32
	Cl_3	CC_1	0.625	140.1	1.86	20.39	10.99
		CC_2	0.624	140.9	1.86	20.38	10.98
		CD	0.652	180.0	1.36	5.82	4.30
	Cl_4	CC_1	0.624	141.1	1.86	20.42	11.00
		CC_2	0.624	140.4	1.86	20.41	11.00
		CD	0.652	180.0	1.36	5.89	4.33
	Cl_5	CC_1	0.624	141.9	1.86	20.40	10.99
		CC_2	0.624	140.1	1.86	20.44	11.01
		CD	0.652	180.0	1.36	5.86	4.32
C_6Br_6	Br_1	CC_1	0.839	99.5	1.07	1.21	1.13
		CD	0.982	180.0	0.51	−2.89	−5.73
C_6Br_5OH	Br_1	CC_1	0.844	94.8	11.0	1.46	1.37
		CC_2	0.842	101.5	1.04	0.92	0.88
		CC_3	0.842	101.5	1.04	0.92	0.88
		CD	0.973	180.0	0.53	−2.83	−5.37
	Br_2	CC_1	0.840	98.7	1.07	1.23	1.15
		CC_2	0.840	100.1	1.07	1.13	1.06
		CD	0.976	180.0	0.52	−2.88	−5.59
	Br_3	CC_1	0.840	99.3	1.07	1.20	1.12
		CC_2	0.840	99.6	1.07	1.18	1.10
		CD	0.975	180.0	0.52	-2.89	-5.61
	Br_4	CC_1	0.840	99.7	1.07	1.19	1.11
		CC_1	0.840	99.3	1.07	1.19	1.12
		CD	0.977	180.0	0.52	−2.88	−5.59
	Br_5	CC_1	0.840	99.9	1.07	1.20	1.12
		CC_1	0.839	99.5	1.07	1.19	1.11
		CD	0.977	180.0	0.51	−2.89	−5.63
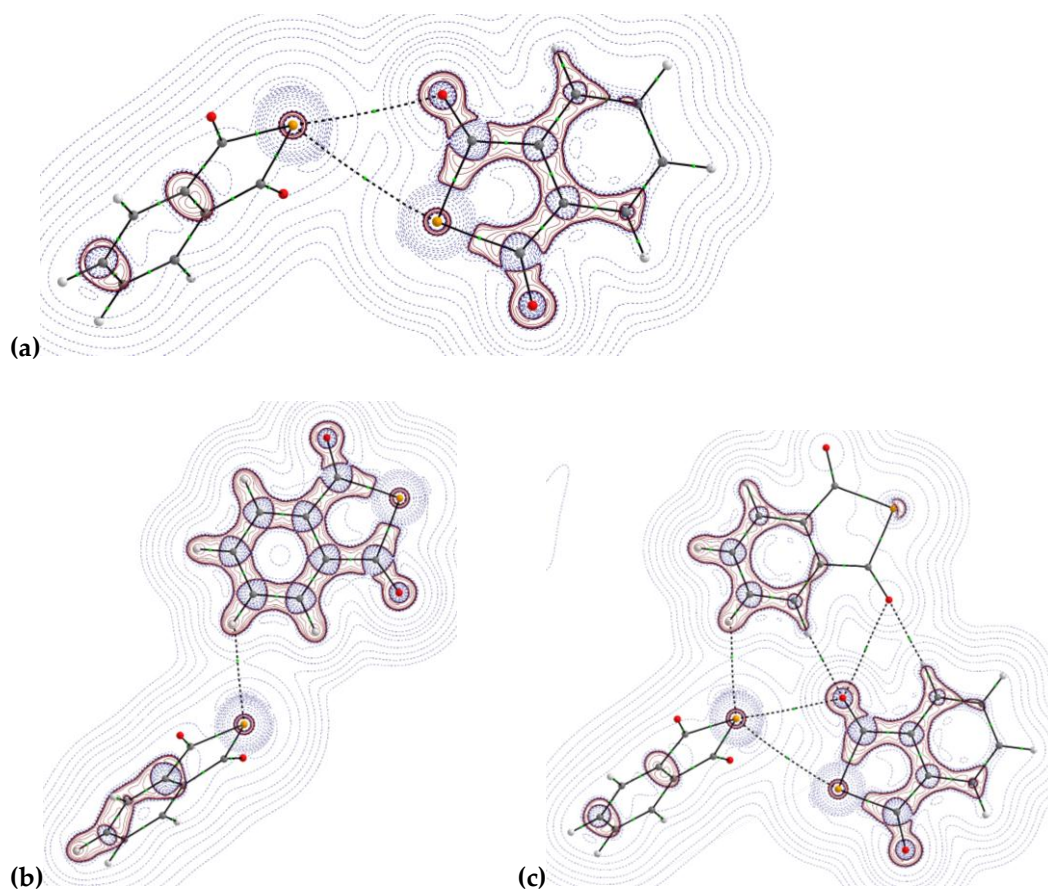
Figure 2. Molecular structures used in the theoretical calculations in the crystal phase of $C_8H_4O_2Se$ on isolated dimers and trimer, superimposed on $L(\mathbf{r})$ maps displaying Se···Se, Se···O, Se···H, O···H, and O···O interactions. (a) dimer 1, (b) dimer 2, (c) trimer. $L(\mathbf{r})$ contours are in logarithmic scale, positive – red, negative – blue.

References

[1]   Lewis G. N. *J. Am. Chem. Soc.* **1916**, *38*, 762-785.

[2]   Bader R. F. W. Atoms in Molecules – A Quantum Theory; Clarendon: Oxford, U.K., **1990**.

[3]   Hohenberg P., Kohn W. *Phys. Rev. B*, **1964**, *136*, 864-871.

[4]   Popelier P. L. A. Atoms in molecules: an introduction; Prentice Hall: London, **2000**.

[5]   (a) Tsirelson V. G., Ozerov R. P. Electron density and bonding in crystals, theory and X-ray diffraction experiments in solid state physics and chemistry; Institute of Physics Publishing: New York, **1996** (b) Gatti C., Macchi P. Modern Charge Density Analysis; Springer: Berlin, **2012**.

[6]   Blake A. J., Clegg W., Cole J. M., Evans J. S. O, Main P., Parsons P., Watkin D. J. Crystal Structure Analysis, Principles and Practice; Oxford University Press, **2009**.

[7]   Zhurov V. V., Zhurova E. A., Pinkerton A. A. *J. Appl. Cryst*. **2008**, *41*, 340-349.

[8]   Rowbotham F. J. Story-lives of the Great Scientists. New York, **1918**.

[9]   (a) Coppens P., Volkov A. *Acta Crystallogr.* **2004**, *A60*, 357–364. (b) Koritsanszky T., Volkov A., Coppens P. *Acta Crystallogr.* **2002**, *A58*, 464-472.

[10]   Sabino J. R., Coppens P. *Acta Crystallogr.* **2003**, *A59*, 127-131.

[11]   (a) Dovesi R., Saunders V. R., Roetti C., Causà M., Harrison N. M., Orlando R., Aprà E. "CRYSTAL95 User's Manuel", Technical Report, University of Torino, **1996**. (b) Blaha P., Schwarz K.-H., Madsen G. K. H., Kvasnicka D., Luitz J. Technical Report, Technische Universitat Wien, **1999**.

[12]   (a) Blöchl P. E. *J. Phys. Rev., Sect B* **1994**, *50*, 17953-17958. (b) Kresse G., Joubert D. *J. Phys. Rev., Sect B* **1999**, *59*, 1758-1775.

[13]   (a) Kresse G., Hafner *J. Phys. Rev., Sect B* **1993**, *47*, 558-561. (b) Kresse G., Hafner J. *J. Phys. Cond. Matt.* **1994**, *6*, 8245-8257. (c) Kresse G., Furthmüller J. *Comp. Materials Science* **1996**, *6*, 15-50. (d) Kresse G., Furthmüller J. *Phys. Rev., Sect B* **1996**, *54*, 11169-11186.

[14]   Aubert E., Lebègue S., Marsman M., Bui T. T. T., Jelsch C., Dahaoui S., Espinosa E., Ángyán J. G. *J. Phys. Chem. A* **2011**, *115*, 14484-14494.

[15]   Coppens P. X-ray charge densities and chemical bonding, IUCr, Oxford University Press, **1997**.

[16]   (a) Coppens P. *Science* **1967**, *158*, 1577-1579. (b) Lecomte C. In Advances in molecular structure research, ed. by I. and M. Hargittai. Greenwich, CT, USA, JAI Press, Inc. **1995**, *1*, 261-302.

[17]   Yasubnez M., Stewart R. F. *Acta Crystallogr*. **1978**, *A34*, 648-662.

[18]   Hansen N. K., Coppens P. *Acta Crystallogr*. **1978**, *A34*, 909-921.

[19]   (a) MoPro: Jelsch C., Guillot B., Lagoutte A., Lecomte C. *J. Appl. Crystallogr*. **2005**, *38*, 38-54. (b) MoProViewer: Guillot B. *Acta Crystallogr*. **2011**, *A67*, C511-C512. (c) Guillot B., Viry L., Guillot R., Lecomte C., Jelsch C. *J. Appl. Cryst*. **2001**, *34*, 214-223.

[20]   El Haouzi A., Hansen N. K., Le Hénaff C., Protas J. *Acta Crystallogr*. **1996**, *A52*, 291-301.

[21] (a) Pérès, N., Bouhkris A., Souhassou M., Gavoille G., Lecomte C. *Acta Crystallogr*. **1999**, *A55*, 1038-1048. (b) Volkov A., Abromov Y. A., Coppens P., Gatti C. *Acta Crystallogr*. **2000**, *A56*, 332-339.

[22] Paul A., Kubicki M., Kubas A., Jelsch C., Fink K., Lecomte C. *J. Phys. Chem. A* **2011**, *115*, 12941-12952.

[23] (a) Espinosa E. PhD Thesis, University of Barcelona **1994**; (b) Moss G. R., Souhassou M., Blessing R. H. *Acta Crystallogr*. **1995**, *B51*, 650-660.

[24] Dahaoui S., Pichon-Pesme V., Howard J. A. K., Lecomte C. *J. Phys. Chem. A* **1999**, *103*, 6240-6250.

[25] Dominiak P. M, Coppens P. *Acta Crystallogr*. **2006**, *A62*, 224-227.

[26] Espinosa E., Molins E., Lecomte C. *Phys. Rev. B* **1997**, *56*, 1820-1833.

[27] (a) Meindl K., Herbst-Irmer R., Henn J. *Acta Crystallogr*. **2010**, *A66*, 362-371. (b) Scheins S., Zheng, S.-L.; Benedict, J. B.; Coppens, P. Acta Crystallogr. 2010, B66, 366-372.

[28] (a) Restori R., Schwarzenbach D. *Acta Crystallogr*. **1996**, *A52*, 369-378. (b) Iversen B. B.,Larsen F. K., Pinkerton A. A., Martin A., Darovsky A., Reynolds P. A. *Acta Crystallogr*. **1999**, **B55**, 363-374. (c) Henn J., Meindl K., Schwab G., Oechsner A., Stalke D. *Angew. Chem. Int. Ed*. **2010**, *49*, 2422-2426. (d) Zhurova E. A., Tsirelson V. G. *Acta Crystallogr*. **2002**, *B58*, 567-575.

[29] Watkin D. *J. Appl. Crystallogr*. **2008**, *41*, 491-522.

[30] Hirshfeld F. L. *Acta Crystallogr*. **1976**, *A32*, 239-244.

[31] Matta C., Boyd, R. J. The Quantum theory of atoms in molecules; Wiley-VCH: Weinheim, **2007**.

[32] Amezaga N. J. M., Pemies S. C., Peruchena N. M., Sosa G. L. *J. Phys. Chem. A*, **2010**, *114*, 552-562.

[33] Bader R. W. F., Beddall P. M. *J. Chem. Phys*. **1972**, *56*, 3320-3329.

[34] (a) Espinosa E., Molins E., Lecomte C. *Chem. Phys. Lett*. **1998**, *285*, 170-173. (b) Espinosa E., Alkorta I., Rozas I., Elguero J., Molins E. *Chem. Phys. Lett*. **2001**, *336*, 457-461. (c) Espinosa E., Molins E., Alkorta I., Elguero J. *J. Chem. Phys*., **2002**, *117*, 5529-5542.

[35] Abramov Yu. A. *Acta Crystallogr*. **1997**, *A53*, 264-272.

[36] (a) Gillespie R. J., Hargittai I. The VSEPR Model of Molecular Geometry; Allyn & Bacon and Prentice Hall, **1991**. (b) Gillespie R. J. Molecular Geometry; Van Nostrand Reinhold, **1972**. (c) Gillespie R. J., Nyholm R. S. Q. *Rev. Chem. Soc.*, **1957**, 339-380.

[37] Popelier P. L. A. *Coord. Chem. Rev*. **2000**, *197*, 169-189. (b) Gillespie R. J., Popelier P. L. A. Chemical bonding and molecular geometry; Oxford University Press, Inc.: New York. **2001**.

[38] (a) Politzer P., Truhlar D. G. Chemical applications of atomic and molecular electrostatic potentials; Plenum Press: New York, **1981**. (b) Náray-Szabó G., Ferenczy G. G. *Chem. Rev*. **1995**, *95*, 829-847. (c) Murray J. S, Sen K. D. Molecular electrostatic potentials concepts and applications; Elsevier Science B. V., Amsterdam, **1996**. (d) Murray J. S., Politzer P. *Theochem*, **1998**, *425*, 107-114. (b) Politzer P., Murray J. S., Concha M. C. *Int. J. Quantum Chem*., **2002**, *88*, 19-27.

[39] (a) Ghermani N. E., Bouhmaida N., Lecomte C. *Acta Crystallogr*. **1993**, *A49*, 781-789. (b) Bouhmaida N., Ghermani N. E., Lecomte C., Thalal A. *Acta Crystallogr*. **1997**, *A53*, 556-563.

[40] Ghermani N., Lecomte C., Bouhmaida N. *Z. Naturforsch*, **1993**, *A48*, 91-98.

[41] Mata I., Molins E., Alkorta I., Espinosa E. *J. Phys. Chem. A* **2007**, *111*, 6425-6433.

[42] Tsirelson V. G., Avilov A. S., Lepsehov G. G., Kulygin A. K., Stahn J., Pietsch U., Spence J. C. H. *J. Phys. Chem. B* **2001**, *105*, 5068-5074.

[43] Clark T. *Comp. Mol. Sci.* **2013,** *3*, 13-20.

[44] (a) Chalasinski G., Szczesniak M. M. *Chem. Rev*. **2000**, *100*, 4227-4252. (b) Hobza P., Zahradnik R., Müller-Dethlefs K. *Coll Czech Chem. Commun*. **2006**, *71*, 443-531. (c) Jeziorski B., Moszynski R., Szalewicz K. *Chem. Rev*. **1994**, *94*, 1887-1930.

[45] Hobza P., Zahradnik R. *Chem Rev*. **1988**, *88*, 871-897.

[46] Stone A. J. The theory of intermolecular forces; Oxford University Press: Oxford, England, **1996**.

[47] Spackman M. A. *J Chem. Phys*. **1986**, *85*, 6587-6601.

[48] (a) Chen J., Martinez T. J. *Chem. Phys. Lett*. **2007**, *438*, 315-320. (b) Sokalski W. A., Roszak S. M. *J. Mol. Struct. (Theochem)* **1991**, *80*, 387-400. (c) Ma Y. G., Politzer P. *J. Chem. Phys*. **2004**, *120*, 3152-3157.

[49] (b) Foster J. P., Weinhold F. J. *J. Am. Chem. Soc*. **1980**, *102*, 7211-7218. (b) Reed A. E., Curtiss L. A., Weinhold F. *Chem. Rev*. **1988**, *88*, 899-926 (and references therein).

[50] Bickelhaupt F. M., Baerends E. *J. Rev. Comput. Chem*. **2000**, *15*, 1-86.

[51] (a) Spackman M. A. *J. Chem. Phys*. **1986**, *85*, 6579-6686.

[52] Price S. L. In Theoretical aspects and computer modeling of the molecular solid state (ed. A. Gavezzotti), Wiley, Chichester **1997**, 31-60.

[53] Desiraju G. R., Vittal J. J., Ramanan A. Crystal Engineering. A Textbook. World Scientific Publishing, Singapore, **2011**.

[54] (a) Werner A. Über Haupt- und Nebenvalenzen und die Constitution der Ammoniumverbindungen. *Liebig's Annalen der Chemie*, **1902**, *322*, 261-97. (b) Hantzsch A. Uber die Isomeriegleichgewichte des Acetessigesters und die sogenannte Isorrhopesis seiner Salze. *Chemische Berichte*, **1910**, *43*, 3049-3076. (c) Pfeiffer P. Zur Theorie der Farblacke, II. *Liebig's Annalen der Chemie*, **1913**, *398*, 137-196. (d) Moore T. S., Winmill T. F. The state of amines in aqueous solution. *J. Chem. Soc.*, **1912**, *101*, 1635-1676. (e) Latimer W. M., Rodebush W. H. Polarity and ionization from the standpoint of the Lewis theory of valence. *J. Am. Chem. Soc.*, **1920**, *42*, 1419-1433. (f) Pauling L. The structure and entropy of ice and of other crystals with some randomness of atomic arrangement. *J. Am. Chem. Soc.*, **1935**, *57*, 2680-2684. (g) Pauling L. The nature of the chemical bond. Cornell University Press, Ithaca, New York, **1939**.

[55] Arunan E., Desiraju G. R., Klein R. A., Sadlej J., Scheiner S., Alkorta I., Clary D. C., Crabtree R. H., Dannenberg J. J., Hobza P., Kjaergaard H. G., Legon A. C., Mennucci B., Nesbitt D. *Pure Appl. Chem*. **2011**, *83*, 1637-1641.

[56] Umeyama H., Morokuma K. *J. Am. Chem. Soc*. **1977**, *99*, 1316-1332.

[57] Desiraju G. R., Steiner T. The Weak Hydrogen Bond in Structural Chemistry and Biology. **1999**.

[58] Van Mourik T., van Duijneveldt F. B. *J. Mol. Struct. (Theochem)*, **1995**, *341*, 63-73.

[59] (a) Espinosa E., Lecomte C., Molins E. *Chem. Phys. Lett*. **1999**, *300*, 745-748. (b) Espinosa E., Souhassou M., Lachekarb H., Lecomte C. *Acta Crystallogr*. **1999**, *B55*, 563-572.

[60] Mata I., Alkorta I., Molins E., Espinosa E. *Chem. Eur. J.* **2010**, *16*, 2442-2452.

[61] Metrangolo P., Resnati G. Eds. Halogen Bonding: Fundamentals and Applications; Springer: Berlin, **2008**.

[62] Colin M. *Ann. Chim*. **1814,** *91*, 252.

[63] Guthrie F. *J. Chem. Soc.* **1863**, *16*, 239-244.

[64] Prescott A. B. *J. Am. Chem. Soc*. **1896**, *18*, 91-96.

[65] Vonnegut B., Warren B. E. *J. Am. Chem. Soc*. **1936**, *58*, 2459-2461.

[66] Collin R. L. *Acta Crystallogr*. **1952**, *5*, 431-432.

[67] Benesi H. A., Hildebrand J. H. *J. Am. Chem. Soc*. **1949**, *71*, 2703-2707.

[68] (a) Mulliken R. S. *J. Am. Chem. Soc*. **1950**, *72*, 600-608. (b) Mulliken R. S. *J. Am. Chem. Soc*. **1952**, *74(3)*, 811-824. (c) Mulliken R. S. *J. Am. Chem. Soc*. **1952**, *56*, 801-822.

[69] (a) Keefer R. M., Andrews L. J. *J. Am. Chem. Soc*. **1950**, *72*, 4677-4681. (b) Andrews L. J., Keefer R. M. Holden-Day: San-Francisco, **1964**.

[70] (a) Hassel O., Hvoslef J., Vihovde E., Hadler E. *Acta. Chem. Scand*. **1954**, *8*, 873-873. (b) Hassel O., Rømming C. *Quart. Rev. Chem. Soc*. **1962**, *16*, 1-18.

[71] Hassel O. *Science*, **1970**, *170*, 497-502.

[72] Bent H. A. *Chem. Rev*. **1968**, *68*, 587-648.

[73] Dumas J. M. Bulletin de la Société Chimique de France, **1976**.

[74] Dumas J. M., Peurichard H., Gomel M. *J. Chem. Research*, **1978**, 54-55 Synopses.

[75] (a) Murray-Rust P., Stallings W. C., Monti C. T., Preson R. K., Gluster J. P. *J. Am. Chem. Soc.* **1983**, *105*, 3206-3214. (b) Ramasubbu N., Parthasarathy R., Murray-Rust P. *J. Am. Chem. Soc.* **1986**, *108*, 4308-4314. (c) Desiraju G. R., Parthasarathy R. *J. Am. Chem. Soc*. **1989**, *111*, 8725-8726.

[76] Legon A. C. *Angew. Chem.* **1999**, *38*, 2686-2714.

[77] (a) Murray J. S., Paulsen K., Politzer P. *Proc. Indian Acad. Sci. Ser. Chim*. **1994**, *106*, 267-275. (b) Politzer P., Lane P., Concha M. C., Ma Y. G., Murray J. S. *J. Mol. Model*. **2007**, *13*, 305-311. (c) Clark T., Hennemann M., Murray J. S., Politzer P. *J. Mol. Model*. **2007**, *13*, 291-296. (d) Politzer P., Murray J. S., Concha M. C. *J. Mol. Model*. **2008**, *14*, 659-665. (e) Murray J. S., Lane P., Politzer P. *J Mol. Model*. **2009**, *15*, 723-729. (f) Politzer P., Murray J. S., Lane P. *Int. J. Quant. Chem*. **2007**, *107*, 3046-3052.

[78] Metrangolo P., Resnati G. *Chem. Eur. J.* **2001**, *7*, 2511-2519.

[79] Desiraju G. R. Crystal Engineering: The Design of Organic Solids; Elsevier: Amsterdam, **1989**.

[80] (a) Sakurai T., Sundaralingam M., Jeffrey G. A. *Acta Crystallogr*. **1963,** *16*, 354-363.

[81] Pedireddi V. R., Reddy D. S., Goud B. S., Rae D. C., Desiraju G. R. *J. Chem. Soc., Perkin Trans. 2* **1994**, 2353-2360.

[82] Desiraju G. R., Ho P. S., Kloo L., Legon A. C., Marquardt R., Metrangolo P., Politzer P. A., Resnati G., Rissanen K. Definition of the halogen bond. Recommendation submitted by the IUPAC task groupP.O. 13757, Research Triangle Park, NC (919) 485-8700.

[83] Bui T.T.T., Dahaoui S., Lecomte C., Desiraju G. R., Espinosa E. *Angew. Chem. Int. Ed*., **2009**, *48*, 3838-3841.

[84] (a) Dunitz J. D., Taylor R. *Chem.-Eur. J.* **1997**, *3*, 89. (b) Dunitz J. D. *ChemBioChem*, **2004**, *5*, 637-643; (c) Cozzi F., Bacchi S., Filippini G., Plati T., Gavezzotti, A. *Chem.-Eur. J.* **2007**, *13*, 7177-7184.

[85] Dikundwar A. G. Guru Row T. N. *Cryst. Growth Des.* **2012**, *12*, 1713-1716.

[86] Riley K. E., Hobza P. J. *J. Chem. Thoer. Comput.* **2008**, *4*, 232-242.

[87] Eskandari K., Zariny H. *Chem. Phys. Lett.* **2010**, *492*, 9-13.

[88] (a) Tsirelson V. G., Zou P. F., Tang T. H., Bader R. F. W. *Acta Crystallogr.* **1995**, *A51*, 143-153. (b) Boese R., Boese A. D., Blaser D., Antipin M. Yu., Ellern A., Seppelt K. *Angew. Chem. Int. Ed.* **1997**, *36*, 1489-1492.

[89] Hathwar V. R., Guru Row T. N. *Phys. Chem. A*, **2010**, *114*, 13434-13441.

[90] Williams D. E., Hsu L. Y. *Acta Crystallogr.* **1985**, *A41*, 296-301.

[91] Hathwar V. R., Guru Row T. N. *Cryst. Growth Des.* **2011**, *11*, 1338-1346.

[92] (a) Bianchi R., Forni A., Pilati T. *Chem. Eur. J.* **2003**, *9*, 1631-1638. (b) Bianchi R., Forni A., Pilati T. *Acta Crystallogr.* **2004**, *B60*, 559–568. (c) Forni A. *J. Phys. Chem. A*, **2009**, *113*, 3403-3412.

[93] Bui T. T. T. PhD Thesis, University of Nancy I, France, **2010**.

[94] Hathwar V. R., Gonnade R. G., Munchi P., Bhadbhade M. M., Guru Row T. N. *Cryst. Growth Des.* **2011,** *11*, 1855-1862.

[95] Nelyubina Y. V., Antipin M. Y., Dunin D. S., Kotov V. Y., Lyssenko K. A. *Chem. Commun.* **2010**, *46*, 5325-5327.

[96] (a) Nyburg S. C., Wong-Ng W. *Inorg. Chem.* **1979**, *18*, 2790-2791. (b) Nyburg S. C., Wong-Ng W. *Proc. R. Soc. London, Ser. A* **1979,** *367*, 29-45.

[97] (a) Thakur T. S., Kirchner M. T., Blaser D., Boese R., Desiraju G. R. *CrystEngComm*, **2010**, *12*, 2079-2085. (b) Mehta G., Sen S. *Eur. J. Org. Chem.* **2010**, 3387-3394. (c) Choudhury A. R., Nagarajan K., Guru Row T. N. *Cryst. Eng.* **2004**, *6*, 43-55.

[98] (a) Mallinson P. R., Barr G., Coles S. J., Guru Row T. N., MacNicol D. D., Teat S. J., Wozniak K. J. *Synchrotron Radiat*, **2000**, *7*, 160-166. (b) Chopra D., Cameron T. S., Ferrera J. D., Guru Row T. N. *J. Phys. Chem. A*, **2006**, *110*, 10465-10477. (c) Stash A. I., Civalleri B., Ellern A., Tsirelson V. G. *Mendeleev Commun*, **2010**, *20*, 161-164. (d) Bach A., Lentz D., Luger P. J. *Phys. Chem. A*, **2001**, *105*, 7405-7412 (and references therein).

[99] (a) Zou J. W., Jiang Y. J., Guo M., Hu G. X., Zhang B., Lui H. C., Yu Q. S. *Chem. Eur. J.* **2005**, *11*, 740-750. (b) Lu Y., Zou J., Wang H., Yu Q., Zhang H., Jiang Y. *J. Phys. Chem. A*, **2005**, *109*, 11956-11961. (c) Lu Y. X., Zou J. W., Wang Y. H., Yu Q. S. *J. Mol. Struct.* **2006**, *776*, 83-87. (d) Lu Y. X., Zou J. W., Wang Y. H., Zhang H. X., Yu Q. S., Jiang Y. J. *J. Mol. Struct.* **2006**, *776*, 119-124. (e) Lu Y. X., Zou J. W., Wang Y. H., Yu Q. S. *J. Mol. Struct.* **2006**, *767*, 139-142. (f) Lu Y. X., Zou J. W., Wang Y. H., Jiang Y.J., Yu Q. S. *J. Phys. Chem.* **2007**, *111*, 10781-10788.

[100] Zhou P. P., Qiu W. Y., Liu S., Jin N. Z. *Phys. Chem. Chem. Phys.* **2011**, *13*, 7408-7418.

[101] Awwadi F. F., Willett R. D., Peterson K. A., Twamley B. *Chem. Eur. J.* **2006**, *12*, 8952-8960.

[102] Devillanova F. A Handbook of chalcogen chemistry. New perspectives of Sulfer, Selenium, and Tellurium. The royal society of chemistry Wileys-VCH, Cambridge, UK, **2007**.

[103] Anderson P. W., Lee P. A., Saitoh M. *Solid State Commun.* **1973**, *13*, 595-598.

[104] (a) Rosenfield R. E., Parthasarathy R., Dunitz J. D. *J. Am. Chem. Soc.* **1977**, *99*, 4860-4862. (b) Guru Row T. N., Parthasarathy R. *J. Am. Chem. Soc.* **1981**, *103*, 477-479.

[105] Novoa J. J., Rovira M. C., Rovira C., Veciana J., Tarrés J. *Adv. Mater*. **1995**, *7*, 233-237.

[106] (a) Werz D. B., Staeb T. H., Benisch C., Rausch B. J., Rominger F., Gleiter R. *Org. Lett*. **2002**, *4*, 339-342. (b) Werz D. B., Gleiter R., Rominger F. *J. Am. Chem. Soc*. **2002**, *124*, 10638-10639. (c) Werz D. B., Gleiter R., Rominger F. *J. Org. Chem*. **2004**, *69*, 2945-2952.

[107] (a) Gleiter R., Werz D. B., Rausch B. J. *Chem. Eur. J*. **2003**, *9*, 2676-2683. (b) Gleiter R., Werz D. B. *Chem. Lett*. **2005**, *34*, 126-131.

[108] (a) Werz D. B., Rausch B. J., Gleiter R. *Tetrahedron Lett*. **2002**, *43*, 5767-5769. (b) Schulte J. H., Werz D. B., Rominger F., Gleiter R. *Org. Biomol. Chem*. **2003**, *1*, 2788-2794.

[109] Yi Y., Fa S., Cao W., Zeng L., Wang M., Xu H., Zhang X. *Chem. Commun*., **2012**, *48*, 7495-7497.

[110] Goldstein B. M., Kennedy S. D., Hennen W. J. *J. Am. Chem. Soc*. **1990**, *112*, 8265-8268.

[111] Iwaoka M., Komatsu H., Katsuda T., Tomoda S. *J. Am. Chem. Soc*. **2002**, *124*, 1902-1909.

[112] Cozzolino A. F., Vargas-Baca I., Mansour S., Mahmoudkhani A. H. *J. Am. Chem. Soc*. **2005**, *127*, 3184-3190.

[113] (a) Suturina E. A., Semenov N. A., Lonchakov A. V., Bagryanskaya I. Y., Gatilov Y. V., Irtegova I. G., Vasilieva N. V., Lork E., Mews R., Gritsan N. P., Zibarev A. V. *J. Phys. Chem. A* **2011**, *115*, 4851-4860. (b) Santi C., Santoro S., Tiecco M. conference article ECSOC-15. http://www.sciforum.net/conf/ecsoc-15.

[114] Iwaoka, M., Tomoda, S. J. Am. Chem. Soc. 1996, 118, 8077-8084.

[115] Behera R. N., Panda A. *RSC Adv*. **2012**, *2*, 6948-6956.

[116] (a) Madzhidov T. I., Chmutova G. A. *J. Phys. Chem*. **2011,** *A115*, 10069-10077. (b) Madzhidov T., Chmutova G. *J. Mol. Struct. (Theochem)* **2010**, *959*, 1-7.

[117] (a) Bleiholder C., Werz D. B., Köpel H., Gleiter R. *J. Am. Chem. Soc*. **2006**, *128*, 2266-2274. (b) Bleiholder C., Gleiter R., Werz D. B., Köpel H. *Inorg. Chem*. **2007**, *46*, 2249-2260.

[118] Sánchez-Sanz G., Trujillo C., Alkorta I., Elguero J. *ChemPhysChem* **2012**, *13*, 496-503.

[119] Li Q.-Z., Li R., Guo P; Li H., Li W.-Z., Cheng J.-B. *Comput. Theor. Chem*. **2012**, *980*, 56-61.

[120] Wang W. Z, Ji B. M., Zhang Y. *J. Phys. Chem. A* **2009**, *113*, 8132-8135.

[121] Li Q.-Z., Qi H., Li R., Liu X.-F., Li W.-Z., Cheng J.-B. *Chem. Chem. Phys*. **2012**, *14*, 3025-3030.

[122] Lee C.-R., Tang T.-H., Chen L., Wang C.-C., Wang Y. *J. Phys. Chem. Sol*. **2004**, *65*, 1957-1966.

[123] Scherer W., Spiegler M., Pedersen B., Tafipolsky M., Hieringer W., Reinhard B., Downs A., McGrady G. S. *Chem. Commun*. **2000**, 635-636.

[124] Komatsu H., Iwaoka M., Tomoda S. *Chem. Commun*. **1999**, 205-206.

[125] Iwaoka M., Komatsu H., Katsuda T., Tomoda S. *J. Am. Chem. Sos*. **2004**, *126*, 5309-5317.

[126] Iwaoka M., Katsuda T., Komatsu H., Tomoda S. *J. Org. Chem*. **2005**, *70*, 321-327.

[127] Iwaoka M., Takemoto S., Okada M., Tomoda S. *Bull. Chem. Soc. Jpn*. **2002**, *75*, 1611-1625.

[128] Koketsu M., Nada F., Hiramatsu S., Ishihara H. *J. Chem. Soc. Perkin Trans.1*, **2002**, 737-740.

[129] Domercq B., Devic T., Fourmigué M., Auban-Senzier P., Canadell E. *J. Mater. Chem*. **2001**, *11*, 1570-1575.

[130] CrysAlisPro CCD and CrisAlisPro RED, Oxford Diffraction Ltd, **2009**.

[131] DeTitta G. T. *J. Appl. Cryst*. **1985**, *18*, 75-79.

[132] Blessing R. H. *Crystallogr. Rev*. **1987**, *1*, 3-58.

[133] Altomare A., Cascarano G., Giacovazzo C., Guagliardi A., Burla M. C., Polidori G., Camalli M. *J. Appl. Crystallogr*. **1994**, *27*, 435-436.

[134] Sheldrick G. M. *Acta Crystallogr. Sect. A* **2008**, *64,* 112-122.

[135] Farrugia L. J. WinGX (Version 1.80.05). *J. Appl. Crystallogr*. **1999**, *32*, 837-838.

[136] Allen F.H., Kennard O., Watson D.G., Brammer L., Orpen A.G. *J. Chem. Soc. Perkin Trans. II*, **1987**, *12*, S1-S19.

[137] Macrae C. F., Edgington P. R., McCabe P., Pidcock E., Shields G. P., Taylor R., Towler M. van de Streek J. *J. Appl. Crystallogr*. **2006**, *39*, 453-457.

[138] Perdew J. P., Burke K., Ernzerhof M. *J. Chem. Phys*. **1996**, *77*, 3865-3868.

[139] Frisch M. J., Trucks G. W., Schlegel H. B., Scuseria G. E., Robb M. A. et al. Gaussian 09, Revision C.01, Gaussian, Inc., Wallingford, CT, **2010**.

[140] Keith T. A. TK Gristmill Software, Overland Park KS, USA, 2012 (aim.tkgristmill.com), AIMAll (Version 12.06.03).

[141] Domagala S., Jelsch C. *J. Appl. Cryst*. **2008**, *41*, 1140-1149.

[142] (a) Bendeif E. E. PhD Thesis, University of Nancy I, **2006**. (b) Garcia P. PhD Thesis, University of Nancy I, **2007**.

[143] Stewart R. F., Davidson E. R., Simpson W. T. *J. Chem. Phys.* **1965**, *42*, 3175-3187.

[144] Dominiak P. M., Espinosa E., Ángyán J. G. In Modern Charge Density Analysis; Gatti C., Macchi P., Eds.; Springer: Berlin, **2012**, 387-434.

[145] (a) Matta C. F., Castillo N., Boyd R. *J. J. Phys. Chem. B* **2006**, *110*, 563-578. (b) Lyssenko K. A., Borissova A. O., Burlov A. S., Vasilchenko I. S., Garnovskii A. D., Minkin V. I., Antipin M. Y. *Mendeleev Commun*. **2007**, *14*, 164-166. (c) Nelyubina Y. V., Antipin M. Y., Lyssenko K. A. *J. Phys. Chem. A* **2009**, *113*, 3615-3620. (d) Lyssenko K. A., Barzilovich P. Y., Aldoshin S. M., Antipin M. Y., Dobrovolsky Y. A. *Mendeleev Commun*. **2008**, *18*, 312-314. (e) Nelyubina Y. V., Troyanov S. I., Antipin M. Y., Lyssenko K. A. *J. Phys. Chem. A* **2009**, *113*, 5151-5156. (f) Lyssenko K. A., Nelubina Y. V., Safronov D. V., Haustova O. I., Kostyanovsky R. G., Lenev D. A., Antipin M. Y. *Mendeleev Commun*. **2005**, *15*, 32-36. (g) Korlyukov A. A., Lyssenko K. A., Antipin M. Y., Grebneva E. A., Albanov A. I., Trofimova O. M., Zel'bst E. A., Voronkov M. G. *J. Organomet. Chem*. **2009**, *694*, 607-615. (h) Nelyubina Y. V., Lyssenko K. A., Kostyanovsky R. G., Bakulin D. A., Antipin M. Y. *Mendeleev Commun*. **2008**, *18*, 29-31. (i) Nelyubina Y. V., Lyssenko K. A., Golovanov D. G., Antipin M. Y. *CrystEngComm.* **2007**, *9*, 991-996. (j) Nelyubina Y. V., Antipin M. Y., Lyssenko K. A. *J. Phys. Chem. A* **2007**, *111*, 1091-1095. (k) Borissova A. O., Antipin M. Y., Perekalin D. S., Lyssenko K. A. *CrystEngComm* **2008**, *10*, 827-832. (l) Lyssenko K. A., Korlyukov A. A., Golovanov D. G., Ketkov S. Y., Antipin M. Y. *J. Phys. Chem. A* **2006**, *110*, 6545-6551. (m) Borissova A. O., Korlyukov A. A., Antipin M. Y., Lyssenko K. A. *J. Phys. Chem. A* **2008**, *112*, 11519-11522. (n) Peganova T. A., Valyaeva A., Kalsin A. M., Petrovskii P. V., Borissova A. O., Lyssenko K. A., Ustynyuk N. A. *Organometallics* **2009**, *10*, 3021-3028. (o) Puntus L. N., Lyssenko K. A., Antipin M. Y., Büunzli J. C. G. *Inorg. Chem*. **2008**, *47*, 11095-11107. (p) Bushmarinov I. S., Antipin M. Y., Akhmetova V. R., Nadyrgulova G. R., Lyssenko K. A. *J. Phys. Chem. A* **2008**, *112*, 5017-5023.

[146] Baharie E., Pawley G. S. *Acta Crystallogr. Sect. A* **1979**, *35*, 233-235.

[147] Brown G. M., Strydom O. A. W. *Acta Crystallogr. Sect. B* **1974**, *30*, 801-804.

[148] Bondi A. *J. Phys. Chem.* **1964**, *68*, 441-451.

[149] Reddy C. M., Kirchner M. T., Gundakaram R. C., Padmanabhan K. A., Desiraju G. R. *Chem. Eur. J.* **2006**, *12*, 2222-2234.

[150] Wójcik G., Toupet L., Gors C., Foulon M. *Phys. Stat. Sol. Sect. A* **1995**, *147*, 99-109.

[151] Betz R., Klüfers P., Mayer P. *Acta Crystallogr. Sect E* **2008**, *64*, o1921.

[152] (a) Das D., Banerjee R., Mondal R., Howard J. A. K., Boese R., Desiraju G. R. *Chem. Commun.* **2006**, 555-557. (b) Taylor R., Macrae C. F. *Acta Crystallogr., Sect. B* **2001**, *57*, 815-827. (c) Oswald D. H., Allan D. R., Motherwell W. D. S., Parsons S. *Acta Crystallogr., Sect. B* **2005**, *61*, 69-79. (d) Gdaniec M. *CrystEngComm.* **2007**, *9*, 286-288.

[153] (a) Nobeli I., Price S. L. *J. Phys. Chem., Sect. B* **1999**, *103*, 6448-6457. (b) Desiraju G. R. *CrystEngComm.* **2007**, *9*, 91-92.

[154] Garcia P., Dahaoui S., Katan C., Souhassou M., Lecomte C. *Faraday Discuss.* **2007**, *135*, 217-235.

[155] Sakurai T. *Acta Crystallogr.* **1962**, *15*, 1164-1173.

[156] Wójcik G., Rohleder J. W. *Acta Phys. Polon. A* **1976**, *49*, 485-494.

[157] Majeed Z., McWhinnie W. R., Paxton K., Hamor T. A. *J. Organomet. Chem.* **1999**, *577*, 15-18.

[158] Cole J. M., Goeta A. E., Howard J. A. K., Mclntyre G. *J. Acta Cryst.* **2002**, *B58*, 690-700.

[159] Bader R. F. W. *Chem. Rev.*, **1991**, *91*, 893-928

[160] Anthony A., Desiraju G. R., Kuduva S. S., Madhavi N. N. L., Nangia A., Thaimattam R., Thalladi V. R. *Cryst. Eng.* **1998**, *1*, 1-18.

[161] Jetti R. K. R., Xue F., Mak T. C. W., Nangia A. *Cryst. Eng.* **1999**, *2*, 215-224.

[162] Bosch E., Barnes C. L. *Cryst. Growth Des*. **2002**, *2*, 299-302.

[163] Saha B. K., Jetti R. K. R., Reddy L. S., Aitipamula S., Nangia A. *Cryst. Growth Des*. **2005**, *5*, 887-899.

[164] Solimannejad M., Malekani M., Alkorta I. *J. Phys. Chem. A* **2010**, *114*, 12106-12111.

[165] (a) Ermer O. *Angew. Chem. Int. Ed. Engl*. **1994**, *33*, 471-476. (b) Brock C. P., Duncan L. L. *Chem. Mater.* **1994**, *6*, 1307-1312.

[166] Zhang X., Zeng Y., Li X., Meng L., Zheng S. *Struct. Chem.* **2011**, *22*, 567-576.

[167] Prasanna M. D.; Guru Row T. N. *Cryst. Eng.* **2000**, *3*, 135-154.

[168] Bresciani N.; Caligaris M. *Acta. Cryst.* **1975**, *B31*, 2685-2686.

[169] (a) Bader R. F. W. *J. Phys. Chem. A* **1998**, *102*, 7314-7323. (b) Bader R. F. W. *J. Phys. Chem. A* **2009**, *113*, 10391-10396.

[170] Aakeröy C. B., Fasulo M., Schultheiss N., Desper J., Moore C. *J. Am. Chem. Soc.* **2007**, *129*, 13772-13773.

[171] (a) Di Paolo T., Sandorfy C. *Chem. Phys. Lett.* **1974**, *26*, 466-469. (b) Riley K. E., Murray J. S., Concha M. C., Politzer P., Hobza P. *J. Chem. Theor. Comp.* **2009**, *5*, 155-163. (c) Corradi E., Meille S. V., Messina M.T., Metrangolo P., Resnati G. *Angew. Chem. Int. Ed.* **2000**, *39*, 1782-1786. (d) Alkorta I., Blanco F., Solimannejad M., Elguero J. *J. Phys. Chem. A* **2008**, *112*, 1085-10863. (e) Metrangolo P., Neukirch H., Pilati T., Resnati G. *Acc. Chem. Res.* **2005**, *38*, 386-395.

[172] Li Q.-Z., Xu X.-S., Liu T., Jing B., Li W. Z., Cheng J. B., Gong B. A., Sun J. Z. *Phys. Chem. Chem. Phys.* **2010**, *12*, 6837-6843.

[173] Li Q.-Z., Jing B., Li R., Liu Z. B., Li W. Z., Luan F., Cheng J. B., Gong B. A., Sun J. Z. *Phys. Chem. Chem. Phys.* **2011**, 13, 2266-2271.

[174] Li Q.-Z., Jing B., Liu Z. B., Li W. Z., Cheng J. B., Gong B. A., Sun J. Z. *J. Mol. Struct. Theochem* **2010**, *952*, 90-95.

[175] (a) Gavezzotti A. *J. Phys. Chem. Sect. B* **2003**, *107*, 2344-2353. (b) Gavezzotti A. OPiX University of Milano: Italy **2003**.

[176] Abbou M., Kadimi A., Mamane V., Aubert E. *Acta Crystallogr. Sect. C* **2010**, *66*, o381-384.

[177] (a) Boyd R. J., Choi S. C. *Chem. Phys. Lett.* **1985**, *120*, 80-85. (b) Knop O., Boyd R. J., Choi S. C. *J. Am. Chem. Soc.* **1988**, *110*, 7299-7301.

[178] (a) Knop O., Rankin K. N., Boyd R. J. *J. Phys. Chem. A* **2001**, *105*, 6552-6566. (b) Knop O., Rankin K. N., Boyd R. J. *J. Phys. Chem. A* **2003**, *107*, 272-284.

[179] Dominiak P. M., Makal A., Mallinson P. R., Trzcinska K., Eilmes J., Grech E., Chruszcz M., Minor W., Wozniak K. *Chem. Eur. J.* **2006**, *12*, 1941-1949.

[180] Vener M. V., Manaev A. V., Egorova A. N., Tsirelson V. G. *J. Phys. Chem. A* **2007**, *111*, 1155 - 1162.

[181] Costales A., Blanco M. A., Marten Pendos A., Mori-Sanchez P., Luaka V. *J. Phys. Chem. A* **2004**, *108*, 2794-2801.

[182] (a) Gibbs G. V., Wallace A. F., Cox D. F., Dove P. M., Downs R. T., Ross N. L., Rosso K. M. *J. Phys. Chem.* **2009**, *113*, 736-749. (b) Gibbs G. V., Wallace A. F., Downs R. T., Ross N. L., Cox D. F., Rosso K. M. *Phys. Chem. Min.* **2011**, *38*, 267-291.

[183] (a) Brezgunova M., Shin K.-S., Auban-Senzier P., Jeannin O., Fourmigué M. *Chem. Commun.* **2010**, *46*, 3926-3928. (b) Shin K.-S., Brezgunova M., Jeannin O., Roisnel T., Camerel F., Auban-Senzier P., Fourmigué M. *Cryst. Growth Des.* **2011**, *11*, 5337-5345.